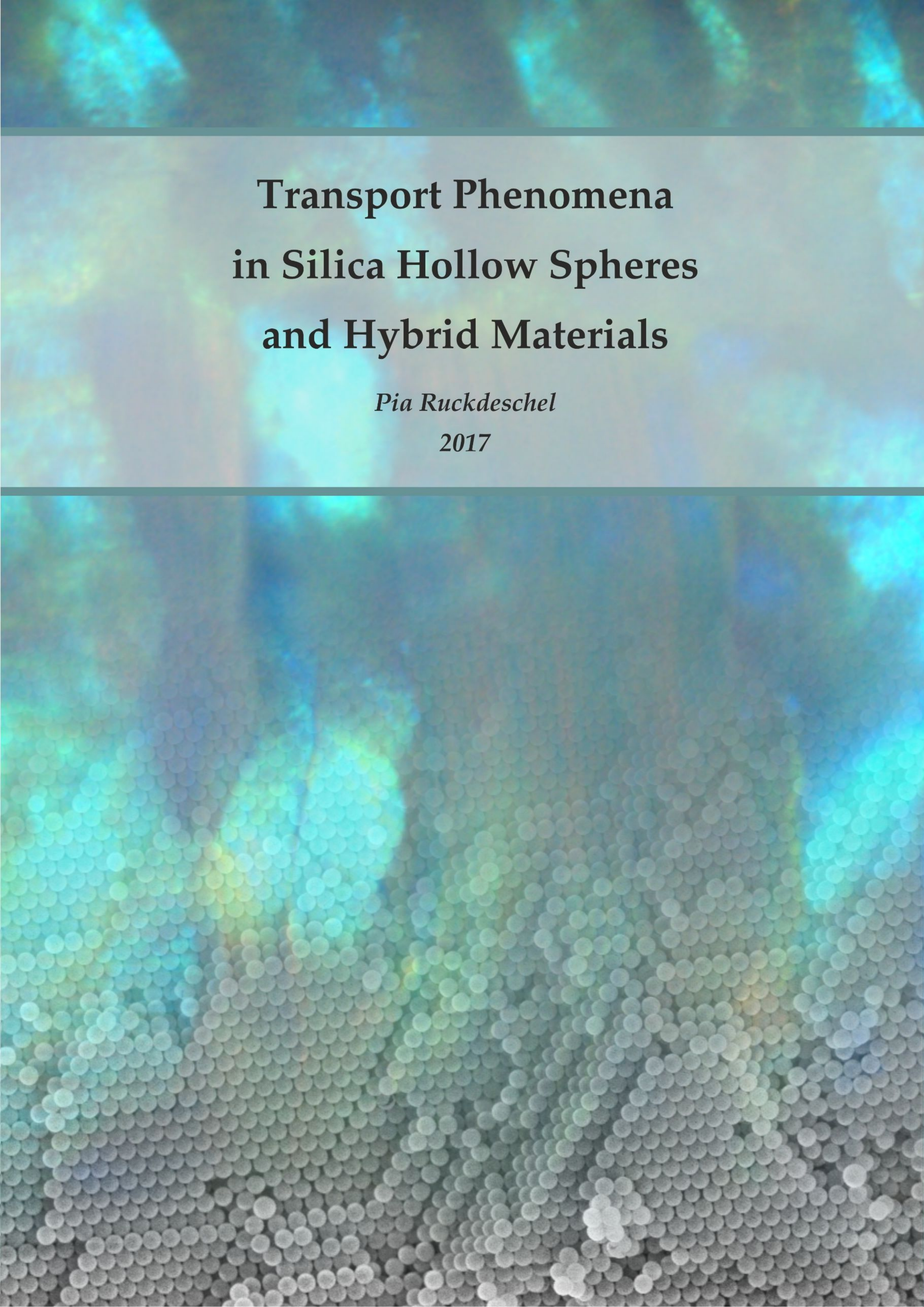

Transport Phenomena in Silica Hollow Spheres and Hybrid Materials

Pia Ruckdeschel

2017

Transport Phenomena in Silica Hollow Spheres and Hybrid Materials

DISSERTATION

zur Erlangung des akademischen Grades
Doktor der Naturwissenschaften (Dr. rer. nat.)
im Promotionsfach Chemie

vorgelegt von

Pia Ruckdeschel

geboren in Münchberg

Bayreuth 2017

Die vorliegende Arbeit wurde in der Zeit von März 2014 bis August 2017 unter der Betreuung von Herrn Prof. Markus Retsch, Physikalische Chemie I – Polymere Systeme, an der Universität Bayreuth angefertigt.

Dissertation eingereicht am: 28.08.2017

Zulassung durch die Promotionskommission: 28.09.2017

Wissenschaftliches Kolloquium: 06.02.2018

Amtierender Dekan: Prof. Dr. Stefan Peiffer

Prüfungsausschuss:

Prof. Dr. Markus Retsch	Erstgutachter
Prof. Dr. Andreas Greiner	Zweitgutachter
Prof. Dr. Mukundan Thelakkat	Vorsitz
Prof. Dr. Mirijam Zobel	

Für meine
Familie ♡

Table of Contents

Abbrevations

AIBA	2,2′-azobis(2-methylpropionamidine) dihydrochloride
BET	according to Brunauer, Emmett, and Teller
CC	colloidal crystal
CLEM	correlative light and electron microscopy
CS	core-shell
DFT	density functional theory
DLS	dynamic light scattering
DLVO	according to Derjaguin, Landau, Verwey, and Overbeek
DS	dielectric spectroscopy
DSC	differential scanning calorimetry
EA	elemental analysis
fcc	face-centered cubic
FEM	finite element modeling
hcp	hexagonal close-packed
HS	hollow spheres
HSNP	hollow silica nanoparticles
MAS	magic-angle spinning
MFP	mean free path
MTC	[2-(methacryloyloxy)ethyl]trimethylammonium chloride
NLDFT	non-local density functional theory
NMR	nuclear magnetic resonance
PMMA	poly(methyl methacrylate)
PS	polystyrene
PVP	polyvinylpyrrolidone
SAXS	small-angle X-ray scattering
SEM	scanning electron microscopy
SLS	static light scattering
TEM	transmission electron microscopy
TEOS	tetraethyl orthosilicate
T_g	glass transition temperature
XFA	xenon flash analysis

List of Publications

(1) *Hollow silica sphere colloidal crystals: insights into calcination dependent thermal transport.*

P. Ruckdeschel, T. W. Kemnitzer, F. A. Nutz, J. Senker, and M. Retsch, *Nanoscale*, **2015**, 7, 10059.

(2) *Polystyrene colloidal crystals: Interface controlled thermal conductivity in an open-porous mesoparticle superstructure.*

F. A. Nutz, P. Ruckdeschel, M. Retsch, *Journal of Colloid and Interface Science*, **2015**, 457, 96.

(3) *Monodisperse hollow silica spheres: An in-depth scattering analysis.*

P. Ruckdeschel, M. Dulle, T. Honold, S. Förster, M. Karg, and M. Retsch, *Nano Research*, **2016**, 9 (5), 1366.

(4) *Homogeneous Nucleation of Ice Confined in Hollow Silica Spheres.*

Y. Yao, P. Ruckdeschel, R. Graf, H.-J. Butt, M. Retsch, and G. Floudas, *The Journal of Physical Chemistry B,* **2017**, 121 (1), 306.

(5) *Understanding Thermal Insulation in Porous, Particulate Materials.*

P. Ruckdeschel, A. Philipp, and M. Retsch, *Advanced Functional Materials,* **2017,** 27 (38), 1702256.

(6) *Thermal Transport in Colloidal Crystals.*

F. A. Nutz§, P. Ruckdeschel§, and M. Retsch, *submitted,* **2017**.

§ Both authors contributed equally to the work.

(7) *Interface and Morphology Control of the Thermal Conductivity in Core-Shell Particle Colloidal Crystals.*

P. Ruckdeschel, and M. Retsch, *Advanced Materials Interfaces,* **2017**, 4 (24), 1700963.

(8) *Thermal Transport in Binary Colloidal Glasses: Composition Dependence and Percolation Assessment.*

P. Ruckdeschel, A. Philipp, B. A. F. Kopera, F. Bitterlich, M. Dulle, N. W. Pech-May and M. Retsch, *Physical Review E*, **2017**, 97 (2), 022612.

List of Contributions

(1) Oral presentation about *„Thermal Conductivity of Hollow Silica Nanoparticle Colloidal Crystals – Microstructure Dependent Study“* at the Zsigmondy Colloquium of the German Colloid Society, **2015**, Regensburg (DE).

(2) Poster presentation about *"Thermal Conductivity of Hollow Silica Nanoparticle Colloidal Crystals"* at the Material Research Society Spring Meeting and Exhibit (MRS), **2015**, San Francisco (US).

(3) Oral presentation about *„Thermal Conductivity of Silica Hollow Spheres and Polystyrene-Silica Core-Shell Particles: Size and Composition Dependent Study“* at the Zsigmondy Colloquium of the German Colloid Society, **2016**, Bielefeld (DE).

(4) Poster presentation about *"Thermal Transport of Hollow Silica Sphere and Polystyrene-Silica Core-Shell Particle Colloidal Crystals"* at the Conference of the European Colloid and Interface Society (ECIS), **2016**, Rome (IT).

Summary

Heat transport is a key energetic process in nanostructured materials and devices, e.g., for (opto)electronics, thermoelectrics, and thermal insulation. The indispensable comprehension of nanoscale thermal transport can be motivated by (i) the demand for novel technologies to solve energy problems by using more efficient ways of energy generation, storage, and usage, and by (ii) the demand for heat management due to the miniaturization of electronic devices which may lead to localized, increased energy densities in devices. Accordingly, thermal transport in nanostructured materials is in the focus of current research activities.

Notwithstanding, little is known about thermal transport in colloidally structured materials. This is all the more surprising considering their unique properties, for instance, the flexibility of the material composition (e.g., polymers, inorganic materials, or hybrid materials), and the possibility to adjust the packing symmetry and the interfaces or surface chemistry. Furthermore, colloidal assemblies are readily available on relatively large scales. Therefore, colloidal superstructures represent a suitable model system, which allows for developing a detailed understanding of the underlying physics and for studying the governing structure-property relationships.

In this thesis, colloidal crystals consisting of silica hollow spheres or hybrid materials were used to understand heat transport phenomena. First, the extremely low polydispersity of the silica hollow sphere particles was highlighted using transmission electron microscopy (TEM), and different scattering methods: dynamic and static light scattering (DLS and SLS), as well as small-angle X-ray scattering (SAXS). The well-defined structure of the silica hollow spheres – tens of nanometer shell thickness and hundreds of nanometer particle size – is of great importance to assemble them into highly ordered colloidal assemblies.

These hierarchically structured 3D nanomaterials based on such hollow spheres were characterized in the second part regarding the heat transport. Here, the influence of the geometry of the hollow silica spheres (size and shell thickness), the gaseous conduction (open- vs. closed-pore conduction), the symmetry of the whole assembly (close-packing vs. random close-packing), the bonding strength between adjacent spheres, and the microstructure within the silica shell were elucidated. Additionaly, finite element modeling helped to clarify the heat transport in colloidal assemblies further. Generally, the silica hollow sphere colloidal assemblies are highly insulating. This can be traced back to the amorphous nature of the silica, a large number of interfaces, and the low density of the arrays. The lower limit of the thermal conductivity was found to be less than 10 $\mathrm{mW m^{-1} K^{-1}}$ in vacuum.

In the final part, nanoscale heat transport phenomena were studied in hybrid materials: core-shell particle colloidal crystals and binary colloidal assemblies.

In binary colloidal assemblies comprising hollow silica spheres and polymer latex particles, the colloids were randomly mixed. The thermal conductivity increases in these colloidal glasses with increasing polymer content without any percolation threshold. This trend can be well described by the effective medium theory. Finite element modeling clarified that a percolation threshold is only apparent for large thermal conductivity contrasts of the two types of particles. However, by heating the binary mixtures above the glass transition temperature of the polymer, a continuous polymer network was formed with nanoinclusions of the hollow spheres leading to a distinctly increased thermal conductivity at a certain polymer volume fraction.

Instead of mixing silica hollow spheres with polymer particles, one can also tune the polymer/silica ratio just by the core-shell particle morphology. Here, in contrast to the hollow capsules, the core is filled with polystyrene instead of air. It has been shown that the effective thermal conductivity increased with an increasing polymer volume fraction. The temperature-dependent transport properties, however, strongly depended on the encapsulation efficiency of the polymer core. Leakage can occur for shell thicknesses up to about 15 nm. Nevertheless, temperatures much higher than the glass transition temperature of the polymer were necessary for the polymer to leak out of the capsule.

The understanding of heat transport in core-shell particles is of peculiar interest for phase change materials. Quite importantly, nanostructured phase change materials may suffer severe undercooling effects. The undercooling effect in confined systems was investigated using water inside the hollow silica spheres. Heterogeneous nucleation is suppressed due to the confined geometry leading to a delayed ice crystallization by as much as −40 °C. The effect of undercooling is shown for water but also matters for encapsulated polymer.

In conclusion, this thesis demonstrates the enormous potential offered by colloidally structured materials to the emerging field of smart thermal nanomaterials. Prospectively, a wide range of further studies can be conceived to exploit the potential that has been demonstrated within this thesis. One focus may be laid on multifunctional materials, in which the thermal properties are combined with (i) electrical conductivity leading to thermoelectric materials, (ii) optical properties to obtain for instance transparent insulation materials, or (iii) improved mechanical properties.

Zusammenfassung

Wärmetransport ist ein wichtiger energetischer Prozess in nanostrukturierten Materialien und Bauteilen, z.B. im Bereich der (Opto)elektronik, der Thermoelektrik und der Wärmeisolation. Das Verständnis für Wärmetransport in nanostrukturierten Materialien ist dabei insbesondere relevant wegen (i) der Nachfrage nach neuartigen Technologien zur Lösung von Energieproblemen durch effizientere Methoden der Energieerzeugung, -speicherung und -nutzung und (ii) der Notwendigkeit des Wärmemanagements aufgrund der Miniaturisierung von elektronischen Bauteilen. Letzteres kann zu lokalisierten, erhöhten Energiedichten in Bauteilen führen. Dementsprechend hat die Untersuchung des Wärmetransports in nanostrukturierten Materialien einen wichtigen Platz in der aktuellen Forschung eingenommen.

Trotzdem ist bisher nur wenig über Wärmetransport in kolloidal-strukturierten Assemblierungen bekannt. Dies ist umso verwunderlicher, betrachtet man die einzigartigen Eigenschaften, wie zum Beispiel die Bandbreite an möglichen Materialien (Polymere, anorganische Materialien oder Hybridmaterialien) und die Möglichkeit, die Symmetrie der Packung und die Grenzflächen- und Oberflächenchemie einzustellen. Weiterhin sind kolloidale Baugruppen relativ einfach in großen Mengen herstellbar. Somit stellen kolloidale Assemblierungen ein geeignetes Modellsystem dar, um ein fundiertes Verständnis der zugrunde liegenden Physik zu erhalten und die Struktur-Eigenschafts-Beziehungen zu untersuchen.

In dieser Arbeit wurden Wärmetransport-Phänomene mit Hilfe von kolloidalen Kristallen untersucht, welche aus Silica-Hohlkugeln oder Hybridmaterialien bestehen. Zunächst wurde die extrem niedrige Polydispersität der Hohlkugel-Partikel mit verschiedenen Streumethoden (dynamische und statische Lichtstreuung, sowie Kleinwinkel-Röntgenstreuung) herausgestellt. Die gut

definierte Struktur – ~10 – 100 nm Schalendicke und ~100 – 1000 nm Partikelgröße – ist von großer Bedeutung, um hochgeordnete kolloidale Strukturen aufzubauen.

Diese dreidimensionalen Materialien, welche auf Hohlkugeln basieren, wurden im zweiten Teil hinsichtlich des Wärmetransports charakterisiert. Dabei wurden insbesondere der Einfluss der Geometrie der Hohlkugeln (Größe und Schalendicke), des Wärmetransports über die Gasphase (offenporiges vs. geschlossenporiges Volumen), der Symmetrie der Packung (dichteste vs. ungeordnete Kugelpackung), der Bindungsstärke zwischen benachbarten Partikeln und der Mikrostruktur innerhalb der Schale im Detail aufgeklärt. Zusätzlich wurden die Untersuchungen mit der Finite-Elemente-Methode unterstützt. Zusammenfassend konnte der stark wärmeisolierende Charakter der Silica-Hohlkugeln gezeigt werden. Dies kann auf die amorphe Struktur des Siliciumdioxids, der großen Anzahl an Grenzflächen zwischen den Partikeln und die geringe Dichte des Materials zurückgeführt werden. Die niedrigste Wärmeleitfähigkeit betrug dabei weniger als 10 $\mathrm{m\,W\,m^{-1}\,K^{-1}}$ in Vakuum.

Im letzten Teil wurden Wärmetransport-Phänomene auf der Nanoskala in Hybrid-Materialien untersucht: Binäre kolloidale Kristalle und kolloidale Kristalle bestehend aus Kern-Schale-Partikeln.

Für die binären kolloidalen Assemblierungen wurden Silica-Hohlkugeln und Polymerlatex-Partikel mit dem Ziel einer zufälligen Anordnung gemischt und hinsichtlich des Wärmetransports charakterisiert. Dabei konnten eine Abnahme der Wärmeleitfähigkeit mit zunehmendem Polymergehalt und eine Übereinstimmung mit der Effektiv-Medium Theorie nachgewiesen werden. Eine Perkolation trat jedoch nicht auf, da die Unterschiede in den Wärmeleitfähigkeiten zwischen den beiden Partikeln zu gering waren. Diese Ergebnisse wurden mit der Finite-Elemente-Methode unterstützt. Erst durch das Erhitzen der binären Mischungen über die Glasübergangstemperatur des Polymers konnte ein perkolationsfähiges Polymernetzwerk gebildet werden, was zu einer deutlich erhöhten Wärmeleitfähigkeit ab einem bestimmten Polymer-Volumenanteil führte.

Anstelle des Mischens von Hohlkugeln mit Polymerpartikeln kann das Polymer/Silica-Verhältnis auch durch die Kern-Schale-Partikelmorphologie abgestimmt werden. Hier ist – im Gegensatz zu den Hohlkugeln – der Kern mit Polystyrol anstelle von Luft gefüllt. Dabei zeigte sich eine Zunahme der Wärmeleitfähigkeit mit zunehmendem Anteil an Polymervolumen. Bei temperaturabhängigen Messungen stellte sich heraus, dass bei einer Schalendicke bis ~15 nm, Polymer aus den Kapseln austrat und somit die Wärmeleitfähigkeit aufgrund der Vergrößerung der Grenzfläche anstieg. Allerdings waren hierfür Temperaturen weit über der Glasübergangstemperatur des Polymers nötig. Das Verständnis des Wärmetransports in Kern-Schale-Partikeln ist insbesondere für *Phase-Change*-Materialien von Interesse. Allerdings kann bei nanostrukturierten Kern-Schale-Materialien eine Unterkühlung (verzögerte Kristallisation) auftreten. Dies wurde im Folgenden anhand von wassergefüllten Silica-Hohlkugeln untersucht. Dabei zeigte sich eine verzögerte Eiskristallisation bei etwa -40 °C, da die heterogene Keimbildung aufgrund der begrenzten Geometrie unterdrückt wurde. Die Wirkung der Unterkühlung wurde für Wasser gezeigt, ist aber auch für verkapseltes Polymer relevant.

Zusammenfassend zeigt diese Arbeit das enorme Potenzial von kolloidal-strukturierten Materialien in dem aufstrebenden Bereich der intelligenten thermischen Nanomaterialien. Vorausblickend kann ein breites Spektrum weiterer Studien konzipiert werden, um das in dieser Arbeit bewiesene Potenzial auszuschöpfen. Ein Schwerpunkt kann dabei auf multifunktionelle Materialien gelegt werden, bei welchen die thermischen Eigenschaften mit weiteren Eigenschaften kombiniert werden. Beispiele hierfür wären (i) eine Kombination mit elektrischer Leitfähigkeit, um thermoelektrische Materialien zu bekommen, (ii) eine Verbesserung der optischen Eigenschaften, um beispielsweise transparente Isoliermaterialien zu erhalten, oder (iii) die Optimierung der mechanischen Eigenschaften.

1 Motivation

Heat transport and the thermal performance of nanostructured materials is of major interest for many technological applications, such as insulation materials[1], thermal cloaks[2], thermal barrier coatings[3], and thermoelectric materials[4-6]. However, there are many other technologies for which the ability to manipulate heat is important even if it is not the primary goal, for instance for phase change materials[7] or for nanoscale (opto)electronic devices[7-8]. While nanostructured materials can solve energy problems by using more efficient ways of energy storage, usage, and generation, the miniaturization of electronic devices and the increasing energy density can lead to localized, high temperatures (hot spots). Thus, nanoscale heat transfer is a key energetic issue for the functioning and stability of nanostructured materials and devices.[9-10]

Colloidally self-assembled materials represent a versatile model system to understand the fundamentals of heat transport in nanostructured materials and the governing structure-property relationships. This can be traced back to numerous key features of colloidal crystals (Figure 1.1): (i) ease of fabrication, (ii) approachability to hierarchical nano- and mesostructured materials, (iii) flexibility of the material composition (polymers, metal oxides, composite materials, etc.), (iv) adjustment of the packing symmetry, and (v) adjustment of the interfaces/surface chemistry. These unique properties, which are unified in colloidal assemblies are utilized in this work to show the great potential to understand and tune heat transport on the nanoscale. As a model system, hollow silica colloidal crystals are in the focus of this work. These arrays distinguish themselves as a highly insulating material class. Importantly, the hollow sphere assemblies provide the opportunity to tune the microporosity, the geometry of the capsules (size and shell thickness of the hollow spheres), the pore arrangement (close-packing and random close-packing), and even the bonding strength between adjacent spheres properly. Moreover, this concept was transferred to other hybrid materials, such as core-shell particle colloidal crystals and binary particle mixtures consisting of hollow spheres and polymer particles. These two materials can be used as a model system to understand heat transport in phase change materials and even assess the percolation mechanism.[11]

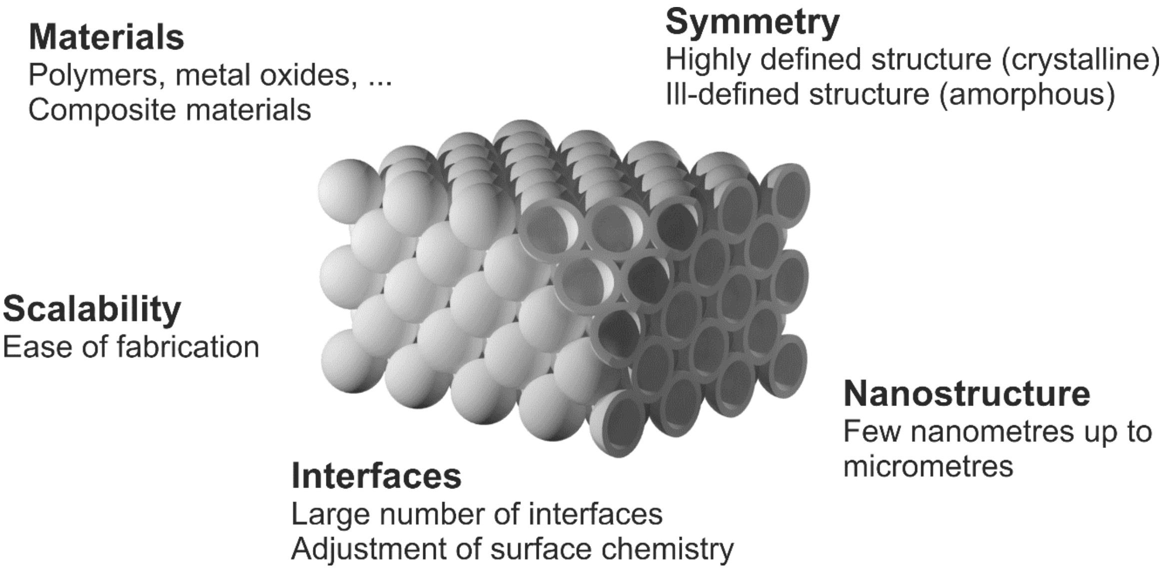

Figure 1.1. Overview of the benefits of colloidal assemblies regarding their heat transport properties.

This thesis will start with an overview of the fundamentals of colloidal assemblies (Chapter 2.1) with a general introduction to colloidal materials, their stability, and their assembly. Subsequently, the basics of heat transfer in dielectric materials are introduced in Chapter 2.2 with a focus on thermal transport in bulk matter, porous matter, and colloidal crystals. After the introduction about colloids and their heat transport properties, a 'Materials and Methods' part follows in Chapter 3. Here, the synthesis and characterization of the particles and the particle assemblies are described. Chapter 4 gives an overview of the different contributions, which follow in Chapter 6 – 11. In the last chapter, the main results and concepts of the presented publications are wrapped up. Based on these results implications for future research directions will be given, and the attention for the underexplored world of thermal transport in colloidal materials will be raised.

2 Theoretical Overview

2.1 Colloidal Crystals

Colloids have been gaining an increasingly scientific and technological interest in the last decades. Significant progress has been made in the preparation of colloidal particles of various sizes, shapes and surfaces chemistry. These particles are used as building blocks to create colloidal assemblies with a great potential for a new generation of devices.

The topics in the following chapters cover the key aspects of synthesis of colloids and their assembly into ordered three-dimensional particle arrays.

2.1.1 Colloids

Colloids are defined as objects with at least one dimension in the range of 1 nm to 1 µm, dispersed in a medium.[12] They can exist of any nature (solid, liquid, or gas). Well-known examples for colloids in nature are concrete, milk, and smoke.[13]

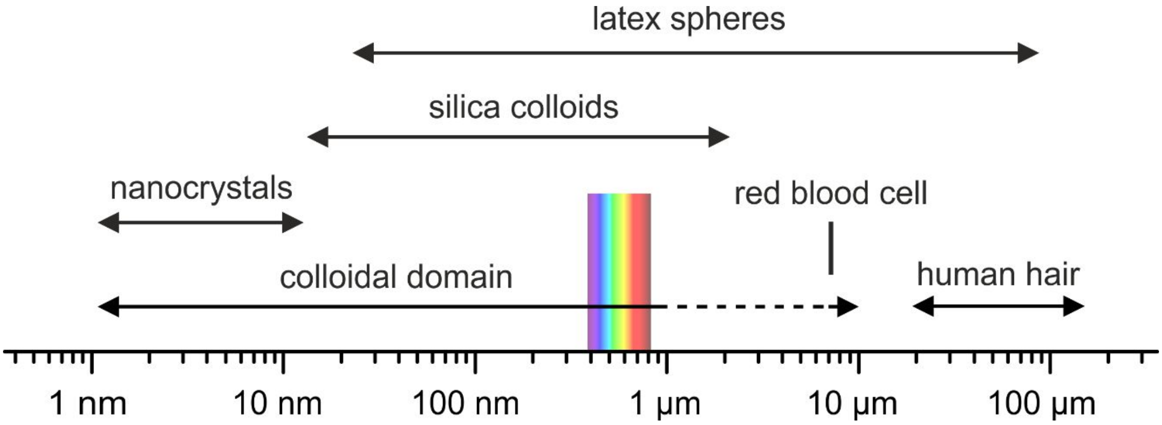

Figure 2.1. Overview of typical dimensions in the range of the colloidal domain. Adapted from Wang et al.[14] with permission from The Royal Society of Chemistry.

Colloids can be further distinguished between colloidal dispersions, association colloids (micelles) and colloidal molecules.[15] Due to their relevance as building blocks for the formation of colloidal assemblies, solid colloidal dispersions are used in this work. They can be synthesized with a broad range of structural features including (i) the particle size and the size distribution, (ii) the type of material, (iii) the shape, and (iv) the surface functionalization.[16] This diversity of parameters enables the tuning of the properties of the colloids, and their assembled structures, leading to a material class with a great potential for devices with novel properties in various fields, such as chemical sensing and biosensing[17], filtering/sieving[18], or photonics[19-20], to name a few.

The majority of colloidal particles are spherical. This shape is driven by the minimization of the interfacial free energy during the nucleation and growth process in bottom-up approaches.[21] In case, the particles are monodisperse in size (<5 % size distribution), spherical particles favor the hexagonal closed-packed structure (fcc and hcp).[22] Thus, the shape of the colloids is one of the driving force which determines the symmetry of the assembled structure.

Various synthesis methods can be found in the literature to obtain spherical colloids, from organic (polymer) and inorganic materials. Well-kown methods used to synthesize polymer colloids are the emulsion polymerization[21, 23], micro-[24-25] and miniemulsion[26-29], emulsifier-free emulsion polymerization[30-31], and dispersion polymerization[32-33]. The particle sizes available by these methods span the whole range of the colloidal domain. For the synthesis of monodisperse particles in a sufficient amount, the emulsifier-free emulsion polymerization and dispersion polymerization are suitable methods. Therefore, the polymer colloids are prepared with the help of these two approaches in this work. More details about the mechanisms can be found therefore in the Material Part in Chapter 3.1.1.

Inorganic colloidal particles with a low polydispersity are typically synthesized by precipitation or sol-gel processes.[34] Among the available building blocks, amorphous silica spheres are the most studied inorganic particles. The synthesis of monodisperse silica colloids is usually done by the so-called Stoeber method.[35] In this process, a dilute solution of tetraethyl orthosilicate (TEOS) in ethanol is hydrolyzed under basic conditions. As a result, particle diameters in the range of 50 nm to 2 µm are obtained.[21]

The concept to achieve monodisperse particles is similar for both, inorganic and organic particles. In most cases, they involve a nucleation and growth step. These two steps need to be separated to obtain monodisperse particles. This is summarized by the so-called LaMer theory.[36-37]

The properties of spherical colloids can be extended by modifying their surface.[38-39] This concept can be expanded by coating of colloidal particles with a shell of a different material. Moreover, the opportunity arises to remove the core by either calcination or by dissolution.[40] As a result, a new material class, hollow spheres, are formed. In this thesis, polymer particles are coated with a silica shell of variable thickness using a modified Stoeber process. By calcining the core-shell particles, hollow silica nanoparticles were obtained. Details about the synthesis method and the tuning of the structural properties are further described in Chapter 3.1.2.

2.1.2 Colloidal Stability

In general, colloids in dispersion are thermodynamically unstable with respect to the bulk phase.[41] This originates from the surface energy minimization phenomenon.[41] However, colloids can be kinetically stabilized. The Derjaguin-Landau-Verwey-Overbeek (DLVO) theory explains the kinetic stability.[42-44] It elucidates the conditions of stability and instability of colloidal dispersions by a combination of van der Waals attraction and electrostatic repulsion. These forces are also referred as DLVO forces and are briefly described in the following.

Attractive van der Waals forces arise from the orientation of dipoles which may be (i) two permanent dipoles, (Keesom orientation forces), (ii) dipole – induced dipole (Debye induction forces), (iii) induced dipole – induced dipole (London dispersion forces). The magnitude and range depends on the size and geometry of the particles, their surface chemistry, and the medium via the Hamaker constant A. For monodisperse, spherical colloids with a radius R, and interparticle distance d, with $R >> d$, the van der Waals free energy V_A is given by Equation (2.1).

$$V_A = -\frac{AR}{12d} \tag{2.1}$$

Electrostatic stabilization results from charges distributed over the colloidal objects causing an electric field. This electric field attracts counter ions leading to the formation of an electrical double layer. As a result, the approach of two like-charged particles causes a repulsion. The origin of the surface charge can be traced back, e.g., on dissociation of surface groups. The charge densities and spatial distribution functions are described by the Poisson-Boltzmann equation.[13] For low potentials, the analytical solution is expressed by the linearized Poisson-Boltzmann equation with the electrostatic repulsion being proportional to $e^{-\kappa d}$, where κ is the inverse Debye length and d the interparticle distance.

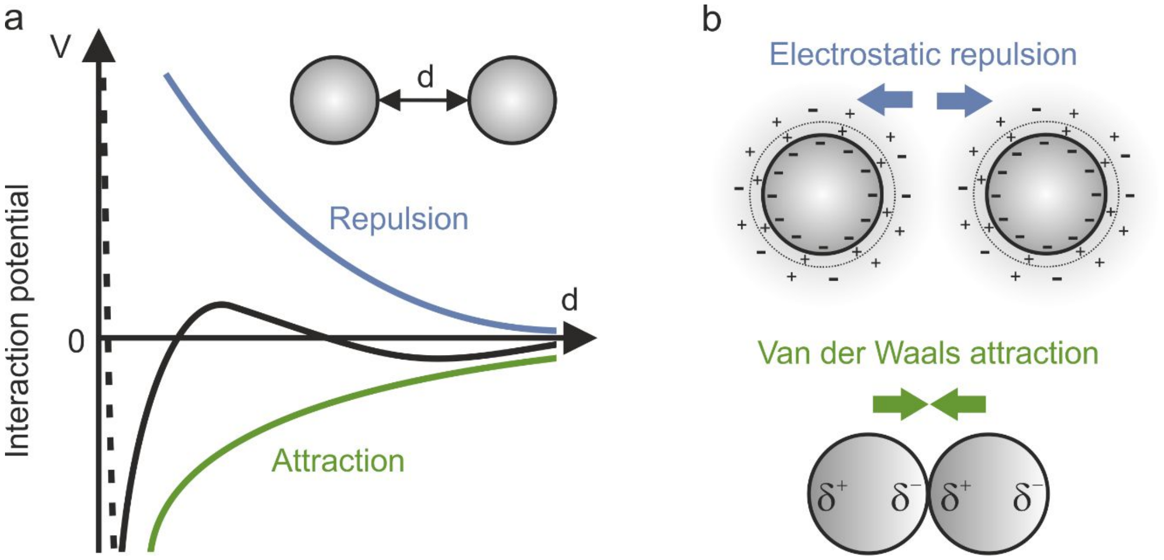

Figure 2.2. DLVO theory. (a) Energy-distance curve for electrostatically stabilized colloids. The total interaction potential (black curve) results from attractive and repulsive interactions between two colloidal particles. The dashed line represents the Born repulsion at very small distances. (b) Schematic representation of the electrostatic repulsion and the van der Waals interaction. Adapted from Israelachvili[45] with permission from Elsevier.

The DLVO potential, as a sum of the electrostatic repulsion and the van der Waals attraction forces as a function of the interparticle distance *d*, is shown in Figure 2.2. Furthermore, the hard-sphere repulsion potential due to the overlap of atomic electron clouds (Born repulsion) at distances smaller than the particle radius is included, usually modeled as d^{-12} dependence.

The repulsive interaction energy decreases exponentially with interparticle distance, while the attractive interaction energy decreases inversely with the interparticle distance. Figure 2.2 shows the predomination of the van der Waals interactions at small and large distances. At extremely small (Born repulsion) and intermediate (electric double layer) distances, the repulsive forces predominate. This interplay leads to two minima and one maximum. The latter one is sometimes referred to as energy barrier. Particles which reach the primary minimum irreversibly agglomerate. This can be prevented by a sufficiently high energy barrier depending on the surface charge and the salt concentration. The second minimum is referred to as flocculation which is usually a reversible process. Thus, the requirement for colloidal stability is to have an energy barrier that is much larger than the thermal energy of the particles (~k_bT).

Apart from the stabilization by an electrical double layer (electrostatic repulsion), colloids can be stabilized by macromolecules, which are attached to the surface of the particles. This steric repulsion emerges as soon as the interparticle distance becomes less than twice the unperturbed layer thickness, resulting in either overlapping, or compression of the polymer chains.[46] This induces an increase in the polymer density in the interaction zone, leading to strong repulsion due to (i) the osmotic pressure increase, and (ii) the entropy reduction by the restriction.[46] The steric repulsion depends on many parameters, such as the polymer coverage of the colloidal surface, the solvent, and the type of the surface bonding. Advantages of the steric repulsion are the relative insensitivity to the presence of electrolytes, and the polarity of the dispersion medium. However, the presence of polymers can lead to attractive forces between particles by bridging flocculation[47] or depletion attraction[48] as well.

Apart from the repulsive and attractive forces, external forces are present in colloidal dispersions.[22] These are Brownian motion (diffusion force) and gravitational forces, which cause particles to sediment. As long as the Brownian force is stronger than the gravitational force, the particles remain suspended.[49] With increasing particle size, gravitational forces become more important, leading to a sedimentation. Apart from the particle dimension, the density contrast between colloids and medium plays an major role in the sedimentation process.[50]

Sedimentation is one way to assemble colloids. In the following, various assembly processes are presented.

2.1.3 Colloidal Assembly

Colloidal particles with well-defined size distributions can self-assemble into long-range ordered lattices.[51-52] Thereby, multiple reversible interactions occur to assemble subunits into stable arrays. The formed structure is in a thermodynamic minimum, resulting from the equilibration of various interactions.[52]

Three-dimensional colloidal self-assembly strategies are most relevant to receive nanostructured materials for various applications, such as the heat transport.[53-56] Common methods to achieve colloidal assemblies are sedimentation[57-58], centrifugation[59-60], vertical (lifting) deposition[61-64], spray coating[65], doctor blade coating[66], spin-coating[67-68], filtering[69-70], and evaporation-induced self-assembly[71-73]. These methods are schematically depicted in Figure 2.3.

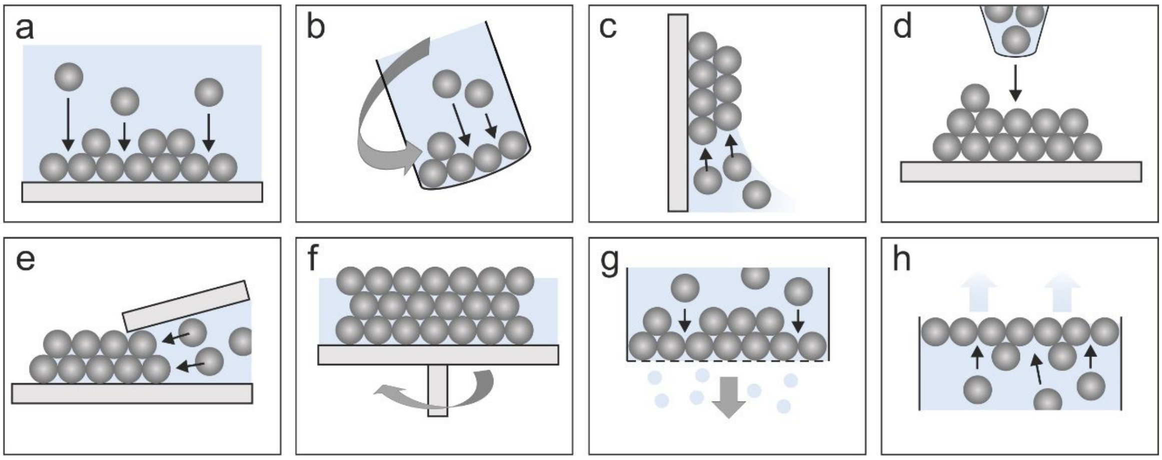

Figure 2.3. Schematic representation of common 3D assembly methods. (a) Sedimentation, (b) centrifugation, (c) vertical deposition, (d) spray coating, (e) doctor blade coating, (f) spin-coating, (g) filtering, (h) plain dispersion drying. Adapted with permission from Vogel et al.[22]. Copyright 2015 American Chemical Society.

The main difference between the assembly methods presented in Figure 2.3 is the accessible thickness of the colloidal assemblies and the quality and size of the crystalline domains. For instance, highly ordered colloidal crystals can be obtained by evaporation-induced self-assembly of monodisperse polymer particle dispersions. On the other hand, colloidal glasses with a random close-packing can be fabricated rapidly by filtering the colloidal dispersions. These two processes were also used in this work due to their simplicity and the high quality of the resulting free-standing colloidal assemblies, and are therefore further described in Chapter 3.1.3.

2.2 Basics of Heat Transfer in Dielectric Hard Materials

Colloidal assemblies are commonly composed of amorphous materials. For a complete understanding of thermal transport in such materials, a comparative introduction to heat transport in crystalline and amorphous bulk materials is given (Chapter 2.2.1). Subsequently, the attention is directed towards the features of thermal transport in porous materials (Chapter 2.2.2). The last chapter deals with the heat transport in colloidal crystals.

2.2.1 Heat Transfer in Bulk Matter

The heat in materials is transferred from high to low temperature areas. The heat flow can be described by Fourier's law of heat conduction:

$$q = -\kappa \cdot \nabla T \tag{2.2}$$

where κ is the thermal conductivity, q the heat flux density and ∇T the temperature gradient. The law of heat conduction states that the time rate of heat transfer through a material is proportional to the negative temperature gradient ($\delta T/\delta x$), which is the driving force.

Three different mechanisms exist for thermal transport: radiative (mediated by photons), convective (mediated by the physical movement of heat carriers), and conductive.[74] For many materials, like colloidal assemblies, the dominant mechanism is thermal conduction.

Crystalline materials

In dielectric, crystalline materials, the thermal energy is conducted by propagating lattice vibrations with a set of characteristic frequencies. The energies of the lattice vibrations are quantized by

$$E = \left(n + \frac{1}{2}\right) h\nu \tag{2.3}$$

where n is an integer, which is zero at 0 °C and h is the Planck's constant. If the solid is heated/cooled, E will increase/decrease in integer steps of hv. The similarity between this process and the absorption/emission of light (photons) is evident. Therefore, the quantum unit of lattice vibrational energy is called a phonon.

By treating phonons as quasi-particles, the thermal conductivity can be described by the Debye equation:

$$\kappa = \frac{1}{3} C_v v_g \Lambda \tag{2.4}$$

where C_v is the heat capacity, v_g the phonon velocity, and Λ the average phonon mean free path (MFP), which is the average traveling distance between two successive collisions.

Table 2.1. Typical heat transfer properties at 293 K: Lattice spacing l, Debye temperature θ_D, phonon MFP Λ, and thermal conductivity κ.[75-76]

	θ_D [K]	**Λ [nm]**	**κ [W/mK]**
Diamond[c]	1860	315	2300
Sapphire[c]	600	4.0	46
Silicon[c]	645	43	153
Silica[a]	290	0.6	1.4

[c] crystalline structure, [a] amorphous structure.

The phonon MFP can range from 1 nm to more than 1 µm, depending on the material and its temperature and as a result on the existing scattering mechanisms (see Table 2.1). Conceivable interactions are (i) phonon-phonon scattering, (ii) phonon-boundary scattering (iii) phonon-impurity scattering, (iv) phonon-imperfection scattering, and (v) phonon-grain boundary scattering. The different scattering mechanisms are depicted in Figure 2.4a.

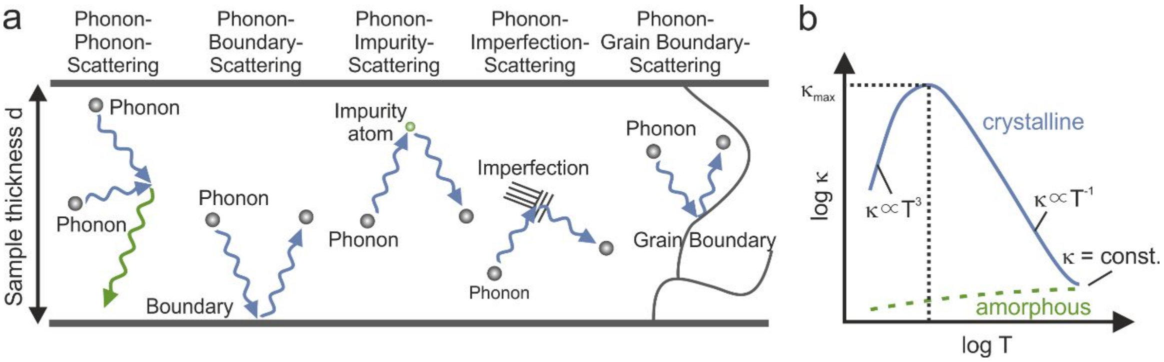

Figure 2.4. (a) Phonon scattering mechanism in dielectric materials: Phonon-phonon scattering, phonon-boundary scattering, phonon-impurity scattering, phonon-imperfection scattering, and phonon-grain boundary scattering. Adapted from Ashegi[77] with permission from AIP Publishing. (b) Typical temperature-dependence of dielectric materials. Adapted from Kaviany[78] with permission from Cambridge University Press.

Phonon-phonon collisions result from the anharmonicity of the lattice potential and dominate in pure crystals. The process can be divided into the normal process (N-process) and the Umklapp process (U-process).[79] The U-process is necessary to obtain thermal equilibrium, due to the formation of a thermal resistance (i.e., finite thermal conductivity). This process is almost entirely dominating at high temperatures. The probability of these processes decreases with decreasing temperatures. As a result, the phonon MFP and the thermal conductivity increase with T^{-1} until reaching a maximum at about 10 % of the Debye temperature θ_D (compare Table 2.1).[80] Further temperature reduction leads to a decrease of the thermal conductivity, following the T^3 dependence of the heat capacity.[81] In this temperature regime, boundary scattering dominates. The location of the maximum depends on the sample size, defects, and crystal size. In nanostructured materials, the maximum is lower in magnitude and shifted to higher temperatures.[74, 81]

At very high temperatures, the thermal conductivity is independent of the temperature leading to a minimum thermal conductivity value due to the MFP being comparable to the interatomic spacing. However, most materials melt below this temperature. A typical temperature dependency of a dielectric crystalline material in comparison to an amorphous one is depicted in Figure 2.4b. The thermal conductivity in amorphous materials is significantly reduced compared to crystalline materials. Furthermore, the temperature-dependency is different. This is discussed in the following section, covering heat transport in amorphous materials.

Amorphous materials

Amorphous materials exhibit no translational symmetry or periodicity. The structural defects/disorder leads to significant wave scatterings and even localization of the wave propagation.[82] Thus, the thermal conductivity is strongly reduced (e.g., amorphous silicon has a thermal conductivity of ~1 – 4 $\mathrm{W\,m^{-1}K^{-1}}$, while its crystalline counterpart has a thermal conductivity of 148 $\mathrm{W\,m^{-1}K^{-1}}$).[81] Therefore, the vibrational modes cannot be longer named extended phonon waves. A new concept arose by Allen and Feldman to describe disordered vibrational modes (vibrons).[83-84] They classify these vibrons in propagons, diffusons, and locons. Propagons are propagating and delocalized (i.e., phonon-like), and are typically found in the low-frequency range of the vibrational spectrum (see the spectrum of vibrons for a model of amorphous silicon, Figure 2.5). Diffusons are non-propagating and delocalized modes, located in the middle-frequency range. Propagons and diffusons are also called extendons due to their delocalization. The mobility edge marks the transition from delocalized to localized modes (locons). Locons are non-propagating and spatially localized modes and are typically found in the high frequency range of the vibrational spectrum.

The fundamental differences in the vibrating modes between amorphous and crystalline materials lead to completely different temperature dependencies of the thermal conductivity.[85] While the thermal conductivity of crystalline materials decreases at high temperatures, the thermal conductivity of amorphous materials increases monotonically over the whole temperature range.[86] Moreover, the dependency at low temperatures is different for disordered materials. They show a T^2-dependence, instead of a T^3-dependence.[87] The increase at high temperatures results not only from the increased heat capacity but also from stronger anharmonic coupling between the modes.[85, 88]

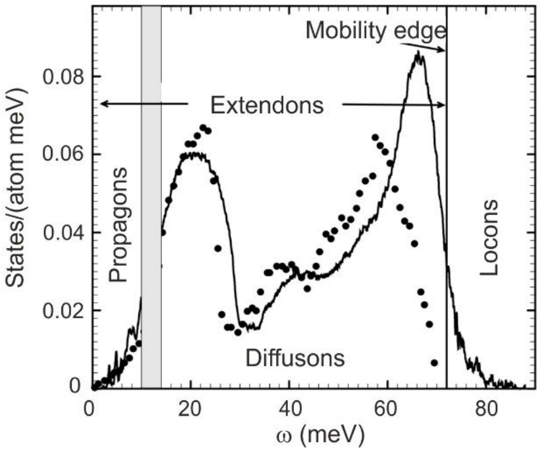

Figure 2.5. Vibrational spectrum of a model of amorphous silicon. Adapted from Allen et al.[84] with permission from Taylor & Francis Group.

2.2.2 Heat Transfer in Porous Matter

Colloidal crystals comprise nanosized pores. Therefore, for a complete understanding of heat transfer in these materials, one has to consider further contributions emerging from the heat transfer through the gaseous phase.

Besides, the heat transport *via* solid conduction (Chapter 2.2.1), gaseous conduction, convection, and radiation contribute to the overall thermal conductivity κ_{tot} (see Equation (2.5)).

$$\kappa_{tot} = \kappa_{solid} + \kappa_{gas} + \kappa_{rad} + \kappa_{conv} \tag{2.5}$$

Radiation (κ_{rad}) describes a phenomenon by which solid pore surfaces emit a radiation spectrum, centered in the infrared (IR), which is absorbed by other solid pore surfaces and reemitted. Radiative transport increases with decreasing density.[89] Thus, it plays a tremendous role in low-density materials, like aerogels. For colloidal crystals, the contribution is negligible due to their relatively high density.

Convection (κ_{conv}) is the transfer of heat due to the movement within the gas phase. It is negligible in materials with pore sizes below 4 mm.[90] Thus, it does not influence the heat transport through colloidal crystals either.

While radiation and convection are negligible in colloidal assemblies, the gaseous conduction (κ_{gas}) is an important process. It is affected by the size of the pores. In smaller pores, the number of elastic collisions between gas molecules is reduced. This mechanism becomes dominant when the pore size reaches the mean free path of the gaseous phase (Knudsen effect). In this regime, the gaseous thermal conductivity is governed by the following equation:

$$\kappa_{gas} = \frac{\kappa_{gas,0} \cdot \Phi}{(1 + 2\beta \cdot Kn)} = \frac{\kappa_{gas,0} \cdot \Phi}{(1 + \frac{p_{1/2}}{p})} \tag{2.6}$$

where $\kappa_{gas,0}$ is the thermal conductivity of the gas when moving freely, β is a constant for the effectiveness of the energy transfer between gas molecules and the solid pore walls (commonly between 1.5 and 2)[91], Kn is the Knudsen number, Φ is the porosity of the sample and $p_{1/2}$ is the pressure p, at which the value of the gaseous thermal conductivity is half of the maximum value for the free gas. The Knudsen number is defined as the ratio of the mean free path to the characteristic system size. The MFP at ambient pressure and ambient temperature is ~70 nm in air and ~200 nm in helium.[92] Thus, in colloidal crystals, the gaseous conduction is strongly influenced by the Knudsen effect.

Porous materials are composite materials, consisting of a gaseous and a solid phase. The effective thermal conductivity of composite materials can be described by using binary mixing models. The most noted ones are the parallel, the series, the Maxwell-Eucken 1 and 2 and the effective medium theory (EMT) model.[93-94] The respective equations of the models and their schematic structures are shown in Figure 2.6. The lower and upper bound are provided by the series and parallel model, in which the layers are aligned either perpendicular or parallel to the heat flow. These models are not realistic assumptions for colloidal crystals. A better description is provided the Maxwell-Eucken models or the EMT model. The

Maxwell-Eucken model assumes inclusions of a dispersed phase in a continuous matrix, which are not in contact with each other. In the Maxwell-Eucken 1 model, the thermal conductivity of the dispersed phase is lower than the thermal conductivity of the continuous phase, contrary to Maxwell-Eucken 2 model. The EMT model describes a two-component system with a random distribution of the single components.

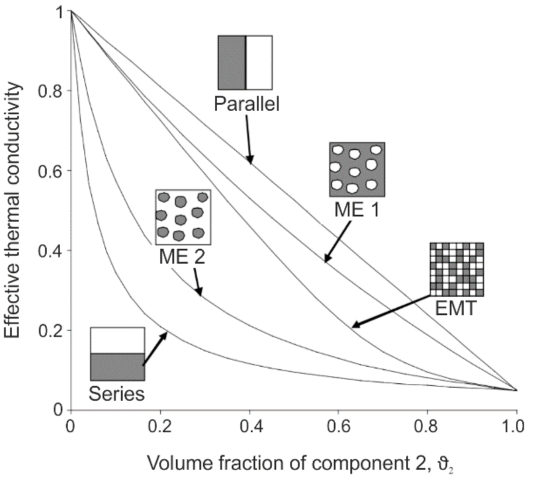

Series model	$\kappa_e = \dfrac{1}{\dfrac{1-\vartheta_2}{\kappa_1} + \dfrac{\vartheta_2}{\kappa_2}}$
Parallel model	$\kappa_e = (1-\vartheta_2)\kappa_1 + \vartheta_2\kappa_2$
Maxwell-Eucken 1	$\kappa_e = \kappa_1 \dfrac{2\kappa_1 + \kappa_2 - 2(\kappa_1 - \kappa_2)\vartheta_2}{2\kappa_1 + \kappa_2 + (\kappa_1 - \kappa_2)\vartheta_2}$
Maxwell-Eucken 2	$\kappa_e = \kappa_2 \dfrac{2\kappa_2 + \kappa_1 - 2(\kappa_2 - \kappa_1)(1-\vartheta_2)}{2\kappa_2 + \kappa_1 + (\kappa_2 - \kappa_1)(1-\vartheta_2)}$
Effective medium theory (EMT)	$\kappa_e = 1/4((3\vartheta_2 - 1)\kappa_2 + [3(1-\vartheta_2) - 1]\kappa_1$ $+\sqrt{[(3\vartheta_2 - 1)\kappa_1 + (3\{1-\vartheta_2\} - 1)\kappa_1]^2 + 8\kappa_1\kappa_2}$

Figure 2.6. Binary mixing models describing the thermal conductivity of a two-component system: The series, the parallel, the Maxwell-Eucken (ME) and the effective medium theory (EMT) model and the corresponding equations. In the ME 1 model, 1 is the continuous phase, whereas, in the ME 2 model, 1 is the dispersed phase. Adapted from Carson et al.[93] with permission from Elsevier.

2.2.3 Heat Transfer in Colloidal Crystals

As mentioned in the motivation, colloidal assemblies possess several interesting key features: (i) singular structural control, (ii) flexibility of material composition (polymers, metal oxides, composites, etc.), (iii) approachability to nano- and mesostructured length scales, (iv) adjustment of the symmetry (close-packing vs. random close-packing), and (v) adjustment of the interfaces. Furthermore, they are readily available in large quantities due to the ease of fabrication.

These characteristics of colloidal crystals enable to use them as a model system to understand heat transport in nanostructured materials. The conceptual insight gained from colloidal assemblies can be adapted easily to other nanostructured and nanoparticulate systems.

The most relevant contributions to the overall thermal conductivity are (i) solid conduction and (ii) gaseous conduction (compare Chapter 2.2.2). The solid conduction is significantly reduced in colloidal materials. This can be traced back to several scattering mechanisms of the vibrational modes emerging in these nanostructured materials: boundary, grain-boundary, imperfection, or impurity scattering (compare Chapter 2.2.1). Besides the reduced solid conduction, conduction through the gaseous phase is also strongly reduced due to the small pore sizes existing in these ensembles (Knudsen effect, Chapter 2.2.2).

In literature, the thermal transport of colloidal assemblies is barely reported. Besides the contributions in Chapter 6 – 11, two other examples of the heat transport in dielectric colloidal crystals can be found in the literature.[54, 95] These will be introduced in the following.

Nutz et al.[54] investigated the thermal transport properties of sub-micron sized monodisperse polystyrene (PS) particles (366 nm), densely packed in a face-centered cubic lattice (fcc). The freestanding PS colloidal crystals are prepared *via* a simple self-assembly process. The high ordering of the particles is highlighted in Figure 2.7a,b. The light microscopy image (a) shows bright Bragg reflections over the whole assemble due to the regular structure. The high ordering is confirmed by the scanning electron microscopy images (b). The pore sizes are fully controlled by the diameter of the colloidal spheres and occupy 26 vol.% of the nanoporous open-cell structure. The concomitant high amount of interfaces and small interparticle contact area lead to a very low thermal conductivity of only 51 mW m^{-1} K^{-1} in vacuum at a comparatively high density of 0.75 g/cm^{-3}. Compared to its bulk counterpart ($\kappa = 140$ mW m^{-1} K^{-1}), the thermal transport is strongly limited. Furthermore, these soft colloidal assemblies possess an interesting feature upon heating above the glass transition temperature T_g. Due to the loss of the colloidal superstructure during the film formation process, the thermal conductivity increases by about 270 % (Figure 2.7c).

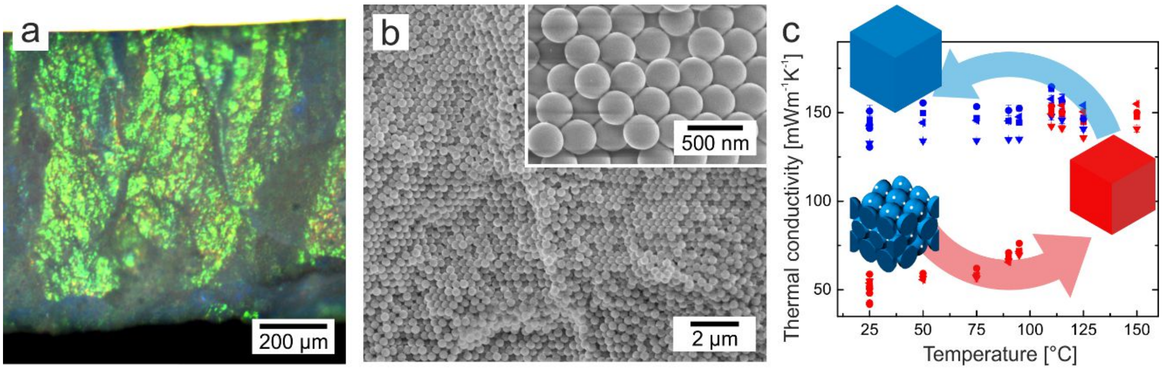

Figure 2.7. Thermal transport properties of polystyrene colloidal crystals. (a) Side-view optical microscopy image, (b) side-view SEM image of the colloidal crystal, and (c) temperature-dependent thermal conductivity. Adapted from Nutz et al.[54] with permission from Elsevier.

A new material class, called inverse opals, can be built up by using the colloidal crystal structure as a template material.[20, 96-98] Inverse opals exhibit a high degree of interconnected porosity with pore sizes usually in the range of <100 – 1000 nm. Ma et al.[95] investigated the thermal transport in silicon inverse opals with pore sizes and shell thicknesses in the range of 420 – 900 nm and 18 – 38 nm. Owing to the low density of the inverse opal, the thermal conductivity range from 0.6 to 1.4 $W m^{-1} K^{-1}$ at 300 K. Interestingly, the temperature dependence of these structures varies significantly from the expected $\kappa \sim T^3$ scaling law at low temperatures (Chapter 2.2.1), following a $k \sim T^{1.8}$ dependency. The different behavior can be traced back to coherent phonon grain boundary scattering due to uniform grains across the sample.

This is an impressive example how colloidal assemblies can help to understand fundamental heat transport features due to their structural control and small accessible length scales.

3 Materials and Methods

3.1 Materials

Monodisperse colloidal particles are well-defined building blocks. Due to their low polydispersity, these particles can be assembled into highly ordered three-dimensional materials with a remarkably precise structural control, i.e., colloidal crystals.

The following section provides the preparation of monodisperse polymer particle. Afterwards, the coating of the polymer particles with silica and the subsequent calcination step to obtain silica hollow spheres are indicated. The last section covers the assembly methods used to prepare colloidal crystals and colloidal glasses.

The following materials were used as received: styrene (≥99%, Aldrich), 2,2′-azobis(2-methylpropionamidine)dihydrochloride (AIBA; 97 %, Aldrich), [2-(methacryloxy)ethyl]-trimethylammonium chloride (MTC; 70 % solution in water, Polyscience), polyvinyl-pyrrolidone K30 (PVP; Mw ~ 55 $\mathrm{kgmol^{-1}}$, Aldrich), tetraethylorthosilicate (TEOS; ≥ 99%, Aldrich), and ammonium hydroxide solution (30-33 % in water, Aldrich). Ethanol (EtOH) was used in technical grade, and water was taken from a Millipore Direct Q3UV unit for the entire synthesis and purification steps.

3.1.1 Synthesis of Polymer Nanoparticles

Basics of Emulsifier-free Emulsion Polymerization

The focus in this section will be laid on the synthesis of polystyrene particles via emulsifier-free emulsion polymerization.[30] This method was used to obtain PS latex beads in the size range of up to ~450 nm. Larger polymer particles were synthesized by using dispersion polymerization.

The schematic illustration of an emulsifier-free emulsion polymerization is depicted in Figure 3.1.

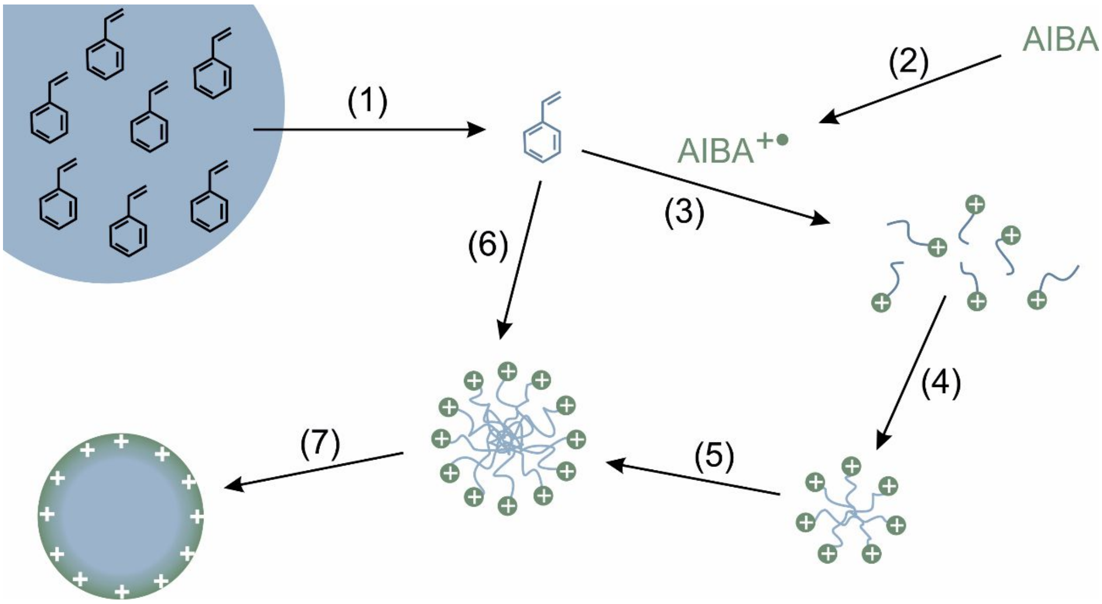

Figure 3.1. Schematic illustration of the emulsifier-free emulsion polymerization using AIBA as an initiator. Adapted from Vollmert[99] with permission from Springer Verlag.

The mechanism of the emulsifier-free emulsion polymerization was studied by Hansen and Ugelstad.[100] Macroscopic monomer droplets emerge by vigorous stirring in the continuous water phase. Due to the low, but finite solubility of the monomer, some molecules are dissolved in the aqueous phase (1). The water soluble initiator (e.g., AIBA) is thermally decomposed into charged radicals (2). After initiation in the water phase (3), the radicals add monomer units, until a critical chain length is reached. These oligomers with a charged end group become water insoluble, collapse into globules and form particle nuclei (4). This step is called homogeneous nucleation. Several of such nuclei assemble to form a stable primary particle, which is stabilized by ionic groups at the interface (5). In the following, the polymerization proceeds by diffusion of the monomer from the monomer droplets (6), forming a latex particle (7).

Emulsifier-free Emulsion Polymerization - Experimental Procedure

The synthesis was carried out in a three-necked flask, equipped with a reflux condenser and a gas inlet, under a slight argon flow. The flask was charged with 230 mL water, 26 mL styrene, 0-300 µL MTC, and 1.8 g PVP K-30. The reaction mixture was heated to the reaction temperature of 70 °C at a stirring speed of 850 rpm. After an equilibration time of 30 min, 0.6 g AIBA dissolved in 10 mL water, were added to initiate the polymerization. After nucleation, the stirring speed was reduced to 450 rpm. The reaction was carried out overnight. To terminate the polymerization, the mixture was exposed to ambient atmosphere.

Emulsifier-free Emulsion Polymerization - Results and Discussion

The emulsifier-free emulsion polymerization offers the opportunity to tune the overall particle size in a broad range. Therefore different parameters are adjusted: the concentration of the (co)monomer and the initiator, the temperature, the stirring rate, the ionic strength, and the amount of steric stabilizer. Without disregarding the monodispersity, the best results can be affected using the comonomer concentration.

The particle diameter as a function of the comonomer concentration is shown in Figure 3.2.

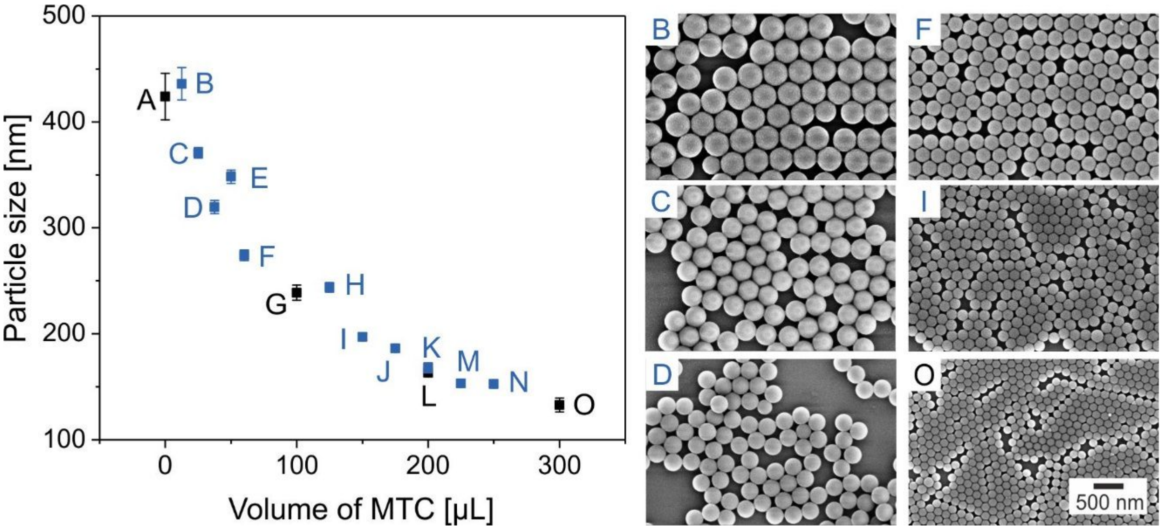

Figure 3.2. The size of the polystyrene particle as a function of the volume of the comonomer solution MTC. The synthesis specifications are described in the main text. The black squares represent a down-scaling of the synthesis by the factor of 0.5. The right column shows scanning electron microscopy (SEM) images of the corresponding particles.

By adjusting the comonomer volume between 0 and 300 µL, the particle size can be varied between 130 and 440 nm with a low polydispersity of less than 5 %. The higher the comonomer concentration, and thus, the electrostatic stabilization is, the smaller the particle diameter gets. Nevertheless, larger particles are hardly achievable using emulsifier-free emulsion polymerization. Therefore, the dispersion polymerization technique was used.

Basics of Dispersion Polymerization

The dispersion polymerization is a type of precipitation polymerization. While the monomer and initiator are soluble in the reaction medium, the formed polymer is insoluble. The dispersion polymerization takes place in a homogeneous medium of monomers with a free-radical initiator and a polymeric stabilizer dissolved in an appropriate solvent. At an elevated temperature, the initiator decomposes, and the radical adds solubilized monomer units, forming oligomeric radicals. This proceeds until a critical chain length is reached, leading to a phase separation and the formation of primary particles. This step is termed nucleation. In the following, the particle formation step starts. The particle nuclei are unstable and rapidly aggregate with each other. The formed particles are stabilized by the dispersing agent which adsorbs at the interface. In this step, all of the oligomeric radicals, and nuclei are captured by the mature particles and the particle formation step is completed. Subsequently, the polymerization proceeds within the particles, leading to monodisperse polymer latex beads.

Dispersion Polymerization - Experimental Procedure

In the following, the dispersion polymerization is described for the particles F, resulting in a particle diameter of 955.8 ± 24.8 nm (see Table 3.1).

Table 3.1. Parameters which can be tuned in a dispersion polymerization to change the particle diameter.

	EtOH [mL]	**Water [mL]**	**MTC [µL]**	**AIBN [g]**	**Diameter [nm]**
A	120	30	500	0.068	493.7 ± 13.5
B	136	14	400	0.136	587.1 ± 13.0
C	120	30	350	0.068	724.2 ± 41.3
D	136	14	100	0.136	830.3 ± 14.1
E	120	30	200	0.102	889.9 ± 23.4
F	120	30	200	0.136	955.8 ± 24.8
G	136	14	200	0.136	1278.6 ± 15.5

The dispersion polymerization was carried out in a single-neck flask connected to a KPG stirrer. First, 130 mL ethanol, 14 mL water, 10 mL styrene, and 5 g PVP were purged with argon, while heating the reaction mixture to 75 °C. After an equilibration time of 30 min, the gas inlet was removed, and 0.136 g AIBN dissolved in 6 mL ethanol were added to initiate the polymerization. At once, the stirrer was set to 60 rpm. After 1.5 h, 400 µL MTC were added. The reaction was carried out overnight. To terminate the polymerization, the mixture was exposed to ambient atmosphere.

Dispersion Polymerization - Results and Discussion

The particle size can be tuned by several parameters in a dispersion polymerization.[101-102] In this thesis, the ethanol/water-ratio, the amount of comonomer, and initiator was varied, as depicted in Table 3.1. This enables the tuning of the particle diameter in the range of 490 and 1280 nm. The SEM images of the particles A, D, F, and G are shown in Figure 3.3.

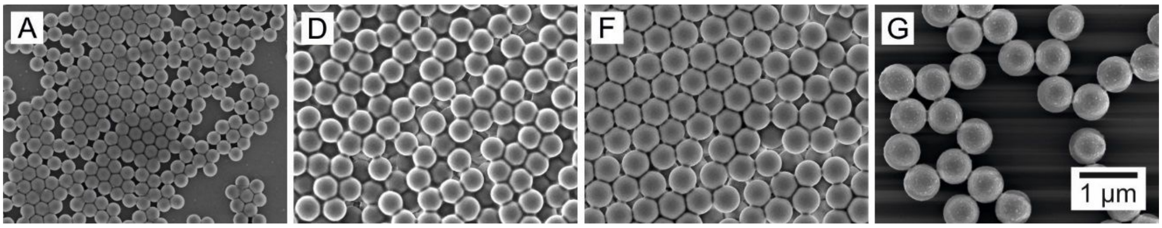

Figure 3.3. Scanning electron microscopy (SEM) images of polystyrene particles, synthesized via dispersion polymerization.

Larger particle sizes can be achieved by reducing the comonomer (A and C, B and D) and the initiator concentration (E and F), and by reducing the ethanol/water ratio (F and G). The increase of the comonomer concentration increases the amine functional groups at the surface of the PS spheres, and therefore the surface electric charge.[101] This reduces the size of the particles. The increase of the initiator concentration reduces the number of free radicals in the polymerization. This leads to lower molecular weight oligomers, which are more stable in the medium. Thus, fewer nuclei are generated, which grow to larger polymer spheres.[103] By changing the ethanol/water ratio, the polarity of the dispersion medium increases, leading to a reduction of the size of the polymer spheres.[101]

3.1.2 Synthesis of Hollow Silica Nanoparticles

Basics of the Hollow Silica Nanoparticle Synthesis

For the above-mentioned polymerization techniques, polyvinylpyrrolidone (PVP) is used as a steric stabilizer. This enables the direct coating of a silica shell upon the polymer particles without any further modifications, like charge inversion.[42, 44] The prepared core-shell particles can be calcined afterward to remove the polymer core and to obtain silica hollow spheres. The different steps to get silica hollow nanospheres are schematically shown in Figure 3.4.

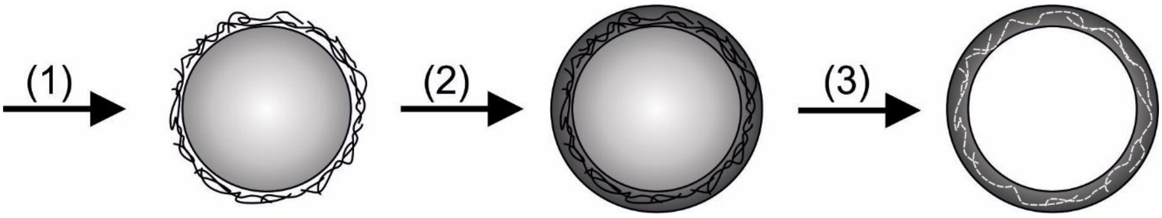

Figure 3.4. Schematic representation of the synthesis of silica hollow spheres. (1) Synthesis of the polystyrene template particles, stabilized by polyvinylpyrrolidone, (2) coating of the polymer particles with silica to obtain core-shell particles and (3) removal of the polystyrene core by calcining at temperatures above 500 °C.

The coating of the polystyrene template particles with a silica shell is achieved by a modified Stoeber condensation process.[35] The amount of precursor, used in the synthesis, allows the adjustment of the silica shell thickness. The experimental procedure is described in the following.

Hollow Silica Nanoparticle Synthesis – Experimental Procedure

For the core-shell particle synthesis, a certain amount of TEOS was added to 17.5 mL ethanol, 1.3 mL ammonium hydroxide solution, and 2.5 mL aqueous polystyrene dispersion (~10 wt.%). The TEOS volume was adjusted to obtain a certain shell thickness (see next section). After stirring at 500 rpm for ~18 h, the particle dispersion was purified by several centrifugation steps. Subsequently, the polystyrene core was removed by calcining the particles at 500 °C for 12 h in air.

Hollow Silica Nanoparticle Synthesis – Results and Discussion

The facile synthesis method of the silica hollow nanoparticles enables the opportunity to change the particle morphology broadly. Parameters, which can be tuned are the diameter of the particles, the shell thickness, and the microstructure/porosity of the silica shell.

The size of the inner pore diameter can be adjusted by changing the size of the polystyrene template particles. A size series of particles between 185 and 990 nm is shown in Figure 3.5. Here, the shell thickness, which is given by the dark shaded ring surrounding the hollow core, is comparable for all capsules (~20 nm).

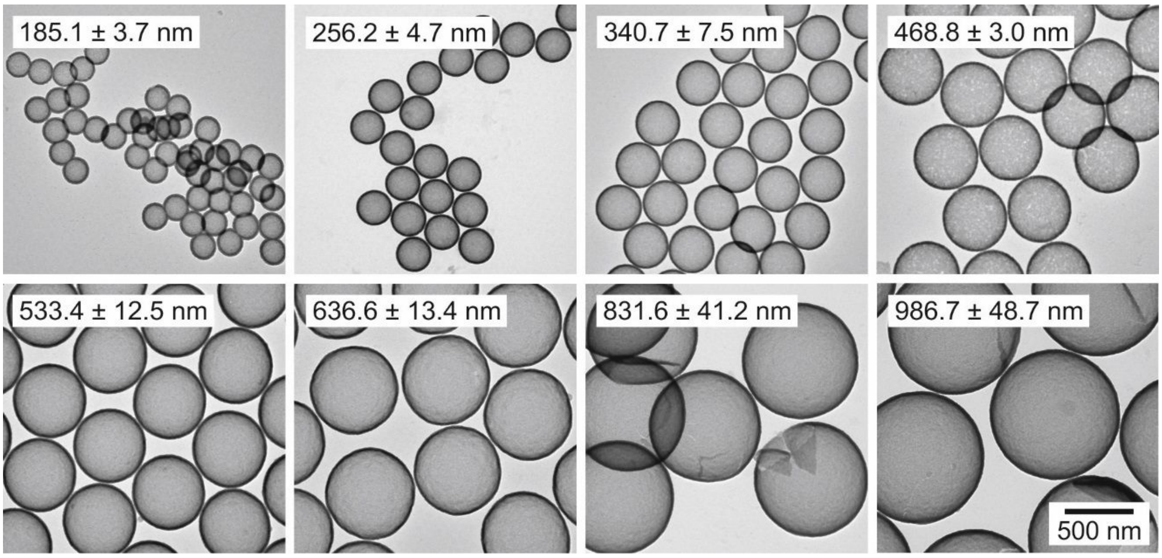

Figure 3.5. Transmission electron microscopy (TEM) images of silica hollow nanoparticles with a diameter of 185 – 990 nm and a comparable shell thickness of about 20 nm.

The size series in Figure 3.5 shows the impressively low polydispersity of the size and the shell thickness. The surface of the particles appears smooth. Furthermore, no formation of aggregates/clusters or sinter necks between the spheres is observed. The particles are rather individually redispersed in ethanol by ultrasonication and deposited on a carbon-coated TEM grid. For the larger particles, some buckling is observable. This can be traced back to the preparation of the TEM samples and the forces affecting the stability of the hollow spheres. The problem can be avoided by increasing the shell thickness. A shell thickness series with a size of 15 – 55 nm is shown in Figure 3.6. Here, the inner core diameter is comparable (~300 nm) for all particles.

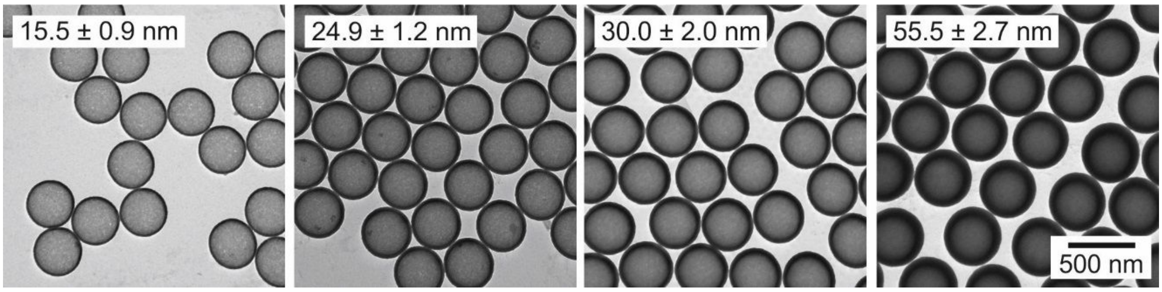

Figure 3.6. Transmission electron microscopy (TEM) images of silica hollow nanoparticles with shell thicknesses between ~15 and 55 nm and a comparable inner core diameter of ~300 nm.

For the shell thickness series depicted in Figure 3.6 and two other series, the shell thickness versus the particle diameter is shown in Figure 3.7a. Impressively, it shows the broad range of shell thicknesses and particle diameters available by this synthesis method. Furthermore, it is possible to predict the shell thickness of the particles (t), knowing the diameter of the polystyrene template particle (d) and the volume of tetraethyl orthosilicate (V_{TEOS}) added during the synthesis:

$$t = 111.55 \cdot \frac{V(TEOS)}{\pi \cdot d^2} + 7.36 = 35.51 \cdot \frac{V(TEOS)}{d^2} + 7.36 \tag{3.1}$$

Figure 3.7b shows the plot to determine the shell thickness. Therefore, the volume of TEOS per particle surface area is plotted versus the shell thickness. It is evident that a good correlation exists between the different shell thickness series. Furthermore, the fit of Equation (3.1) describes the correlation. Thus, it is easily possible to predict the shell thickness.

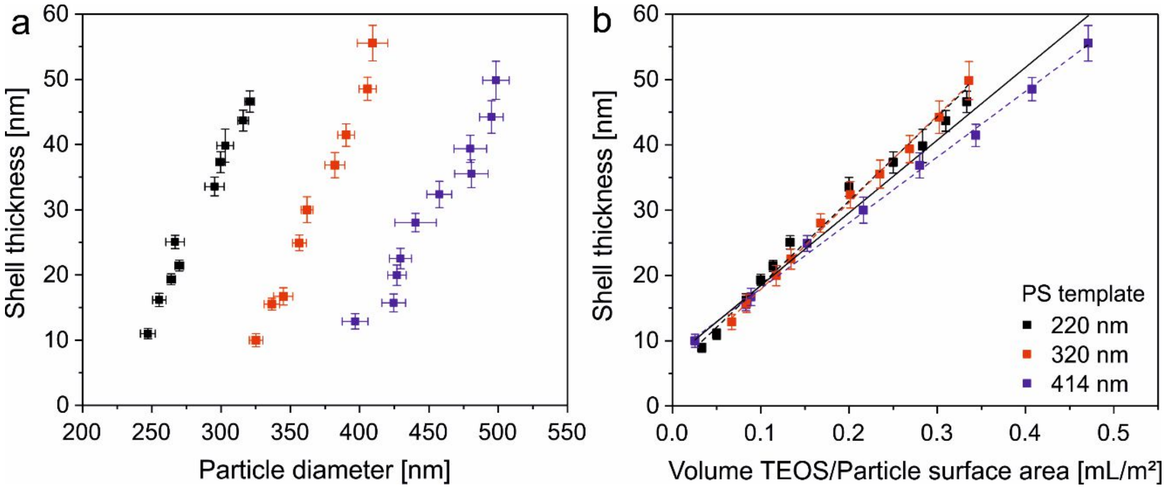

Figure 3.7. Shell thickness series of hollow silica nanoparticles for three different polystyrene template particles with diameters of 220, 320 and 414 nm. (a) Shell thickness versus particle diameter and (b) shell thickness versus volume TEOS per particle surface area. The black line represents the fit of Equation (3.1).

Another significant advantage of this synthesis method is the possibility to prepare large amounts of hollow silica nanoparticles. Figure 3.8 shows large scale approaches of silica hollow spheres with quantities of several grams.

Figure 3.8. Large-scale synthesis approaches of silica hollow spheres with quantities of several grams. The color of the particle powders differs according to the size of the particles. The size increases from left to right: 256 ± 5 nm, 319 ± 5 nm, 423 ± 8 nm.

The color of the particle powders in Figure 3.8 depends on the size of the hollow spheres and can be traced back to Mie scattering.[104] The size of the particles increases from left to right from 256 to 423 nm.

3.1.3 Colloidal Assembly

The assembly methods, used in this thesis, are introduced in the following. For the preparation of highly ordered colloidal particle assemblies (colloidal crystals), the evaporation-induced self-assembly process was applied.[73] This method is illustrated in Figure 3.9 and shows the fabrication of silica hollow sphere colloidal crystals.

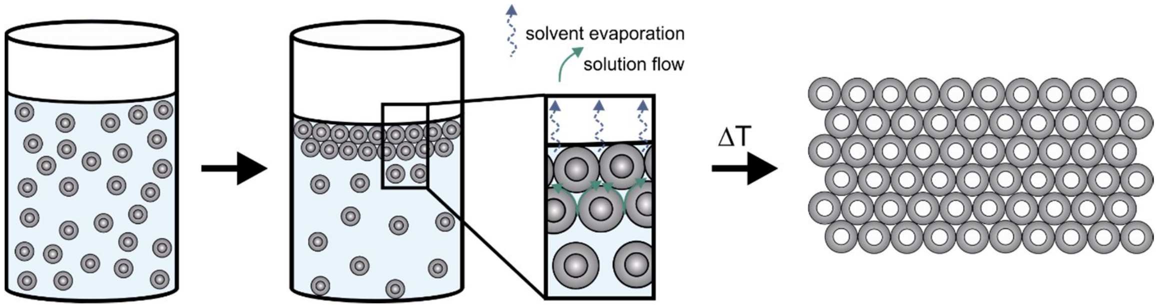

Figure 3.9. Schematic illustration of the evaporation-induced self-assembly of the core-shell particles and the subsequent calcination step to obtain silica hollow sphere colloidal crystals. Reprinted from Ruckdeschel et al.[105] with permission from Wiley VCH.

The evaporation of the water occurs mainly near the air-water interface. This pushes the colloids towards the meniscus. After the formation of a few array layer, the solution flow will start to compensate the water loss caused by the evaporation in the top layers. This forces the colloids to move into the vacancies between the spheres, forming a close-packed structure. The assembled close-packed particle arrays possess a (111)-like plane parallel to the air-water interface.[73]

For the preparation of HSNP colloidal crystals (Figure 3.9), core-shell particles are assembled and calcined afterward. Photographic images of these monoliths are shown in Figure 3.10. The color of the colloidal crystals is purple due to their comparable outer diameter of ~270 nm. From (a) to (c), the color is less pronounced due to an increased scattering, originating from the increasing shell thickness (14, 27, and 42 nm).

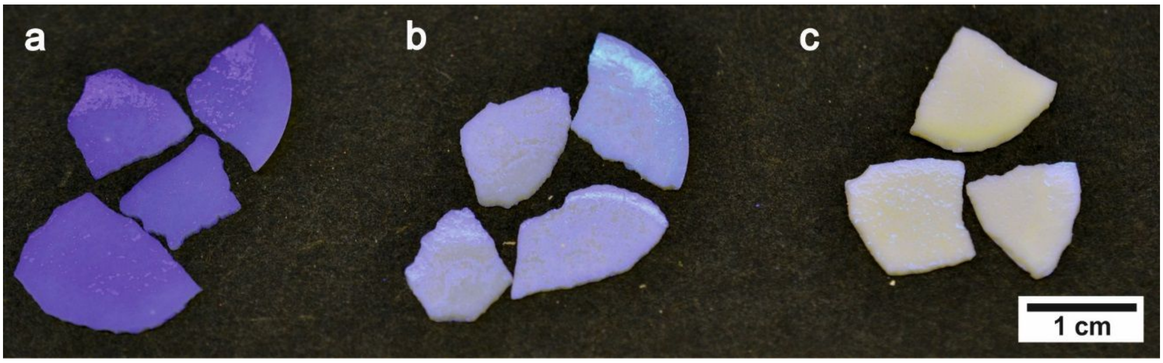

Figure 3.10. Photographic image of colloidal crystals, consisting of silica hollow spheres. The size of the particles is about 270 nm for all samples. However, the shell thickness increases from a to c (14, 27, and 42 nm). Reprinted from Ruckdeschel et al.[105] with permission from Wiley VCH.

A disadvantage of the described assembly process is the relatively long preparation time (~several days) due to the slow evaporation of the solvent. A faster process (~several minutes) to obtain colloidal arrays represent the vacuum filtration process (Figure 3.11). Due to the rapid assembly, the ordering of the particles is random, leading to colloidal glasses. Thus, this is a facile preparation method for random close-packed structures.

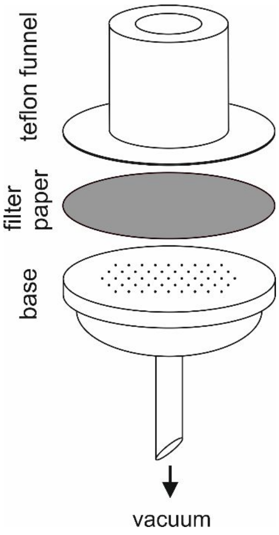

Figure 3.11. Schematic setup of the vacuum filtration system to prepare colloidal glasses. Reprinted from Ruckdeschel et al.[105] with permission from Wiley VCH.

The difference in the ordering by using these two methods is highlighted by the SEM and optical microscopy images in Figure 3.12. Whereas the crystalline arrangement features Bragg colors in the optical microscopy image (a), the amorphous one shows only a diffusive scattering (b). This is validated by the corresponding SEM images (c, d).

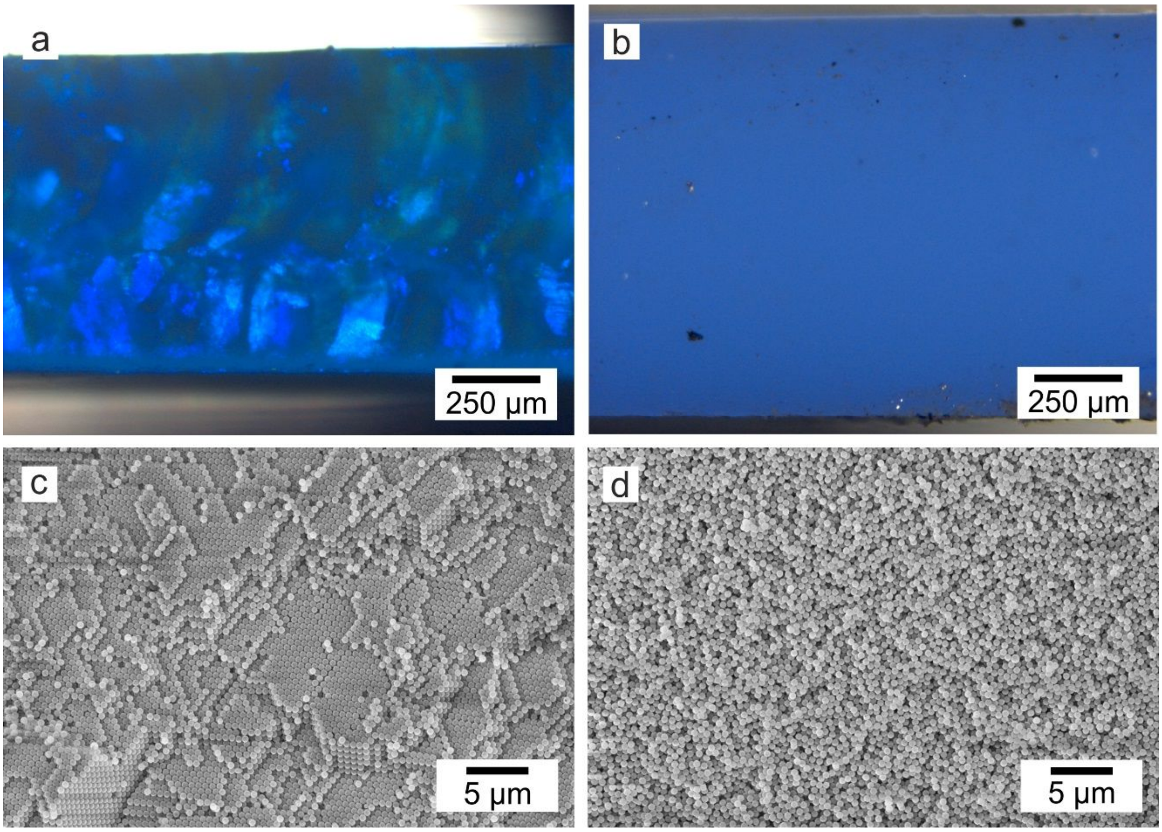

Figure 3.12. Scanning electron microscopy images (a, b) and optical microscopy images (c, d) of hollow silica nanoparticle colloidal assemblies showing either a crystalline packing (a, c) or an amorphous ordering (b, d). Adapted from Ruckdeschel et al.[105] with permission from Wiley VCH.

3.2 Methods

Several methods were used in this thesis to characterize the particles (shape, size, size distribution, and microstructure), the assemblies (symmetry, and density), and the thermal properties (specific heat capacity, and thermal diffusivity). The most frequently used techniques are summarized in Figure 3.13.

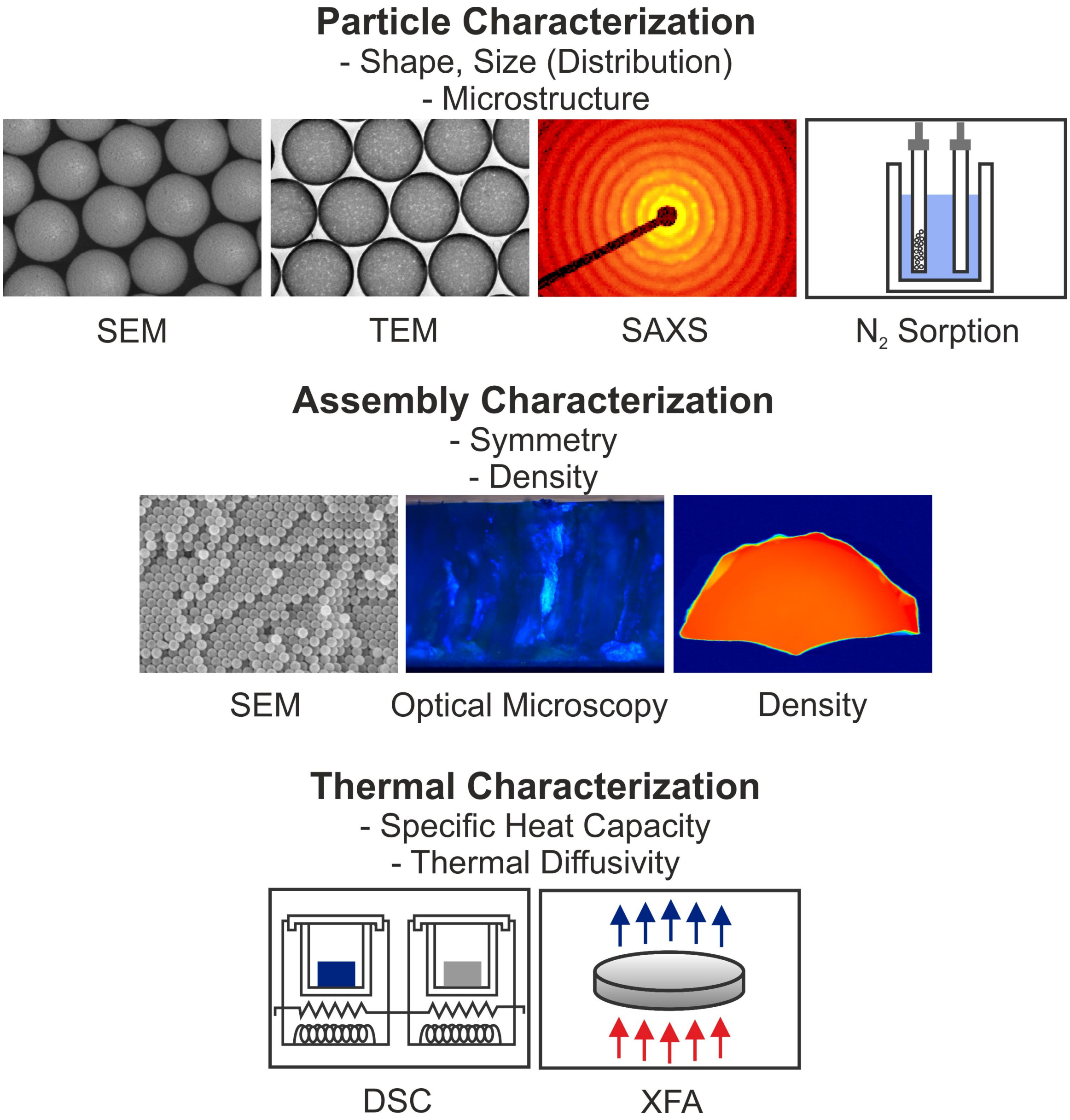

Figure 3.13. Overview of the most frequently used characterization methods in this work.

In the following, the different methods will be introduced shortly. For more detailed information, the cited literature is recommended.

3.2.1 Particle Characterization

The particles were characterized by scanning and transmission electron microscopy (SEM, TEM), small-angle X-ray scattering (SAXS), and nitrogen sorption measurements.

SEM[106] is a type of electron microscope which creates images of a sample by scanning the surface with a focused electron beam. By the interaction of the electrons with the sample, various scattering events occur, which give information about the surface topography and the composition. In this work, the SEM was used as a tool to analyze the shape, size, and size distribution of the polystyrene particles and the polystyrene-silica core-shell particles. For the imaging of the hollow silica spheres, the **TEM**[107-108], another type of electron microscope, was used. It produces images of a sample by an electron beam transmitting the specimen. The interaction of the electrons within the sample creates an image. Due to the transmission of the electrons, information about the size and the shell thickness of silica hollow spheres are received. The shell thickness is given by the dark shaded ring surrounding the hollow core (Figure 3.13). Furthermore, the porosity of the shell is imaged. However, at large shell thicknesses, the contrast between the inner core and the silica shell becomes too weak. In that case, the **SAXS**[109] technique is the preferred method to determine the shell thickness. Small-angle X-ray scattering clarifies the structure of particles in terms of averaged particle sizes or shapes. Thereby, a sample is illuminated by X-rays, and the scattered intensity is measured by a detector as a function of the scattering angle. The measurements are typically made at very small angles (~0.1 – 5°). Thus, with decreasing scattering angle, increasingly larger structural features on the length scale of nanometers (~1 – 100 nm) can be resolved. This clearly covers the range of the silica shell thicknesses of the hollow spheres. For finer geometric information about the microporosity of the shell and the overall surface area, **Nitrogen sorption**

measurements[110-111] were performed. The isotherms were recorded at 77 K between 0 and 100 kPa which corresponds to the full range of p/p_0 (p_0 is the saturation pressure). During the measurement, nitrogen is passed over the sample at 77 K, and the adsorbed quantity is determined (adsorption). Subsequent pressure reduction within the apparatus releases some of the nitrogen molecules from the surface. The result is an adsorption-desorption isotherm. In a certain pressure range ($p/p_0 = 0.05 - 0.3$), the quantity of the adsorbed or released gas is proportional to the surface, the so-called BET surface area. The pore volumes and the pore sizes are usually determined by the non-local density functional theory (NLDFT) based on statistical methods.[110]

3.2.2 Assembly Characterization

The colloidal assemblies were characterized by scanning electron microscopy (SEM), optical microscopy, and density measurements.

SEM[106] is briefly described in the section before. It was used for the particle and the assembly characterization. However, for the latter one, the colloidal arrays were mounted in a particular specimen holder to enable the imaging of the side-view images. Hence, the packing symmetry could be determined. However, for an extensive impression of the symmetry, the use of the **optical microscopy**[112] is useful. Thereby, the sample is placed under the bright-field optical microscope to obtain side-view images of the colloidal assembly. For a close-packing of particles in the size range of the light, distinct Bragg reflections are detected. Whereas for random close-packed structures, only a diffusive scattering is observed.

Moreover, the **densities** of the colloidal assemblies were determined. This is of peculiar interest for the thermal transport properties, because of the necessity to know this parameter to calculate the thermal conductivity (Chapter 3.2.3). The density was most frequently resolved by measuring the weight and the volume of the colloidal assembly. For the volume determination, a 3D non-contact surface profiler was used. It captures the volume by scanning the surface.

3.2.3 Thermal Characterization

The thermal conductivity can be calculated by multiplying the thermal diffusivity by the density and by the specific heat capacity. The latter one was measured with the help of the differential scanning calorimetry (DSC), and the thermal diffusivity was measured by using xenon flash analysis (XFA).

The specific heat is the amount of heat per unit mass required to raise the temperature by one degree Celsius. It was measured in this work by **DSC**[113] using a sapphire standard calibration. Thereby, the measured heat flow can be converted into the specific heat capacity [$Jg^{-1}K^{-1}$].

The most important method, used in this thesis, was the **XFA**. It is described in the following in more detail. With the xenon flash analysis, the thermal diffusivity α [cm^2s^{-1}] was measured. This thermophysical property describes how fast temperature diffuses through a material. The XFA setup and a typical measurement signal, fitted with an appropriate fit model, are depicted in Figure 3.14.

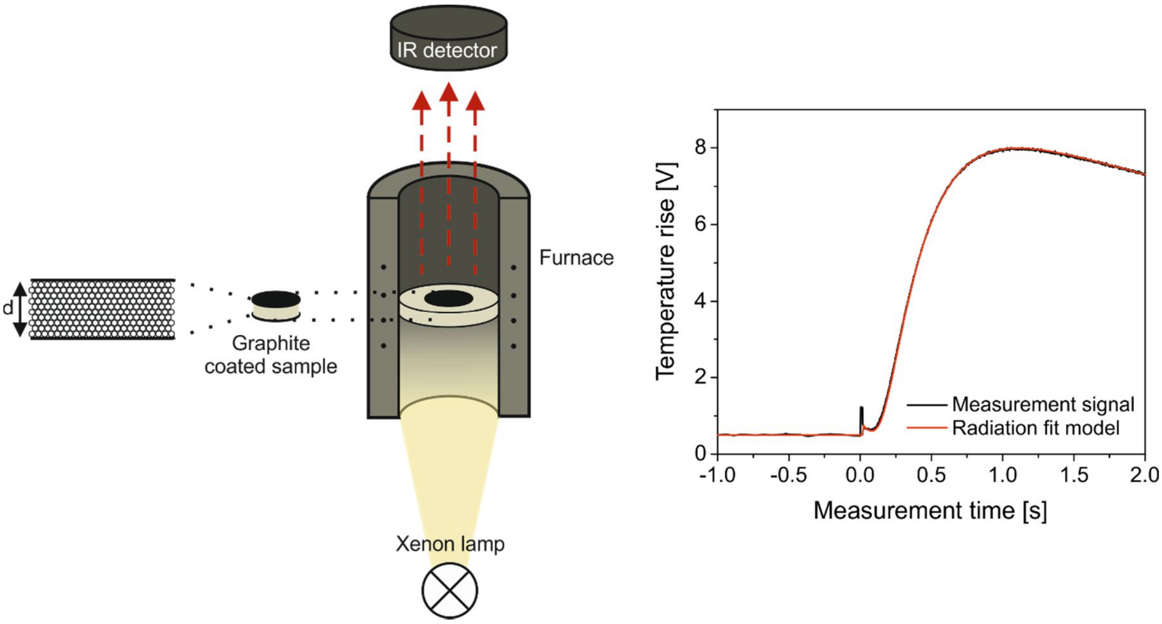

Figure 3.14. Setup of the xenon flash analysis (XFA), and a typical measurement signal of a hollow silica sphere colloidal crystal, fitted by the radiation fit model. Reprinted from Ruckdeschel et al.[105] with permission from Wiley VCH.

Before the measurements, the 3D colloidal assemblies were coated with a thin graphitic layer (high emissivity) on both sides to ensure a proper absorption of the applied energy. Then, the specimen was subjected to a temperature increase at the bottom of the sample by a short xenon light flash. As a result, heat is conducted through the sample due to the temperature gradient. At the rear surface, an infrared (IR) detector measures the time-dependent temperature increase. By fitting the measurement signal with an appropriate model, the effective thermal diffusivity of the measured sample is received. For most cases, the radiation fit model is suitable. This model represents an extension to the finite-pulse and heat loss corrections given by the Combined fit model from Dusza[114]. In contrast, it allows for an amount of the xenon flash to be directly transmitted to the rear sample surface, leading to an instantaneous temperature jump analogous to Blumm et al.[115].

4 Overview of the Thesis

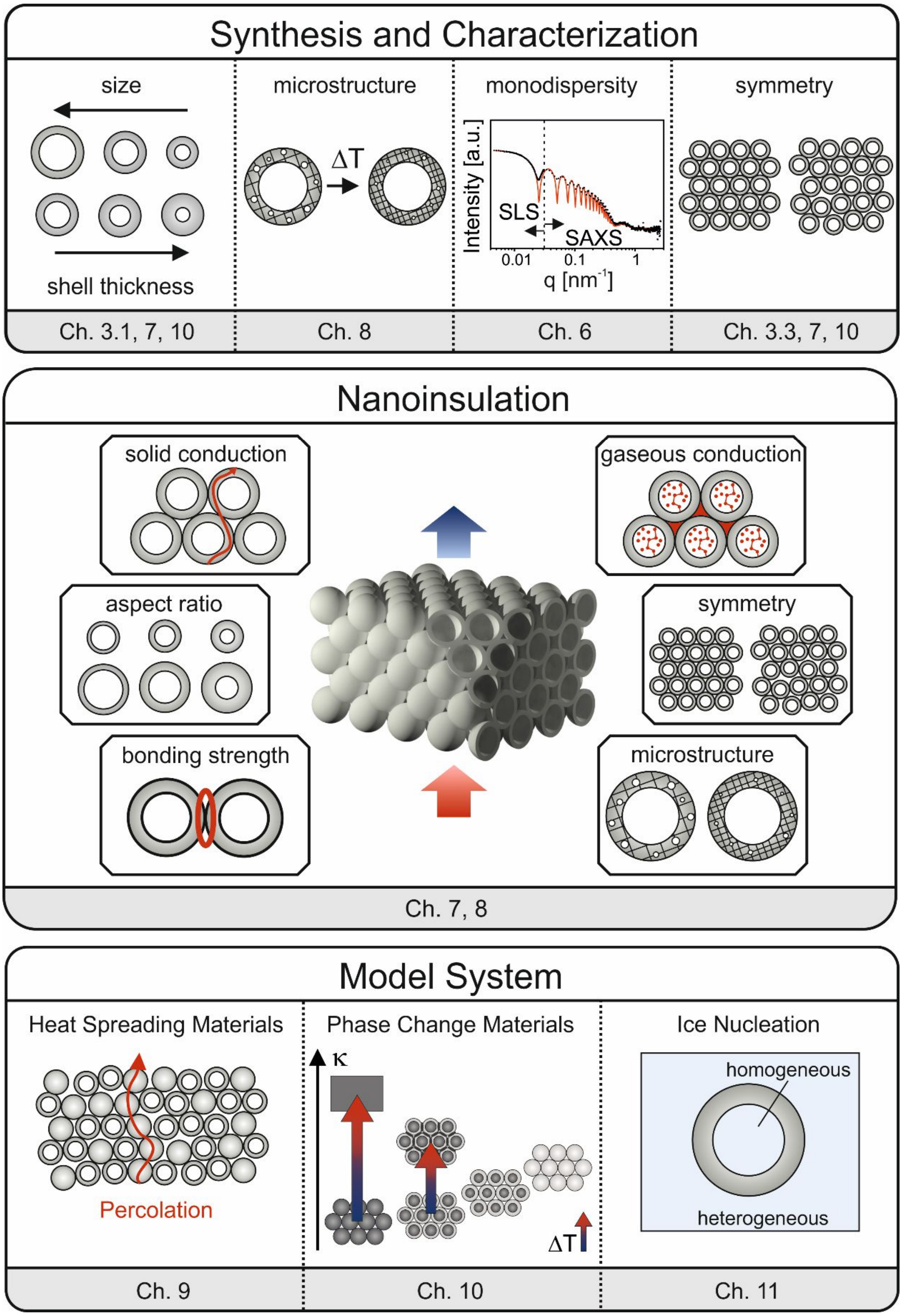

Figure 4.1. Graphical overview of the thesis.

4.1 Synopsis

This work consists of six individual contributions, which are presented in the form of manuscripts, dealing with transport phenomena in silica hollow spheres and hybrid materials. Four of the contributions are published in peer-reviewed journals, and two of them are currently submitted to peer-reviewed journals (see Chapter 4.2). A graphical overview of the different contributions is given in Figure 4.1. In the following, the main results and the connection between the individual manuscripts will be presented.

Monodisperse colloidal hollow spheres are well-defined building blocks that inherently possess two distinct length scales – tens of nanometer shell thickness, and hundreds of nanometer particle size. These structural features can be easily adjusted during the synthesis with high precision (**Chapter 3.1.1** and **3.1.2**). Remarkably, these hollow spheres exhibit an extremely low polydispersity in size and shell thickness. This was addressed in a detailed scattering study (**Chapter 6**) using dynamic and static light scattering (DLS and SLS), small-angle X-ray scattering (SAXS), as well as transmission electron microscopy (TEM).

The low polydispersity of the silica hollow spheres facilitates to use them as building blocks in 3D assembly processes (see **Chapter 3.1.3**). The received hierarchically structured materials, i.e., colloidal crystals, feature a uniquely well-defined structure across multiple length scales. Hence, these materials can be used as a model system to study open- and closed-porous nanoscale heat transport (**Chapter 7 – 8**). The different structural properties, which influence the thermal transport in colloidal assemblies are schematically depicted in Figure 4.1 (Nanoinsulation).

Chapter 7 describes the influence of the geometry of the hollow silica spheres (size and shell thickness), the gaseous conduction (open- vs. closed-pore conduction), the symmetry of the whole assembly (close-packing vs. random close-packing), and the bonding strength between adjacent spheres on the heat transport. The experimental data was further supported by finite element modeling (FEM). While the bonding strength was decreased in this study, it was increased in **Chapter 8** by calcining the colloidal crystals at elevated temperatures (500 – 950 °C). This did change not only the bonding strength, but also the microstructure of the silica shell (microporosity and rigidity). The elucidation of the influence of these two effects on the heat transport is the purpose of this work (**Chapter 8**). In general, hollow silica colloidal assemblies were found to be highly insulating. This can be traced back to the low density, the small pore sizes (Knudsen effect, Chapter 2.2.2), the amorphous structure with its various scattering phenomena, and a large number of interfaces. Thus, HSNP colloidal arrays are a nanoinsulation material with superior properties compared to alternatives such as polymer foams – which may be flammable – and silica aerogels – which may be challenging to produce. In general, the thermal conductivity decreases for large diameters and thin shell thicknesses, a large microporosity and a less rigid silica network (low calcination temperatures), a lower symmetry of the particle array, and a low interfacial bonding between adjacent spheres. The lower limit in vacuum was found to be less than 10 $\mathrm{mW\,m^{-1}\,K^{-1}}$.

The previous studies reveal the great potential to comprehend heat transport phenomena in nanostructured materials. In the following, the concept is transferred to hybrid materials: binary colloidal crystals (**Chapter 9**) and core-shell particle colloidal crystals (**Chapter 10**).

In **Chapter 9**, the heat transport through binary colloidal crystals is discussed. For this purpose, hollow silica spheres and poly(methyl methacrylate-co-*n*-butyl acrylate) (P(MMA-co-nBA)) particles were mixed in different particle volume fractions from 100 % polymer to 100 % hollow spheres. The thermal conductivity increases with increasing polymer content without any percolation threshold. By FEM, it was found, that a percolation threshold is only apparent for large thermal conductivity contrasts of the two particle types ($\kappa_1/\kappa_2 > 500$). However, one kind of percolation network can be formed by heating the assembly above the glass transition temperature of the polymer. As a result, a continuous polymer network was formed with nanoinclusions of the hollow spheres leading to a distinctly increased thermal conductivity at a certain polymer volume fraction. This temperature-induced percolation is a measure of the structural integrity of the particle ensemble accompanied by a demixing of the hollow spheres during film formation.

Chapter 10 deals with the thermal transport properties of core-shell particle colloidal assemblies. In these structures, the core is filled with polystyrene instead of air. Additionally, to the investigation of the thermal properties as a function of the composition (size and shell thickness) at room temperature, the heat transport was monitored in dependence of the temperature. As opposed to a monotonous increase as observed for the silica hollow spheres (**Chapter 8**), the thermal transport increases significantly at temperatures way above the glass transition temperature of the polystyrene for some of the assemblies. As this strongly depends on the morphology, core-shell particle colloidal crystals are a suitable model system due to their versatility. The understanding of heat transport in these systems is of peculiar interest for phase change materials. Notably, for the phase change application, the suppression of the crystallization must be considered when reducing the size of the particles. This is shown for water in Chapter 11, but matters also for encapsulated polymer.

The nucleation in confined systems is studied on individually dispersed silica hollow spheres in water (**Chapter 11**). The focus was laid on finding of homogeneous nucleation inside the capsules beside the common heterogeneous nucleation in the bulk water phase. Therefore, the particles with an inner pore diameter of ~140 – 590 nm and a comparable shell thickness of ~20 nm were redispersed in water, and the ice nucleation process was monitored using differential scanning calorimetry (DSC) and dielectric spectroscopy (DS). It was found that with decreasing pore diameter, the heterogeneous nucleation is suppressed due to the confined geometry.

In the following, the individual contributions are summarized separately.

Monodisperse Hollow Silica Spheres: An In-Depth Scattering Analysis – Chapter 6

In this chapter, impressively narrowly size-distributed hollow silica nanoparticles are analyzed using transmission electron microscopy (TEM) and different scattering techniques: dynamic and static light scattering (DLS and SLS), as well as small-angle X-ray scattering (SAXS). A quantitative agreement among all methods was found as described in the following.

The monodisperse HSNPs inherently possess distinct length scales – hundreds of nanometer of the total diameter (262 – 316 nm), tens of nanometer of the shell (16 – 44 nm), a few nanometer micropores within the shell. The homogeneity and the morphology of the capsules were determined by transmission electron microscopy. A TEM image of the particles with the smallest diameter and the thinnest shell is depicted in the inset in Figure 4.2a. The shell is represented by the dark rim surrounding the hollow core. The size and the shell thickness were studied on a statistical ensemble using DLS. The obtained hydrodynamic radii R_h are in good agreement with the results obtained from TEM measurements. Furthermore, SLS experiments were performed to investigate the radius of gyration R_g and the form factor $P(q)$. Considerably, for the particle with the thinnest shell, the ratio R_g/R_h equals almost 1, which is the value for an ideal homogeneous hollow sphere with an infinitely thin shell. Consistently, this ratio decreases with increasing shell thickness. The SLS measurements can assess a second length scale, the shell thickness by using a form factor model. It delivers values comparable to the TEM measurements. However, the SLS is restricted to very small q-values, and the form factor is, therefore, only partially accessible. The q-range can be expanded by using SAXS. As a result, up to 20 diffraction orders of the silica hollow sphere form factor were resolved, proving the narrow size distribution. Furthermore, the data obtained from SLS and SAXS could be combined to a master curve (Figure 4.2a) covering a q-range of four orders of magnitude. This scattering profile comprises two sorts of contributions: one originating from the particle diameter, and one from the shell thickness. A core-shell form factor analysis (red line in Figure 4.2a) is suitable to describe all structural features across all length scales.

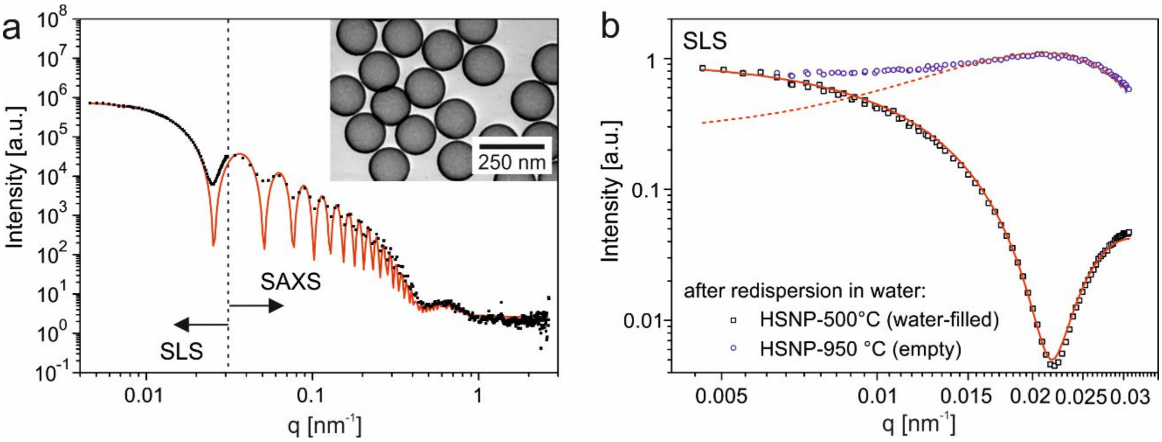

Figure 4.2. Hollow silica nanoparticles with a diameter of 262 nm and a shell thickness of 16 nm. (a) Superposition of static light scattering (SLS) and small-angle X-ray scattering (SAXS). The structural features of the master curve (black dots) can be fitted by a single analysis using a core-shell form factor (red line). The inset shows a transmission electron microscopy (TEM) image of the corresponding silica hollow spheres. (b) Form factor analysis by SLS to investigate the scattering contrast of water-filled HSNP-500 °C (black squares) and air-filled HSNP-950 °C (blue circles) particles. The red lines represent a form factor model for spherical core-shell particles with equal (solid line) or different (dashed line) scattering contrasts between the core and the surrounding medium (water). All data shown are normalized to 1. Adapted from Ruckdeschel et al.[116] with permission from Springer International Publishing.

Moreover, the hollow silica particles were calcined at high temperatures (950 °C instead of the calcination at 500 °C). This leads to microstructural changes (decrease in BET surface area and closure of the micropores) and, therefore, to an even better resolved SAXS pattern, especially in the high q-region. However, the closure of the micropores prevents the water infiltration into the capsule for thick shells. This leads to a strongly altered SLS profile due to a different scattering contrast between the core and the surrounding medium (blue squares, Figure 4.2b). Notably, the SAXS profiles of the capsules calcined at 950 °C do not show any significant changes due to the insensitivity to the change in the scattering contrast.

In summary, the tight control over the two structural length scales – size and shell thickness- enables the application as a future calibration standard for TEM, and for scattering techniques (DLS, SLS, and SAXS). Furthermore, the low distribution in size opens the opportunity to use them as a model system for ice nucleation, as described in the following, or as building blocks to prepare colloidal assemblies.

Understanding Thermal Insulation in Porous, Particulate Materials – Chapter 7

In colloidal assemblies, heat is mainly conducted through the solid, and the gaseous phase (open- and closed-pore volume). The other heat transport mechanisms (via convection or radiation) are negligible due to the small pore sizes, the transient measurement, and the small temperature difference applied in the used characterization method (xenon flash analysis, XFA). The different thermal transport pathways are depicted in Figure 4.3.

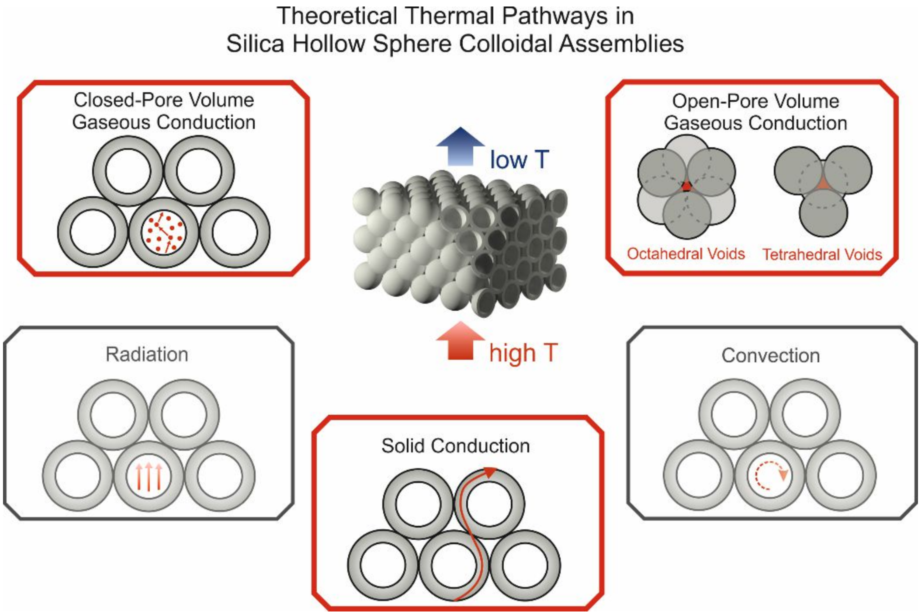

Figure 4.3. Thermal transport pathways in silica hollow sphere colloidal assemblies. The red-framed boxes mark the relevant contributions. Reprinted from Ruckdeschel et al.[105] with permission from Wiley VCH.

In the following, the heat conduction through the solid and gaseous phase is described as a function of the structure of the HSNP colloidal assemblies. Structural parameters, which influence the heat transport are, e.g., the geometry of the capsules (size and shell thickness), the packing symmetry (close-packing vs. random close-packing), and the bonding strength. These structural features will be elucidated concerning the heat transport, starting with the geometry of the particles. Therefore, two sets of series were synthesized: the size series and the shell thickness series. In the size series, the diameter of the particles was altered between 267 and 469 nm with a comparable shell thickness of ~15 nm, whereas in the shell thickness series, the diameter of the particles was kept constant at ~270 nm while the shell thickness was adjusted between 14 and 40 nm. The corresponding TEM images of the HSNPs are depicted in Figure 4.4a. These reveal the extremely low distribution in size and in shell thickness, which is essential for the assembly process when building up colloidal crystals.

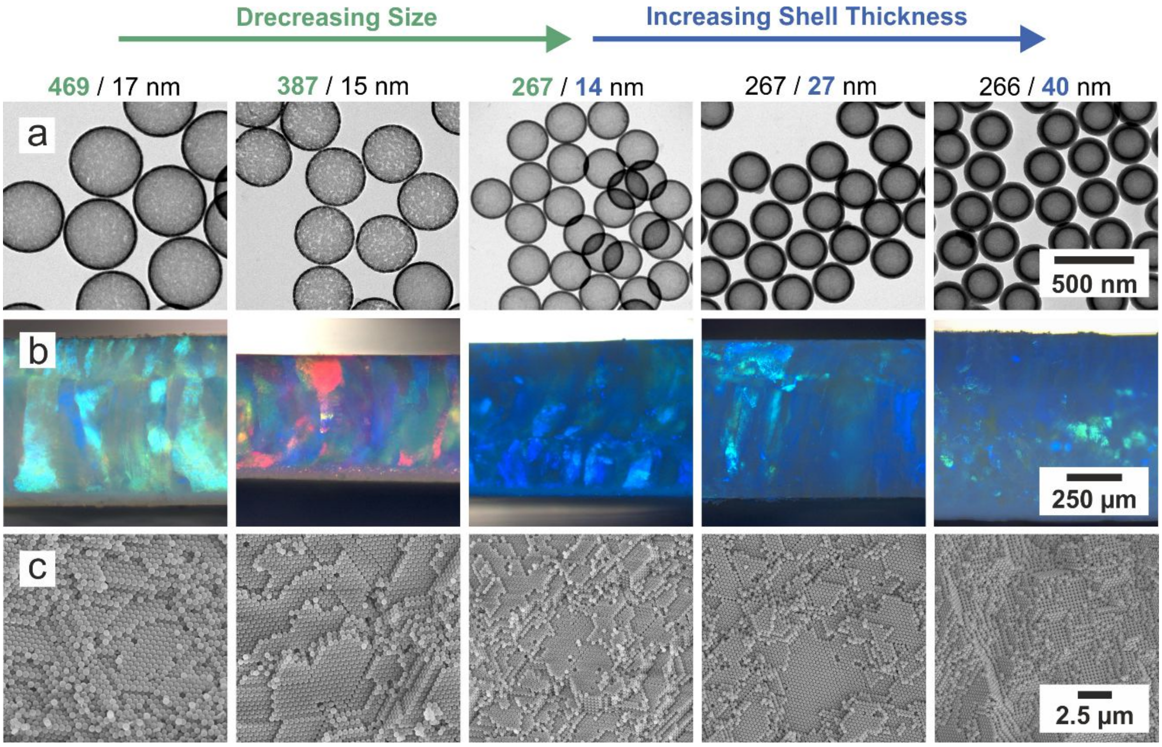

Figure 4.4. Silica hollow sphere colloidal crystals. (a) Transmission electron microscopy (TEM) images of the particles, (b) optical microscopy, and (c) scanning electron microscopy (SEM) side-view images of the colloidal crystals. Reprinted from Ruckdeschel et al.[105] with permission from Wiley VCH.

The highly ordered structure is featured by bright colors resulting from Bragg reflections in the optical microscopy side-view images (Figure 4.4b), as well as by the SEM side-view images (Figure 4.4c). Detailed information about the synthesis and the assembly process can be found in Chapter 3.1.

The geometry of the silica hollow spheres influences the thermal transport properties significantly. Counter-intuitively, a decreasing particle size and increasing shell thickness lower the temperature diffusion through the assembly, which is expressed by a reduced thermal diffusivity α [cm^2s^{-1}]. By contrast, the thermal conductivity κ [$Wm^{-1}K^{-1}$] behaves inversely. It increases with decreasing core/shell ratio as depicted in Figure 4.5a. This behavior is observed in vacuum (0.05 mbar) and helium (1000 mbar). However, due to the additional transport pathway through the gaseous phase, the thermal conductivity in helium is substantially higher. The lowest thermal conductivity in vacuum is found to be ~27 $mWm^{-1}K^{-1}$ and in helium ~43 $mWm^{-1}K^{-1}$ for the particles HS-469/17 with the largest diameter (469 nm) and a thin silica shell (17 nm). To quantify the individual contributions of the solid and gaseous transport (open-pore volume and closed-pore volume), finite element modeling (FEM) is used. The simulated heat flux density image is illustrated as an inset in Figure 4.5a. It already shows the preferred thermal transport through the solid silica shell, and the lower contribution of the closed-pore volume to the total thermal conductivity compared to the open-pore volume. This is also quantitatively confirmed by an integration of the heat flux densities.

However, the geometry is not the only decisive parameter for the heat transport properties of silica hollow sphere colloidal crystals. The number and strength of the interparticle contact points are also relevant features. The number of contact points is decreased by reducing the packing symmetry from a close-packing (HS-469/17-c) to a random close-packing (HS-469/17-a). Thereby, for the largest particles, the effective thermal conductivity is lowered by 23 % to only 21 $mWm^{-1}K^{-1}$ in vacuum (see Figure 4.5b). In helium, the additional gaseous conduction overwhelms, leading to a comparable effective thermal conductivity of the crystalline and the amorphous sample.

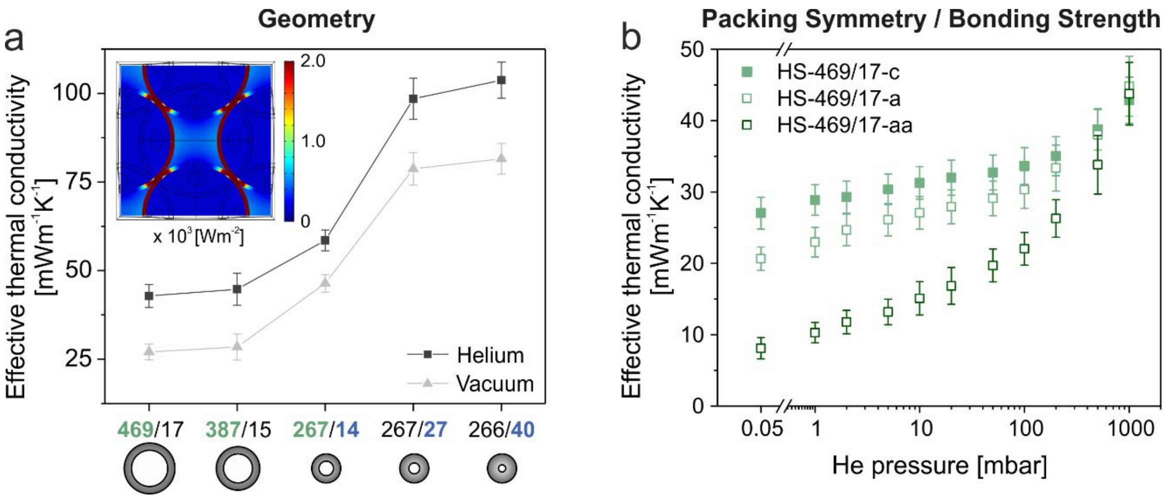

Figure 4.5. Heat transport properties of silica hollow sphere colloidal assemblies. (a) Influence of the particle geometry on the effective thermal conductivity in vacuum (0.05 mbar) and helium (1000 mbar). The inset shows the heat flux density image for a cross-section through the colloidal crystal consisting of the largest particles HS-469-17, obtained from finite element modeling (FEM). (b) Influence of the packing symmetry and bonding strength on the colloidal assembly consisting of the particles HS-469/17. The acronym *c* represents the crystalline particle array, the *a* stands for the amorphous packing, and the *aa* represents the amorphous packing with a reduced interparticle bonding strength. Adapted from Ruckdeschel et al.[105] with permission from Wiley VCH.

The reduction of the interparticle bonding strength was achieved by calcining the core-shell particles *before* the assembly process (HS-469/17-aa). As a result, the spheres possess only weak interparticle van der Waals forces. In all previous cases, the core-shell particles were calcined after the assembly. Thus, covalent bonds are formed between adjacent spheres. The reduction of the interparticle bonding strength further reduces the effective thermal conductivity in vacuum to only 8 mWm^{-1}K^{-1}. However, the low thermal conductivity cannot be maintained under atmospheric conditions due to the overwhelming thermal transport through the gaseous phase, as described beforehand (see Figure 4.5b). In air under ambient conditions, the effective thermal conductivity is as low as ~35 mWm^{-1}K^{-1}. Overall, these particulate materials can be considered as a non-flammable and dispersion processable insulation material as a replacement for commercial polymer foams.

In this contribution, the colloidal crystals were calcined at 500 °C. In the following, the impact of higher calcination temperatures (up to 950 °C) on the structural properties and, hence, on the heat transport of HSNP colloidal crystals will be further characterized.

Hollow Silica Sphere Colloidal Crystals: Insights into Calcination Dependent Thermal Transport – Chapter 8

In the previous section, the influence of various structural parameters on the transport of heat was investigated and adjusted to find the lower limit of the thermal conductivity in HSNP colloidal assemblies. In this contribution, the aim is not to get a record-breaking ultra low thermal conductivity, but to use the highly defined hierarchical structure as a platform to study further fundamentals of heat transport in amorphous particle-based materials regarding the calcination temperature.

Therefore, we prepared colloidal crystals consisting of HSNPs with a diameter of 316 ± 4 nm and a shell thickness of 44 ± 2 nm (Chapter 3.1). Correlative light and electron microscopy (CLEM) side-view images of the colloidal ensembles in Figure 4.6a, calcined at 500 °C, highlight the highly ordered close-packed array of the building blocks. By using simple calcination steps (500, 650, 800, and 950 °C), (i) the internal microstructure and (ii) the interfacial contact points are significantly changed. The altered microstructure is expressed by a reduction of the total surface area and a loss of the microporosity, by an increase of the Q^4 Si atoms, and by an increase of the rigidity of the silica network. These microstructural changes were received from nitrogen sorption analysis, hyperpolarized ^{129}Xe NMR studies, and solid-state MAS ^{29}Si NMR measurements. Despite the microstructural changes, the macroscopic structure of the hollow spheres and their colloidal crystals remain unchanged with higher calcination temperatures.

The influence of the calcination temperature on the heat transport is shown in Figure 4.6b. Here, the focus is on the solid conduction through the silica network. Thus, the thermal conductivity was determined in vacuum. At room temperature, the thermal conductivity increases with increasing calcination temperature from 71 mWm^{-1}K^{-1} (500 °C) to 140 mWm^{-1}K^{-1} (950 °C). For all samples, the thermal conductivity increases with increasing measurement temperatures. However, the slope differs. It decreases from $\kappa \sim T^{0.5}$ for 500 °C to $\kappa \sim T^{0.4}$ for 950 °C calcination, hinting to the stiffening of the silica network. As a reference, quartz glass possesses a proportionality of $\kappa \sim T^{0.3}$.

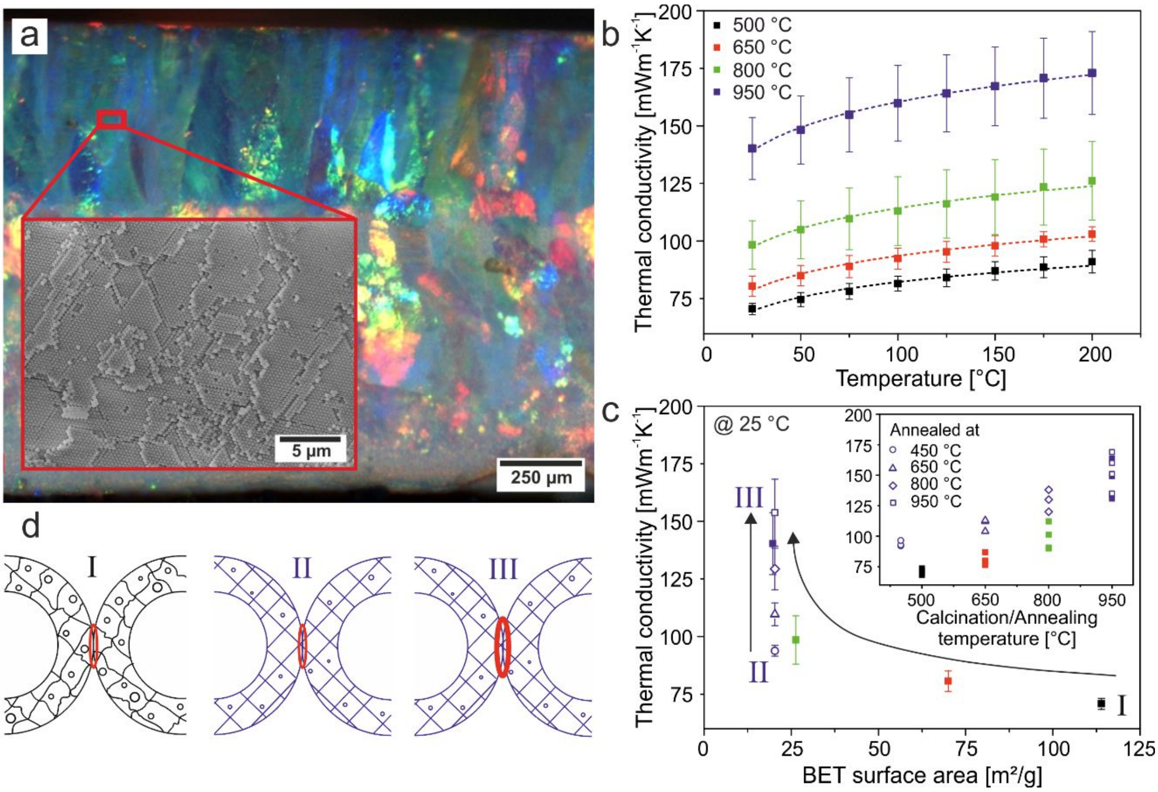

Figure 4.6. (a) Correlative light and electron microscopy (CLEM) side-view images of the HSNP colloidal crystal calcined at 500 °C. (b) Thermal conductivity of HSNP colloidal crystals calcined at different temperatures (500 – 950 °C) as a function of the measurement temperature in vacuum. (c) Thermal conductivity as a function of the BET surface area and the calcination/annealing temperature (inset) in vacuum at 25 °C. (d) Schematic representation of the internal structural changes and the increase of the interparticle bonding within the colloidal ensemble. Adapted from Ruckdeschel et al.[55] with permission from The Royal Society of Chemistry.

In the further discussion, the focus is laid on the measurements at 25 °C, still in vacuum. Figure 4.6c depicts the influence of the microstructural changes in the thermal conductivity. With increasing calcination temperature, the BET surface area decreases, leading to a significantly reduced heat transport. However, this change in the microstructure is accompanied by a closure of the micropores, a small increase in Q^4 Si atoms, a higher rigidity (increased spin-lattice relaxation time), and an increase of the interparticle bonding (Figure 4.6d). To grade the interfacial bonding in comparison to the microstructural changes, the thermal properties of *annealed* colloidal crystals are investigated. For this purpose, the core-shell particles are calcined at 950 °C *before* the assembly process. Subsequently, the colloidal crystals are annealed at 450 – 950 °C. As a result, these particle arrays are only sensitive to changes in the interparticle bonding strength since the internal structure already resembles a highly condensed network with a small surface area, a high rigidity, and closed micropores. The thermal conductivity data of the *annealed* samples are depicted as open symbols in Figure 4.6d. They reveal the higher contribution of the interfacial bonding than microstructural changes in the amorphous shell material.

With this study and the previous one, the great potential of silica hollow spheres as an insulation material, and a model system to understand fundamental heat transport in particulate, porous materials was demonstrated. It was found that the thermal conductivity decreases for large diameters and thin shell thicknesses, a large microporosity and a less rigid silica network (low calcination temperatures), a lower symmetry of the particle array, and a low interfacial bonding between adjacent spheres. The lower limit was found to be less than $10\,\mathrm{mW\,m^{-1}K^{-1}}$ in vacuum and ~$35\,\mathrm{mW\,m^{-1}K^{-1}}$ in air. Moreover, it was shown that the inner pore gaseous conduction has a minor contribution to the overall heat transport. In the following the study is expanded towards hybrid materials.

Thermal Transport in Binary Colloidal Glasses: Composition Dependence and Percolation Assessment – Chapter 9

In this chapter, important aspects of binary colloidal assemblies regarding the heat transport properties are addressed. Firstly, nanostructured binary composite materials of any mixing ratio without any cluster formation or demixing were fabricated by a simple filtering method (Chapter 3.2.2). As a result, random close-packed structures with well-distributed HSNPs and polymer particles are formed. Secondly, the thermal transport properties of these binary composites are studied in vacuum, and compared with various mixing models (Figure 4.7a).

In pure silica hollow sphere colloidal glasses (particle diameter ~420 nm and shell thickness ~25 nm), the heat transport is limited due to several structural parameters (low density, large amount of interfaces, low packing symmetry, and low interfacial bonding) and amounts to only 13 $\mathrm{mW\,m^{-1}\,K^{-1}}$. These features are examined in detail in Chapter 7. The thermal conductivity of P(MMA-*co*-nBA) polymer particle colloidal glasses is about 57 $\mathrm{mW\,m^{-1}\,K^{-1}}$. By mixing these two types of particles, the thermal conductivity can be adjusted within these boundaries. The small contrast between the two thermal conductivities results in the absence of percolation. By FEM, it was found, that a thermal conductivity ratio of at least 1:500 is needed to observe percolation through binary colloidal glasses. On that account, a particle mixture of HSNPs and diamond particles features percolation pathways with a threshold at 27 % diamond particles.

The comparison of the experimental data to the most common mixing models (Figure 4.7a) shows that the EMT model delivers the best agreement. However, at low and high ratios, the Maxwell-Eucken model also fits quite well to the data. In these regions, the assumption of separated inclusions is valid since the minority particle phase is dispersed in the majority phase.

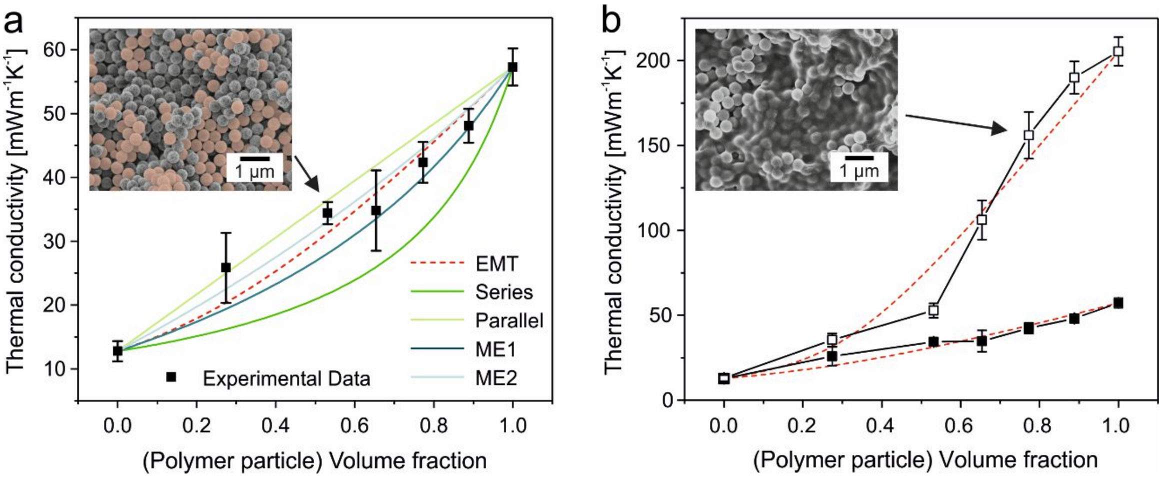

Figure 4.7. (a) Thermal conductivity of binary colloidal glasses measured at 25 °C in vacuum in comparison to common mixing models: effective medium theory (EMT), series, parallel, Maxwell-Eucken (ME) 1 and 2 model. The inset shows a side-view scanning electron microscopy (SEM) image of a binary colloidal glass with 50 % polymer particles and 50 % HSNPs (red-colored). (b) Thermal conductivity of the binary colloidal glasses before (closed symbols) and after heating to 150 °C (open symbols), measured at 25 °C in vacuum. The red dashed line represents the EMT model. The inset depicts a side-view SEM image of a binary colloidal glass with 50 % polymer particles and 50 % HSNPs after the heating process. Reprinted with permission from Ruckdeschel et al.[117].

In the second part of the work, the binary colloidal assemblies were heated up to 150 °C. Thereby, the polymer particles soften, leading to a loss of the interparticle interfaces. Accordingly, a continuous polymer network forms at a polymer content >50 %, which can be understood as a threshold for structural integrity. This is manifested by an increased heat transport as depicted in Figure 4.7b. By considering the structural changes of the assembly upon heating, the temperature-induced percolation is rather a measure of the structural integrity of the overall particle ensemble. As soon as the polymer particles constitute the majority phase, the structural integrity starts to break down. Hence, the EMT model (red dashed line in Figure 4.7b) is not suitable anymore to describe the system due to the concomitant phase separation upon annealing. The SEM image (inset in Figure 4.7b) qualitatively supports this assertion.

Interface and Morphology Control of the Thermal Conductivity in Core-Shell Particle Colloidal Crystals – Chapter 10

In this contribution, the heat transport properties of polystyrene-silica core-shell particle colloidal crystals are investigated. The purpose is to quantify the influence of the core-shell particle dimensions (size and shell thickness) on the thermal transport. Therefore, two series were synthesized: a size series with particle diameters in the range of ~270 – 480 nm and a comparable shell thickness of ~15 nm, and a shell thickness series with a silica shell of 15 – 42 nm and an overall particle diameter of ~270 nm. All hybrid particles possess a high structural precision, which facilitates the subsequent assembly into hexagonally ordered colloidal crystals.

For the size series, the thermal conductivity decreases with increasing size from 61 $\mathrm{mW\,m^{-1}K^{-1}}$ to 44 $\mathrm{mW\,m^{-1}K^{-1}}$ in vacuum. By heating the colloidal assemblies up to 200 °C, a step-like increase is observed at temperatures above the glass transition temperature T_g of the polystyrene (Figure 4.8a). This can be attributed to polymer leaking through the silica shell. Thus, the contact between adjacent spheres is improved, and the interfacial contact resistance is decreased. The leakage temperature depends on the overall particle size and increases with decreasing particle diameter.

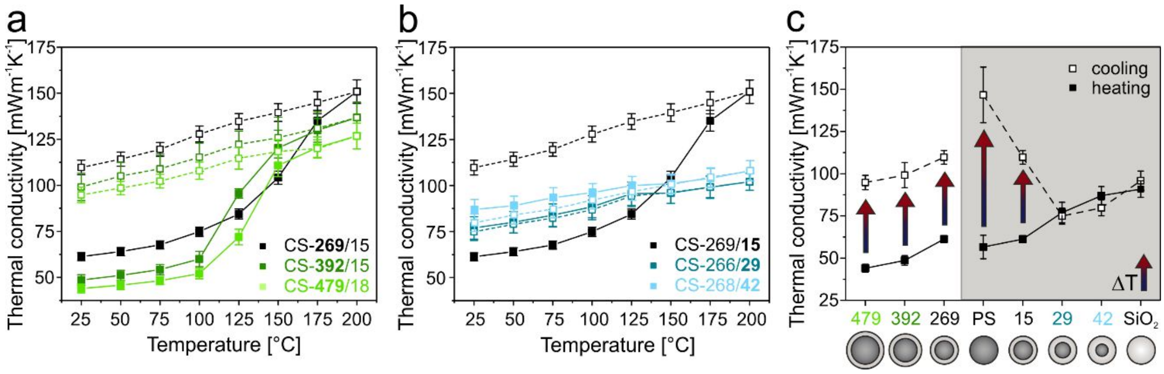

Figure 4.8. Thermal conductivity of polystyrene-silica core-shell particles in vacuum. (a) Size series, (b) shell thickness series, and (c) comparison of the core-shell particle assemblies with polystyrene and silica colloidal crystals. Reprinted from Ruckdeschel et al.[118].

For the shell thickness series, the thermal conductivity increases with increasing shell thickness from 61 to 87 $\mathrm{mW\,m^{-1}K^{-1}}$ in vacuum (Figure 4.8b). Notably, the increasing shell thickness leads to a suppression of the polymer leakage. As a result, the thermal conductivity stays at a comparable level after heating. Slight differences can be traced back to the loss of absorbed water during the heating process.

In the following, the core-shell particles are compared to polystyrene latex and silica particle colloidal crystals. The thermal conductivities at room temperature are depicted in Figure 4.8c. For the same outer diameter (shaded in gray), the colloidal crystals of the solid silica spheres possess the highest thermal conductivity, and the pure polystyrene beads the lowest. However, by heating of the colloidal arrays, this trend reverses. While the thermal conductivity of the silica colloidal crystals does not increase upon heating, the thermal conductivity of the polystyrene arrays increases significantly up to 147 $\mathrm{mW\,m^{-1}K^{-1}}$. The large increase can be explained by the softening of the polystyrene upon heating above the T_g leading to a loss of interfaces.

For a phase change application, the size and the shell thickness have to be adjusted, so that the capacity of latent heat storage is maximal. Important is the shell thickness to seal the inner core. While the increase of the thermal conductivity helps to distribute heat, the leakage of the core material restricts the storage capacity in the long term. Furthermore, for the phase change application, the suppressing of the crystallization must be considered when reducing the size of the particles. This is shown for water in Chapter 11 but also matters for encapsulated polymer.

Homogeneous Nucleation of Ice Confined in Hollow Silica Spheres – Chapter 11

In this work, hollow silica nanoparticles are employed as a confining medium to control the ice nucleation mechanism. For this purpose, a series of hollow capsules with comparable shell thicknesses (~20 nm) and comparable microporous cavities

(~2 – 3 nm), but different diameters (~190 – 640 nm), were redispersed in water. The length scales available in HSNPs significantly affect the ice nucleation. This is studied by differential scanning calorimetry (DSC) and dielectric spectroscopy (DS). The DSC measurements at a cooling rate of 10 °C/min show two exothermic peaks: a major one at about -20 °C and a smaller one at about -40 °C. The two peaks can be assigned to water crystallization outside (heterogeneous nucleation) and inside (homogeneous nucleation) of the hollow particles. The major part of the water is outside of the spheres and produces, therefore, the main signal (-20 °C).

Similar results were obtained by DS. The high dielectric permittivity and its temperature dependence can serve as a fingerprint for the mechanism of ice nucleation. For bulk water, the dielectric permittivity increases upon cooling. After freezing, a low value corresponding to the limiting high-frequency permittivity of hexagonal ice (ε'_∞~3.2) is reached. At a cooling rate of 5 °C/min, bulk water freezes at -7.9 °C. A similar behavior of the dielectric permittivity is observed for the redispersed hollow spheres. First, the value increases upon cooling, followed by a discontinuous decrease within the range from -7 to -11 °C to a permittivity value of ~4.5. On further cooling, a second small step exists toward a permittivity of ~3.7, which can be assigned to the homogeneous nucleation process. Moreover, we showed that the homogeneous nucleation process could be enhanced compared to the heterogeneous one by increasing the concentration of hollow spheres in the water phase. The results are validated by measuring polystyrene-silica core-shell particles as a reference material. Expectably, the homogeneous nucleation does not occur in this system. Overall, the narrow size distributed hollow silica particles have a great potential to use them to understand fundamental phenomena, like ice nucleation.

4.2 Individual Contribution to Joint Publications

The results presented in this thesis were obtained in collaboration with others and are published or submitted as indicated below. In the following, the contributions of all authors to the publications are designated. The asterisk denotes the corresponding authors.

Apart from the following contributions, I want to refer to a review written in collaboration with Fabian Nutz under the supervision of Prof. Markus Retsch. In this review with the title "Thermal Transport in Colloidal Crystals", submitted to a peer-reviewed journal in 2017, we provide a fundamental introduction to the physics of thermal transport, followed by an overview of common assembly strategies to obtain colloidal assemblies and the measurement methods to determine the thermal properties of colloidal materials. Finally, the recent literature about heat transport in colloidal assemblies is presented.

Chapter 6

This work was published as a full paper in Nano Research (*Nano Res.*, **2016**, 9, 1366) with the title

"Monodisperse Hollow Silica Spheres: An In-Depth Scattering Analysis"

by Pia Ruckdeschel, Martin Dulle, Tobias Honold, Stephan Förster, Matthias Karg, and Markus Retsch*.

I planned the experiments, synthesized the hollow silica nanoparticles and characterized them using TEM and SEM. I did the SAXS fitting under the guidance of Martin Dulle, who performed the measurements. Furthermore, I was involved in scientific discussions and wrote parts of the manuscript (experimental part). Tobias Honold and Matthias Karg performed the SLS and DLS measurements and the corresponding evaluation. Stephan Förster was involved in scientific discussions. The manuscript was written by Matthias Karg and Markus Retsch.

Chapter 7

This work was published as a full paper in Nanoscale (*Nanoscale*, **2015**, 7, 10059) with the title

"Hollow Silica Sphere Colloidal Crystals: Insights into Calcination Dependent Thermal Transport"

by Pia Ruckdeschel, Tobias W. Kemnitzer, Fabian Nutz, Jürgen Senker, and Markus Retsch*.

A significant part of the experimental work of this publication was conducted during my master thesis in the group of Prof. Retsch. I planned the experiments, designed and synthesized all particles and performed the characterization, except for the solid-state NMR measurements. In addition, I wrote parts of the manuscript. The NMR spectra were recorded by Tobias Kemnitzer. Fabian Nutz was involved in scientific discussions. Jürgen Senker co-supervised the project, and Markus Retsch supervised the project and wrote the manuscript.

Chapter 8

This work was published as a full paper in Advanced Functional Materials (*Adv. Funct. Mat.*, **2017**, 27, 1702256) with the title

"Understanding Thermal Insulation in Porous, Particulate Materials"

by Pia Ruckdeschel, Alexandra Philipp, and Markus Retsch*.

I planned all experiments, designed and synthesized all particles and performed the necessary characterization. Furthermore, I wrote the manuscript. Alexandra Philipp performed the FEM simulations and was involved in scientific discussions. Markus Retsch supervised the project and corrected the manuscript.

Chapter 9

This work was published as a full paper in Physical Review E (*Phys. Rev. E.*, **2018**, 97, 022612) with the title

"Thermal Transport in Binary Colloidal Glasses: Composition Dependence and Percolation Assessment"

by Pia Ruckdeschel, Alexandra Philipp, Bernd A. F. Kopera, Flora Bitterlich, Martin Dulle, Nelson W. Pech-May, and Markus Retsch*.

I planned all experiments, designed and synthesized all particles and performed the necessary characterization. Furthermore, I wrote the manuscript. Alexandra Philipp performed the FEM simulations and was involved in scientific discussions. Bernd A. F. Kopera, Martin Dulle, and Flora Bitterlich supported the FEM simulations. Nelson W. Pech-May helped with the formatting of the manuscript. Markus Retsch supervised the project and corrected the manuscript.

Chapter 10

This work was published as a full paper in Advanced Materials Interfaces (*Adv. Mater. Interf.*, **2017**, 4, 1700963) with the title

"Interface and Morphology Control of the Thermal Conductivity in Core Shell Particle Colloidal Crystals"

by Pia Ruckdeschel and Markus Retsch*.

I planned all experiments, designed and synthesized all particles and performed the necessary characterization. Furthermore, I wrote the manuscript. Markus Retsch supervised the project and corrected the manuscript.

Chapter 11

This work was published as a full paper in Journal of Physical Chemistry B (*J. Phys. Chem. B,* **2017**, 121 (1), 306-313) with the title

"Homogeneous Nucleation of Ice Confined in Hollow Silica Spheres"

by Yang Yao, Pia Ruckdeschel, Robert Graf, Hans-Jürgen Butt, Markus Retsch, and George Floudas*.

I synthesized all particles (core-shell and hollow silica nanoparticles) and characterized them using TEM and nitrogen sorption analysis. Furthermore, I helped Yang Yao with the DSC and DS measurements and was involved in scientific discussions. Markus Retsch co-supervised the project. George Floudas supervised the project and wrote the manuscript. Robert Graf and Hans-Jürgen Butt were involved in scientific discussions.

4.3 Graphical Table of Contents

Monodisperse Hollow Silica Spheres: An In-Depth Scattering Analysis

Pia Ruckdeschel, Martin Dulle, Tobias Honold, Stephan Förster, Matthias Karg, and Markus Retsch
(*Nano Res.*, **2016**, 9, 1366)

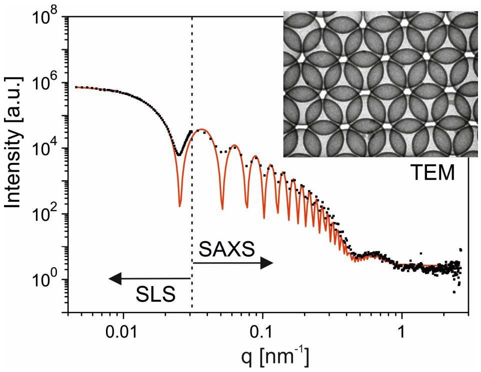

Well-defined hollow silica spheres are an important class of building blocks for hierarchically structured materials, drug delivery, and catalysis. Using a q-range covering four orders of magnitude by combining SLS and SAXS, we highlight their exceptionally narrow size distribution, the influence of scattering contrast, and demonstrate quantitative agreement with TEM and DLS measurements.

Understanding Thermal Insulation in Porous, Particulate Materials

Pia Ruckdeschel, Alexandra Philipp, and Markus Retsch
(*Adv. Funct. Mat.*, **2017**, 27, 1702256)

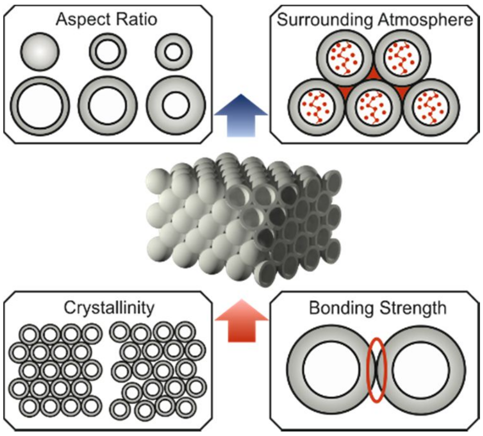

Colloidal assemblies represent a model platform to understand heat transport in nanostructured materials. Using the uniquely well-defined structure of monodisperse hollow silica particles, a material with an extremely low effective thermal conductivity of 8 $\mathrm{mW\,m^{-1}K^{-1}}$ in vacuum can be systematically designed. Control parameters are the particle geometry, the interparticle bonding strength, and the ensemble symmetry.

Hollow Silica Sphere Colloidal Crystals: Insights into Calcination Dependent Thermal Transport

Pia Ruckdeschel, Tobias W. Kemnitzer, Fabian Nutz, Jürgen Senker, and Markus Retsch
(*Nanoscale*, **2015**, 7, 10059)

This versatile study demonstrates the calcination dependent thermal transport of silica hollow sphere colloidal crystal for the first time. Calcining the assembly, noticeably changes the microstructure and the interfacial contact points, and, subsequently, changes the thermal conductivity. Overall the thermal conductivity changes from only 71 to 141 mWm^{-1}K^{-1} by changing the calcination temperature from 500 to 950 °C.

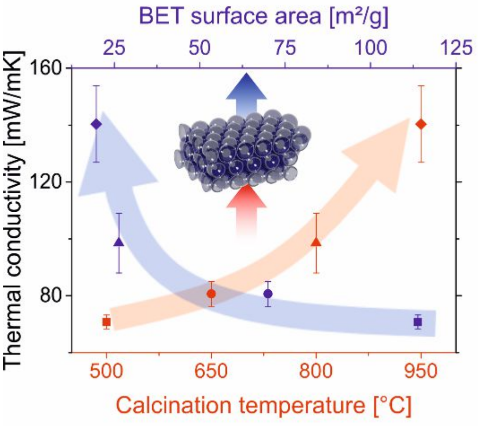

Thermal Transport in Binary Colloidal Glasses: Composition Dependence and Percolation Assessment

Pia Ruckdeschel, Alexandra Philipp, and Markus Retsch
(*Phys. Rev. E*, **2018**, 97, 022612)

The random mixing of hollow silica spheres and polymer latex particles forms a composite material, which can be used as a model system to determine the heat transport properties of binary colloidal mixtures. The effective thermal conductivity can be well described by the effective medium theory. However, upon heating film formation of the polymer leads to a mismatch to existing mixing models. We confirm our experimental data by finite element modeling with a focus on the percolation mechanism.

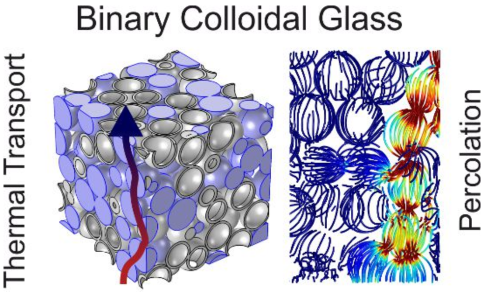

Interface and Morphology Control of the Thermal Conductivity in Core Shell Particle Colloidal Crystals

Pia Ruckdeschel and Markus Retsch
(*Adv. Mater. Interf.*, **2017**, 4, 1700963)

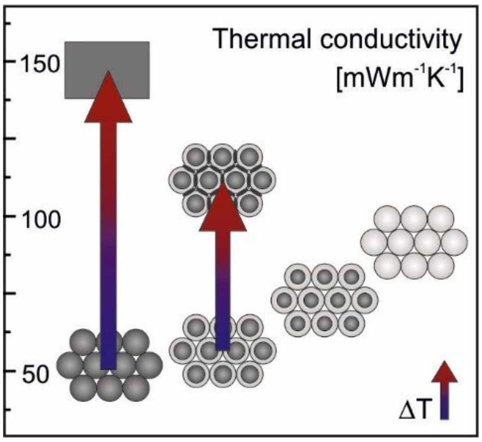

Nanostructured composite materials are investigated concerning their thermal properties. These materials show interesting effects depending on the size and the shell thickness. A precise structure-property relationship study was conducted, finding the lowest thermal conductivity of particles with a large diameter, a thin shell thickness, and the highest polymer content. The polymer leakage and further effects concerning core-shell particles are studied in detail.

Homogeneous Nucleation of Ice Confined in Hollow Silica Spheres

Yang Yao, Pia Ruckdeschel, Robert Graf,
Hans-Jürgen Butt, Markus Retsch, and George Floudas
(*J. Phys. Chem. B*, **2017**, 121, 306)

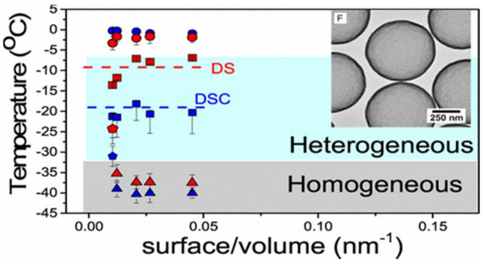

Ice nucleation is studied in hollow silica (HS) spheres. These hierarchical materials comprise micropores within the silica network, which are confined to a ~20 nm shell of a hollow sphere (with diameters in the range ~190 – 640 nm). The multiple length scales involved in HS spheres affect the ice nucleation mechanism. We find homogeneous nucleation inside the water-filled capsules, whereas heterogeneous nucleation prevails in the surrounding dispersion medium. We validate our findings for a series of hollow sphere sizes and demonstrate the absence of homogeneous nucleation in the case of polystyrene-silica core-shell particles.

5 References

1. Gao, T.; Jelle, B. P.; Sandberg, L. I. C.; Gustavsen, A., Monodisperse Hollow Silica Nanospheres for Nano Insulation Materials: Synthesis, Characterization, and Life Cycle Assessment. *ACS Appl. Mater. Inter.* **2013,** *5* (3), 761-767.

2. Farhat, M.; Chen, P. Y.; Bagci, H.; Amra, C.; Guenneau, S.; Alù, A., Thermal invisibility based on scattering cancellation and mantle cloaking. *Scientific Reports* **2015,** *5*, 9876.

3. Lima, R. S.; Marple, B. R., Thermal spray coatings engineered from nanostructured ceramic agglomerated powders for structural, thermal barrier and biomedical applications: a review. *Journal of Thermal Spray Technology* **2007,** *16* (1), 40-63.

4. Mingo, N.; Hauser, D.; Kobayashi, N. P.; Plissonnier, M.; Shakouri, A., "Nanoparticle-in-Alloy" Approach to Efficient Thermoelectrics: Silicides in SiGe. *Nano Lett.* **2009,** *9* (2), 711-715.

5. Dresselhaus, M. S.; Chen, G.; Tang, M. Y.; Yang, R. G.; Lee, H.; Wang, D. Z.; Ren, Z. F.; Fleurial, J. P.; Gogna, P., New Directions for Low-Dimensional Thermoelectric Materials. *Adv. Mater.* **2007,** *19* (8), 1043-1053.

6. Poudel, B.; Hao, Q.; Ma, Y.; Lan, Y.; Minnich, A.; Yu, B.; Yan, X.; Wang, D.; Muto, A.; Vashaee, D.; Chen, X.; Liu, J.; Dresselhaus, M. S.; Chen, G.; Ren, Z., High-Thermoelectric Performance of Nanostructured Bismuth Antimony Telluride Bulk Alloys. *Science* **2008,** *320* (5876), 634-638.

7. Tan, F. L.; Tso, C. P., Cooling of mobile electronic devices using phase change materials. *Appl. Therm. Eng.* **2004,** *24* (2), 159-169.

8. Moore, A. L.; Shi, L., Emerging challenges and materials for thermal management of electronics. *Materials Today* **2014,** *17* (4), 163-174.

9. Cahill, D. G.; Ford, W. K.; Goodson, K. E.; Mahan, G. D.; Majumdar, A.; Maris, H. J.; Merlin, R.; Phillpot, Sr., Nanoscale thermal transport. *J. Appl. Phys.* **2003,** *93* (2), 793-818.

10. Cahill, D. G.; Braun, P. V.; Chen, G.; Clarke, D. R.; Fan, S. H.; Goodson, K. E.; Keblinski, P.; King, W. P.; Mahan, G. D.; Majumdar, A.; Maris, H. J.; Phillpot, S. R.; Pop, E.; Shi, L., Nanoscale thermal transport. II. 2003-2012. *Appl. Phys. Rev.* **2014,** *1* (1), 45.

11. Stauffer, D.; Aharony, A., *Introduction To Percolation Theory*. Taylor & Francis: 1994.

12. Belhadj, W.; Boukari, O.; Gamra, D.; AbdelMalek, F.; Bouchriha, H., Thermal properties of photonic crystals. *Synthetic Metals* **2005,** *151* (1), 6-9.

13. Butt, H. J.; Graf, K.; Kappl, M., *Physics and Chemistry of Interfaces*. Wiley: 2006.

14. Wang, D.; Möhwald, H., Template-directed colloidal self-assembly - the route to 'top-down' nanochemical engineering. *Journal of Materials Chemistry* **2004,** *14* (4), 459.

15. Dorfler, H. D., *Grenzflachen Und Kolloid-Disperse Systeme: Physik Und Chemie*. Springer: 2010.

16. Vogel, N.; Retsch, M.; Fustin, C. A.; Del Campo, A.; Jonas, U., Advances in Colloidal Assembly: The Design of Structure and Hierarchy in Two and Three Dimensions. *Chem Rev* **2015,** *115*, 6265-6311.

17. Fenzl, C.; Hirsch, T.; Wolfbeis, O. S., Photonic Crystals for Chemical Sensing and Biosensing. *Angew. Chem. Int. Ed.* **2014,** *53* (13), 3318-3335.

18. Zeng, Y.; Harrison, D. J., Self-Assembled Colloidal Arrays as Three-Dimensional Nanofluidic Sieves for Separation of Biomolecules on Microchips. *Analytical Chemistry* **2007,** *79* (6), 2289-2295.

19. Fudouzi, H.; Xia, Y., Colloidal Crystals with Tunable Colors and Their Use as Photonic Papers. *Langmuir* **2003,** *19* (23), 9653-9660.

20. López, C., Materials Aspects of Photonic Crystals. *Adv. Mater.* **2003,** *15* (20), 1679-1704.

21. Xia, Y.; Fudouzi, H.; Lu, Y.; Yin, Y., Colloidal Crystals: Recent Developments and Niche Applications. In *Colloids and Colloid Assemblies*, Wiley-VCH Verlag GmbH & Co. KGaA: 2004; pp 284-316.

22. Vogel, N.; Retsch, M.; Fustin, C.-A.; del Campo, A.; Jonas, U., Advances in Colloidal Assembly: The Design of Structure and Hierarchy in Two and Three Dimensions. *Chem. Rev.* **2015,** *115* (13), 6265-6311.

23. Harkins, W. D., A General Theory of the Mechanism of Emulsion Polymerization1. *Journal of the American Chemical Society* **1947,** *69* (6), 1428-1444.

24. Antonietti, M.; Bremser, W.; Mueschenborn, D.; Rosenauer, C.; Schupp, B.; Schmidt, M., Synthesis and size control of polystyrene latices via polymerization in microemulsion. *Macromolecules* **1991,** *24* (25), 6636-6643.

25. Pavel, F. M., Microemulsion Polymerization. *Journal of Dispersion Science and Technology* **2004,** *25* (1), 1-16.

26. Landfester, K., Miniemulsion Polymerization and the Structure of Polymer and Hybrid Nanoparticles. *Angew. Chem. Int. Ed.* **2009,** *48* (25), 4488-4507.

27. Asua, J. M., Miniemulsion polymerization. *Prog. Polym. Sci.* **2002,** *27* (7), 1283-1346.

28. Schork, F. J.; Luo, Y.; Smulders, W.; Russum, J. P.; Butté, A.; Fontenot, K., Miniemulsion Polymerization. In *Polymer Particles: -/-*, Okubo, M., Ed. Springer Berlin Heidelberg: Berlin, Heidelberg, 2005; pp 129-255.

29. Landfester, K., Synthesis of Colloidal Particles in Miniemulsions. *Annual Review of Materials Research* **2006,** *36* (1), 231-279.

30. Goodwin, J. W.; Hearn, J.; Ho, C. C.; Ottewill, R. H., Studies on the preparation and characterisation of monodisperse polystyrene laticee. *Colloid Polym. Sci.* **1974,** *252* (6), 464-471.

31. Goodwin, J. W.; Hearn, J.; Ho, C. C.; Ottewill, R. H., The preparation and characterisation of polymer latices formed in the absence of surface active agents. *British Polymer Journal* **1973,** *5* (5), 347-362.

32. Tseng, C. M.; Lu, Y. Y.; El-Aasser, M. S.; Vanderhoff, J. W., Uniform polymer particles by dispersion polymerization in alcohol. *J. Polym. Sci. Part A* **1986,** *24* (11), 2995-3007.

33. Kawaguchi, S.; Ito, K., Dispersion Polymerization. In *Polymer Particles: -/-*, Okubo, M., Ed. Springer Berlin Heidelberg: Berlin, Heidelberg, 2005; pp 299-328.

34. Cushing, B. L.; Kolesnichenko, V. L.; O'Connor, C. J., Recent Advances in the Liquid-Phase Syntheses of Inorganic Nanoparticles. *Chemical Reviews* **2004,** *104* (9), 3893-3946.

35. Stoeber, W.; Fink, A.; Bohn, E., Controlled growth of monodisperse silica spheres in the micron size range. *J. Colloid Interf. Sci.* **1968,** *26* (1), 62-69.

36. LaMer, V. K.; Dinegar, R. H., Theory, Production and Mechanism of Formation of Monodispersed Hydrosols. *Journal of the American Chemical Society* **1950,** *72* (11), 4847-4854.

37. LaMer, V. K., Nucleation in Phase Transitions. *Industrial & Engineering Chemistry* **1952,** *44* (6), 1270-1277.

38. Badley, R. D.; Ford, W. T.; McEnroe, F. J.; Assink, R. A., Surface modification of colloidal silica. *Langmuir* **1990,** *6* (4), 792-801.

39. Kango, S.; Kalia, S.; Celli, A.; Njuguna, J.; Habibi, Y.; Kumar, R., Surface modification of inorganic nanoparticles for development of organic–inorganic nanocomposites—A review. *Prog. Polym. Sci.* **2013,** *38* (8), 1232-1261.

40. Caruso, F.; Caruso, R. A.; Möhwald, H., Nanoengineering of inorganic and hybrid hollow spheres by colloidal templating. *Science* **1998,** *282* (5391), 1111-1114.

41. Atkins, P. W.; De Paula, J., *Physikalische Chemie*. Wiley-VCH: 2013.

42. Derjaguin, B. V.; Landau, L., Theory of the Stability of Strongly Charged Lyophobic Sols and of the Adhesion of Strongly Charged Particles in Solutions of Electrolytes. *Acta Phys. Chim. URSS* **1941,** *14*, 633-662.

43. Derjaguin, B., A theory of interaction of particles in presence of electric double layers and the stability of lyophobe colloids and disperse systems. *Progress in Surface Science* **1939,** *43* (1), 1-14.

44. Verwey, E. J. W.; Overbeek, J. T. G., *Theory of the Stability of Lyophobic Colloids: The Interaction of Sol Particles Having an Electric Double Layer*. Elsevier Publishing Company: 1948.

45. Israelachvili, J. N., *Intermolecular and Surface Forces*. Elsevier Science: 2015.

46. Tadros, T., General Principles of Colloid Stability and the Role of Surface Forces. In *Colloid Stability*, Wiley-VCH Verlag GmbH & Co. KGaA: 2006; pp 1-22.

47. Dickinson, E.; Eriksson, L., Particle flocculation by adsorbing polymers. *Advances in Colloid and Interface Science* **1991,** *34*, 1-29.

48. Jenkins, P.; Snowden, M., Depletion flocculation in colloidal dispersions. *Advances in Colloid and Interface Science* **1996,** *68*, 57-96.

49. Haw, M. D., Colloidal suspensions, Brownian motion, molecular reality: a short history. *Journal of Physics: Condensed Matter* **2002,** *14* (33), 7769.

50. Dokou, E.; Barteau, M. A.; Wagner, N. J.; Lenhoff, A. M., Effect of Gravity on Colloidal Deposition Studied by Atomic Force Microscopy. *J. Colloid Interf. Sci.* **2001,** *240* (1), 9-16.

51. Edwards, E. W.; Wang, D.; Möhwald, H., Hierarchical Organization of Colloidal Particles: From Colloidal Crystallization to Supraparticle Chemistry. *Macromolecular Chemistry and Physics* **2007,** *208* (5), 439-445.

52. Li, Q.; Jonas, U.; Zhao, X. S.; Kappl, M., The forces at work in colloidal self-assembly: a review on fundamental interactions between colloidal particles. *Asia-Pacific Journal of Chemical Engineering* **2008,** *3* (3), 255-268.

53. Cong, H.; Yu, B.; Tang, J.; Li, Z.; Liu, X., Current status and future developments in preparation and application of colloidal crystals. *Chem. Soc. Rev.* **2013,** *42* (19), 7774-800.

54. Nutz, F. A.; Ruckdeschel, P.; Retsch, M., Polystyrene colloidal crystals: Interface controlled thermal conductivity in an open-porous mesoparticle superstructure. *J. Colloid Interf. Sci.* **2015,** *457*, 96-101.

55. Ruckdeschel, P.; Kemnitzer, T. W.; Nutz, F. A.; Senker, J.; Retsch, M., Hollow silica sphere colloidal crystals: insights into calcination dependent thermal transport. *Nanoscale* **2015,** *7* (22), 10059-10070.

56. Zhang, J.; Sun, Z.; Yang, B., Self-assembly of photonic crystals from polymer colloids. *Current Opinion in Colloid & Interface Science* **2009,** *14* (2), 103-114.

57. Zhu, J.; Li, M.; Rogers, R.; Meyer, W.; Ottewill, R. H.; Crew, S. T. S. S. S.; Russel, W. B.; Chaikin, P. M., Crystallization of hard-sphere colloids in microgravity. *Nature* **1997,** *387* (6636), 883-885.

58. Davis, K. E.; Russel, W. B.; Glantschnig, W. J., Settling suspensions of colloidal silica: observations and X-ray measurements. *Journal of the Chemical Society, Faraday Transactions* **1991,** *87* (3), 411-424.

59. Fan, W.; Chen, M.; Yang, S.; Wu, L., Centrifugation-assisted Assembly of Colloidal Silica into Crack-Free and Transferrable Films with Tunable Crystalline Structures. **2015,** *5*, 12100.

60. Ma, C.; Jiang, Y.; Yang, X.; Wang, C.; Li, H.; Dong, F.; Yang, B.; Yu, K.; Lin, Q., Centrifugation-Induced Water-Tunable Photonic Colloidal Crystals with Narrow Diffraction Bandwidth and Highly Sensitive Detection of SCN−. *ACS Appl. Mater. Inter.* **2013,** *5* (6), 1990-1996.

61. Kim, M. H.; Im, S. H.; Park, O. O., Rapid Fabrication of Two- and Three-Dimensional Colloidal Crystal Films via Confined Convective Assembly. *Adv. Funct. Mater.* **2005,** *15* (8), 1329-1335.

62. Dimitrov, A. S.; Nagayama, K., Continuous Convective Assembling of Fine Particles into Two-Dimensional Arrays on Solid Surfaces. *Langmuir* **1996,** *12* (5), 1303-1311.

63. Ye, Y.-H.; LeBlanc, F.; Haché, A.; Truong, V.-V., Self-assembling three-dimensional colloidal photonic crystal structure with high crystalline quality. *Appl. Phys. Lett.* **2001,** *78* (1), 52-54.

64. Cheng, W.; Wang, J.; Jonas, U.; Fytas, G.; Stefanou, N., Observation and tuning of hypersonic bandgaps in colloidal crystals. *Nat. Mater.* **2006,** *5* (10), 830-836.

65. Cui, L.; Zhang, Y.; Wang, J.; Ren, Y.; Song, Y.; Jiang, L., Ultra-Fast Fabrication of Colloidal Photonic Crystals by Spray Coating. *Macromolecular Rapid Communications* **2009,** *30* (8), 598-603.

66. Yang, H.; Jiang, P., Large-Scale Colloidal Self-Assembly by Doctor Blade Coating. *Langmuir* **2010,** *26* (16), 13173-13182.

67. Mihi, A.; Ocaña, M.; Míguez, H., Oriented Colloidal-Crystal Thin Films by Spin-Coating Microspheres Dispersed in Volatile Media. *Adv. Mater.* **2006,** *18* (17), 2244-2249.

68. Jiang, P.; McFarland, M. J., Large-Scale Fabrication of Wafer-Size Colloidal Crystals, Macroporous Polymers and Nanocomposites by Spin-Coating. *Journal of the American Chemical Society* **2004,** *126* (42), 13778-13786.

69. Velev, O. D.; Jede, T. A.; Lobo, R. F.; Lenhoff, A. M., Porous silica via colloidal crystallization. *Nature* **1997,** *389* (6650), 447-448.

70. Holland, B. T.; Blanford, C. F.; Stein, A., Synthesis of Macroporous Minerals with Highly Ordered Three-Dimensional Arrays of Spheroidal Voids. *Science* **1998,** *281* (5376), 538.

71. Liu, Y.; Wang, S.; Lee, J. W.; Kotov, N. A., A Floating Self-Assembly Route to Colloidal Crystal Templates for 3D Cell Scaffolds. *Chem. Mater.* **2005,** *17* (20), 4918-4924.

72. Im, S. H.; Lim, Y. T.; Suh, D. J.; Park, O. O., Three-Dimensional Self-Assembly of Colloids at a Water–Air Interface: A Novel Technique for the Fabrication of Photonic Bandgap Crystals. *Adv. Mater.* **2002,** *14* (19), 1367-1369.

73. Guo, W.; Wang, M.; Xia, W.; Dai, L., Evaporation-induced self-assembly of capillary cylindrical colloidal crystal in a face-centered cubic structure with controllable thickness. *Journal of Materials Research* **2012,** *27* (13), 1663-1671.

74. Goddard, W. A.; Brenner, D.; Lyshevski, S. E.; Iafrate, G. J., *Handbook of Nanoscience, Engineering, and Technology, Third Edition*. Taylor & Francis: 2012.

75. Chen, G., Nonlocal and Nonequilibrium Heat Conduction in the Vicinity of Nanoparticles. *Journal of Heat Transfer* **1996,** *118* (3), 539-545.

76. Kaviany, M., *Principles of Heat Transfer*. Wiley: 2002.

77. Asheghi, M.; Kurabayashi, K.; Kasnavi, R.; Goodson, K. E., Thermal conduction in doped single-crystal silicon films. *J. Appl. Phys.* **2002,** *91* (8), 5079-5088.

78. Kaviany, M., *Essentials of Heat Transfer: Principles, Materials, and Applications*. Cambridge University Press: 2011.

79. Peierls, R., Zur kinetischen Theorie der Wärmeleitung in Kristallen. *Ann. Phys.* **1929,** *395* (8), 1055-1101.

80. Hofmann, P., *Solid State Physics: An Introduction*. Wiley: 2015.

81. Marconnet, A. M.; Asheghi, M.; Goodson, K. E., From the Casimir Limit to Phononic Crystals: 20 Years of Phonon Transport Studies Using Silicon-on-Insulator Technology. *Journal of Heat Transfer* **2013,** *135* (6), 061601-061601.

82. Klemens, P. G., The Thermal Conductivity of Dielectric Solids at Low Temperatures (Theoretical). *Proceedings of the Royal Society of London. Series A. Mathematical and Physical Sciences* **1951,** *208* (1092), 108-133.

83. Allen, P. B.; Feldman, J. L., Thermal conductivity of disordered harmonic solids. *Phys. Rev. B* **1993,** *48* (17), 12581-12588.

84. Allen, P. B.; Feldman, J. L.; Fabian, J.; Wooten, F., Diffusons, locons and propagons: character of atomic vibrations in amorphous Si. *Philosophical Magazine B-Physics of Condensed Matter Statistical Mechanics Electronic Optical and Magnetic Properties* **1999,** *79* (11-12), 1715-1731.

85. Shenogin, S.; Bodapati, A.; Keblinski, P.; McGaughey, A. J. H., Predicting the thermal conductivity of inorganic and polymeric glasses: The role of anharmonicity. *J. Appl. Phys.* **2009,** *105* (3).

86. Dames, C., Solid-State Thermal Rectification With Existing Bulk Materials. *Journal of Heat Transfer* **2009,** *131* (6), 061301-061301-7.

87. Zeller, R. C.; Pohl, R. O., Thermal Conductivity and Specific Heat of Noncrystalline Solids. *Phys. Rev. B* **1971,** *4* (6), 2029-2041.

88. Alexander, S.; Entin-Wohlman, O.; Orbach, R., Phonon-fracton anharmonic interactions: The thermal conductivity of amorphous materials. *Phys. Rev. B* **1986,** *34* (4), 2726-2734.

89. Koebel, M.; Rigacci, A.; Achard, P., Aerogel-based thermal superinsulation: an overview. *Journal of Sol-Gel Science and Technology* **2012,** *63* (3), 315-339.

90. Hrubesh, L. W.; Pekala, R. W., Thermal-Properties of Organic and Inorganic Aerogels. *Journal of Materials Research* **1994,** *9* (3), 731-738.

91. Baetens, R.; Jelle, B. P.; Gustavsen, A., Aerogel insulation for building applications: A state-of-the-art review. *Energ. Buildings* **2011,** *43* (4), 761-769.

92. Haynes, W. M., *CRC Handbook of Chemistry and Physics, 97th Edition*. CRC Press: 2016.

93. Carson, J. K.; Lovatt, S. J.; Tanner, D. J.; Cleland, A. C., Thermal conductivity bounds for isotropic, porous materials. *International Journal of Heat and Mass Transfer* **2005,** *48* (11), 2150-2158.

94. Wang, J.; Carson, J. K.; North, M. F.; Cleland, D. J., A new approach to modelling the effective thermal conductivity of heterogeneous materials. *International Journal of Heat and Mass Transfer* **2006,** *49* (17–18), 3075-3083.

95. Ma, J.; Parajuli, B. R.; Ghossoub, M. G.; Mihi, A.; Sadhu, J.; Braun, P. V.; Sinha, S., Coherent Phonon-Grain Boundary Scattering in Silicon Inverse Opals. *Nano Lett.* **2013,** *13* (2), 618-624.

96. Stein, A.; Schroden, R. C., Colloidal crystal templating of three-dimensionally ordered macroporous solids: materials for photonics and beyond. *Current Opinion in Solid State and Materials Science* **2001,** *5* (6), 553-564.

97. Stein, A.; Li, F.; Denny, N. R., Morphological Control in Colloidal Crystal Templating of Inverse Opals, Hierarchical Structures, and Shaped Particles. *Chem. Mater.* **2008,** *20* (3), 649-666.

98. Thomas, A.; Goettmann, F.; Antonietti, M., Hard Templates for Soft Materials: Creating Nanostructured Organic Materials. *Chem. Mater.* **2008,** *20* (3), 738-755.

99. Vollmert, B., Synthesis and Reactions of Macromolecular Compounds. In *Polymer Chemistry*, Vollmert, B., Ed. Springer Berlin Heidelberg: Berlin, Heidelberg, 1973; pp 33-321.

100. Hansen, F. K.; Ugelstad, J., Particle nucleation in emulsion polymerization. II. Nucleation in emulsifier-free systems investigated by seed polymerization. *Journal of Polymer Science: Polymer Chemistry Edition* **1979,** *17* (10), 3033-3045.

101. Cho, Y.-S.; Shin, C. H.; Han, S., Dispersion Polymerization of Polystyrene Particles Using Alcohol as Reaction Medium. *Nanoscale Research Letters* **2016,** *11,* 46.

102. Tuncel, A.; Kahraman, R.; Pişkin, E., Monosize polystyrene microbeads by dispersion polymerization. *Journal of Applied Polymer Science* **1993,** *50* (2), 303-319.

103. Ober, C. K.; Hair, M. L., The effect of temperature and initiator levels on the dispersion polymerization of polystyrene. *J. Polym. Sci. Part A* **1987,** *25* (5), 1395-1407.

104. Retsch, M.; Schmelzeisen, M.; Butt, H.-J.; Thomas, E. L., Visible Mie Scattering in Nonabsorbing Hollow Sphere Powders. *Nano Lett.* **2011,** *11* (3), 1389-1394.

105. Ruckdeschel, P.; Philipp, A.; Retsch, M., Understanding Thermal Insulation in Porous, Particulate Materials. *Adv. Funct. Mater.* **2017**, 27 (38), 1702256-1702266.

106. Goldstein, J.; Newbury, D. E.; Joy, D. C.; Lyman, C. E.; Echlin, P.; Lifshin, E.; Sawyer, L.; Michael, J. R., *Scanning Electron Microscopy and X-ray Microanalysis: Third Edition*. Springer US: 2012.

107. Williams, D. B.; Carter, C. B., *Transmission Electron Microscopy: A Textbook for Materials Science*. Springer: 2009.

108. Reimer, L.; Kohl, H., *Transmission Electron Microscopy: Physics of Image Formation*. Springer New York: 2008.

109. The SAXS Guide - Getting acquainted with the principles. Schnablegger, H.; Singh, Y., Eds. Anton Paar GmbH: 2013.

110. Lowell, S.; Shields, J. E.; Thomas, M. A.; Thommes, M., *Characterization of Porous Solids and Powders: Surface Area, Pore Size and Density*. Springer Netherlands: 2012.

111. Thommes, M., Physical Adsorption Characterization of Nanoporous Materials. *Chemie Ingenieur Technik* **2010,** *82* (7), 1059-1073.

112. Spencer, M., *Fundamentals of Light Microscopy*. Cambridge University Press: 1982.

113. Höhne, G.; Hemminger, W. F.; Flammersheim, H. J., *Differential Scanning Calorimetry*. Springer Berlin Heidelberg: 2013.

114. Dusza, L., Combined solution of the simultaneous heat loss and finite pulse corrections with the laser flash method. *High Temperatures-High Pressures* **1995,** *27* (5), 467-473.

115. Blumm, J.; Henderson, J. B.; Ove, N.; Fricke, J., Laser flash measurement of the phononic thermal diffusivity of glasses in the presence of ballistic radiative transfer. *High Temperatures-High Pressures* **1997,** *29* (5), 555-560.

116. Ruckdeschel, P.; Dulle, M.; Honold, T.; Förster, S.; Karg, M.; Retsch, M., Monodisperse hollow silica spheres: An in-depth scattering analysis. *Nano Res.* **2016,** *9* (5), 1366-1376.

117. Ruckdeschel, P.; Philipp, A.; Kopera, B. A. F.; Bitterlich, F.; Dulle, M.; Pech-May, N. W.; Retsch, M., Thermal Transport in Binary Colloidal Glasses: Composition Dependence and Percolation Assessment. **2017**, 97 (2), 022612-022621

118. Ruckdeschel, P.; Retsch, M., Interface and Morphology Control of the Thermal Conductivity in Core-Shell Particle Colloidal Crystals. **2017**, 4 (24), 1700963-1700971.

6 Monodisperse Hollow Silica Spheres: An In-Depth Scattering Analysis

Pia Ruckdeschel, Martin Dulle, Tobias Honold, Stephan Förster, Matthias Karg, and Markus Retsch

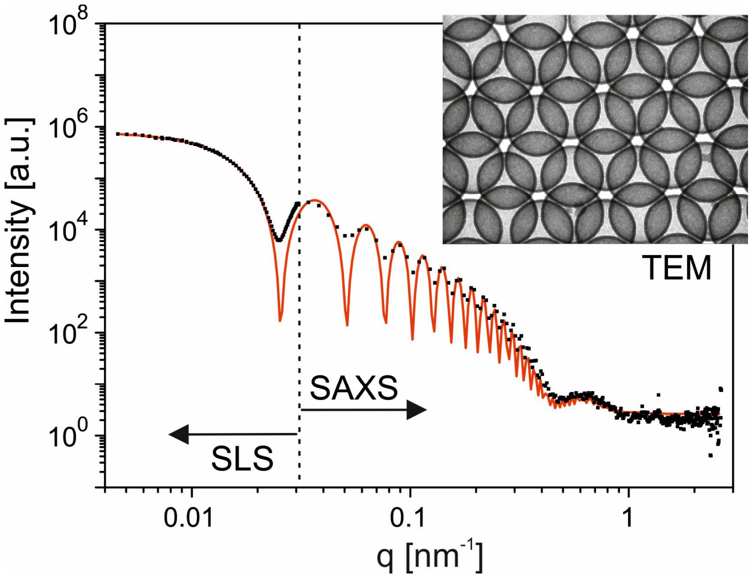

Reprinted with permission from Ruckdeschel *et al.*, *Nano Res.*, **2016**, 9, 1366-1376.

Abstract

We fabricated exceptionally narrowly distributed hollow silica nanoparticles that inherently possess two distinct length scales – tens of nanometer of the shell, and hundreds of nanometer of the total diameter. We characterize these structural entities in great detail using dynamic and static light scattering (DLS and SLS), small-angle X-ray scattering (SAXS) and transmission electron microscopy (TEM). We demonstrate quantitative agreement among all methods. Highlights of this materials class unraveled by this in-depth characterization are: The ratio between the radius of gyration (SLS) and the hydrodynamic radius (DLS) equals almost unity corresponding to ideal capsules. We are able to resolve up to 20 diffraction orders of the hollow sphere form factor in SAXS proving their narrow size distribution. Data from light and X-ray scattering can be combined to a master curve covering a q-range of four orders of magnitude assessing all hierarchical length scales of the form factor. The measured SLS intensity profiles strongly change, when the scattering contrast between the interior and exterior is altered, whereas the SAXS intensity profiles do not show any significant change. This tight control on two structural length scales in one simple and robust colloidal building block renders them suitable as a future calibration standard.

6.1 Introduction

The ability to generate highly defined, hierarchically structured materials from a few nanometer up to a several micrometer scale is a key prerequisite for the realization of future functional devices. Potential applications for such hierarchically structured materials lie in the field of energy conversion, energy storage, catalysis, and separation.[1-4] Generally, two strategies are being followed to access such structures, namely top-down and bottom-up approaches. Top-down approaches allow for an exquisite control on the symmetry and shape of the desired nanostructure. Bottom-up approaches rely on the (directed) self-assembly of molecular or colloidal building blocks into superstructures of defined length scales and symmetries.[5-6] Their size and shape translate directly into the assembled superstructure.[7-8] Quite expectedly, any short-comings such as ill-defined shapes or a polydisperse particle size will deteriorate the properties of bottom-up constructed devices and structures.

For building blocks, which range in the colloidal domain, from a few nm up to several µm, scattering techniques such as small-angle X-ray scattering (SAXS) or light scattering (dynamic: DLS or static: SLS) are well-established and commonly being used. These techniques, which yield reciprocal space information, can be complemented by imaging techniques such as atomic force microscopy (AFM), scanning, or transmission electron microscopy (SEM or TEM).[9-10] On the contrary, all of these techniques require reliable standards for instrument calibration. In particular for scattering techniques, current calibration standards such as Ag-behenate,[11-13] Ag-stearate,[13] or rat collagen[14-15] only embody one single length scale and may be prawn to light degradation or dehydration. Alternatively, narrowly distributed colloidal suspensions consisting of polystyrene, poly(methyl methacrylate), or silica are being used.[16-20] In these cases, several standards of different sizes need to be employed to cover the desired q-range. This can be overcome by using monodisperse silica hollow spheres.

Such hollow sphere structures have increasingly been in the focus of research.[10, 21] Potential applications such as dye-sensitized solar cells, gas sensor, heterogeneous catalysis, supercapacitors, or drug delivery vehicles[10, 21] capitalize on the high surface area, microporosity and free volume of these hollow objects. Furthermore, due to their intrinsically hierarchical structure (the overall particle diameter and the shell thickness), hollow spheres feature a powerful platform to generate three-dimensional materials, which embody multiple length scales.

In this communication, we employ hollow silica nanoparticles with an extremely small polydispersity. This allows us to resolve unprecedented details in ensemble averaging techniques, which are typically compromised by the particle size distribution. In particular, we compare the characterization by transmission electron microscopy (TEM), dynamic light scattering (DLS), static light scattering (SLS), and small-angle X-ray scattering (SAXS). We will discuss in detail how these methods can be used to extract in-depth information and emphasize the potential application of silica capsules as calibration standard material. Furthermore, we will investigate the influence of the scattering contrast within such particles on the different scattering techniques.

6.2 Results and Discussion

We focus on three distinct hollow spheres, which are based on the same template core particle but with increasing shell thickness. Transmission electron microscopy is able to resolve the overall structural information such as particle diameter and shell thickness, as well as local information on the homogeneity of the capsule. Figure 6.1 shows a two-dimensional projection of the hollow spheres, deposited on a carbon-coated grid.

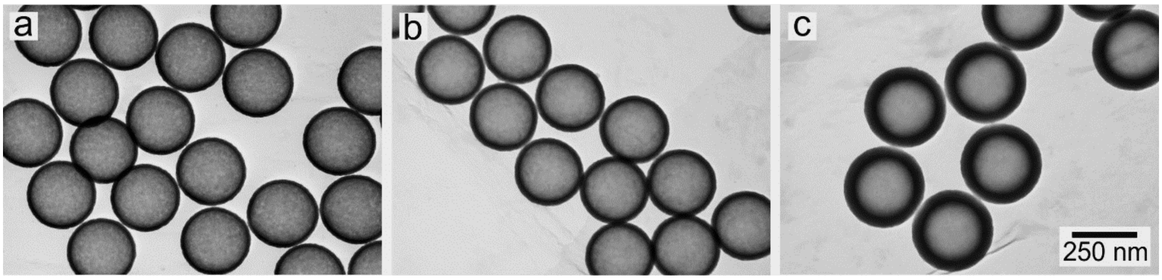

Figure 6.1. Transmission electron microscopy analysis of hollow silica spheres with increasing shell thickness. (a) 15.7 nm shell thickness features a granular shell, which becomes smoother with increasing silica layer thickness (b) 21.4 nm and (c) 43.7 nm.

The shell thickness can be deduced from the dark rim around the hollow center, as this represents the area of highest matter density along the electron beam path. Since we used the same template particles for our system the outer diameter increases with increasing shell thickness, accordingly. The particles cover a range from 131 nm to 158 nm in radius. The shell thickness was measured to be 15.7 nm (A-500), 21.4 nm (B-500), and 43.7 nm (C-500), respectively. TEM gives an additional qualitative insight into the homogeneity of the shell as can be deduced from the gray scale contrast across the hollow center. One can recognize that a slight variation on a length scale of a few nanometers is visible for the thinnest shell, which can be explained by the fabrication process. This is done by Stöber condensation, where silicate nanoclusters nucleate in the ethanolic dispersion and precipitate onto the oppositely charged template surface. Further growth of these initial clusters leads to the formation of a homogenous surface, which becomes smoother with increasing shell thickness. It is also apparent that the PS core removal step by calcination does neither impede the integrity of the silica shell nor change the crystallinity (see XRD spectra of amorphous silica material in Figure S6.1 in the Supporting Information, Chapter 6.7). The integrity of the silica shell can also be confirmed by SEM images in Figure S6.2 and Figure S6.3a. No holes or cracks are visible. Furthermore, the particles can be redispersed on an individual level with no cluster or sintered necks being present in the TEM images.

To study the size and size distribution of the hollow particles on a statistical ensemble, we employed dynamic and static light scattering. Figure 6.2a shows typical intensity-time autocorrelation functions measured at a scattering angle of 45° which is sufficiently lower than the first form factor minimum of the colloids. All correlation functions show a monomodal decay, which could be analyzed by the method of inverse Laplace transformation based on the CONTIN algorithm (red solid lines). The distribution functions of the hydrodynamic radius R_h obtained from this CONTIN analysis (Figure 6.2b) provide only single size distributions with small variances. In order to proof the diffusive behavior of the particles in dispersion, angle dependent measurements were performed. The mean relaxation rates Γ, obtained from CONTIN analysis of each autocorrelation function, depend linearly on the square of the scattering vector q and feature intercepts close to zero (Figure 6.2c). This is indicative of purely translational diffusion being probed in the scattering volume.

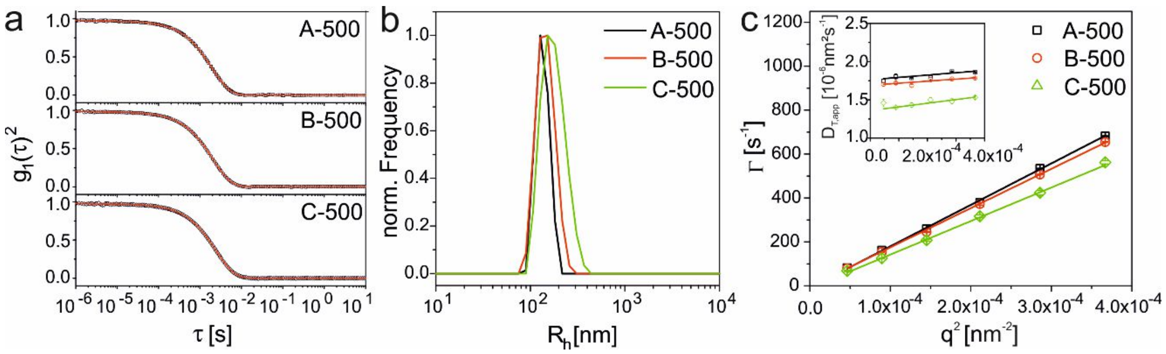

Figure 6.2. DLS analysis of hollow spheres after redispersion in water. (a) Intensity-time autocorrelation functions recorded at a scattering angle of 45°. The red solid lines are fits from CONTIN analysis. (b) Distribution of the hydrodynamic radius as obtained from the relaxation rate distributions *G(Γ)* from CONTIN analysis of the autocorrelation data. (c) Angle-dependent analysis of the relaxation rate *Γ*. The inset demonstrates a slight dependency of the diffusion coefficient on the scattering angle.

However, the inset in Figure 6.2c shows a slight dependence of the apparent diffusion coefficient $D_{T,app} = \frac{\Gamma}{q^2}$ on the scattering angle. A potential reason for this angle dependence is a concentration effect within the hollow sphere dispersion. In order to determine the hydrodynamic radius with very high accuracy we extracted the translational diffusion coefficient by linear regression of the angular dependent data shown in the inset in Figure 6.2c. The intercept of the linear fits provided the diffusion coefficients $D_{T,0}$ according to $D_{T,app} = D_{T,0}(1 + A \cdot q^2)$. The respective hydrodynamic radii R_h obtained from the diffusion coefficients using the Stokes-Einstein equation ($D_{T,0} = \frac{k_B T}{6\pi\eta R_h}$) are listed in Table 6.1. The hydrodynamic radii are increasing from sample A-500 to C-500 and hence with increasing shell thickness, which is in very good agreement with the results from TEM analysis.

SLS was used to investigate the radius of gyration R_g and the form factor *P(q)* of the samples. Due to the relatively small size of the particles, the Guinier region is sufficiently covered for measurements at small angles. Figure 6.3a shows the results of SLS measurements in the low q limit in a Guinier representation. All datasets show a linear dependence and could be analyzed by linear regression (solid lines) providing the radius of gyration according to $\ln(I) = -\frac{q^2 R_g^2}{3}$. The obtained values for R_g are listed in Table 6.1 and show an increase with increasing shell thickness (A-500 to C-500). For an ideal homogeneous hollow sphere with an infinitely thin shell the, ratio between R_g and R_h should equal unity. In contrast for a solid sphere one, would expect a ratio of R_g/R_h = 0.775. In fact, sample A-500, which has the thinnest silica shell, provides a ratio R_g/R_h = 0.988 which is very close to unity. As expected, the ratio decreases with increasing shell thickness.

Table 6.1. Summary of the results from DLS and SLS measurements at 25°.

Sample	**DLS**	**SLS**		**SLS**			**TEM**	
	R_h [nm]	**R_g [a] [nm]**	**R_g/R_h**	**R_{hollow} [b] [nm]**	**$R_{C/S}$ [c] [nm]**	**ΔR [c] [nm]**	**R [nm]**	**d_{shell} [nm]**
A-500	138 ± 3	136 ± 1	0.988	126	133	14.6	131 ± 2	15.7 ± 1.0
B-500	144 ± 2	142 ± 1	0.987	129	140	21.6	135 ± 2	21.4 ± 0.8
C-500	179 ± 1	166 ± 1	0.928	143	167	48.6	158 ± 1	43.7 ± 1.6

[a] *The values were obtained from the slope analysis of linear fits in the Guinier plots shown in Figure 6.3 (first 8 data points not considered). Considering all data points measured with the HeNe laser (632.8 nm) the values are: 134 nm, 139 nm and 165 nm for sample A-500, B-500, C-500.*

[b] *These values were obtained from fits to the SLS scattering curves using a form factor model for an ideal hollow sphere with an infinitely thin shell using Equation (6.1).*

[c] *These values were obtained from fits to the SLS scattering curves using a form factor model for a spherical core/shell particle using Equation (6.2) and (6.3).*

Figure 6.3b shows the scattering intensity as a function of the scattering vector as obtained from SLS. In order to cover a broad range of momentum transfer q, we employed two lasers with different wavelengths (632.8 nm and 532 nm) for the SLS investigation and merged the datasets by simple multiplication with constant multipliers. The first form factor minimum is resolved for all samples in the higher q-region of the SLS profiles. With increasing shell thickness the position of the minimum shifts to lower q values, which is in good agreement with the increasing particle radii. As a first attempt to describe the experimental data, we used the simple form factor model for hollow spheres with infinitely thin shells to fit the SLS data:

$$I(q, R_{hollow}) = \left[\frac{\sin qR_{hollow}}{qR_{hollow}}\right]^2 \tag{6.1}$$

The fits using this model are shown as red lines in Figure 6.3b. Very good agreement between the experimental data and this fit is found for all samples. The sphere radii from this analysis are listed in Table 6.1 and follow nicely the trend of the radii obtained from DLS and TEM. Compared to the values of Rg from Guinier analysis the sphere radii from this simple form factor (Equation (6.1)) are slightly smaller which illustrates that the shell thickness is finite.

Due to the very good data quality and the small error bars of the SLS data, we employed a more complex form factor model to describe the experimental data. For this, we used a spherical core-shell model:[22]

$$I(q,R,\Delta R,\Delta\eta_1,\Delta\eta_2) = [K(q,R+\Delta R,\Delta\eta_2) - K(q,R,\Delta\eta_2-\Delta\eta_1)]^2 \tag{6.2}$$

with

$$K(q,R,\Delta\eta) = \frac{4}{3}\pi R^3 \Delta\eta \cdot 3 \cdot \frac{\sin qR - qR\cos qR}{(qR)^3} \tag{6.3}$$

Here, R is the radius of the core, ΔR the thickness of the shell, $\Delta\eta_1$ the scattering contrast between the core and the surrounding matrix (here: $\Delta\eta_1 = 0$, implying that the core of the hollow spheres is infiltrated by water) and $\Delta\eta_2$ the scattering contrast between the shell and the matrix (water). The radius of the core-shell particle is consequently, $R_{C/S} = R + \Delta R$. The fits are shown as black lines in the graphs of Figure 6.3b. Again the fits describe the experimental data very accurately. The values for R and ΔR obtained from this analysis are listed in Table 6.1. The values for the shell thickness are very close to the values obtained from TEM analysis and show the expected increase in shell thickness from sample A-500 to C-500. The sphere radii show the same tendency and are in very good agreement with the radii from TEM. Moreover, the radii from this form factor analysis are very close to the values of Rg obtained from Guinier analysis.

The results from DLS and SLS measurements reveal the very low polydispersity in size and shell thickness of all three hollow particle systems. They perform equally well to known colloidal particle standards but have the advantage of assessing a second length scale – the shell thickness – in SLS measurements. Furthermore, looking at the R_g/R_h ratio, hollow silica spheres should be considered as a calibration standard for both DLS and SLS.

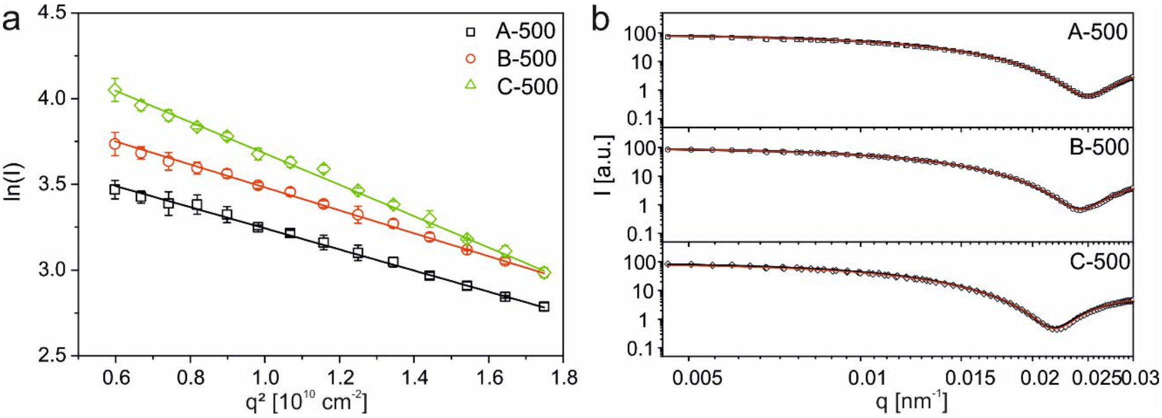

Figure 6.3. Results from SLS measurements: (a) Guinier plot for hollow spheres with increasing shell thickness. The solid lines are linear fits. (b) Form factor analysis demonstrates a minimum at high q, which shifts to lower q for larger particle diameters, i.e. particles with increasing shell thickness. The red solid lines are fits using a form factor of hollow spheres with an infinitely thin wall according to Equation (6.1). The black solid lines are fits using a form factor for spherical core-shell particles according to Equation (6.2) and (6.3). The scattering contrast of the core was set equal to the surrounding medium (water).

However, these light scattering measurements are restricted to very low values of q and the form factor is only partially accessible. Hence, we used SAXS (Figure 6.4) covering a much broader q-range and in particular larger values of q to investigate the form factor and size distribution of the colloids. The high contrast of the silica hollow spheres (in air) made it possible to measure to very low q values of 0.026 nm^{-1} in our SAXS setup (see Materials and Methods) and it also resulted in a very good signal/noise ratio even at high q values. The samples were measured as a dry powder in air. The first apparent feature in all SAXS measurements is the low polydispersity of the different spheres. Usually, the form factor minima that arise from the overall size of such a hollow sphere are being smeared out due to a slight size variation. In contrast, all our samples under investigation showed many form factor oscillations (over 2 orders of magnitude in *q*). In the case of these samples, the usually negligible effect of pinhole smearing is the main reason for the suppression of highest orders of form factor oscillations.

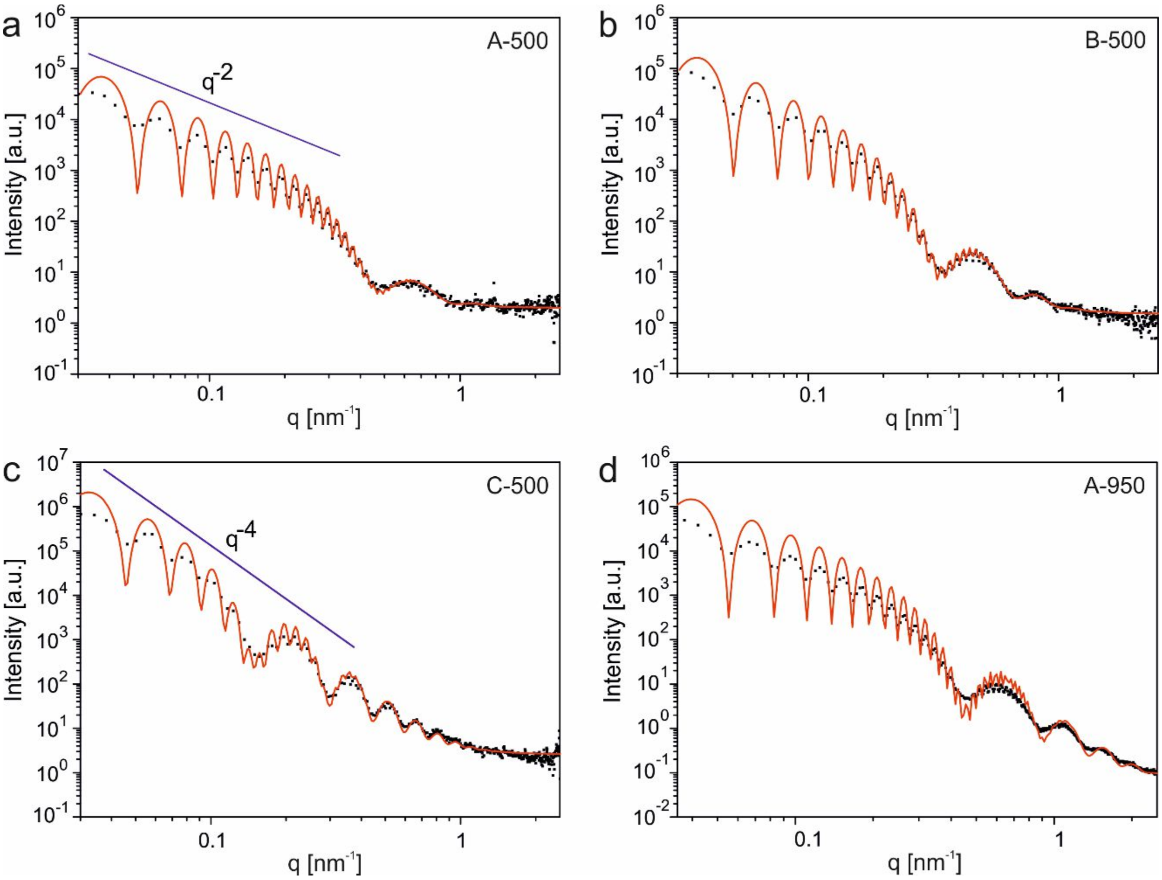

Figure 6.4. SAXS analysis of hollow silica spheres (black dots) and the corresponding fits using a form factor for spherical core-shell particles (red lines). (a)-(c) Due to the monodispersity of our hollow sphere particles, up to 20 diffraction orders can be resolved. The scattering profile consists of the superposition of contributions from the total particle diameter and the shell thickness, respectively. The shell thickness increases from 14 nm (A-500), to 19 nm (B-500), and 43 nm (C-500). The initial slope decreases from q^{-2} to q^{-4} indicative of a change in local curvature. (d) Calcination of sample A at 950 °C leads to microstructural changes within the SiO_2 network, which results in an even better resolved SAXS spectrum.

It is apparent that the scattering profile comprises two sorts of contributions: one originating from the total particle size, one from the shell thickness. The particle radius results in narrowly spaced oscillating modes, for which up to 20 diffraction orders can be resolved. These are superimposed by fewer oscillations originating from the silica shell. While for the 15 nm shell only one minimum can be inferred, up to six additional minima contribute to the scattering profile in case of the 44 nm shell. The SAXS curves were quantitatively analyzed by the same core-shell model as the SLS data. The fits to the data are the red lines in Figure 6.4. The model can very accurately describe the scattering of the different samples and allows us to obtain very precise values for the shell thickness and total particle radius. The fitted data are summarized in Table 6.2. The agreement for both, shell thickness and total particle radius, are excellent compared to TEM and SLS. For comparison, the TEM data are listed in Table 6.2 as well.

Table 6.2. Summary of the results from SAXS measurements and comparison to the TEM analysis.

Sample	*SAXS*					*TEM*	
	R_o [nm]	**σ (R_o)**	**R_i [nm]**	**σ (R_i)**	**d_{shell} [nm]**	**R [nm]**	**d_{shell} [nm]**
A-500	128.0	0.15	114.5	0.015	13.5	131 ± 2	15.7 ± 1.0
B-500	134.0	0.09	115.0	0.015	19.0	135 ± 2	21.4 ± 0.8
C-500	157.5	0.04	115.0	0.020	42.5	158 ± 1	43.7 ± 1.6
A-950	120.5	0.06	106.5	0.011	14.0	123 ± 2	15.9 ± 1.1

With increasing shell thickness the local environment of the hollow sphere changes. Its scattering properties transition towards the behavior of solid spheres, which can also be seen in the SAXS curves. The initial decay of intensity with momentum transfer is shifting from q^{-2} (sample A-500) to q^{-4} (sample C-500). This is due to the local curvature that in case of sample A-500 is very small and similar to a thin flat sheet. With increasing thickness of the silica shell, this changes and starts to resemble the curvature of a solid sphere.

Another interesting effect can be observed by calcination of sample A at high temperatures (950 °C). As discussed recently, calcination at elevated temperatures leads to a range of microstructural changes within the SiO_2 network.[23] These changes are reflected in an even better-resolved SAXS curve, especially in the high q-region. The background is reduced by one order of magnitude and allows an even more precise evaluation of size and polydispersity (see Table 6.2). As mentioned above all samples are so narrowly distributed that the pin hole setup with a beam size of 100 µm x 100 µm and a 300K Pilatus detector is causing more smearing than the sample itself. We interpret this sharpening of the SAXS spectrum as a decrease of randomly distributed scattering sites within the silica shell, which manifests itself in a decrease of BET surface area and a loss in microporous volume.[23] The overall geometry of the hollow sphere remains by and large unchanged during the calcination process. The form factor fitting yields an outer and inner radius R_o = 120.5 nm and R_i = 106.5 nm, respectively, which corresponds to a shrinkage of about 6 %. The shell thickness remains unchanged at d_{shell} = 14.0 nm. For comparison, the TEM images of the sample A-950 are shown in the Figure S6.3b, c. The data of the size and shell thickness are listed in Table 6.2 as well. The TEM measurements are comparable to the SAXS data, showing a shrinkage of 6 %.

Hollow silica spheres feature a range of advantages over existing calibration standards. They possess a high scattering contrast (SiO_2 – air), which reduces the measurement time necessary to obtain spectra of low noise and embody two length scales in their form factor, which can be precisely tuned from 10 nm to several 100 nm. Furthermore, SiO_2 is a chemically robust material, which is stable as an aqueous colloidal dispersion as well as dry powder and does not need to be protected from light or heat. The colloidal stability is underpinned by light scattering data of sample B-500*, measured more than six months after redispersion in water (see Figure S6.4 and Table S6.1). The form factor analysis demonstrates no detectable changes to the monodispersity or the particle dimensions.

In order to fully assess the hierarchical structure of hollow silica spheres, we demonstrate the possibility to combine the form factor data from SLS and SAXS to a single master curve (Figure 6.5a). As can be seen, the respective q-ranges hardly overlap but can be nicely stitched to result in a full q-range coverage of almost four orders of magnitude. With the appropriate adjustment of the absolute scattering intensity, this master curve can be built for all three samples under investigation. This full master curve can then again be fitted by the core-shell form factor (Equation (6.2), Figure 6.5b). The fit curve (red line) captures all relevant features of both, the SLS and SAXS data.

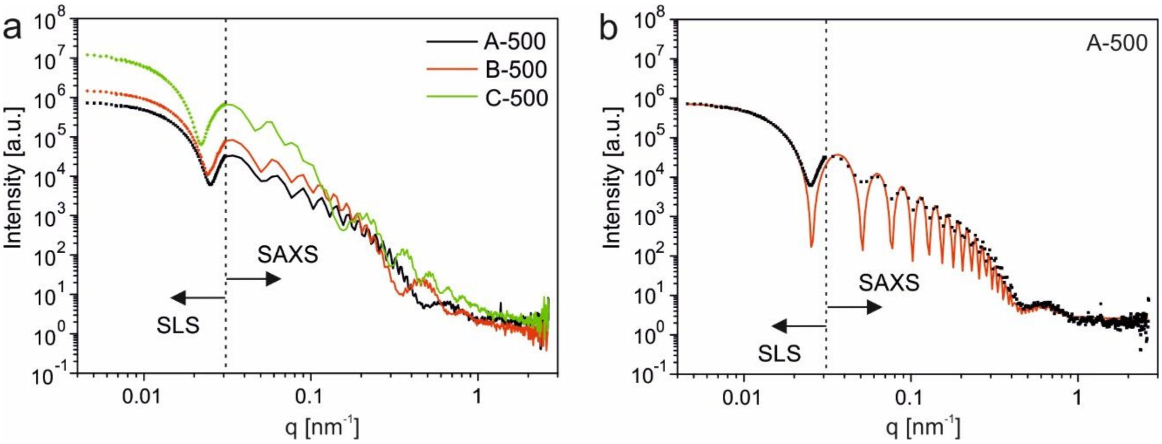

Figure 6.5. Superposition of SLS and SAXS. (a) Adjusting the absolute scattering intensities of SLS and SAXS measurements allows for the construction of a master curve. The scattering data span a range of almost four orders of magnitude for the samples under investigation. (b) All structural features of the master curve can be fitted by a single analysis using a core-shell form factor.

This master curve is only accessible when comparable relative scattering contrasts are present in both, the SLS and SAXS measurements. We demonstrate this by the investigation of air-filled (empty) silica spheres dispersed in water. Such particles are accessible via calcination at 950 °C, which closes the micropores in the silica shell as demonstrated previously.[23] For the case of the thickest shell (sample C-950), the micropores are completely closed so that water cannot infiltrate anymore. This is proved by cryo-TEM images in Figure S6.5b, c.

The SLS measurements of the sample C-950 (see Figure 6.6a) show that different scattering contrasts between the core and the surrounding matrix strongly influences the SLS profile ($\Delta\eta_1$ from Equation (6.2) changes from $\Delta\eta_1 = 0$ to $\Delta\eta_1 < 0$). Instead of a minimum at high q values, a broad maximum is present for sample C-950. The dashed red line represents a simulation of the form factor using the same geometric parameters, but with an adjusted scattering contrast to resemble the air-filled core. On the contrary SAXS is not sensitive to this change in scattering contrast, as the scattering cross section of the Si atoms in the shell is the dominant contribution in this case. This is corroborated by nearly identical SAXS profiles of the dry powder (indicated by vertical grey lines in Figure 6.6b) and its water-filled and dispersed counterpart (C-500). Consequently, the shape of the form factor is not altered. A slight shift towards higher q values in case of the C-950 sample can be explained by a small shrinkage during calcination in analogy to sample A-950 outlined above (see Table S6.2 in the Supporting Information, Chapter 6.7).

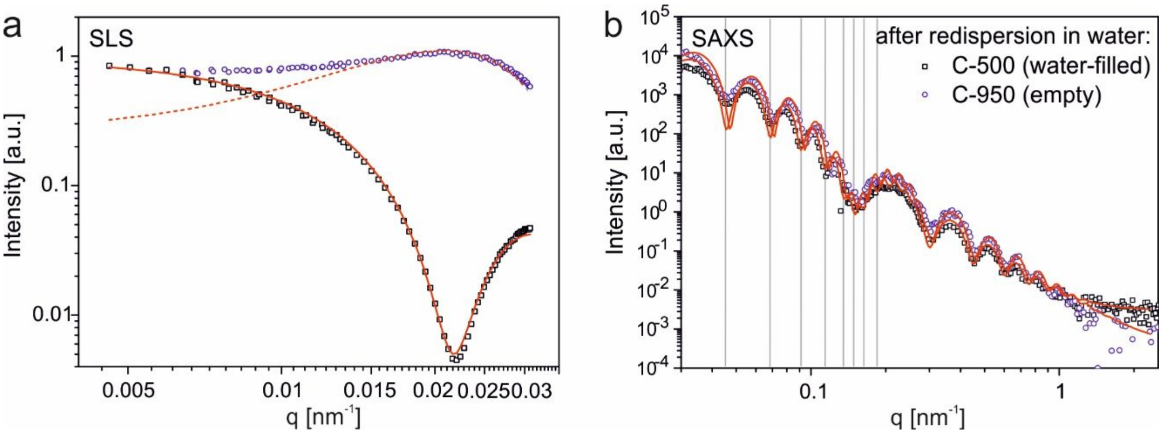

Figure 6.6. Influence of the scattering contrast. (a) Form factor analysis by static light scattering. SLS data of water filled C-500 (black squares) and air-filled C-950 (blue circles) in water. The red line is the corresponding fit of sample C-500 using a form factor for spherical core-shell particles with equal scattering contrasts of the core and the surrounding medium (see Figure 6.3b). The red dotted line is a simulation of the form factor for spherical core-shell particles with different scattering contrasts between the core (air) and the surrounding medium (water). All data shown are normalized to 1. (b) SAXS analysis of hollow silica spheres C-500 (black squares) and C-950 (blue circles) after redispersion in water. The SAXS curves were quantitatively analyzed by the same core-shell model as the SLS data. The small shift of the form factor towards higher q-values is due to a small amount of shrinkage of the hollow spheres upon calcination at 950 °C.

We find a similar trend for sample B-950 with a thinner shell. In this case, however, some capsules can still be infiltrated by water leading to a mixture of empty and water-filled silica capsules (see Figure S6.5a). The SLS profile, therefore, presents an intermediate between the fully filled and fully empty case (Figure S6.6).

6.3 Conclusion

In this contribution, we demonstrated a detailed and thorough analysis of impressively narrowly size-distributed hollow silica particles. These hierarchically structured objects comprise two distinct length scales: the total particles radius (hundreds of nm) and the shell thickness (tens of nm). We used TEM, (angle-dependent) DLS, SLS, and SAXS measurements to describe their structural features and scattering properties fully. The size of the hollow spheres ranged from 131 to 158 nm in radius and 16 to 44 nm shell thickness, respectively. Our results show an outstanding quantitative consistency among the various methods. These hollow spheres possess a close to ideal capsule morphology with the ratio R_g/R_h being almost unity for the thinnest, yet stable, shell. We further investigated the scattering properties of these hollow spheres over a range of four orders of magnitude. A simple core-shell form factor analysis is sufficient to describe all structural features across all length scales. SAXS analysis gave further insight into the bending curvature, which transitions from membrane-like towards solid spheres with increasing shell thickness. Changes to the relative scattering contrast between the particle interior and exterior lead to marked changes in the SLS data, whereas the intensity profile of the SAXS measurement is not influenced.

This detailed analysis shall be used as reference and guidance for the investigation of well-defined colloidal objects. Whereas the presented methods are being considered "standard" techniques and have been widely applied in many fields, we want to emphasize the good agreement between ideal theoretical models and the corresponding experimental data. Furthermore, we advocate monodisperse hollow silica spheres to be used as a calibration standard for small-angle scattering experiments in the future. Their core advantages are high scattering contrast for visible light and X-rays, long-term stability as a dry powder and aqueous dispersion, as well as incorporation of two defined length scales.

6.4 Experimental Section

Materials

Styrene (≥99 %, Aldrich), 2,2′-azobis(2-methylpropionamidine) dihydrochloride (AIBA; 97 %, Aldrich), [2-(methacryloyloxy)ethyl]trimethylammonium chloride (MTC; 70 % solution in water, Polyscience), Polyvinylpyrrolidone K30 (PVP; Mw ~ 55 kg/mol, Aldrich), tetraethyl orthosilicate (TEOS; ≥ 99 %, Aldrich) and Ammonium hydroxide solution (30 – 33 % in water, Aldrich) were used as received. Ethanol (EtOH) was used in technical grade and water was taken from a Millipore Direct Q3UV unit for the entire synthesis and purification steps.

Synthesis of Monodisperse Hollow Silica Nanoparticles

The synthesis of monodisperse hollow silica nanoparticles comprises three steps. First monodisperse polystyrene (PS) latex particles were synthesized by emulsifier-free emulsion polymerization. The reaction was carried out in a 500 mL three-neck flask, equipped with a gas inlet and a reflux condenser. Solid chemicals were dissolved in water prior to addition. Firstly, 200 mL water, 26 mL styrene, 1.8 g PVP and 100 µL MTC were heated to the reaction temperature of 70 °C at a stirring speed of 850 rpm using a large egg-shaped magnetic stirring bar. After equilibrating for 20 min, 600 mg AIBA initiator, dissolved in 40 mL water, were quickly added to initiate the polymerization. After nucleation, the stirring speed was reduced to 450 rpm and the polymerization was allowed to continue overnight at 70 °C under a slight inert gas flow. In the second step, the PS template particles were coated with a silica shell to obtain core/shell particles. The silica coating was achieved by a Stoeber condensation process.[24] Therefore, various amounts of TEOS were added to an 81.2 vol.% EtOH, 10.7 vol.% H2O, 6.1 vol.% NH_4OH solution containing 10.7 gL^{-1} PS latex beads. The thin, medium and thick shell was achieved by adjusting the TEOS content to 2.1 vol.%, 3.2 vol.%, and 8.7 vol.%, respectively. The condensation reaction was conducted at room temperature overnight with stirring at 500 rpm with a magnetic stirring bar. The core/shell particles were purified by repeated centrifugation and redispersion in water. In order to prepare hollow spheres, the sample was dried and calcined in a furnace (Nabertherm L5/11/P33) at 500 °C or 950 °C in air for 12 h. The hollow spheres could be redispersed in water using mild sonication in a sonication bath.

Characterization

SLS and DLS measurements were performed on a standard goniometer setup (ALV, Langen, Germany) equipped with a HeNe laser (JDSU, USA) with $\lambda = 632.8$ nm and a maximum output power of 35 mW as well as a Verdi V-2 (Coherent, USA) with $\lambda = 532$ nm and a maximum output power of 2 W. All measurements were performed at 25 °C. The temperature was adjusted by a toluene matching/temperature bath. The temperature was controlled by a PT100 thermocouple placed in the toluene next to the sample. For SLS measurements in angular steps of 2° were performed in a range of 25 – 155° ($\lambda = 532$ nm) and 20-60° ($\lambda = 632.8$ nm) to cover a q-range of 0.005 – 0.03 nm^{-1}. DLS measurements were performed in an angular range of 25 – 75° ($\lambda = 532$ nm) in steps of 10°. At each angle, three intensity-time autocorrelation functions were recorded. The samples were prepared from dry material. A small amount of the solid was dispersed in water using 30 minutes of sonication at low power (50 %). When the sample was completely dispersed, a small amount of the dispersion was further diluted with water and filtered using a 5 µm PTFE syringe filter. The sample was directly filtered into dust-free cylindrical quartz cells for light scattering. The intensity-time autocorrelation functions measured in DLS were analyzed by inverse Laplace transformation with the CONTIN algorithm using the software AfterALV 1.0d by Dullware. This analysis provided the average relaxation rate $<\Gamma>$ as a function of scattering angle. The SLS data measured with two different laser wavelength were merged and fitted using the software SASfit (version 0.93.2) by J. Kohlbrecher.[22]

All SAXS data reported here were measured using the small-angle X-ray system "Double Ganesha AIR" (SAXSLAB, Denmark). The X-ray source of this laboratory-based system is a rotating anode (copper, MicoMax 007HF, Rigaku Corporation, Japan) providing a micro-focused beam at $\lambda = 0.154$ nm. The data are recorded by a position sensitive detector (PILATUS 300K, Dectris). To cover the range of scattering vectors between 0.026 – 2.5 nm^{-1} different detector positions were used. The samples were put inside a small envelope made of Kapton (powder) or filled in a capillary (liquid samples). The circularly averaged data were normalized to the incident beam, sample thickness, and measurement time before subtraction of the signal of the Kapton envelope/air. Then the resulting curves from different detector distances were merged to yield one curve. The fitting was done using Scatter with the vesicle model.[25]

Transmission electron microscopy (TEM) images were performed on a Zeiss CEM 902 instrument in bright field imaging mode at an acceleration voltage of 80 kV. Samples were prepared by dropping 10 µL of a diluted colloidal dispersion of redispersed silica hollow nanoparticles onto carbon-coated copper grids. After 10 s excess solution was blotted with a filter paper.

For cryo-TEM imaging, diluted colloidal dispersion of redispersed silica hollow spheres was dropped on a copper grid coated with a lacey carbon film. Subsequently, most of the liquid was blotted with a filter paper, leaving a thin film stretched over the holes. Then the sample was instantly shock frozen by plunging them rapidly into liquid ethane and cooled to approximately 90 K by liquid nitrogen in a temperature-controlled freezing unit (Zeiss Cryobox). The frozen specimen was inserted into a cryo transfer holder (CT3500, Gatan) and transferred to a Zeiss EM922 Omega energy-filtered TEM instrument. The imaging was carried out at an acceleration voltage of 200 kV and temperatures around 90 K.

Powder X-ray diffraction (XRD) measurements were carried out using a STOE STADI P (CuKα1 radiation) diffractometer in transmission geometry, equipped with a fast, high-resolution silicon strip detector DECTRIS Mythen1K. The samples were mounted on a flat disk using Scotch® tape. A step size of 0.2° and integration time of 20 s was used.

6.5 Acknowledgements

The German Research Foundation (SFB840) funded this project. P.R. thanks the Elite Network Bavaria (ENB). We acknowledge Dr. Markus Drechsler for assistance with the cryo-TEM measurements, Tobias Kemnitzer for XRD measurements and Dr. Sabine Rosenfeldt for fruitful discussions.

6.6 References

1. Choi, H.; Sofranko, A. C.; Dionysiou, D. D., Nanocrystalline TiO2 Photocatalytic Membranes with a Hierarchical Mesoporous Multilayer Structure: Synthesis, Characterization, and Multifunction. *Adv Funct Mater* **2006,** *16* (8), 1067-1074.

2. Rhee do, K.; Jung, B.; Kim, Y. H.; Yeo, S. J.; Choi, S. J.; Rauf, A.; Han, S.; Yi, G. R.; Lee, D.; Yoo, P. J., Particle-nested inverse opal structures as hierarchically structured large-scale membranes with tunable separation properties. *ACS Appl Mater Interfaces* **2014,** *6* (13), 9950-4.

3. Su, B.-L.; Sanchez, C.; Yang, X.-Y., *Hierarchically Structured Porous Materials*. Wiley-VCH Verlag GmbH & Co. KGaA: 2011; p I-XXV.

4. Cho, C.-Y.; Moon, J. H., Hierarchical twin-scale inverse opal TiO2 electrodes for dye-sensitized solar cells. *Langmuir* **2012,** *28* (25), 9372-9377.

5. Wang, D.; Möhwald, H., Template-directed colloidal self-assembly - the route to 'top-down' nanochemical engineering. *J Mater Chem* **2004,** *14* (4), 459.

6. von Freymann, G.; Kitaev, V.; Lotsch, B. V.; Ozin, G. A., Bottom-up assembly of photonic crystals. *Chem Soc Rev* **2013,** *42* (7), 2528.

7. Vogel, N.; Retsch, M.; Fustin, C. A.; Del Campo, A.; Jonas, U., Advances in Colloidal Assembly: The Design of Structure and Hierarchy in Two and Three Dimensions. *Chem Rev* **2015,** *115*, 6265-6311.

8. Gröschel, A. H.; Walther, A.; Löbling, T. I.; Schacher, F. H.; Schmalz, H.; Müller, A. H. E., Guided hierarchical co-assembly of soft patchy nanoparticles. *Nature* **2014,** *503* (7475), 247-251.

9. Cosgrove, T., *Colloid Science - Principles, Methods and Applications*. 2nd ed.; Wiley: 2010.

10. Chen, Z. H.; Kim, C.; Zeng, X. B.; Hwang, S. H.; Jang, J.; Ungar, G., Characterizing size and porosity of hollow nanoparticles: SAXS, SANS, TEM, DLS, and adsorption isotherms compared. *Langmuir* **2012,** *28* (43), 15350-61.

11. Blanton, T. N.; Huang, T. C.; Toraya, H.; Hubbard, C. R.; Robie, S. B.; Louër, D.; Göbel, H. E.; Will, G.; Gilles, R.; Raftery, T., JCPDS—International Centre for Diffraction Data round robin study of silver behenate. A possible low-angle X-ray diffraction calibration standard. *Powder Diffraction* **1995,** *10* (02), 91-95.

12. Huang, T. C.; Toraya, H.; Blanton, T. N.; Wu, Y., X-ray powder diffraction analysis of silver behenate, a possible low-angle diffraction standard. *J. Appl. Crystallogr.* **1993,** *26* (2), 180-184.

13. Nyam-Osor, M.; Soloviov, D. V.; Yu, S. K.; Zhigunov, A.; Rogachev, A. V.; Ivankov, O. I.; Erhan, R. V.; Kuklin, A. I., Silver behenate and silver stearate powders for calibration of SAS instruments. *Journal of Physics: Conference Series* **2012,** *351* (1), 012024.

14. Orgel, J. P. R. O.; Irving, T. C.; Miller, A.; Wess, T. J., Microfibrillar structure of type I collagen in situ. *Proceedings of the National Academy of Sciences* **2006,** *103* (24), 9001-9005.

15. Orgel, J. P. R. O.; Miller, A.; Irving, T. C.; Fischetti, R. F.; Hammersley, A. P.; Wess, T. J., The In Situ Supermolecular Structure of Type I Collagen. *Structure* **2001,** *9* (11), 1061-1069.

16. Patel, I. S.; Schmidt, P. W., Small-angle X-ray scattering determination of the electron density of the particles in a colloidal suspension. *J. Appl. Crystallogr.* **1971,** *4* (1), 50-55.

17. Russell, T., An absolute intensity standard for small-angle X-ray scattering measured with position-sensitive detectors. *J. Appl. Crystallogr.* **1983,** *16* (5), 473-478.

18. Perret, R.; Ruland, W., Glassy carbon as standard for the normalization of small-angle scattering intensities. *J. Appl. Crystallogr.* **1972,** *5* (2), 116-119.

19. Russell, T. P.; Lin, J. S.; Spooner, S.; Wignall, G. D., Intercalibration of small-angle X-ray and neutron scattering data. *J. Appl. Crystallogr.* **1988,** *21* (6), 629-638.

20. Dreiss, C. A.; Jack, K. S.; Parker, A. P., On the absolute calibration of bench-top small-angle X-ray scattering instruments: a comparison of different standard methods. *J. Appl. Crystallogr.* **2006,** *39* (1), 32-38.

21. Chen, M.; Ye, C.; Zhou, S.; Wu, L., Recent Advances in Applications and Performance of Inorganic Hollow Spheres in Devices. *Adv Mater* **2013,** *25* (37), 5343-5351.

22. Kohlbrecher, J., SASfit: A program for fitting simple structural models to small angle scattering data. Paul Scherrer Institute Laboratory for Neutron Scattering (LNS): 2010.

23. Ruckdeschel, P.; Kemnitzer, T. W.; Nutz, F. A.; Senker, J.; Retsch, M., Hollow silica sphere colloidal crystals: insights into calcination dependent thermal transport. *Nanoscale* **2015,** *7* (22), 10059-10070.

24. Stoeber, W.; Fink, A.; Bohn, E., Controlled growth of monodisperse silica spheres in the micron size range. *J. Colloid Interf. Sci.* **1968,** *26* (1), 62-69.

25. Förster, S.; Apostol, L.; Bras, W., Scatter: software for the analysis of nano- and mesoscale small-angle scattering. *J. Appl. Crystallogr.* **2010,** *43* (3), 639-646.

6.7 Supporting Information

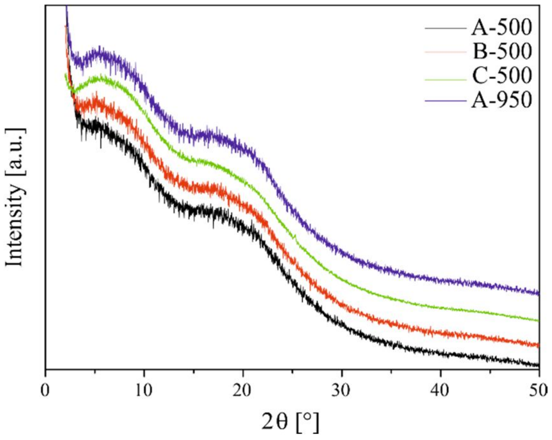

Figure S6.1. Powder XRD measurements of the hollow silica nanoparticle samples A-500, B-500, C-500 and C-950.

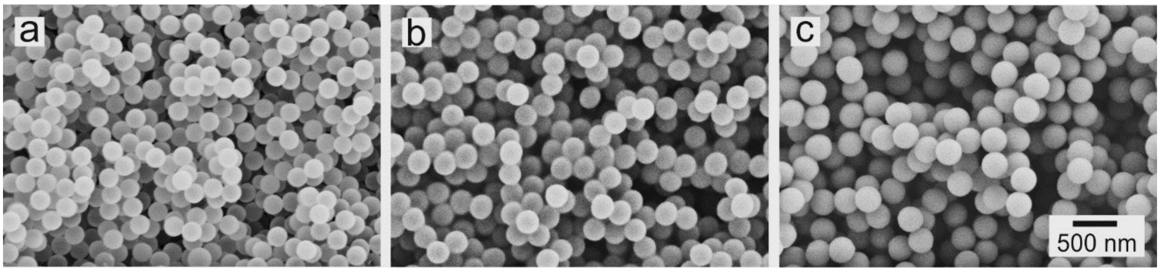

Figure S6.2. Scanning electron microscopy (SEM) images of the samples A-500, B-500 and C-500.

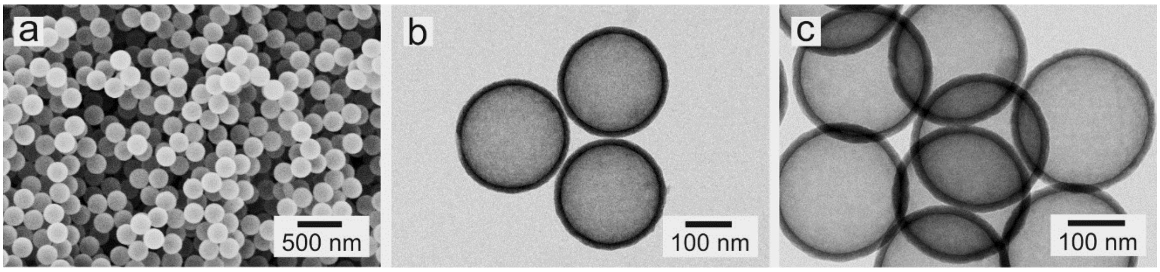

Figure S6.3. (a) Scanning electron microscopy (SEM) image and (b, c) transmission electron microscopy (TEM) images of the samples A-950.

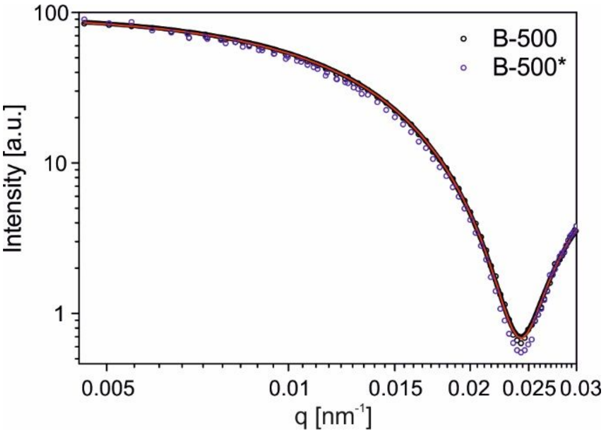

Figure S6.4. Long-term stability of silica hollow spheres in water. The blue circles show static light scattering data of sample B-500*, measured more than six months after redispersion in water. The black circles show SLS data of the sample B-500 measured shortly after redispersion. The red solid lines are fits using a form factor of hollow spheres with an infinitely thin wall according to Equation (6.1). The black solid lines are fits using a form factor for spherical core-shell particles according to Equation (6.2) and (6.3). The scattering contrast of the core was set equal to the surrounding medium (water).

Table S6.1. Long-term stability of silica hollow spheres in water. Comparison of SLS measurements at 25°.of sample B-500 and B-500*, which has been redispersed in water more than six months ago.

Sample	**SLS**		
	R_g [a] [nm]	**$R_{C/S}$ [c] [nm]**	**ΔR [c] [nm]**
B-500	142 ± 1	140	21.6
B-500*	142 ± 1	141	22.0

[a] *The values were obtained from the slope analysis of linear fits in the Guinier plots (first 8 data points not considered).*

[c] *These values were obtained from fits to the SLS scattering curves using a form factor model for a spherical core/shell particle using Equation (6.2) and (6.3)*

* *Sample B-500 has been redispersed in water more than six months ago.*

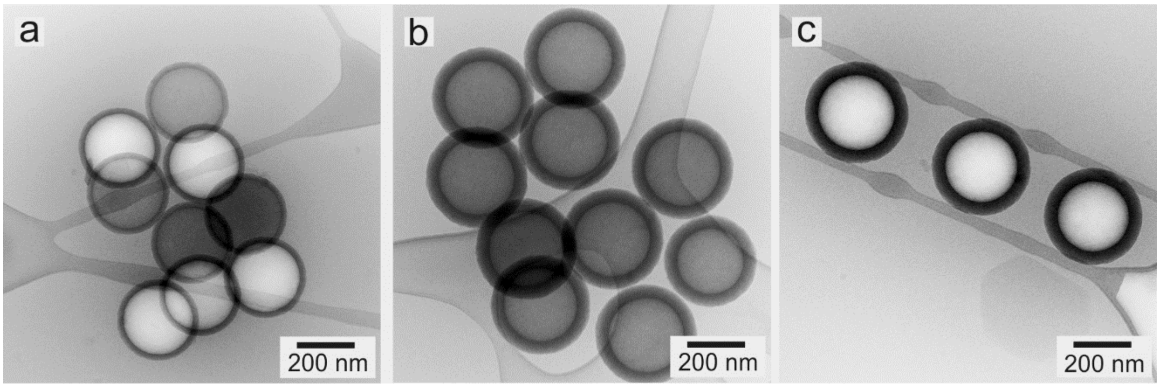

Figure S6.5. Cryo TEM of hollow silica nanoparticles after redispersion in water. (a) B-950, (b) C-500 and (c) C-950.

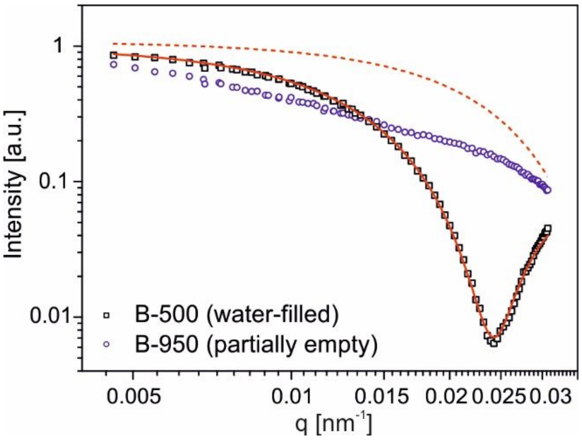

Figure S6.6. Form factor analysis by static light scattering. SLS data of B-500 (black circles) and B-950 (blue circles). The red line is the corresponding fit of sample B-500 using a form factor for spherical core-shell particles with equal scattering contrasts of the core and the surrounding medium (see Figure 6.3b). The grey line is a simulation of the form factor for spherical core-shell particles with different scattering contrasts between the core (air) and the surrounding medium (water). All data shown are normalized to 1.

Table S6.2. Comparison of SAXS measurements of hollow silica spheres as a dry powder (C-500) and dispersed in water (C-500** and C-950**).

Sample	**SAXS**				
	R_o [nm]	**σ (R_o)**	**R_i [nm]**	**σ (R_i)**	**d_{shell} [nm]**
C-500	157.5	0.04	115.0	0.020	42.5
C-500**	157.5	0.04	115.5	0.030	42.0
C-950**	152.5	0.04	111.0	0.025	41.5

7 Understanding Thermal Insulation in Porous, Particulate Materials

Pia Ruckdeschel, Alexandra Philipp, and Markus Retsch

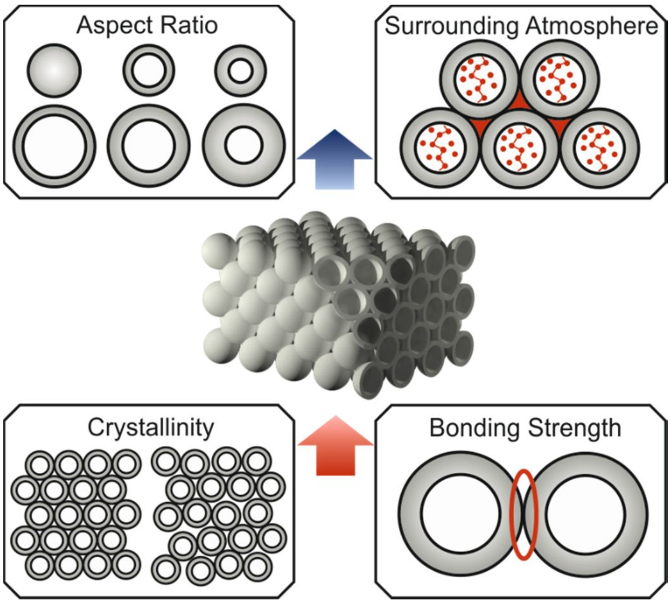

Reprinted with permission from Ruckdeschel *et al.*, *Adv. Funct. Mat.*, **2017**, 27 (38), 1702256. Copyright ©2017 Wiley VCH.

Abstract

Silica hollow nanosphere colloidal crystals feature a uniquely well-defined structure across multiple length scales. This contribution elucidates the intricate interplay between structure and atmosphere on the effective thermal diffusivity as well as the effective thermal conductivity. Using silica hollow sphere assemblies, one can independently alter the particle geometry, the density, the packing symmetry, and the interparticle bonding strength to fabricate materials with an ultralow thermal conductivity. Whereas the thermal diffusivity decreases with increasing shell thickness, the thermal conductivity behaves inversely. However, the geometry of the colloidal particles is not the only decisive parameter for thermal insulation. By a combination of reduced packing symmetry and interparticle bonding strength, the thermal conductivity is lowered by additionally 70 % down to only 8 $\mathrm{mWm^{-1}K^{-1}}$ in vacuum. The contribution of gaseous transport, even in these tiny pores (<200 nm), leads to minimum thermal conductivities of ~35 and ~45 $\mathrm{mWm^{-1}K^{-1}}$ for air and helium atmosphere, respectively. The influence of the individual contributions of the solid and (open- and closed-pore) gaseous conductions is further clarified by using finite element modeling. Consequently, these particulate materials can be considered as a non-flammable and dispersion processable alternative to commercial polymer foams.

7.1 Introduction

In our age of limited energy resources, a strong need for sustainable and efficient thermal insulation technologies has evolved. Thus, the ability to thermally insulate pipes, walls, entire houses, or even ourselves from extreme cold and hot conditions is of high importance. Hence, humans have been developing insulating materials for thousands of years, trying to reduce their thermal conductivity as efficiently as possible. Insulation materials have the natural capacity to inhibit the transmission of heat by exhibiting high volume fractions of a gaseous phase or by introducing a large number of interfaces, leading to an efficient thermal insulation.[1-2] Conventional insulation materials are fiberglass, mineral wool, and polymer foams.[2] The decisive performance quantity is given by the thermal conductivity κ, which describes the steady-state amount of thermal energy (heat) that can be transferred along a given temperature gradient. Current polymer foam based materials possess thermal conductivities of about $20-40\,\mathrm{mW\,m^{-1}\,K^{-1}}$.[3] One approach to achieve even higher thermal insulation properties is the implementation of the Knudsen effect by (i) the replacement of air with other gases or vacuum, or by (ii) reducing the pore size below the mean free path of air.[3] However, maintaining a certain gas or even vacuum inside a porous material is challenging. Thus, the reduction of the pore size seems to be a more promising way to obtain a super-insulating material. Examples for nanoporous materials are aerogels, which in most cases comprise silica (SiO_2) as the solid skeleton backbone.[4-8]

Whereas silica aerogels are excellent materials for thermal insulation due to their nanoporosity, their widespread application is still limited compared to polymer foams or organic fibers and fleeces. Major obstacles are their poor mechanical properties and their laborious and energy intensive fabrication, which in most cases involves supercritical drying using carbon dioxide.[9] The good insulation properties of silica aerogels inspired researchers to find other nanomaterials with similar or better properties.[9-13] Among these materials, silica hollow spheres are a promising insulation material, due to their structural analogy to silica aerogels. Their high thermal insulation capability has already been shown in powder measurements of silica hollow spheres.[14] However, from these measurements, conclusions about the influence of the size and shell thickness are impossible due to the ill-defined order within the powder specimens. Furthermore, it is not possible to detect any influences of the contact area and bonding strength between the silica hollow spheres. In contrast, our contribution unleashes for the first time the full potential of colloidal crystals for the understanding of thermal transport on small length scales. This is based on their periodically ordered structure, their large number of interfaces, and the possibility to adjust the surface chemistry.[15]

Whereas the optical properties are well known for colloidal crystals, the thermal properties are far from being fully understood.[16] Recent contributions in this field are investigations on nanocrystal arrays, inverse opals[17-18], organoclay nanolaminates[1] and colloidal nanoparticle assemblies[12-13, 19-20].

Understanding thermal transport in nanomaterials is not only essential for steady-state thermal insulation, but also for non-steady-state insulation like refrigeration or fire protection.[21-22] In both cases, the aim is to minimize the temperature increase in a closed area, surrounded by heat or fire for a certain time. Thus, there are two requirements for a material used for non-steady-state insulation. First, the material's thermal conductivity should be as low as possible to minimize the amount of energy conducted into the system. Second, the volumetric heat capacity (density and specific heat capacity) should be large, so that the accumulated energy is absorbed to minimize the temperature increase. The material specific property for characterizing the non-steady-state heat conduction is the thermal diffusivity. It is defined as the ratio of thermal conductivity to volumetric heat capacity. Materials with low thermal diffusivities are polymer materials. However, these materials are inherently not flame-retardant without modifying the polymer or incorporating flame retardant compounds.[23] Silica hollow sphere colloidal crystals could contribute to the solution of this problem due to their low thermal diffusivities as shown later.

In this paper, we will address the following questions: What is the fundamental limit of the thermal conductivity that can be achieved by such hollow sphere ensembles? What are the governing structure-property relationships? Therefore, we will present a holistic study of the thermal insulation capabilities of hollow silica nanoparticle assemblies. Our findings are of general importance to rationally understand and improve the thermal insulation capability of nanoporous materials. We will investigate the influence of (i) the aspect ratio of the hollow particles (size and shell thickness), (ii) the symmetry of the colloidal assembly (crystalline *vs.* amorphous packing), (iii) the surrounding atmosphere by gas pressure-dependent thermal conductivity measurements, (iv) the closed- and open-porous volume and (v) the bonding strength between adjacent spheres in the assembly.

7.2 Results and Discussion

Silica Hollow Sphere Colloidal Crystals

The synthesis of monodisperse core-shell particles is divided into two steps: (i) the synthesis of polystyrene (PS) template particles via emulsifier-free emulsion polymerization[24] and (ii) the coating of the PS spheres with a silica shell using a templated Stoeber condensation process[25]. The well-defined colloids are subsequently crystallized into superstructures via a simple evaporation-induced self-assembly process (see Scheme S7.1 in the Supporting Information, Chapter 7.7), followed by a calcination step (heat treatment at 500 °C) to burn out the PS core of the core-shell particles. As a result, hollow silica nanoparticle colloidal crystals are obtained. Further experimental details are described in the Experimental Section.

The narrow size distribution of the core-shell particles leads to ordered colloidal crystals (CCs) with a high packing density straightforwardly and reproducibly. Exemplary photographic images of such hollow sphere (HS) colloidal crystals with different shell thicknesses are shown in Figure S7.1 in the Supporting Information (Chapter 7.7). All three samples exhibit a purple color due to their same outer particle diameter of ~270 nm. However, the CCs become more and more opaque with increasing shell thickness (from left to right), resulting from an increased scattering. Thus, the CCs become more and more opaque.

The thermal transport properties and the density of the assembled HS structures are governed by two structural parameters: the shell thickness and the size of the particles. Our synthetic protocol allows adjusting these two quantities independently and thus, to study their influence on the macroscopic thermal transport. We base our investigation on five different hollow silica nanoparticles as depicted in Figure 7.1.

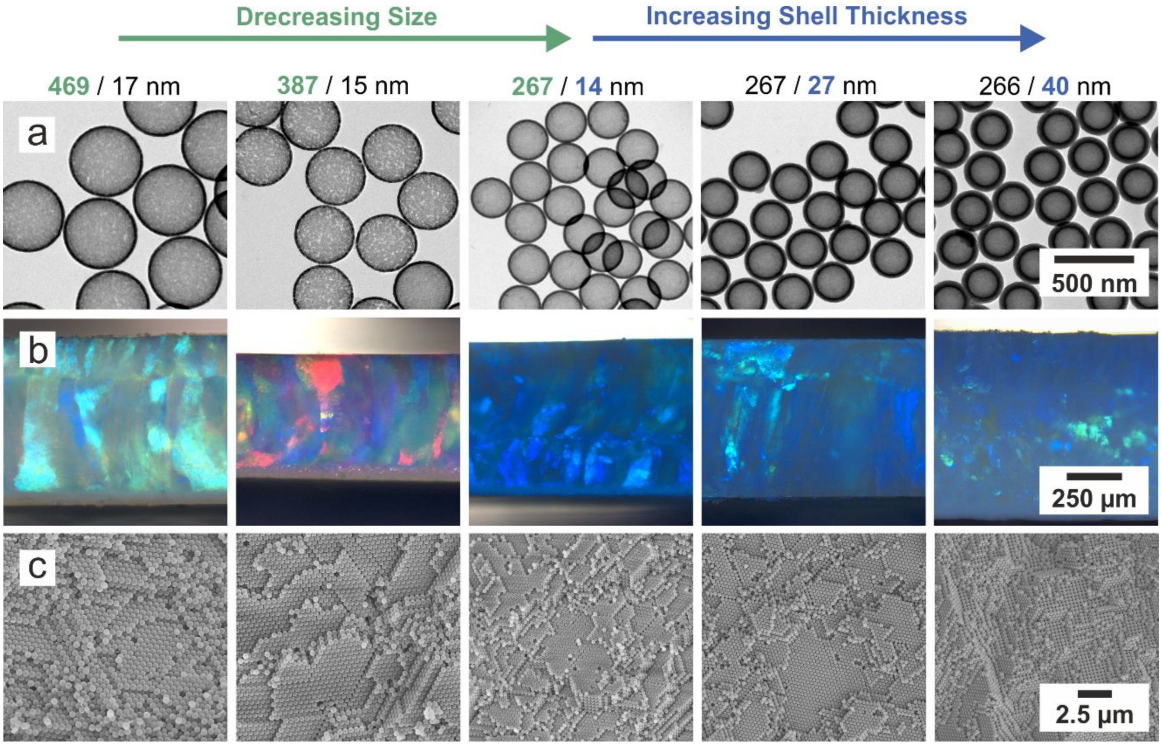

Figure 7.1. Hollow silica nanoparticles and their corresponding colloidal crystals. (a) Transmission electron microscopy (TEM) images of the individual particles, (b) side-view optical microscopy images, and (c) scanning electron microscopy (SEM) images of the colloidal crystals.

To highlight the contribution of the overall particle size and the shell thickness separately, we prepared two different series. In the first, the diameter of the particles was altered between 267 and 469 nm with a constant shell thickness of about 15 nm (size series). In a second set, the size of the particles was kept constant at ~270 nm, while the shell thickness was adjusted between 14 and 40 nm (shell thickness series). The relevant structural parameters obtained from transmission electron microscopy (TEM) are summarized in Table 7.1. All samples exhibit a low polydispersity of about 1 %. Besides TEM measurements, the monodispersity is also confirmed by small-angle X-ray scattering (SAXS, Figure S7.2). The low polydispersity of the particle size results in narrowly spaced form factor minima, which are superimposed by further minima, which indicate the low polydispersity of the shell thickness.[26] The analysis of these scattering curves gives comparable values for the size and shell thickness as the evaluation of the TEM images (Table 7.1). In the following, the values obtained from SAXS analysis are used for the nomenclature of the hollow spheres: HS-xxx/yy, where xxx is the diameter and yy is the shell thickness.

Table 7.1. Summary of data received from TEM, and SAXS measurements, as well as density measurements of the colloidal crystals.

	TEM		***SAXS*** [a)]		***Density*** [b)]
	d [nm]	**t [nm]**	**d [nm]**	**t [nm]**	**ρ(c) [gcm^{-3}]**
HS-469/17	468.8 ± 3.0	18.2 ± 1.2	469.0	16.5	0.235 ± 0.009
HS-387/15	383.5 ± 5.3	15.2 ± 1.1	387.0	14.5	0.244 ± 0.014
HS-267/14	264.4 ± 2.6	12.9 ± 0.6	267.0	14.0	0.370 ± 0.006
HS-267/27	270.5 ± 4.1	26.9 ± 1.0	267.0	27.0	0.702 ± 0.007
HS-267/40	268.7 ± 3.8	40.4 ± 1.4	266.0	40.0	0.883 ± 0.022

[a)]The fitting was performed using the software Scatter with a vesicle model.[27] The standard deviation of the outer radius is 0.014 - 0.022 and for the inner radius 0.06 - 0.15. [b)] The density of the silica shell can be found in Table S7.1.

Figure 7.1b shows optical microscopy side-view images of the CCs of the hollow nanospheres. A bright opalescence is visible in all samples pointing to a close-packed structure. We label these colloidal assemblies with the appendix *c*, referring to the crystalline state (e.g., HS-469/17-c). For the shell thickness series (HS-267/14-c, HS-267/27-c, and HS-266/40-c) the observed color is identical due to the same outer diameter of ~270 nm, as mentioned beforehand (Figure S7.1). In contrast, the size series exhibits different colors depending on the particle diameter. The long-range order of the nanospheres in a hexagonal close-packed structure is further confirmed by scanning electron microscopy (SEM) images (Figure 7.1c). Based on the optical microscopy and SEM images, the volume fraction of the particles in the CCs can, therefore, be assumed to be close to 74 %, which is the theoretical value for an ideal close-packed structure. The densities of the colloidal crystals $\rho(c)$ were determined by measuring the volume, and weight of the CCs (for details see Supporting Information, Chapter 7.7) and are summarized in Table 7.1. Here, values between 0.235 gcm^{-3} for HS-469/17-c and 0.883 gcm^{-3} for HS-266/40-c were obtained. Hence, a broad range of densities below conventional bulk materials ($\rho > 1$ gcm^{-3}) is covered. The density of the silica shell can be calculated with the help of the effective density of the colloidal crystals yielding values between 1.7 and 1.9 gcm^{-3} (see Table S7.1). The sample HS-387/15 exhibits a slightly lower silica density (1.5 gcm^{-3}) caused by an increased microporosity as depicted in the nitrogen sorption data in Figure S7.3 and Table S7.2. The BET surface area (246 m^{2}g^{-1}) and the pore volume (0.41 cm^{3}g^{-1}) of HS-387/15 are slightly higher compared to the other hollow silica spheres, for which the BET surface area ranges between 150 – 180 m^{2}g^{-1} and the pore volume amounts to 0.18 – 0.33 cm^{3}g^{-1}. Thereby, the micropore diameter shows a broad distribution with a maximum < 5 nm for the different silica hollow nanospheres. Overall, no significant influence of the microporosity on the thermal transport is expected.

Thermal Transport Properties of Silica Hollow Sphere Colloidal Assemblies

We investigated the thermal transport properties by the xenon flash analysis (XFA). The setup and a common measurement signal along with its radiation fit are provided in Figure S7.4. In brief, a sample, coated with a thin graphitic layer on both sides, is subjected to a temperature increase due to a short xenon light flash illuminating the bottom surface of the specimen. The absorbed heat is conducted through the sample. At the upper surface, an infrared (IR) detector measures the time-dependent temperature increase. Subsequently, the measurement signal is fitted with an appropriate one-dimensional heat diffusion model (i.e., the radiation model), giving the effective thermal diffusivity of the measured sample. The great advantage of this method is the possibility to control the temperature and the surrounding atmosphere (pressure, gas type) in a precise manner.

The individual contributions of the heat transport in porous materials are solid conduction, open- and closed-pore volume gaseous conduction, radiative transport, and convection. The different mechanisms are depicted in Scheme 7.1. The contribution from convection is negligible due to the small pore sizes. Additionally, radiative thermal transport can be neglected due to the transient measurement and the small temperature difference applied in an XFA. Thus, the heat transport is mainly governed by solid and gaseous conduction. We want to point out that xenon flash analysis measures the *effective* thermal diffusivity owing to the porosity of the colloidal ensemble. For reasons of readability, however, we will talk about thermal diffusivity and conductivity, respectively, throughout this paper. In the following sections, we will describe the individual contributions of the thermal transport as a function of the structure of the silica hollow sphere colloidal crystals.

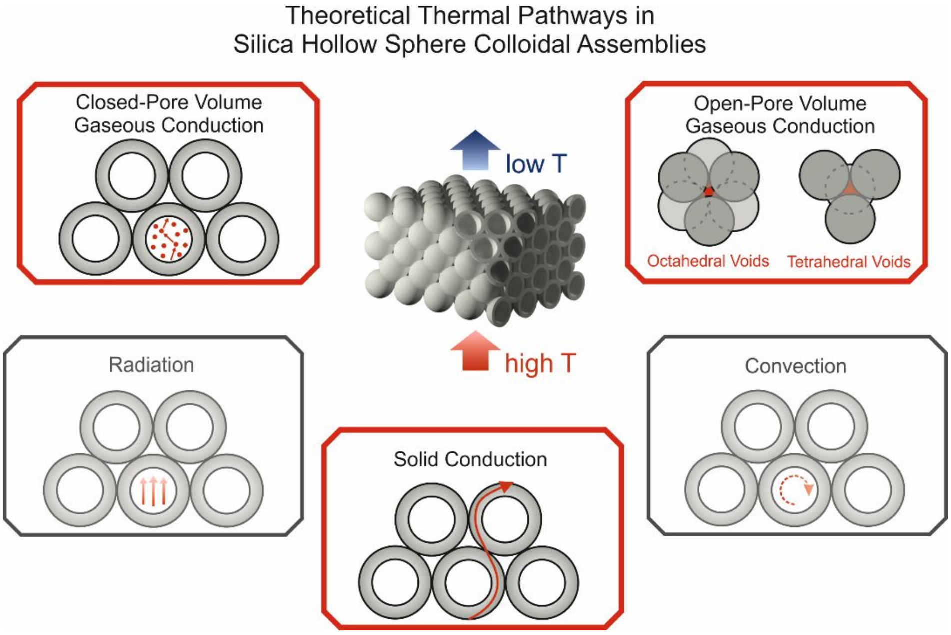

Scheme 7.1. Thermal transport pathways in a silica hollow sphere colloidal crystal: Solid conduction, gaseous conduction through the open-pore and closed-pore volume, radiative transport, and convection. The red framed boxes mark the thermal pathways critical for silica hollow sphere colloidal crystals.

Thermal Diffusivity of Silica Hollow Sphere Colloidal Crystals

How fast is temperature diffusing through a hollow sphere colloidal crystal? Considering that, the thermal diffusivity has to be considered. For an understanding of the contribution of the solid and the gaseous conduction through the colloidal assemblies, the experiments were conducted in vacuum (0.05 mbar) and in helium in the range of 1 and 1000 mbar.

The thermal diffusivity under vacuum conditions (0.05 mbar) is solely governed by the thermal conduction across the solid silica network. It should be noted that the contact area between two adjacent spheres was measured to be comparable for all particles (0.60 – 0.77 % of the particle surface area). Hence, an influence of the contact area can be excluded.[13] Our data show that the actual size of the hollow spheres does not strongly affect the thermal diffusivity, which remains constant at around $1.6 \cdot 10^{-3}$ cm^2s^{-1} (Figure 7.2a). Conversely, the shell thickness exerts a strong impact on the thermal diffusivity, with a systematic decrease by about 27 % when increasing the shell thickness (Figure 7.2b). Thus, a larger amount of material slows down the temperature diffusion. These low thermal diffusivity values are comparable to common bulk polymer materials.[28]

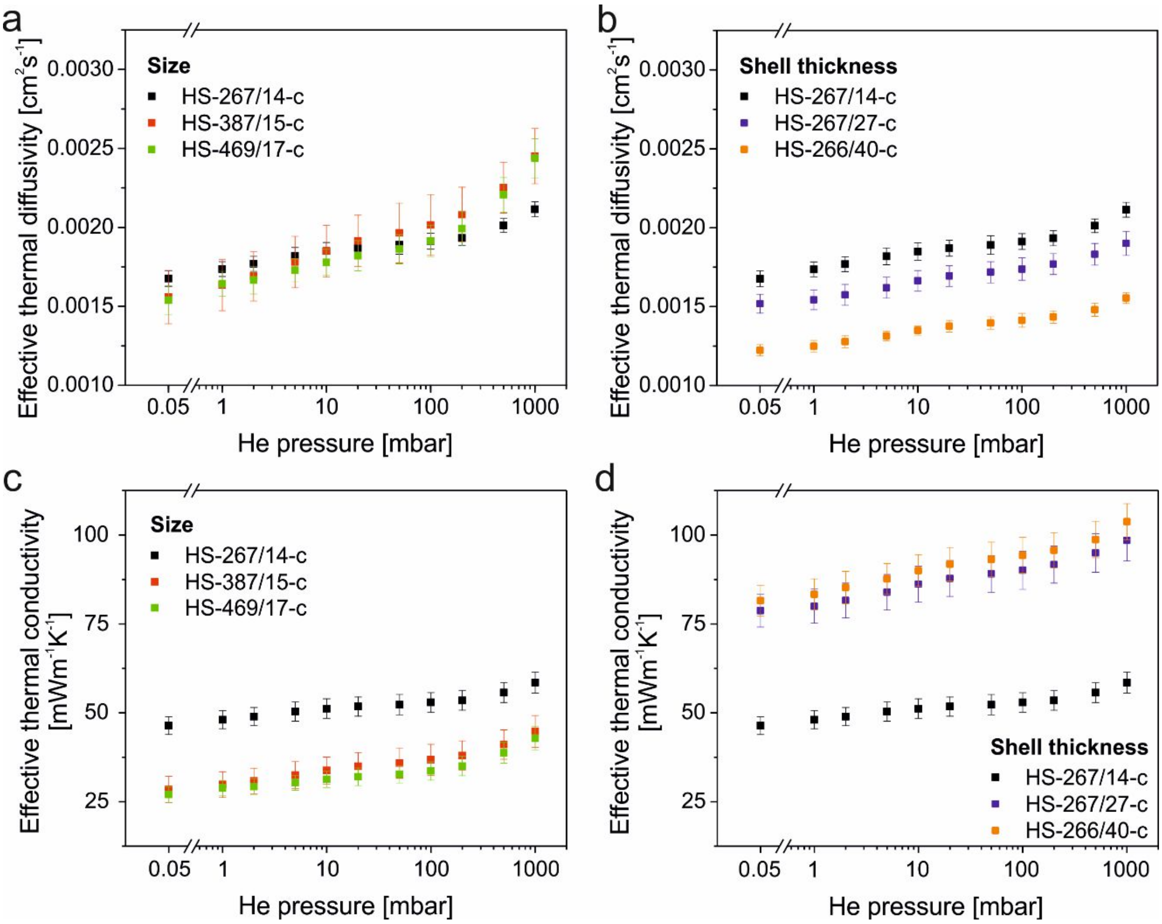

Figure 7.2. Thermal transport properties of silica hollow sphere colloidal crystals. (a, b) Pressure-dependent thermal diffusivity of the size series (a), and the shell thickness series (b). (c, d) Pressure-dependent thermal conductivity of the size series (c), and the shell thickness series (d).

Quite expectedly, for both, the size series (Figure 7.2a) and the shell thickness series (Figure 7.2b), the thermal diffusivity increases with increasing helium pressure. This is due to the additional temperature diffusion pathway through the gaseous phase at high helium pressures. However, it is interesting to consider the quantitative changes. The increase of the thermal diffusivity is more pronounced for larger particles than for smaller ones. It amounts to 37 % ($\alpha = 9.0 \cdot 10^{-4}$ cm²s⁻¹) for the samples HS-469/17-c and HS-387/15-c and only 20 % ($\alpha = 4.3 \cdot 10^{-4}$ cm²s⁻¹) for HS-267/14-c when decreasing the particle size. An explanation for the different sensitivity to helium atmosphere can be given by comparing the interparticle void sizes[29] (see Table S7.3) with the mean free path of helium (~200 nm).[30] The octahedral voids, as a measure for the upper limit, range from 194 to 110 nm for the largest and smallest hollow sphere, respectively. Consequently, the mean free path of helium is comparable or greater than the open-pore volume of the voids. This implies that gas-wall interactions predominate over the collision of the gas molecules with each other (Knudsen diffusion).[31] The confinement effect is the strongest for the smallest particles, resulting in the smallest additional temperature conduction across the gaseous phase, whereas a higher amount of temperature transfer can be expected for the larger particles.

In contrast, the thermal diffusivity increases from vacuum (0.05 mbar) to helium at 1000 mbar by about 20 % for all shell thicknesses. This corresponds to a thermal diffusivity difference $\Delta\alpha$ of $4.3 \cdot 10^{-4}$ cm²s⁻¹ for the thinnest shell to $3.3 \cdot 10^{-4}$ cm²s⁻¹ for the thickest shell. Hence, the increase of the thermal diffusivity from vacuum to helium is rather similar for all shell thicknesses due to the same outer diameter. Slight differences can be explained by the impact of the decreasing inner pore volume. A more detailed investigation on how the heat spreads between the solid phase and the internal and external pore volume is given later on by finite element modeling.

Thermal Conductivity of Silica Hollow Sphere Colloidal Crystals

How much energy is conducted across a hollow sphere colloidal crystal? For this, we determined the *effective* thermal conductivity κ, which can be calculated based on the *effective* thermal diffusivity α, the heat capacity c_p, and the density ρ of the colloidal crystal using the following equation:

$$\kappa = \alpha \cdot c_p \cdot \rho \tag{7.4}$$

The heat capacity was averaged over four different silica hollow spheres with different sizes and shell thicknesses (see Figure S7.5). Its mean value at 25 °C amounts to (0.748 ± 0.031) $Jg^{-1}K^{-1}$. The density values are summarized in Table 7.1. In Figure 7.2c and d, the resulting pressure-dependent thermal conductivities are given.

The lowest thermal conductivity values are observed in vacuum due to the absence of heat transport pathways through the gaseous phase. While the thermal diffusivity is more or less size independent, the thermal conductivity exhibits a clear size dependence (Figure 7.2c). The lowest thermal conductivity is obtained for the colloidal crystal comprising the largest particles (HS-469/17-c). In vacuum, a value of 27 $mWm^{-1}K^{-1}$ is achieved, and in helium, at 1000 mbar the thermal conductivity amounts to 43 $mWm^{-1}K^{-1}$. The comparable density of HS-387/15-c and HS-469/17-c results in a very similar thermal conductivity, whereas the thermal conductivity of HS-267/14-c is significantly higher.

We also found a shell thickness dependent thermal conductivity (Figure 7.2d). In contrast to the thermal diffusivity, an opposing trend is present: The thermal conductivity in vacuum increases by about 43 % from 46 $mWm^{-1}K^{-1}$ to 82 $mWm^{-1}K^{-1}$ with increasing shell thickness. When using helium as a gas medium, the thermal conductivity ranges from 59 $mWm^{-1}K^{-1}$ to 104 $mWm^{-1}K^{-1}$. For decreasing particle sizes, a reduction in the thermal conductivity difference between vacuum and helium is found ($\Delta\kappa = 15.8$ $mWm^{-1}K^{-1}$ for HS-469/17-c to $\Delta\kappa = 12.1$ $mWm^{-1}K^{-1}$ for HS-267/14-c). This agrees with the thermal diffusivity data, and can be traced back to the more pronounced Knudsen effect for the smaller particles. On the other hand, for the shell thickness series, a constant difference between vacuum and helium is expected due to the same outer pore diameter. However, we find that the increase from vacuum to helium is more pronounced for the thickest shell ($\Delta\kappa = 22.1$ $mWm^{-1}K^{-1}$) compared to the thinnest shell ($\Delta\kappa = 12.1$ $mWm^{-1}K^{-1}$). This can be explained by a slight densification of the silica shell with increasing shell thickness. The role of the inner pore volume will be elucidated in the next chapter by FEM simulation.

Figure 7.3 summarizes the thermal diffusivity and thermal conductivity properties of our hollow silica spheres colloidal crystals. From that, insights into the fundamental limit of thermal insulation, solely based on the hollow sphere geometry, can be deduced. From the vacuum measurements, it is apparent that larger shell thicknesses are needed to reduce the thermal diffusivity. However, the reduction in thermal diffusivity is over-compensated by the concomitant density increase. Consequently, the thermal conductivity increases with shell thickness and tends toward a plateau. Increasing the size of the hollow spheres does not strongly influence the thermal diffusivity. Therefore, the density of the colloidal ensemble governs the effective thermal conductivity. Lower thermal conductivities ($< 27\,\mathrm{mW\,m^{-1}K^{-1}}$) could be achieved by larger particles with thin shells. However, this would come at a compromised structural integrity of the colloidal ensemble, since the stiffness of hollow silica particles scales with the square of the shell thickness t^2 and inversely with the radius of the particle R^{-1}.[32] Overall, the thermal diffusivity and thermal conductivity cannot be lowered simultaneously just by the appropriate particle design.

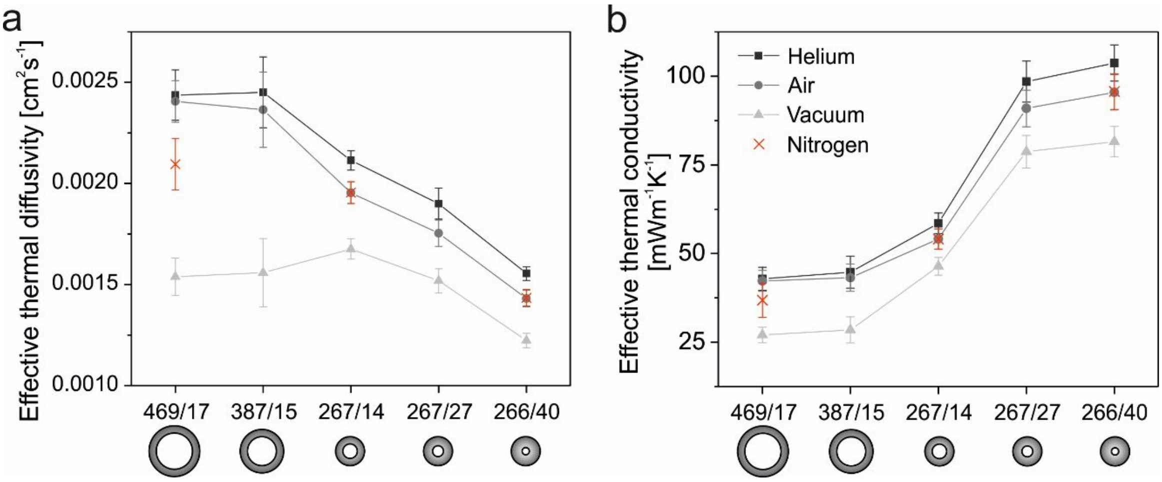

Figure 7.3. Atmosphere dependent thermal transport properties of silica hollow sphere colloidal crystals. (a) Thermal diffusivity and (b) thermal conductivity in helium and air at 1000 mbar as well as vacuum at 0.05 mbar. The lines are a guide to the eye.

Additional thermal transport pathways in the open-porous structure are opened by using nanoporous systems in air or helium. The thermal transport properties in ambient air are located between the helium and vacuum measurements due to a lower gaseous thermal conductivity compared to helium (air: 25 $\mathrm{mW\,m^{-1}\,K^{-1}}$ compared to helium: 153 $\mathrm{mW\,m^{-1}\,K^{-1}}$).[33] However, this is not the case for the larger particle diameter, especially for sample HS-469/17-c, where a similar thermal conductivity is obtained in air and helium. An explanation for this is water condensation, which can be adsorbed by the hygroscopic silica network during measurement in ambient air. The incorporation of water does not occur in helium and vacuum due to preconditioning of the samples at 200 °C in vacuum before the thermal transport determination. When conducting the experiments with dry nitrogen, the thermal conductivity of the assembly with the largest spheres (HS-469/17-c) is reduced by 13 %, compared to moist air, yielding a thermal conductivity of 37 $\mathrm{mW\,m^{-1}\,K^{-1}}$ in nitrogen (red crosses in Figure 7.3). Altogether, our measurements indicate a fundamental limit of the thermal conductivity at around 35 $\mathrm{mW\,m^{-1}\,K^{-1}}$ for hollow silica nanoparticle ensembles in air. This is based on the interplay between solid and gaseous heat conduction. Furthermore, care has to be taken to avoid vapor condensation, which will further increase the overall thermal conductivity. Whereas the measured values of the thermal conductivity are higher compared to silica aerogels, they are well comparable to commercial polymer foams. Yet, these hollow sphere ensembles possess several advantageous features: breathable due to their open porous structure, dispersion-processable like spraying or painting, and non-flammable based on the SiO_2 network.

Finite Element Modeling of the Thermal Transport in HS Colloidal Crystals

In the following, we compare our experimental results to the data obtained from finite element modeling (FEM). The aim of the FEM simulation is to gain insights into the contribution of the open- and closed-pore volume to the total heat transport through silica hollow sphere colloidal assemblies.

For the steady-state simulations, hollow spheres were arranged in a face-centered cubic (*fcc*) unit cell packing (see Figure S7.7). A constant hot and cold temperature is imposed on the entire lower and upper face, while all other boundaries are set thermally insulating. Thus, a temperature gradient is formed, with a heat flux in the direction of the cold face. The effective thermal conductivity is calculated according to Fourier's equation of heat conduction:

$$\kappa = \frac{Q/A}{\Delta T/h} \tag{7.2}$$

where Q is the numerically computed heat flow rate normal to the cross-sectional area A $(= h^2)$ of the unit cell, ΔT the temperature difference $(T_{hot} - T_{cold})$, and h the unit cell edge length. Further details about the model are described in the Supporting Information.

Figure 7.4a shows the calculated thermal conductivity for the different silica hollow sphere geometries in vacuum and helium, with different thermal contact conductances h_c between silica and helium (0 $\mathrm{W m^{-2} K^{-1}}$ – continuity). The solid/gas thermal contact conductance is an unknown variable and needs to be reasonably estimated, while the thermal contact resistance between adjacent spheres is assumed to be zero. In the absence of gas, heat is only transported through the silica network. For this case, the thermal conductivity of the silica shell material was adjusted such that similar values were obtained for the simulation and the experimental data. We found a thermal conductivity of the silica shell material of $\kappa = 331\ \mathrm{mW m^{-1} K^{-1}}$ to describe our system adequately. This is comparable to nanostructured silica thin films reported by Coquil et al.[34]. By introducing helium to the network, additional heat conduction pathways arise. The thermal conductivity of helium was reduced compared to its bulk value due to the Knudsen effect occurring in small pores. The applied thermal conductivities in the open- and closed-pores are summarized in Table S7.5.

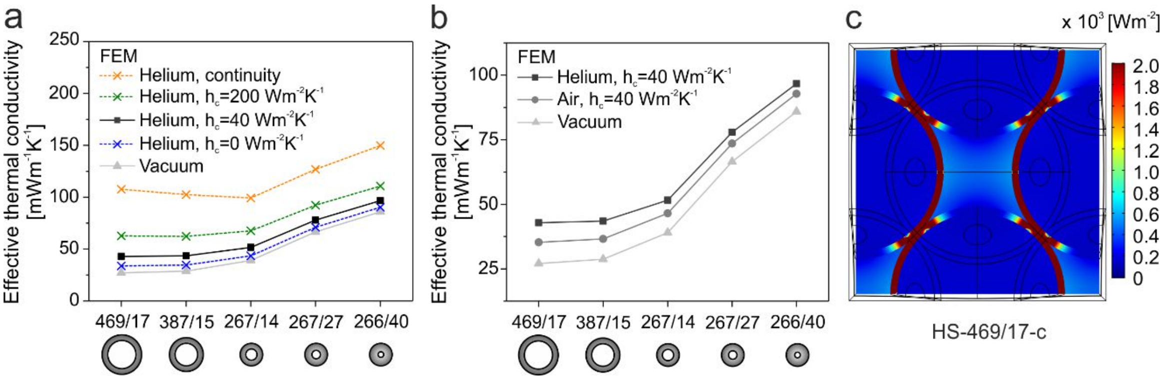

Figure 7.4. Finite element method modeling. (a) Influence of the thermal contact conductance h_c between silica and helium on the total thermal conductivity of silica hollow sphere colloidal crystals and comparison to vacuum. (b) Thermal conductivity of silica hollow sphere colloidal crystals in vacuum, helium, and air assuming a thermal contact conductance h_c of 40 Wm^{-2}K^{-1}. The input data used for the simulations in (a) and (b) can be found in Table S7.4 and Table S7.5, respectively. (c) Heat flux density analysis for a thermal contact conductance of 40 Wm^{-2}K^{-1} between the silica network and helium for HS-469/17-c. The thermal conductivity values used for helium in the open- and closed pores are listed in Table S7.5. The integrated heat flux densities of the different phases are listed in Table S7.7.

At a thermal contact conductance of 0 Wm^{-2}K^{-1}, only the gas in the open-pore volume can contribute to the total heat transport. For this case, the increase in the thermal conductivity was found to be too low compared to the experimentally determined data in helium. Thus, a small amount of the heat has to be also transferred through the closed-pore volume. We found a relatively low thermal contact conductance of 40 Wm^{-2}K^{-1} between the solid spheres and their gaseous environment to be suitable for our system. Higher thermal contact conductance values of 200 Wm^{-2}K^{-1} (green crosses) and continuity (orange crosses), which means that no thermal contact resistance exists, are also shown in Figure 7.4a. It is apparent that these parameters overestimate the thermal conductivity of the colloidal crystals. They also do not replicate the geometry-dependent trend adequately.

The thermal transport properties are plotted in Figure 7.4b for different gases, using a thermal contact conductance of 40 Wm^{-2}K^{-1}. The theoretically obtained values are in good agreement with the measured ones (Figure 7.3). For all surrounding atmospheres, the thermal conductivity decreases with decreasing shell thickness and increasing particle diameter. The additional thermal transport through the gaseous phase increases the thermal conductivity from vacuum to helium. The simulations in (dry) air are located between helium and vacuum. By looking at the helium and vacuum data, it can be seen that the relative change in thermal conductivity is lower for smaller particles. This is based on an increased thermal conductivity reduction of the gas phase due to the geometric constriction. Consequently, the highest increase is obtained for the largest particle diameter and thus, the largest interstitial pore sizes in the assembly (HS-469/17-c). For the shell thickness series, i.e. the same open pore sizes, the increase in the thermal conductivity between vacuum and helium is comparable. This again demonstrates the important interplay between thermal conductance along the solid silica backbone and the gaseous environment. Whereas the specific particle design could greatly reduce the thermal conductivity of the hollow silica nanoparticle network, this high thermal insulation capacity is counteracted by thermal transport across the increased gas volume.

Moreover, heat flux densities and heat flux streamlines can be deduced from the FEM simulation. In Figure 7.4c, the distribution of the heat flux density is shown for a cross-section through HS-469/17-c. One can infer a lower contribution of the closed-pore volume (gas encapsulated in the hollow sphere) to the total thermal conductivity compared to the open-pore volume. Still, thermal transport through the silica shell is preferred. The predominating heat transport through the solid phase is further emphasized by the heat flux streamlines (Figure S7.7b, bottom), which are bent towards the silica shell. Additionally, heat flux density images and streamlines for different helium gas thermal conductivities (153 $\mathrm{mW\,m^{-1}\,K^{-1}}$ for bulk helium, 95 $\mathrm{mW\,m^{-1}\,K^{-1}}$ for 436 nm pores, and 50 $\mathrm{mW\,m^{-1}\,K^{-1}}$ for 135 nm pores) are compared in Figure S7.7a. The decrease of the helium thermal conductivity due to an increased confinement, leads to a decreased heat flux in the open-pore volume, whereas the heat flux in the closed-pore volume stays at a low level. Integration of the heat flux densities provides a quantitative impression of the respective transport pathways. The values are summarized in Table S7.7. For the colloidal crystals consisting of the particles HS-469/17 and a thermal contact conductance of 40 $\mathrm{W m^{-2} K^{-1}}$, 67 % of the heat is transported through the silica, and 33 % through the gaseous phase. From that, 18 % of the heat transport occurs through the open-pore volume and 15 % through the closed-pore volume.

Lower Limit of Thermal Transport Properties of Silica Hollow Sphere Colloidal Assemblies

How can the thermal diffusivity be further reduced in hollow sphere ensembles? Without changing the particle geometry, there are two possibilities: 1) the reduction of the interparticle contact points from 12 (close-packing) to ~6 (random close-packing) and 2) the reduction of the interparticle bonding strength. The first option can be realized by reducing the packing parameter from a colloidal crystal towards a colloidal glass with a random close-packed (*rcp*) structure. The structures of such colloidal glasses are shown in Figure 7.5. In contrast to the crystalline assemblies, these colloidal glasses are labeled with the appendix *a* referring to the amorphous symmetry (e.g., HS-469/17-a).

The SEM images show the random packing of the hollow nanospheres, which causes a diffuse scattering in the optical microscopy image (see Figure 7.5a – c).[35] Thus, due to the missing crystallinity, no Bragg reflections are visible. For these colloidal glasses, the density was measured to be 0.208 – 0.314 $\mathrm{g cm^{-3}}$, which is a reduction of 9 – 15 % compared to the colloidal crystals. The influence of the packing parameter on the thermal diffusivity is shown in Figure 7.5d. In vacuum, the temperature diffusion is slower and causes a drop of the thermal diffusivity by about 15 %. This can be explained by the lower density and the reduction of the interparticle contact points due to the glassy structure. In helium at 1000 mbar, the thermal diffusivity of colloidal glasses is comparable or even higher than the temperature diffusion through the crystalline counterpart. Thus, while a reduced solid conduction persists in the glassy state, an increased gaseous conduction originates due to the greater open-pore volume. The increased gaseous conduction is especially noticeable for large particles (HS-387/15-a and HS-469/17-a). For smaller particles, the Knudsen effect is still dominating and thus, reduces the thermal diffusivity in helium. Noteworthy, the point at which the temperature diffusion of the amorphous glass is higher than the colloidal crystal shifts to lower pressures with increasing pore sizes. In the following, the influence of the density reduction and thermal diffusivity changes on the thermal conductivity will be discussed.

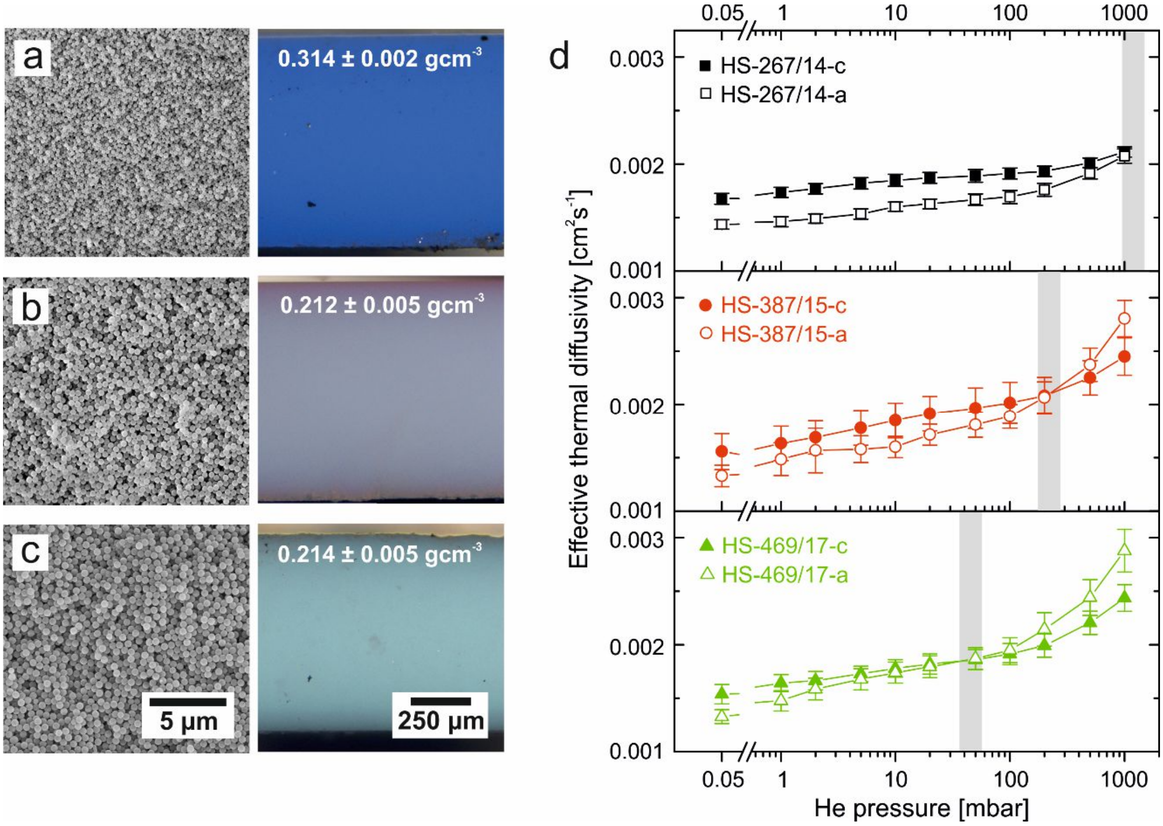

Figure 7.5. Silica hollow sphere colloidal glasses. (a – c) SEM and side-view optical microscopy images of colloidal glasses consisting of hollow spheres (a) HS-267/14, (b) HS-387/15, and (c) HS-469/17. (d) Pressure-dependent thermal diffusivity data of amorphous assemblies (open symbols) in comparison to colloidal crystals (closed symbols).

Figure 7.6a gives the helium pressure-dependent thermal conductivity of hollow nanosphere colloidal crystals (closed symbols) and colloidal glasses (open symbols). Indeed, the reduction of the packing density reduces the solid thermal conduction by 23 – 27 % in vacuum due to the decreasing density and decreasing amount of contact points for all particles under investigation. The lowest thermal conductivity was measured to be 21 mWm^{-1}K^{-1} for HS-469/17-a. However, for the gaseous thermal conductivity, one needs to distinguish between small and large hollow silica nanoparticle packings. The small particles (HS-267/14-a), the thermal conductivity is reduced over the whole pressure range. This is different for the colloidal glasses consisting of the larger particles (HS-387/15-a and HS-469/17-a). For these, the thermal conductivity is comparable or even higher than for the crystalline assemblies, after exceeding a certain helium pressure. This intersection point is located at lower pressures for larger particles due to the increasing pore sizes. Besides the measurements in vacuum and helium, we also determined the thermal conductivity in air. The comparison of the different surrounding atmospheres is shown in Figure 7.6b. Analogous to the crystalline samples, the thermal conductivity in helium and air are comparable for the colloidal glasses. Only in the case of the smallest particles, a significant difference between the measurements in air and helium atmosphere is observed. This can be traced back to the adsorption of water, as discussed beforehand.

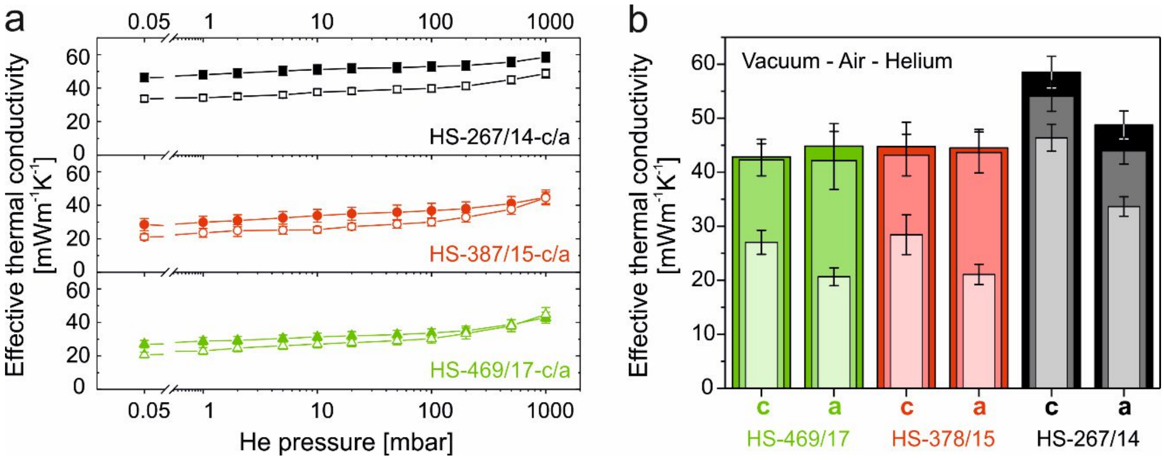

Figure 7.6. Thermal conductivity of silica hollow sphere colloidal crystals and amorphous glasses. (a) Pressure-dependent thermal conductivity of amorphous assemblies (open symbols) in comparison to colloidal crystals (closed symbols). (b) Comparison of different surrounding atmospheres (from bright to dark: vacuum (~0.05 mbar), air (~1000 mbar), and helium (1000 mbar)).

Overall, the transition to a colloidal glass resulted in a lower thermal conductivity AND lower thermal diffusivity for all particles in vacuum. However, this reduction in temperature and heat transport is counteracted by the additional gaseous transport through the concomitantly generated free volume. After all, the lowest thermal conductivity (42 $\mathrm{mWm^{-1}K^{-1}}$) in helium and air was measured for a colloidal crystal with 469 nm large hollow nanospheres (HS-469/17-c).

The adjustment of the bonding strength between adjacent spheres is another possibility to reduce the transport of thermal energy further. The influence of the interparticle bonding strength, and therefore, the interfacial thermal conductance was already shown in an earlier contribution.[12] In this, the bonding strength was enhanced by increasing calcination temperatures from 500 to 950 °C. This led to stronger covalent bonding between adjacent spheres and hence, resulted in an increased thermal conductivity. Here, we want to decrease the interfacial bonding between the hollow silica spheres to reduce heat transport. Thus, we calcined the hollow silica spheres *before* the assembly process. As a result, the spheres will only possess weak van der Waals contact forces. Thus, altered heat transport properties are expected by the reduction of the bonding strength.[36] To access the lower limit of the thermal conductivity for such a colloidal assembly, the hollow spheres with the largest diameter (469 nm) and the lowest packing density (colloidal glass) were utilized. The resulting structure is called HS-469/17-aa (Figure 7.7). Its thermal conductivity in helium at 1000 mbar is comparable to the colloidal glass structure HS-469/17-a and the crystalline assembly HS-469/17-c, introduced beforehand. This shows the predominant thermal transport through the gaseous phase, independent from the symmetry of the assembly. The influence of the contact strength becomes dominant for measurements at lower gas pressures. In vacuum, the thermal conductivity of the colloidal glass (HS-469/17-aa) shows an extremely low thermal conductivity of about 8 $\mathrm{mWm^{-1}K^{-1}}$. Thus, a thermal conductivity reduction of 61 % is achieved solely by reducing the interparticle bonding strength. This significant decrease of the heat transport can be traced back to a simultaneously drastic reduction of the thermal diffusivity (see Figure S7.8). The heat capacity remains unchanged, and the density of 0.190 $\mathrm{gcm^{-3}}$ is comparable. Compared to the hollow spheres assembled in a crystalline symmetry and calcined after the assembly (HS-469/17-c), the thermal conductivity in vacuum is even reduced by 70 % by combining the effect of reduction of interparticle contact points and reducing their bonding strength.

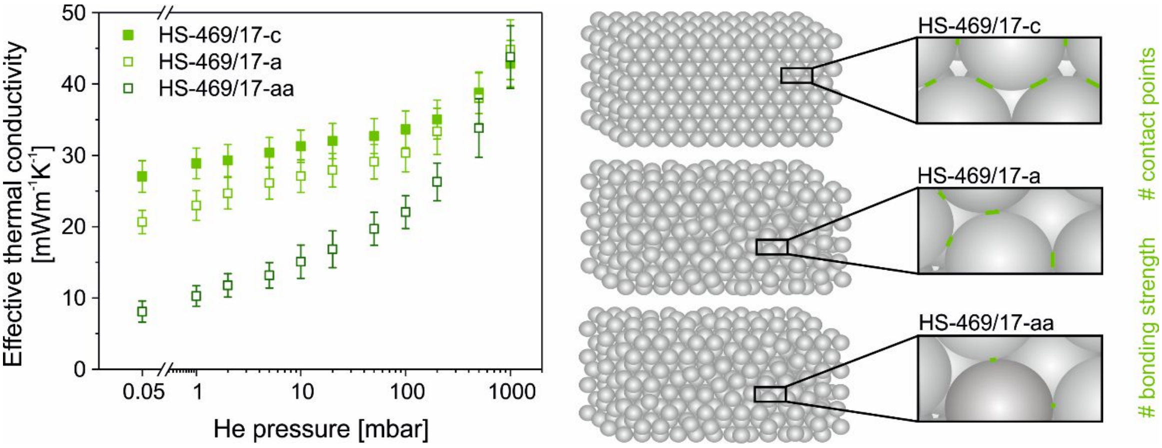

Figure 7.7. Influence of the number of contact points and the interparticle bonding strength on the thermal conductivity for assemblies with 469 nm-sized hollow spheres. HS-469/17-c is a colloidal crystal, HS-469/17-a is an amorphous colloidal glass, and HS-469/17-aa is an amorphous colloidal glass without covalent interparticle bonds.

The effect of the bonding strength can also be rationalized by FEM-simulating a thermal contact conductance between individual spheres (see blue circular areas in Figure S7.9a. By increasing the thermal resistance, the thermal conductivity decreases significantly (see Figure S7.9b). Thus, very low thermal conductivities and diffusivities can be achieved by reducing the bonding strength, and consequently by lowering the thermal contact conductance between adjacent hollow spheres. Nevertheless, this material engineering will be only effective under vacuum conditions, as gaseous conduction will be the path of the least resistance and therefore be the dominant contribution.

7.3 Conclusion

In summary, we presented a holistic picture of the thermal transport properties of dense silica hollow nanoparticle packings. At first, we focused on the influence of the geometry of the hollow spheres: size and shell thickness. Therefore, the thermal diffusivity is mainly influenced by the shell thickness. An increasing shell thickness lowers the temperature diffusion. An opposing trend was found for the thermal conductivity. Here, the thermal conductivity is decreased by increasing the size of the particles and by reducing the shell thickness. Thus, the lower the density, the lower the thermal conductivity. A concomitant reduction of the thermal diffusivity and conductivity by the particle geometry is not possible. Furthermore, using finite element modeling, we were able to show that the heat transport through the gas phase is mainly dependent on the open-pore volume. The internal particle volume plays a less significant role.

In the second part, we focused on the number and strength of the interparticle contact points. Here, we changed the packing density of the spheres in the assembly and the bonding strength between adjacent particles. The combination of both effects resulted in a strong reduction of 70 % of the thermal conductivity and diffusivity in vacuum. This can be advantageous for both, steady- and non-steady-state state, thermal insulation applications. For a colloidal crystal consisting of 469 nm hollow spheres with a shell thickness of 16.5 nm, we found a thermal conductivity of only 8 $\mathrm{mWm^{-1}K^{-1}}$ in vacuum. This ultra-low thermal conductivity, however, cannot be maintained under atmospheric conditions due to the overwhelming thermal transport through the gaseous phase. Nevertheless, a low thermal conductivity (~35 $\mathrm{mWm^{-1}K^{-1}}$) can be achieved with this material class, which is comparable to established polymer based insulation materials. Altogether, this comprehensive study about the interplay of vacuum and gas-dependent thermal diffusivity and thermal conductivity in nanostructured materials will help to create novel insulation materials.

7.4 Experimental Section

Materials

Styrene (≥99%, Aldrich), 2,2′-azobis(2-methylpropionamidine)dihydrochloride (AIBA; 97 %, Aldrich), 2-methacryloxyethyltrimethylammonium chloride (MTC; 70 % solution in water, Polyscience), polyvinylpyrrolidone K30 (PVP; Mw ~ 55 kgmol^{-1}, Aldrich), tetraethylorthosilicate (TEOS; ≥ 99%, Aldrich), and ammonium hydroxide solution (30 – 33 % in water, Aldrich) were used as received. Ethanol (EtOH) was used in technical grade, and water was taken from a Millipore Direct Q3UV unit for the entire synthesis and purification steps.

Synthesis of silica hollow spheres

Monodisperse polystyrene (PS) particles were synthesized by emulsifier-free emulsion polymerization. The synthesis was carried out in a three-necked flask, equipped with a reflux condenser and a gas inlet, under a slight argon flow. For the polystyrene template synthesis of sample HS-267/14, 100 mL water, 13 mL styrene, 100 µL MTC, and 0.9 g PVP K-30 were heated to the reaction temperature of 70 °C at a stirring speed of 850 rpm. After an equilibration time of 30 min, 0.3 g AIBA, dissolved in 20 mL water, were added to initiate the polymerization. After nucleation, the stirring speed was reduced to 450 rpm. The reaction was carried out overnight. Seeds of varying diameter were obtained by using different amounts of MTC, PVP, and AIBA.

The polystyrene particles were used as seeds for coating with a thin silica shell by the Stöber process. For sample HS-267/14, 2.2 vol.% TEOS were added to an 81.3 vol.% EtOH, 10.5 vol.% water, 6.0 vol.% ammonium hydroxide solution containing 93 mgmL^{-1} PS latex particles. Core-shell particles with thicker shell thicknesses were obtained by increasing the TEOS volume.

The polystyrene core was removed by calcining the particles at 500 °C for 12 h in air. For the thermal transport measurements, the core-shell particles were assembled into colloidal assemblies before the calcination process.

Assembly into colloidal crystals and glasses

The colloidal crystals were obtained by slow evaporation of a concentrated particle dispersion (7 wt.%) in a Teflon beaker with a diameter of 2 cm under ambient conditions. To obtain colloidal glasses ~ 1 mL ammonia hydroxide solution was added in several steps during the evaporation process.

Characterization methods

TEM measurements were performed with a JEOL JEM-2200FS energy filtered electron microscope operated at an acceleration voltage of 200 kV. Zero-loss filtered images ($\Delta E \sim 0$ eV) were recorded with a bottom mounted CMOS camera system (OneView, Gatan) and processed DM 3.11 image processing software (Gatan).

SEM images were taken on a Zeiss Leo 1530 instrument using InLens SE detection as well as Everhart-Thornley detection at acceleration voltages of 2 and 3 kV.

SAXS data were measured using the small-angle X-ray system Double Ganesha AIR (SAXSLAB). The X-ray source of this laboratory-based system is a rotating copper anode (MicroMax 007HF, Rigaku Corporation) providing a micro-focused beam at $\lambda = 0.154$ nm. The data were recorded by a position-sensitive detector (PILATUS 300 K, Dectris). To cover the range of scattering vectors between 0.026 and 2.6 nm^{-1} different detector positions were used. The measurement was performed at room temperature, using a powder of hollow silica nanoparticles packed in a capillary tube. The scattering data were evaluated with a vesicle fit in the program SCATTER.[27]

Nitrogen sorption measurements were recorded on a Quantachrome Autosorb AS-1 pore analyzer at 77 K. All samples were preconditioned in vacuum at 350 °C for 12 hours before the measurements. For the data evaluation, the Quantachrome ASiQ v3.0 software was used. The specific surface areas were calculated using the Brunauer-Emmett-Teller (BET) method. Pore volumes and pore size distributions were obtained by applying the nonlocal density functional theory (NLDFT) adsorption branch model for silica materials with cylindrical pore geometry.

Differential scanning calorimetry (DSC) measurements were carried out using a Discovery DSC 2500 (TA Instruments). Compressed powders of the hollow spheres (10 – 16 mg) were scanned in covered aluminum pans under a dry nitrogen purge of 50 mLmin^{-1} over a temperature range from -50 to 210 °C with a heating rate of 20 °Cmin^{-1}. The heat capacity was determined according to the ASTM E1269 standard test method using a standard sapphire sample. Two heating cycles on each sample were conducted. For the evaluation, the second heating cycle was used.

Thermal diffusivity measurements of the colloidal crystals were performed on an XFA 500 XenonFlash apparatus (Linseis) equipped with an InSb infrared detector. Before the measurements, the samples were coated with a thin graphite layer (approx. 15 µm) on each side to ensure a good absorbance at the bottom and a high emissivity at the top side of the sample. The thickness of the graphite layer is negligible compared to the thickness of the colloidal crystals (600 – 1100 µm). The samples were preconditioned at 200 °C for 15 min in vacuum to eliminate any potential contribution from intercalated water inside the silica network. The measurements were performed on at least three samples at 25 °C in vacuum (~0.05 mbar), helium (1 – 1000 mbar), nitrogen (~1000 mbar), and air (~1000 mbar). The pressure-dependent measurements in helium are possible by controlling ventilation valves and two pressure gauges (coarse and fine vacuum). The received data were evaluated by the software AproSoft Laser Flash Evaluation v1.06 using the radiation fit model (see Figure S7.4).

The thicknesses of the colloidal crystals were determined with a Litematic VL-50 (Mitutoyo).

The density of the colloidal crystals was determined from the mass and volume of the monoliths. The volume was measured using a 3D digital surface profiler (Keyence V-3100) and the mass was determined by weighing the colloidal crystals.

7.5 Acknowledgements

This project was funded by a Lichtenberg Professorship provided by the Volkswagen foundation. PR acknowledges support by the Elite Network Bavaria (ENB). Anna Lechner and Fabian Nutz are acknowledged for DSC measurements. Markus Drechsler is acknowledged for TEM measurements. Additional support was provided by the SFB840 and DFG project RE3550/2-1.

7.6 References

1. Losego, M. D.; Blitz, I. P.; Vaia, R. A.; Cahill, D. G.; Braun, P. V., Ultralow Thermal Conductivity in Organoclay Nanolaminates Synthesized via Simple Self-Assembly. *Nano Lett.* **2013,** *13* (5), 2215-2219.

2. Suh, K. W.; Park, C. P.; Maurer, M. J.; Tusim, M. H.; Genova, R. D.; Broos, R.; Sophiea, D. P., Lightweight Cellular Plastics. *Adv. Mater.* **2000,** *12* (23), 1779-1789.

3. Jelle, B. P., Traditional, state-of-the-art and future thermal building insulation materials and solutions – Properties, requirements and possibilities. *Energ. Buildings* **2011,** *43* (10), 2549-2563.

4. Kistler, S. S., Coherent Expanded-Aerogels. *J. Phys. Chem.* **1931,** *36* (1), 52-64.

5. Fricke, J.; Emmerling, A., Aerogels. *J. Am. Ceram. Soc.* **1992,** *75* (8), 2027-2035.

6. Fricke, J.; Tillotson, T., Aerogels: production, characterization, and applications. *Thin Solid Films* **1997,** *297* (1–2), 212-223.

7. Fricke, J.; Emmerling, A., Aerogels. *Adv. Mater.* **1991,** *3* (10), 504-506.

8. Hüsing, N.; Schubert, U., Aerogels—Airy Materials: Chemistry, Structure, and Properties. *Angew. Chem. Int. Ed.* **1998,** *37* (1-2), 22-45.

9. Thapliyal, P. C.; Singh, K., Aerogels as Promising Thermal Insulating Materials: An Overview. *J. Mater.* **2014,** *2014,* 10.

10. Cahill, D. G.; Ford, W. K.; Goodson, K. E.; Mahan, G. D.; Majumdar, A.; Maris, H. J.; Merlin, R.; Sr, P., Nanoscale thermal transport. *J. Appl. Phys.* **2003,** *93* (2), 793-818.

11. Cahill, D. G.; Braun, P. V.; Chen, G.; Clarke, D. R.; Fan, S. H.; Goodson, K. E.; Keblinski, P.; King, W. P.; Mahan, G. D.; Majumdar, A.; Maris, H. J.; Phillpot, S. R.; Pop, E.; Shi, L., Nanoscale thermal transport. II. 2003-2012. *Appl. Phys. Rev.* **2014,** *1* (1).

12. Ruckdeschel, P.; Kemnitzer, T. W.; Nutz, F. A.; Senker, J.; Retsch, M., Hollow silica sphere colloidal crystals: insights into calcination dependent thermal transport. *Nanoscale* **2015,** *7* (22), 10059-10070.

13. Nutz, F. A.; Ruckdeschel, P.; Retsch, M., Polystyrene colloidal crystals: Interface controlled thermal conductivity in an open-porous mesoparticle superstructure. *J. Colloid Interf. Sci.* **2015,** *457*, 96-101.

14. Gao, T.; Jelle, B. P.; Sandberg, L. I. C.; Gustavsen, A., Monodisperse Hollow Silica Nanospheres for Nano Insulation Materials: Synthesis, Characterization, and Life Cycle Assessment. *ACS Appl. Mater. Inter.* **2013,** *5* (3), 761-767.

15. Xia, Y.; Gates, B.; Yin, Y.; Lu, Y., Monodispersed Colloidal Spheres: Old Materials with New Applications. *Adv. Mater.* **2000,** *12* (10), 693-713.

16. Aguirre, C. I.; Reguera, E.; Stein, A., Tunable Colors in Opals and Inverse Opal Photonic Crystals. *Adv. Funct. Mater.* **2010,** *20* (16), 2565-2578.

17. Barako, M. T.; Sood, A.; Zhang, C.; Wang, J.; Kodama, T.; Asheghi, M.; Zheng, X.; Braun, P. V.; Goodson, K. E., Quasi-ballistic Electronic Thermal Conduction in Metal Inverse Opals. *Nano Lett.* **2016,** *16* (4), 2754-2761.

18. Ma, J.; Parajuli, B. R.; Ghossoub, M. G.; Mihi, A.; Sadhu, J.; Braun, P. V.; Sinha, S., Coherent Phonon-Grain Boundary Scattering in Silicon Inverse Opals. *Nano Lett.* **2013,** *13* (2), 618-624.

19. Albrecht, J. D.; Knipp, P. A.; Reinecke, T. L., Thermal conductivity of opals and related composites. *Phys. Rev. B* **2001,** *63* (13), 134303.

20. Nutz, F. A.; Retsch, M., Interfacial and Volumetric Sensitivity of the Dry Sintering Process of Polymer Colloidal Crystals: A Thermal Transport and Photonic Bandgap Study. *Physical Chemistry Chemical Physics* **2017**.

21. Ma, H.-Y.; Tong, L.-F.; Xu, Z.-B.; Fang, Z.-P., Functionalizing Carbon Nanotubes by Grafting on Intumescent Flame Retardant: Nanocomposite Synthesis, Morphology, Rheology, and Flammability. *Adv. Funct. Mater.* **2008,** *18* (3), 414-421.

22. Dong, L.; Hu, C.; Song, L.; Huang, X.; Chen, N.; Qu, L., A Large-Area, Flexible, and Flame-Retardant Graphene Paper. *Adv. Funct. Mater.* **2016,** *26* (9), 1470-1476.

23. Bourbigot, S.; Duquesne, S., Fire retardant polymers: recent developments and opportunities. *J. Mater. Chem.* **2007,** *17* (22), 2283-2300.

24. Goodwin, J. W.; Hearn, J.; Ho, C. C.; Ottewill, R. H., Studies on the preparation and characterisation of monodisperse polystyrene laticee. *Colloid Polym. Sci.* **1974,** *252* (6), 464-471.

25. Graf, C.; Vossen, D. L. J.; Imhof, A.; van Blaaderen, A., A General Method To Coat Colloidal Particles with Silica. *Langmuir* **2003,** *19* (17), 6693-6700.

26. Ruckdeschel, P.; Dulle, M.; Honold, T.; Förster, S.; Karg, M.; Retsch, M., Monodisperse hollow silica spheres: An in-depth scattering analysis. *Nano Res.* **2016,** *9* (5), 1366-1376.

27. Förster, S.; Apostol, L.; Bras, W., Scatter: software for the analysis of nano- and mesoscale small-angle scattering. *J. Appl. Crystallogr.* **2010,** *43* (3), 639-646.

28. Nunes dos Santos, W.; Mummery, P.; Wallwork, A., Thermal diffusivity of polymers by the laser flash technique. *Polym. Test.* **2005,** *24* (5), 628-634.

29. Wang, J.; Ahl, S.; Li, Q.; Kreiter, M.; Neumann, T.; Burkert, K.; Knoll, W.; Jonas, U., Structural and optical characterization of 3D binary colloidal crystal and inverse opal films prepared by direct co-deposition. *J. Mater. Chem.* **2008,** *18* (9), 981-988.

30. Haynes, W. M., *CRC Handbook of Chemistry and Physics, 97th Edition*. CRC Press: 2016.

31. Knudsen, M., Die molekulare Wärmeleitung der Gase und der Akkommodationskoeffizient. *Ann. Phys.* **1911,** *339* (4), 593-656.

32. Yin, J.; Retsch, M.; Thomas, E. L.; Boyce, M. C., Collective Mechanical Behavior of Multilayer Colloidal Arrays of Hollow Nanoparticles. *Langmuir* **2012,** *28* (13), 5580-5588.

33. Schiffres, S. N.; Kim, K. H.; Hu, L.; McGaughey, A. J. H.; Islam, M. F.; Malen, J. A., Gas Diffusion, Energy Transport, and Thermal Accommodation in Single-Walled Carbon Nanotube Aerogels. *Adv. Funct. Mater.* **2012,** *22* (24), 5251-5258.

34. Coquil, T.; Richman, E. K.; Hutchinson, N. J.; Tolbert, S. H.; Pilon, L., Thermal conductivity of cubic and hexagonal mesoporous silica thin films. *J. Appl. Phys.* **2009,** *106* (3).

35. Retsch, M.; Schmelzeisen, M.; Butt, H.-J.; Thomas, E. L., Visible Mie Scattering in Nonabsorbing Hollow Sphere Powders. *Nano Lett.* **2011,** *11* (3), 1389-1394.

36. Losego, M. D.; Grady, M. E.; Sottos, N. R.; Cahill, D. G.; Braun, P. V., Effects of chemical bonding on heat transport across interfaces. *Nat. Mater.* **2012,** *11* (6), 502-506.

7.7 Supporting Information

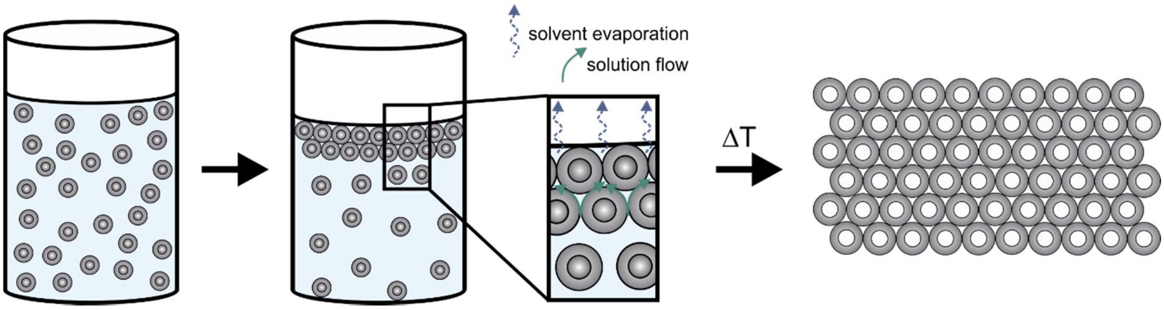

Scheme S7.1. Schematic illustration of the evaporation-induced self-assembly of core-shell particles and the subsequent calcination to obtain silica hollow sphere colloidal crystals.

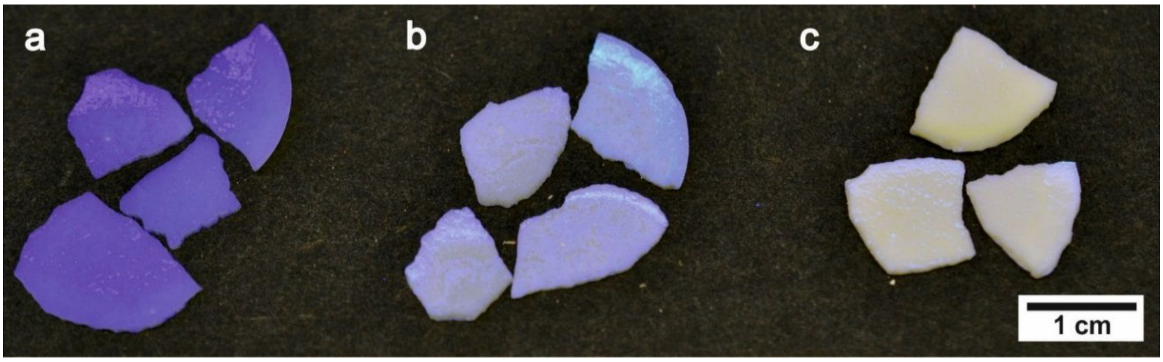

Figure S7.1. Photographic image of silica hollow sphere colloidal crystals with a particle diameter of ~270 nm and shell thicknesses of (a) 14 nm (HS-267/14), (b) 27 nm (HS-267/27), and (c) 40 nm (HS-266/40).

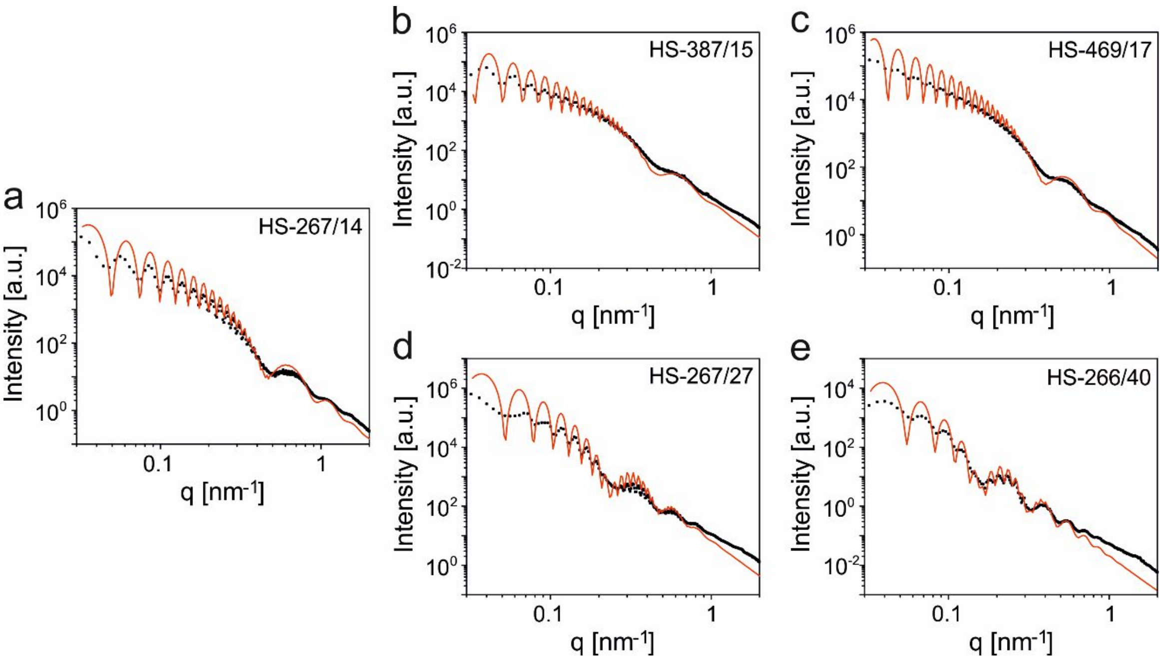

Figure S7.2. Small-angle X-ray scattering (SAXS) analysis of silica hollow nanospheres (black dots) and the corresponding fits using a form factor for spherical core-shell particles (red lines). (a, b, c) Size series, (a, d, e) Shell thickness series.

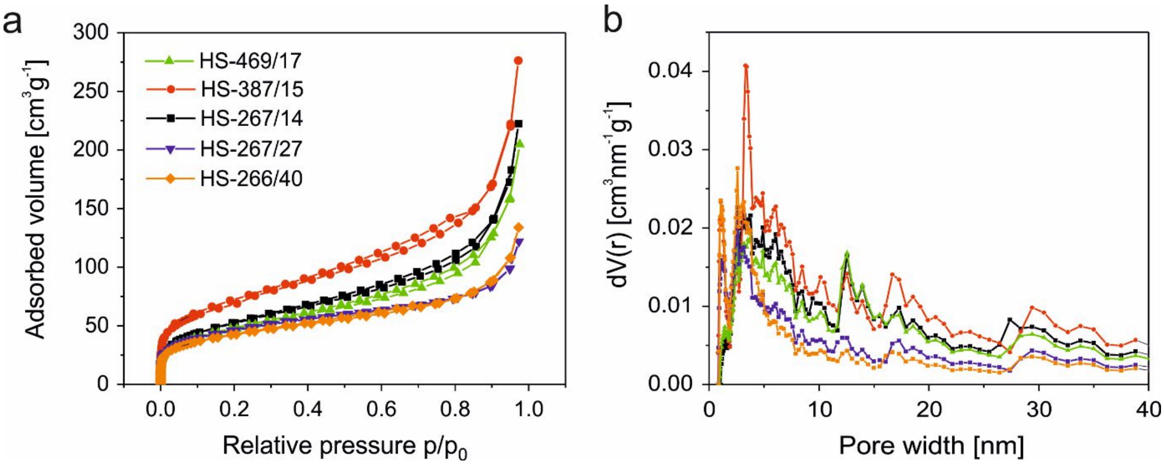

Figure S7.3. Nitrogen sorption data of silica hollow spheres. (a) Nitrogen adsorption/desorption isotherms, and (b) pore size distribution calculated by DFT method. The lines are a guide to the eye.

Table S7.1. Density of the silica shell considering the porosity.[a)]

	HS-469/17	HS-387/15	HS-267/14	HS-267/27	HS-267/40
Calculated density of the shell including meso- and micropores [gcm^{-3}]	1.68	1.52	1.83	1.93	1.81

[a)] Recalculation of the density of the silica shell: The density of the bulk silica measured by helium pycnometry gives a value of 2.2 gcm^{-3}. The bulk silica density has to be corrected due to the porosity of the shell. The recalculation is based on a 74 % volume filling and the geometric parameters of the individual silica spheres.

Table S7.2. Summary of data received from nitrogen sorption measurements.

	N_2 sorption measurements			
	BET surface [m^{2}g^{-1}]	**DFT surface [m^{2}g^{-1}]**	**Pore volume [cm^{3}g^{-1}]**	**Pore size [nm]**
HS-469/17	169.4	142.1	0.30	3.8
HS-387/15	246.3	224.9	0.41	3.3
HS-267/14	184.8	155.0	0.33	2.6
HS-267/27	152.2	136.1	0.20	2.6
HS-266/40	164.5	147.4	0.18	2.6

Table S7.3. Voids in silica hollow sphere colloidal crystals with a packing parameter of 74 %.

Voids	**HS-469/17-c**	**HS-387/15-c**	**HS-267/14-c**
Octahedral	194 nm	160 nm	110 nm
Tetrahedral	105 nm	87 nm	60 nm
Exchange sites	72 nm	60 nm	41 nm

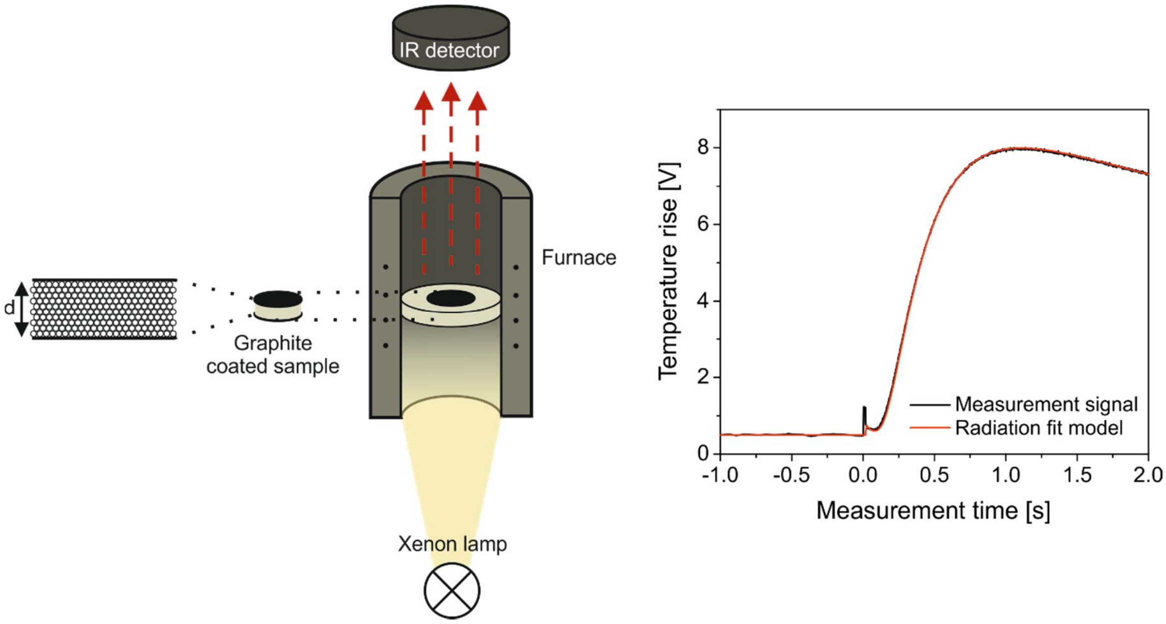

Figure S7.4. a) Schematic setup of the xenon flash analysis (XFA), modified from Ruckdeschel *et al.*[12]. The setup allows controlling the surrounding atmosphere in a precise manner. The measurement chamber is closed during the measurement and holds vacuum conditions of about 0.05 mbar, which is limited by the gas-tightness of the sample chamber. We define this as "vacuum" measurement. Furthermore, we are able to supply air, nitrogen, or helium to the sample chamber. By using controlled ventilation valves and two pressure gauges (coarse and fine vacuum), we can control the respective gas pressure between 1 and 1000 mbar. b) Typical measurement signal of a hollow silica colloidal crystal modeled with a radiation fit. The radiation fit model represents an extension to the finite-pulse and heat loss corrections given by the Combined fit model from Dusza (L. Dusza, *High Temperatures – High Pressures*, **1995**, 27, 467-473). However, it allows for an amount of the Xenon flash to be directly transmitted to the rear sample surface, leading to an instantaneous temperature jump analogous to Blumm *et al.* (J. Blumm, J. Henderson, O. Nilsson and J. Fricke, *High Temperatures-High Pressures*, **1997**, 29, 555-560).

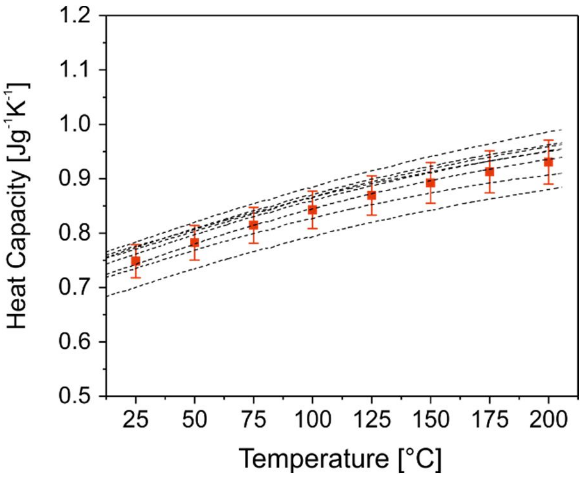

Figure S7.5. Differential scanning calorimetry (DSC) measurements of silica hollow spheres with different sizes and shell thicknesses (dotted lines) and the corresponding mean values calculated from the individual measurements (red squares). The mean heat capacity at 25 °C was found to be (0.748 ± 0.031) $Jg^{-1}K^{-1}$.

Finite element modeling of the thermal transport in HS colloidal crystals

The FEM software COMSOL Multiphysics (version 5.2.1.262) is used for modeling the thermal transport in silica hollow sphere colloidal crystals. For this, hollow spheres are arranged in a face-centered cubic (*fcc*) unit cell packing. The outer radius of the sphere is constant for all systems, while the shell thickness is varied to get the same shell thickness-to-radius ratios as for the synthesized systems (HS-469/17: 0.0704, HS-387/15: 0.0750, HS-267/14: 0.105, HS-267/27: 0.202, HS-266/40: 0.301). The unit cell edge length is chosen such that the contact (or overlap) area per particle is 0.6 % of the particle surface area, and therefore comparable to the experimental systems. For all simulations (except the data in Figure S7.9), the overlapping particles are fused into one object. Thus, no thermal resistance between the particles is considered. For the data plotted in Figure S7.9b, the thermal contact conductance between adjacent particles is varied between 10 and $10^6\,\mathrm{W\,m^{-2}K^{-1}}$. To study the influence of surrounding gas (helium or air) on the total heat conduction, the inverse hollow sphere volume is added. The geometry of the colloidal crystal HS-469/17-c is exemplarily shown in Figure S7.6.

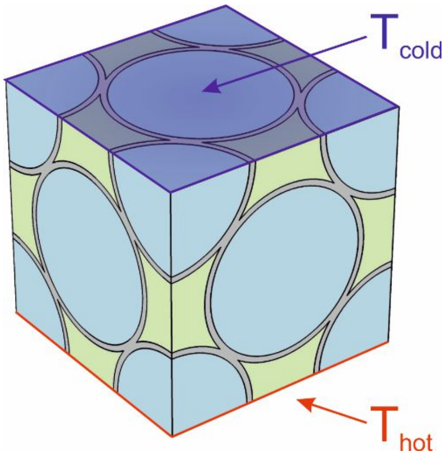

Figure S7.6. The unit cell of the silica hollow sphere colloidal crystal HS-469/17-c. The different colors show the different phases (gray: silica shell, blue: internal pore volume, green: outer pore volume). A constant hot (T_{hot}) and cold (T_{cold}) temperature is applied to the entire upper and lower face. The residual boundaries are thermally insulated. Thus, a temperature gradient forms, with a heat flux in the direction of the cold face.

Three materials, each with its own thermal conductivity, are assigned to the hollow silica colloidal crystal: silica, gas in open-pores, and gas in closed-pores. The properties of the materials are listed in Table S7.4 - Table S7.6. We used bulk material values, except for the gas thermal conductivity. This is justified by the amorphous microstructure of our material, where the thermal transport is governed by diffusive transport. The thermal contact between silica and gas is defined either as a union (no thermal resistance) or with a certain thermal contact conductance h_c (0, 40, and 200 Wm^{-2}K^{-1}). For the simulation, a constant temperature is applied to the lower (T_{hot}) and upper (T_{cold}) face of the unit cell. This defines the temperature gradient across the hollow sphere structure and serves at the same time as heat source and heat sink, respectively. Thermal insulation boundary conditions are imposed on all other surfaces of the unit cell. To obtain the effective thermal conductivity κ_{eff}, the integrated heat flux normal to the upper surface is evaluated. Then, the effective thermal conductivity is calculated using Fourier's equation of heat conduction:

$$\kappa_{eff} = \frac{Q/A}{\Delta T/h} \tag{S7.1}$$

where Q is the heat flow rate normal to the cross-sectional area A of the unit cell, ΔT the temperature difference ($T_{hot} - T_{cold}$), and h the unit cell edge length.

The mesh is chosen fine enough to ensure mesh size independent thermal conductivity values. Detailed information on the FEM simulations is given in the respective figure and table captions.

Table S7.4. Specific heat capacity, density, and thermal conductivity used in FEM simulations.***Table S7.6***

	COMSOL input values		
	Specific heat capacity [Jg^{-1}K^{-1}]	**Density [kgm^{-3}]**	**Thermal conductivity** [mWm^{-1}K^{-1}]
Silica	0.748	2203	331$^{a)}$
Helium	5.195$^{b)}$	0.1615$^{b)}$	Table S7.5
Air	1.005$^{c)}$	1.1845$^{c)}$	Table S7.5

*$^{a)}$ The thermal conductivity of silica is chosen such that for HS-469/17-c (without gas) the same effective thermal conductivity is obtained as experimentally in vacuum, $^{b)}$ The specific heat capacity and density of helium at 1000 mbar and 25 °C was calculated according to Petersen (H. Petersen, The Properties of Helium: Density, Specific Heats, Viscosity, and Thermal Conductivity at Pressures from 1 to 100 Bar and from Room Temperature to about 1800 K, Jul. Gjellerup, **1970**), $^{c)}$ The specific heat capacity and density of air at 1000 mbar and 25 °C was calculated according to Dixon (J. C. Dixon, in The Shock Absorber Handbook, DOI: 10.1002/9780470516430.app2, John Wiley & Sons, Ltd **2007**, p. 375ff.).*

Table S7.5. Pore size-dependent thermal conductivity κ of helium and air in the closed- and open-pores used in the FEM simulations for the determination of the effective thermal conductivity of silica hollow spheres colloidal crystals (see Figure 7.4a and b) as well as for the plot of the heat flux density and streamlines (see Figure 7.4c and Figure S7.7b).$^{a)}$

	Helium		***Air***	
	$\kappa_{\mathrm{He(ClosedPores)}}$ **[mWm^{-1}K^{-1}]**	$\kappa_{\mathrm{He(OpenPores)}}$ **[mWm^{-1}K^{-1}]**	$\kappa_{\mathrm{Air(ClosedPores)}}$ **[mWm^{-1}K^{-1}]**	$\kappa_{\mathrm{Air(OpenPores)}}$ **[mWm^{-1}K^{-1}]**
HS-469/17-c	94.9	50.2	20.9	14.8
HS-387/15-c	87.6	44.1	20.2	13.6
HS-267/14-c	72.2	33.7	18.3	13.7
HS-267/27-c	67.9	33.7	17.7	13.7
HS-266/40-c	62.8	33.6	17.0	13.7

*$^{a)}$ The pore size-dependent thermal conductivity for a pressure of 1000 mbar and a temperature of 25 °C is calculated according to Schiffres et al. (S. N. Schiffres, K. H. Kim, L. Hu, A. J. H. McGaughey, M. F. Islam, J. A. Malen, Adv. Funct. Mater. **2012**, 22, 5251). The pore size of the closed-pores is the inner diameter of the hollow spheres. An average thermal conductivity for the open-pores is calculated from the averaged size of the tetrahedral and octahedral voids (see Table S7.3).*

Table S7.6. Thermal conductivity of helium used in FEM simulations for the plot of heat flux density and streamlines of particle system HS-469/17-c (see Figure S7.7a). Here, the same thermal conductivity of helium is used for the closed- and open-pores.[a]

	Helium		
	$\kappa_{He(bulk)}$ [mWm^{-1}K^{-1}]	**$\kappa_{He(436nm)}$ [mWm^{-1}K^{-1}]**	**$\kappa_{He(135nm)}$ [mWm^{-1}K^{-1}]**
HS-469/17-c	153.2	94.9	50.2

[a] The pore size-dependent thermal conductivity for a pressure of 1000 mbar and a temperature of 25 °C is calculated according to Schiffres et al. (S. N. Schiffres, K. H. Kim, L. Hu, A. J. H. McGaughey, M. F. Islam, J. A. Malen, Adv. Funct. Mater. ***2012****, 22, 5251).*

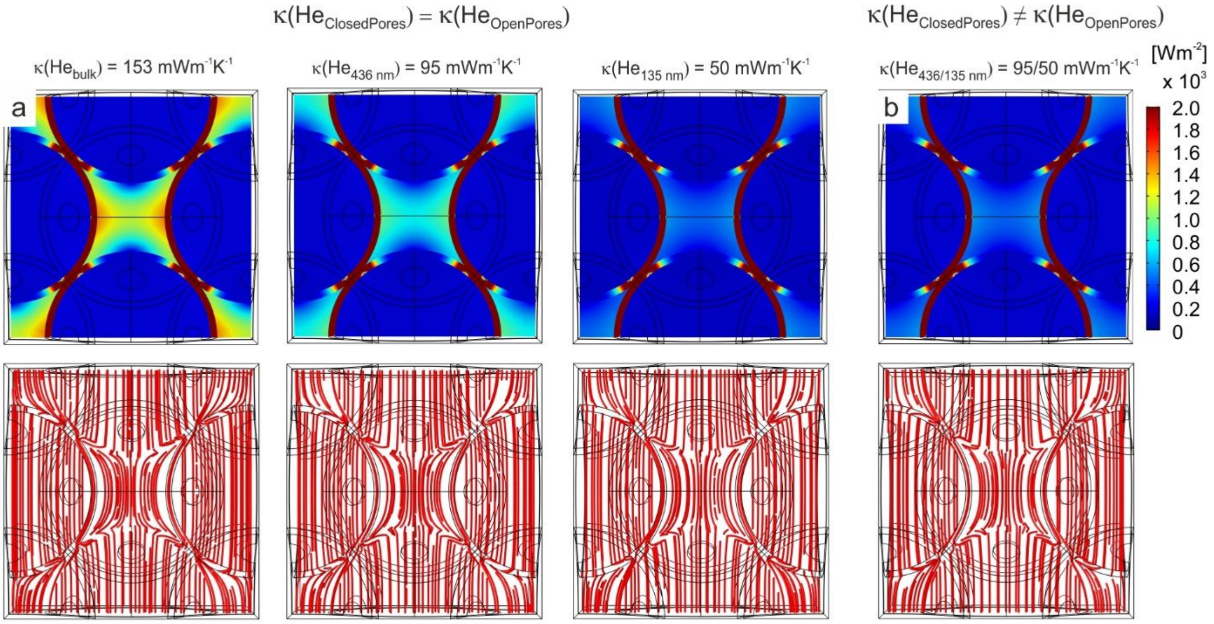

Figure S7.7. Finite element method modeling: Heat flux density (top) and streamlines (bottom) of particle assembly HS-469/17-c with a thermal contact conductance h_c of 40 Wm^{-2}K^{-1} between the silica network and helium. (a) The thermal conductivity of helium is varied (see Table S7.6), with the same thermal conductivity of helium being assumed for the closed- and open-pores. (b) Different thermal conductivity values of helium are applied for the closed- and open-pores (see Table S7.5), taking into account the different helium thermal conductivities in the closed- and open-pore volume due to the Knudsen effect. The integrated heat flux densities of the different phases are listed in Table S7.7.

Table S7.7. Integrated heat flux densities of silica, open-pore, and closed-pore volume of particle assembly HS-469/17-c. For the simulation, a thermal contact conductance h_c of 40 Wm^{-2}K^{-1} between the silica network and helium is used. The thermal conductivity of helium is varied to obtain the same (row 1-3) or different (row 4) helium thermal conductivities for the open- and closed-pore volume (see Table S7.6 and Table S7.5). The assumption of different thermal conductivities is the more realistic case due to different confinements, and thus Knudsen effects, present in a hollow sphere colloidal crystal.

	Silica		*Open-pores*		*Closed-pores*	
	Heat flux density		**Heat flux density**		**Heat flux density**	
	[MWm^{-1}]	[%]	[MWm^{-1}]	[%]	[MWm^{-1}]	[%]
$\kappa(He_{ClosedPores}) = \kappa(He_{OpenPores})$ $\kappa(He_{bulk}) =$ $153\ mWm^{-1}K^{-1}$	1.302	49.4	1.012	38.4	0.322	12.2
$\kappa(He_{ClosedPores}) = \kappa(He_{OpenPores})$ $\kappa(He_{436\ nm}) =$ $95\ mWm^{-1}K^{-1}$	1.303	58.2	0.635	28.3	0.303	13.5
$\kappa(He_{ClosedPores}) = \kappa(He_{OpenPores})$ $\kappa(He_{135\ nm}) =$ $50\ mWm^{-1}K^{-1}$	1.303	68.1	0.345	18.0	0.266	13.9
$\kappa(He_{ClosedPores}) \neq \kappa(He_{OpenPores})$ $\kappa(He_{436/135\ nm}) =$ $95/50\ mWm^{-1}K^{-1}$	1.302	66.8	0.345	17.7	0.302	15.5

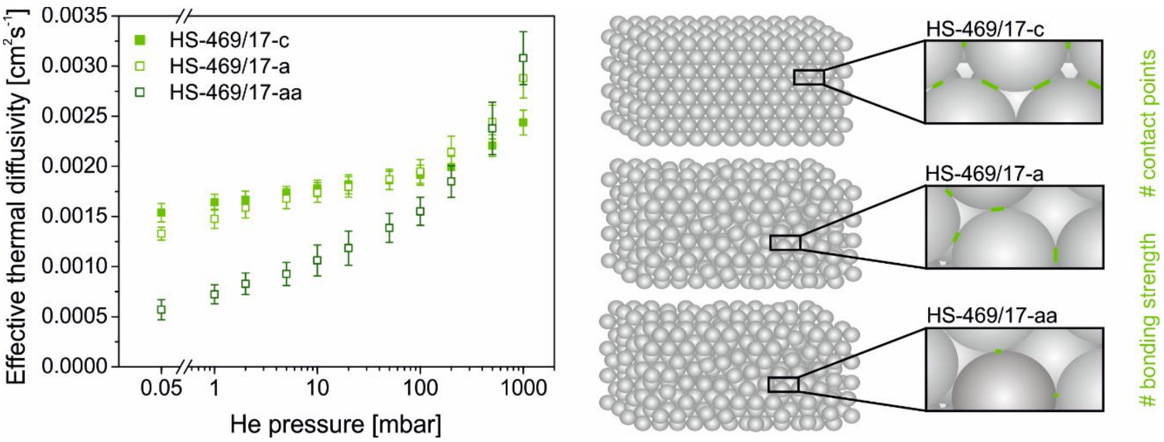

Figure S7.8. Thermal diffusivity of the colloidal assemblies HS-469/17-c/a with different amount of contact points and bonding strength.

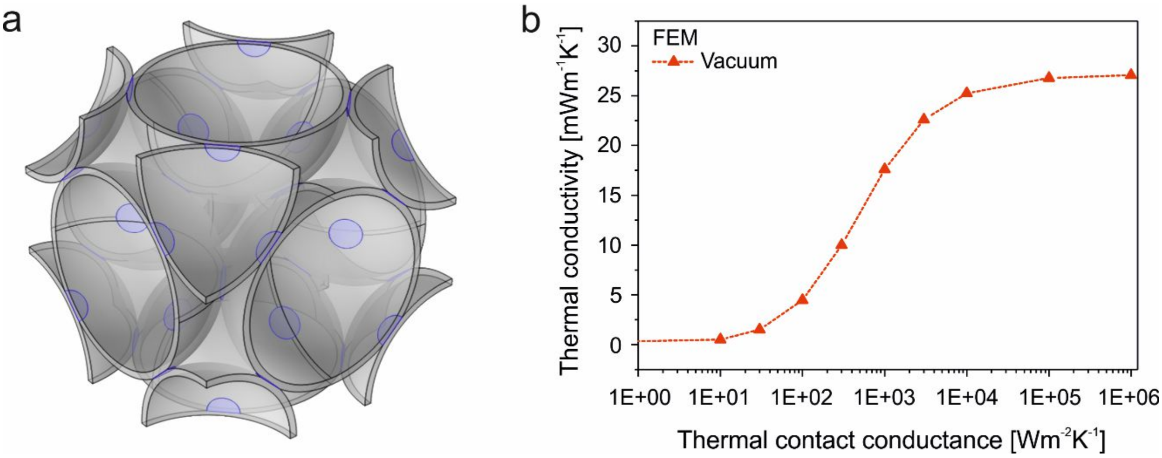

Figure S7.9. Finite element method modeling: (a) Unit cell of a face-centered cubic hollow silica sphere colloidal crystal (HS-469/17-c, without gas). The particles are not fused into one object. The blue circular areas mark the contact area between adjacent spheres. (b) Influence of the thermal contact conductance between the particles on the thermal conductivity.

8 Colloidal Crystals Consisting of Hollow Silica Sphere Colloidal Crystals: Insights into Calcination Dependent Thermal Transport

Pia Ruckdeschel, Tobias W. Kemnitzer, Fabian Nutz, Jürgen Senker, and Markus Retsch

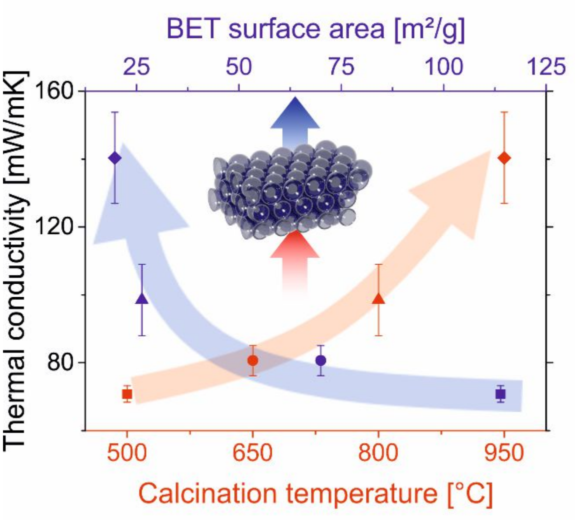

Reprinted with permission from Ruckdeschel *et al.*, *Nanoscale* **2015**, **7**, 10059-10070.

Abstract

Colloidal crystals consisting of monodisperse hollow silica spheres represent a well-defined porous material class, which features a range of interesting optical, mechanical, and thermal properties. These hierarchically structured materials comprise micropores within the silica network, which are confined to a thin shell (tens of nanometers) of a hollow sphere (hundreds of nanometers). Using simple calcination steps, we markedly change the internal microstructure, which we investigate by a multitude of characterization techniques, while the meso- and macrostructure remains constant. Most importantly the rearrangement of the silica condensation network leads to a reduction in total surface area and loss of micropores as demonstrated by N_2 sorption and hyperpolarized ^{129}Xe NMR studies. Spin-lattice relaxation shows a drastic increase of the rigidity of the amorphous network. These microstructural changes significantly influence the thermal conductivity through such a porous silica material. We demonstrate a remarkably low thermal conductivity of only 71 $\mathrm{mW\,m^{-1}\,K^{-1}}$ for a material of a comparatively high density of 1.04 $\mathrm{g\,cm^{-3}}$ at 500 °C calcination temperature. This thermal conductivity increases up to 141 $\mathrm{mW\,m^{-1}\,K^{-1}}$ at the highest calcination temperature of 950 °C. The great strength of hollow silica sphere colloidal crystals lies in its hierarchical structure control, which allows to further investigate how the internal microstructure and the interfacial contact points affect the transport of heat.

8.1 Introduction

Thermal insulation is an important and indispensable part of current strategies to lower our total energy consumption worldwide. For insulation applications most commonly highly porous materials are being used such as foams or mineral wool.[1] These materials feature thermal conductivities between 30 to 40 $\mathrm{mW\,m^{-1}\,K^{-1}}$ due to their combination of an amorphous matrix intercalated by a high volume fraction of air, both being poor heat conductors. Nevertheless, fairly thick layers (tens of cm) of these classic materials are necessary to achieve satisfactorily low values of the overall thermal transmittance for their application in structures and buildings.

Another well-investigated class of materials are silica aerogels.[2-4] Quite similar to polymeric foams, they comprise an amorphous skeleton and a particularly low density. The network is composed of amorphous silica, which is massively nanostructured by the presence of micro-, meso-, and macropores. Aerogels feature one of the lowest reported thermal conductivities of all material classes and can reach below $20\,\mathrm{mW\,m^{-1}\,K^{-1}}$. They can, therefore, be considered super-insulation materials, which could make their way into widespread applications.[5] From a scientific point of view, the total thermal conductivity κ of such an aerogel material is complex as it is influenced by four individual contributions.

$$\kappa_{total} = \kappa_{solid\ conduction} + \kappa_{gas} + \kappa_{radiation} + \kappa_{convection} \tag{8.1}$$

These individual contributions depend critically on the actual porosity and microstructure of the respective aerogel material. Details can be found in the literature,[1, 5-9] whereas we only want to give a short overview here. Convection is typically negligible due to the small pore sizes, which are present in aerogels. κ_{gas} greatly depends on the type of gas used to fill the free volume, which can take up to 99 % in aerogels. The pressure of the atmosphere determines this contribution, which is completely suppressed in vacuum. The dependence on the pressure of the atmosphere is expressed by the Knudsen formalism, which relates the mean free path of the gas molecule to the domain size of the pores, based on kinetic theory.[10-11] $\kappa_{radiation}$ depends on the temperature difference between the two surfaces of the aerogel monolith, the ambient temperature and the emissivity κ of these interfaces, which can be calculated using the Stefan-Boltzmann equation.[8, 12] Assuming that all pores are connected in series by air gaps, leads to a dependence on the pore size. Ideally, the contribution of thermal radiation becomes less with decreasing pore size. However, it has to be noted that pores much smaller than the wavelength of the IR radiation may be less effective in reducing this contribution.[1]

Furthermore, coupling between radiation and solid conduction can significantly alter the temperature distribution between the two material surfaces, which can result in higher contributions from thermal radiation.[8] Ways to suppress radiation contributions are given by the introduction of absorbing or reflecting moieties.[9, 12] $\kappa_{solid\ conduction}$ increases with increasing density. Thermal energy is transported along the amorphous silica network by vibrational modes, which can be classified into propagons (propagating and delocalized) and diffusons (nonpropagating and delocalized).[13-14] The third class of vibrational modes, locons (nonpropagating and localized), do not contribute significantly to thermal transport.[15] Whereas a full atomistic understanding of thermal transport through amorphous silica still has to be established, Larkin *et al.* calculated that the contribution from propagating modes amounts to only ~ 6 % of the total thermal conductivity.[15] At the same time, the thermal conductivity accumulation function saturates at a mean free path (MFP) of only 10 nm for amorphous SiO_2, which reflects in an independence of the thermal conductivity from the layer thickness of the amorphous film.[15] These calculations fit well to experimental data from Regner *et al.*, who used broadband frequency domain thermoreflectance to measure the thermal conductivity accumulation function.[16] More complicated systems, such as silica films with microporosity, however, are still elusive to be described by molecular dynamics or finite element simulations as shown by Coquil *et al.*[17]. Experimentally, no influence of the symmetry of the micropores was observed using the 3ω technique.[18] Considering the situation of silica aerogels, one has to further take the influence of thermal transport across interfaces into account, as the thermal energy has to diffuse through the individual nanoclusters.[19]

Even though much progress has been made to fabricate silica aerogels over the last decades, the mandatory supercritical drying step still presents an obstacle to their widespread use and implementation to other technologies.[2-3, 20] A work-around to this delicate processing step is possible by the use of hollow spheres, which can be used in a vast range of applications by themselves.[21] In particular hollow silica nanoparticles (HSNP) can be conveniently fabricated by a template polystyrene particle process and thereby allow access to monodisperse particles with adjustable size and porosity.[22] Monodisperse hollow silica particles feature intriguing properties such as a coloration effect caused by Mie resonance,[23] as well as rich mechanical properties, both as single spheres[22, 24] and in an ensemble structure.[25-26] Such particles can be processed by standard dispersion technologies into various nano- and mesostructured films or they can be turned into dry nanoparticle powders. Whereas the record low densities of aerogels are hard to achieve in order to retain the structural integrity of the hollow spheres, they yield well-defined porous materials, which comprise a hierarchy of length scales. The silica shell can be as thin as 10 nm with an additional microporosity in the silica network. The size of the particles typically ranges from 100 nm up to several µm, depending on the size of the templating sphere. All these can be adjusted on a single particle level, with an additional length scale and symmetry to be added upon assembling those colloidal building blocks, which can result in crystalline or amorphous meso- or macrostructures.

Despite their structural complexity and ease of fabrication, only little is known up to date on the thermal conductivity of ensembles of hollow silica spheres.[27-30] Previous studies showed indeed the low thermal conductivity of hollow silica powders in the range from 20 to 33 $\mathrm{mW\,m^{-1}\,K^{-1}}$. However, using the transient hot disk, the hotwire, or the 3ω technique, the authors did not specify details on the measurement parameters nor the micro- or mesostructure of the hollow sphere powder under consideration. In such granular materials, the contact points and adhesion between the spheres is of particular importance for the overall transport process along the silica network, as has been appreciated in previous studies, too.[19, 28] Here, we want to fully capitalize on the well-defined structure of colloidal crystals consisting of hollow spheres. Our aim is not to demonstrate a record-breaking ultralow thermal conductivity, but we want to introduce this material class as a platform to study the fundamentals of thermal transport in amorphous particle-based materials. Specifically, we want to answer the question how the internal microstructure of silica and the mutual contact points determine the thermal conductivity of the particle ensemble. We, therefore, measure specifically the thermal transport processes through the solid silica network by the laser flash technique

8.2 Results and Discussion

As outlined in the experimental section we utilize hollow spheres of 316 nm diameter and 44 nm shell thickness. These are prepared by coating a polystyrene (PS) template with silica and ensuing calcination of the core/shell structure. Decomposition of the PS core sets in at about 300 °C. For quantitative combustion of the PS core, calcination has been carried out at 500 °C for 12 h. Thermal elemental analysis confirmed the complete combustion process by a lack of carbon in the 500 °C calcined spheres (see Table S8.1 in the Supporting Information, Chapter 8.7). This is also confirmed by thermogravimetric analysis (TGA), where a loss of ~2 % is observed due to the removal of intercalated water (Figure S8.5). Another 1 % of mass is lost up to 950 °C, which can be attributed to the removal of trace amounts of silica condensation products like water. During this core-removal calcination step, the outer diameter of the core/shell sphere shrinks by about 2 % when transitioning into hollow spheres. Uniformity and monodispersity are most important for a good structural control of the individual particle, as well as for the ensemble into a colloidal crystal, which defines the neighboring contact points. Transmission electron microscopy (TEM) images demonstrate the size and shape of the hollow spheres (Figure 8.1a-d). One can deduce that the spheres remain fully intact during the calcination cycle, they do not feature any cracks or dents. From the projection in the TEM, the shell thickness can be measured, which is given by the dark shaded ring that surrounds the hollow core. The surface of the spheres appears smooth (Figure S8.1), and the particles do not form aggregates or clusters. No sinter necks between the spheres or clusters can be seen in the TEM image, but they are rather individually redispersed in ethanol and deposited on the carbon-coated TEM grid. Quite importantly, the hollow spheres demonstrate only a minor shrinkage of their diameter and shell thickness after being subjected to higher calcination temperatures up to 950 °C. As can be seen in Table 8.1, the diameter slightly shrinks from 316 to 310 nm, whereas the shell thickness remains almost constant at 44 nm. In order to further characterize the shape of the hollow spheres, we performed SAXS measurements (Figure S8.2a). A multitude of diffraction orders can be observed, which are fitted using the form factor of a vesicle. The data match well to the TEM measurement and further prove the monodispersity of the hollow spheres.

The functional properties of the hollow spheres only come into play when being assembled into a colloidal superstructure. We, therefore, used colloidal self-assembly of the core/shell particles as well as hollow spheres calcined at 950 °C, both dispersed in water, in order to fabricate macroscopic monoliths of highly ordered colloidal crystals. Simple drying in PTFE beakers for several days turned out to be the most efficient way to obtain suitable monoliths.

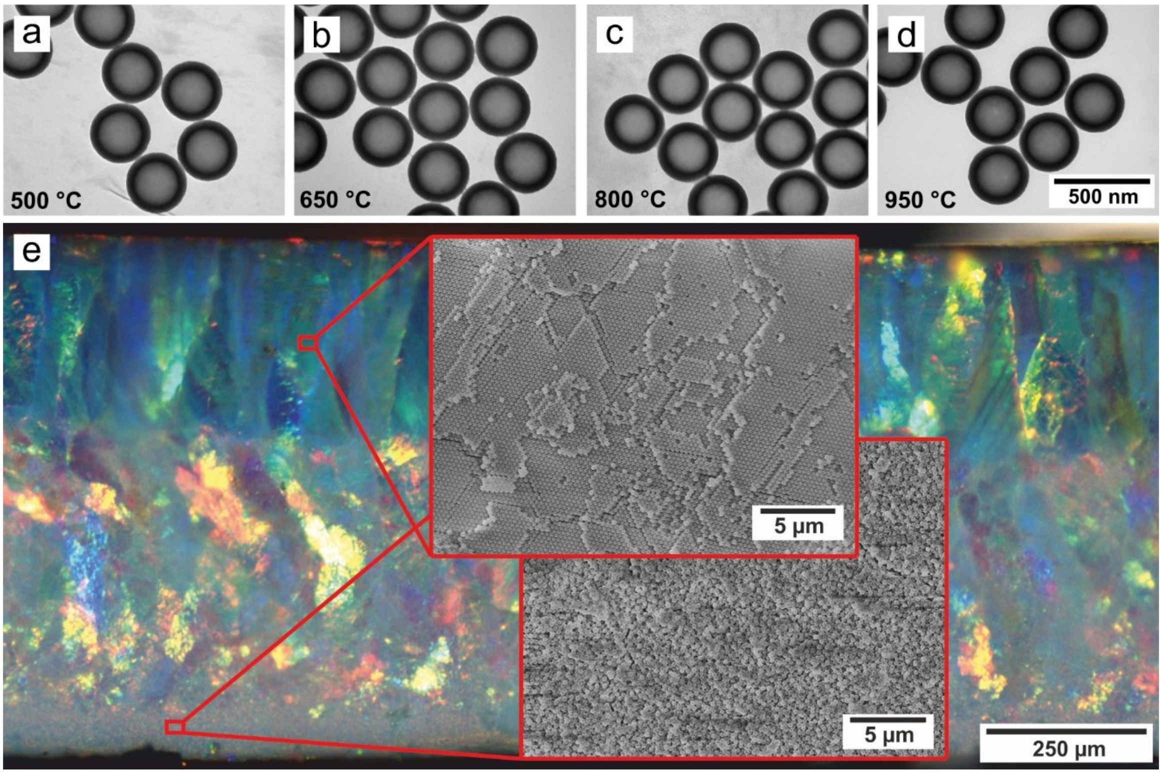

Figure 8.1. (a-d) TEM images of hollow silica nanoparticles at different calcination temperatures (500 - 950 °C). The particle dimensions remain constant for the various calcination temperatures and do not show any clustering. (e) Correlative light and electron microscope (CLEM) images of a HSNP colloidal crystal calcined at 500 °C. The bright colors are caused by coherent Bragg scattering. Most of the crystal is in a fully crystalline state as confirmed by the scanning electron microscopy (SEM) insets.

Figure 8.1e shows the side-view on a representative colloidal crystal after self-assembly from core/shell particles and calcination at 500 °C. The thicknesses of colloidal crystals under investigation here ranged from about 390 to 875 µm. Due to the particle size of 316 nm, the crystallinity of the colloidal crystal can be assessed by its bright opalescent colors. Different lattice orientations are exposed to the surface, which causes a multitude of colors observable in Figure 8.1e. We used correlative light and electron microscopy to determine the crystallinity of the hollow sphere monolith. Two specific areas are highlighted in Figure 8.1e. The top area with greenish opalescence constitutes highly ordered, hexagonal periodicities of the hollow spheres. Such areas expand over a large range as single crystalline domains. As can be inferred by the opalescence, the vast majority of the hollow sphere ensemble is fully crystalline. Only at the very bottom, the long-range crystalline order is compromised and the particles appear to be in a jammed state with only small crystallites persisting. Based on this study, we can safely assume that the volume fraction of the particles in the colloidal crystal is close to its ideal value of 74 %.

Table 8.1. Summary of data received from TEM, Pycnometry, and N_2 sorption measurements.

	TEM		**Density**	**N_2 sorption measurements** [c]			
	d **[nm]**	**t** **[nm]**	**ρ (CC)** [b] **[g/cm^3]**	**S_{BET}** **[m^2/g]**	**$V_{tot,DFT}$** **[cm^3/g]**	**$V_{mic,DFT}$** **[cm^3/g]**	**V_{mic}/V_{tot}** **[%]**
HS-500	316 ± 4	44 ± 2	1.044	113.9	0.101	0.028	27.4
HS-650	316 ± 4	43 ± 2	1.037	70.0	0.087	0.010	11.0
HS-800	314 ± 6	44 ± 2	1.050	26.3	0.053	0	0
HS-950	310 ± 4	43 ± 2	1.047	19.7	0.045	0	0

[a] *d: diameter, t: shell thickness;* [b] *Density of the colloidal crystal (CC) calculated using the density of the silica shell obtained from helium pycnometry measurements (ρ(SiO_2, shell) = 2.27 g/cm^3) and assuming an fcc packing fraction of 0.74;* [c] *S_{BET}: surface area calculated by using BET method, $V_{tot,DFT}$: total pore volume determined by using NLDFT model on silica at 77 K, $V_{mic,DFT}$: pore volume for pores with diameters smaller than 2 nm determined by using NLDFT model on silica at 77 K.*

This value represents an upper limit since the amorphous components will slightly lower the real volume fraction. In combination with He pycnometry measurements, which resulted in a density of the silica shells – independent of the calcination temperature – of $\rho_{\text{silica, shell}} = 2.27$ gcm^{-3}, we can calculate the effective density of the hollow spheres colloidal crystal. For the hollow spheres under consideration here, we obtain $\rho_{\text{HSNP, CC}} \approx 1.04$ gcm^{-3} (see Table 8.1).

Whereas the geometric structure of a colloidal crystal consisting of hollow sphere particles remains almost identical for a large range of calcination temperatures, the internal structure changes quite considerably. Therefore any changes to the thermal conductivity can be linked to the microstructure of the silica shell. This internal structure is characterized by a certain surface area, a porosity defined by micropores, as well as the degree of condensation and the rigidity of the SiO_x network. We used N_2 adsorption isotherms as well as hyperpolarized ^{129}Xe NMR spectroscopy to characterize the surface area and the pore size distribution within the silica shell (Figure 8.2). We find that the particles being calcined at 500 °C feature the largest BET surface area of about 114 m^{2}g^{-1}. Please note that we did not add any structure directing agents to the Stöber process to specifically increase the surface area or to template certain types or symmetries of micropores.[18] The isotherms do not show any pronounced hystereses and point towards the presence of micropores (steep slope at low p/p_0), mesopores of small diameter (shallow slope at intermediate p/p_0), and macropores (Figure 8.2a). Upon calcination at higher temperatures, these mixed isotherms change considerably. The surface area gradually decreases, leading to a BET surface area of only 19.7 m^{2}g^{-1} for the highest calcination temperature used in this study. Estimating the surface area of a hollow sphere powder of our particles leads to a slightly smaller surface area of 12.6 m^{2}g^{-1} when only the outer interface was accessible. Taking into account some surface roughness of the hollow spheres indicates that most of the silica shells are impassable for N_2 after calcination at 950 °C. The drop in surface area is accompanied by a loss of total pore volume (from 0.101 cm^{3}g^{-1} to 0.045 cm^{3}g^{-1}) and micropore volume (Figure 8.2c). In particular, no micropore volume can be derived from the N_2 isotherms at calcination temperatures beyond 800 °C anymore (Table 8.1).

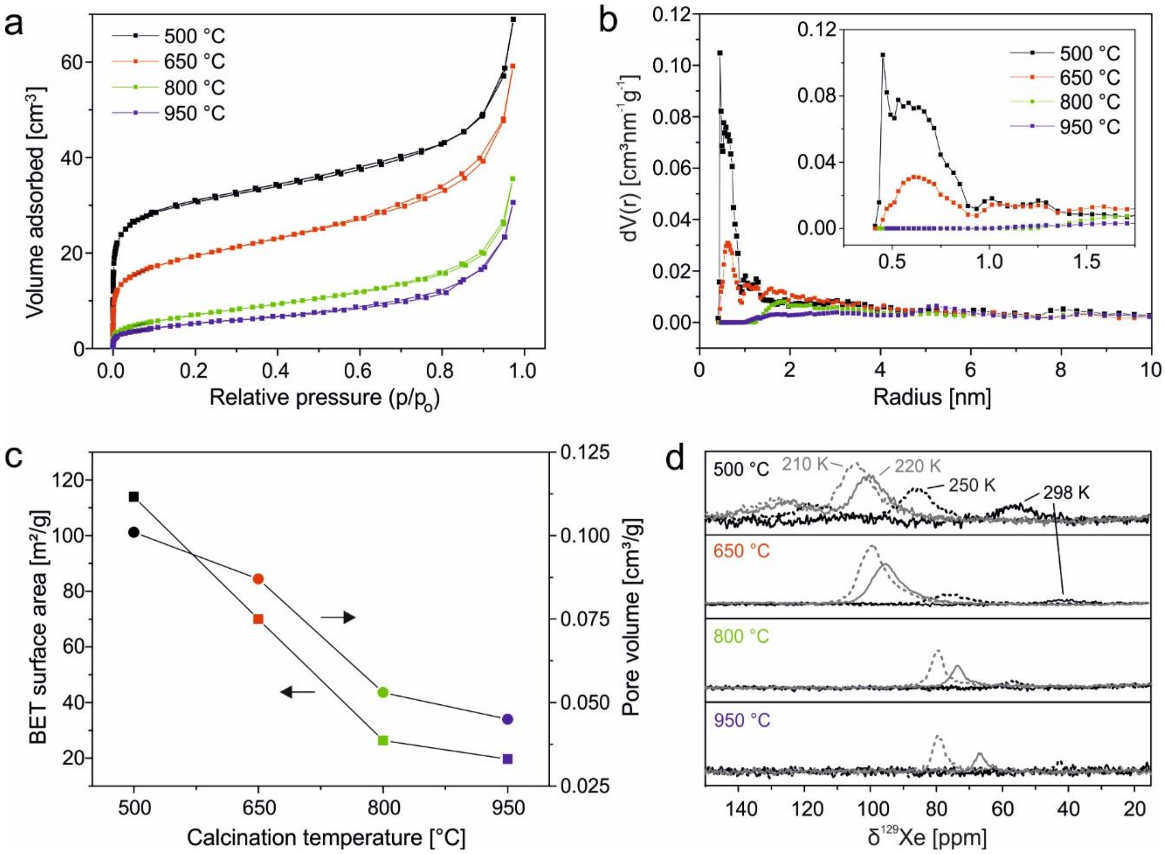

Figure 8.2. Internal structural characterization of hollow silica spheres in dependence of the calcination temperature: (a) Nitrogen adsorption and desorption isotherms measured at 77 K allow the determination of pore volume and surface area. (b) Pore radius distributions, calculated by applying NLDFT silica kernel based on a cylindrical pore model, indicate closure of the micropores at higher calcination temperatures. (c) BET surface area (squares) and pore volume (dots) as a function of calcination temperature. (d) ^{129}Xe NMR spectra of hyperpolarized xenon in silica hollow spheres as a function of the sample temperature. Even for the highest calcination temperatures a few micropores are still present in the silica shell.

The pore size distribution obtained by NLDFT analysis, shown in Figure 8.2b, confirms the closure of micropores of about 5 – 8 Å in radius. Exceeding the information accessible by N_2 sorption, the usage of hyperpolarized ^{129}Xe NMR reveals more details of the internal structure at the highest calcination temperatures (Figure 8.2d). Two trends become obvious in the ^{129}Xe spectra.

Considering the same measurement temperatures the signal intensity decreases with increasing calcination temperatures. This confirms the gradual closure of the micropores with increasing calcination temperature. From the limiting shifts $\delta(^{129}Xe) \sim 57$ ppm and 105 ppm determined at room temperature for the sample calcined at 500 °C two microporous cavities with diameters of 7 Å and 11 Å, respectively, were derived using the Fraissard model for cylindrical pore geometry (compare Table S8.2 in the Supporting Information, Chapter 8.7).[31] This is in good agreement with the pore radius distribution calculated from the N_2 sorption measurements. For all calcination temperatures, the ^{129}Xe signals shift high-field with increasing measurement temperature due to the reducing Xe-Xe interactions as the pores gradually empty. Although for higher calcination temperatures the limiting shift could not be determined experimentally at room temperature due to the decreasing intensity, this trend indicates that even at 800 °C and 950 °C calcination temperature some microporous cavities remain (Figure 8.2d). This is in line with the decreasing micropore volume derived from the sorption data.

The evolution of an asymmetry for the ^{129}Xe gas peak at 0 ppm for all calcination temperatures is in line with filling mesoporous cavities at lower measurement temperatures (Figure S8.3a).[32] These can be rationalized by the geometry of the contact points between adjacent spheres, which can be considered to be conical pores.

Despite the rearrangement, which happens during the high-temperature calcination, the SiO_2 network remains in its fully amorphous state. Powder XRD measurements on all four samples do not show any onset of crystallization (Figure S8.2b). Only broad halos, indicating the glassy state of the SiO_2 network, can be observed.

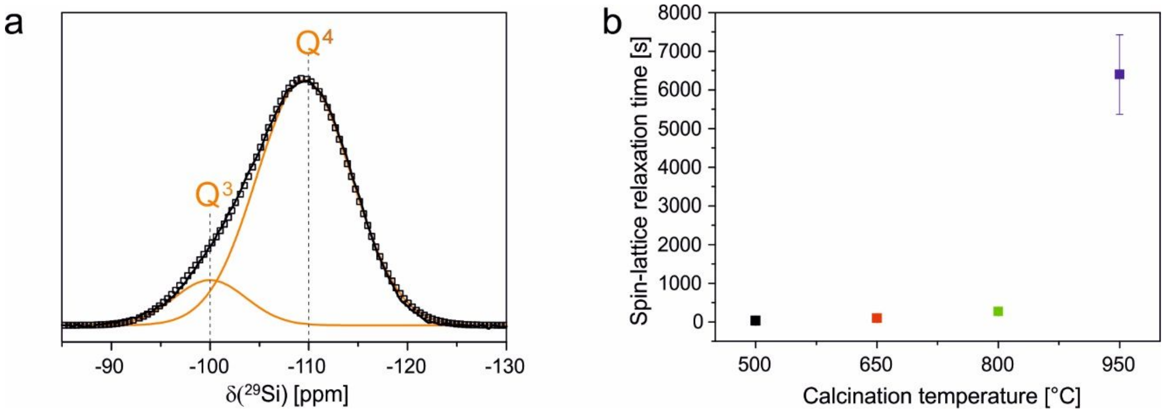

Figure 8.3. Internal structural characterization of hollow silica spheres. (a) Deconvoluted projection of the ^{29}Si spectrum of HSNP calcined at 500 °C; measured signal (black line), cumulative fit (open squares), simulated signals (orange lines), (b) Spin-lattice relaxation time of silica hollow spheres calcined at different temperatures. The closed symbols represent untreated and the open symbol pre-dried powder to remove water residues.

As demonstrated by Zhang *et al.*, silica networks obtained by the Stöber method predominantly consist of Si atoms, which are connected to three (Q^3) or four (Q^4) neighboring -O-Si- units. The ratio between Q^3 and Q^4 changes with increasing calcination temperature and ultimately leads to a fully condensed SiO_2 network.[24] We also characterized our hollow silica spheres by solid state MAS ^{29}Si NMR. The spectrum of a calcined sample at 500 °C is given in Figure 8.3a (the other spectra are shown in Figure S8.4). By deconvoluting the individual contributions from Q^3 and Q^4 using a pseudo-Voigt function, we determined the ratio of Q^4 to be already 88 % in the 500 °C sample. This ratio increases up to 94 % for the case of 950 °C calcination (Table S8.2 in the Supporting Information, Chapter 8.7). It demonstrates a certain degree of rearrangement within the SiO_2 network upon exposure to higher temperatures, yet the size of the particles stays constant. More prominently are the concomitant changes in the spin-lattice relaxation time T_1 (Figure 8.3b). We measured an increase from about 33 s for the hollow spheres calcined at 500 °C up to 6400 s for the highest calcination temperature. This clearly hints towards an increase of the rigidity of the still amorphous silica network, which may also improve the thermal transport capabilities. We confirmed that T_1 is almost independent of the amount of adsorbed water. This was observed at low calcination temperatures by ^{1}H NMR studies (Figure S8.3b). Whereas the broad water peak vanishes in the ^{1}H NMR after the drying procedure, the T_1 changes from 33 s to 20 s for the untreated and pre-dried samples calcined at 500 °C (compare Table S8.2 in the Supporting Information, Chapter 8.7).

All these changes to the internal structure (surface area reduction, closure of micropores, increase of Q^4 content and increase of rigidity) happen simultaneously during calcination and are depicted in Figure 8.4.

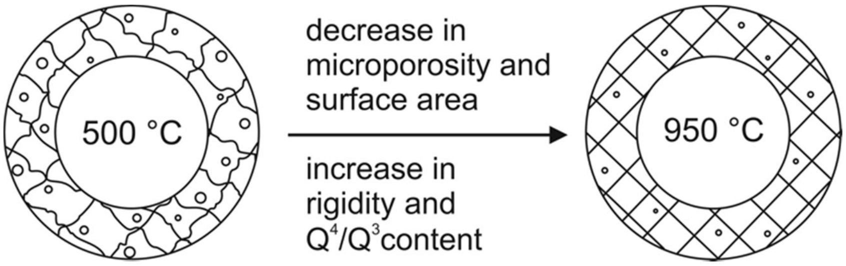

Figure 8.4. Schematic representation of the internal structural changes upon high-temperature calcination.

Besides the marked changes to the internal structure of the silica shell, the contact area between adjacent spheres can also be largely influenced by higher calcination temperatures. Colloidal crystals, with a hexagonally close-packed structure, feature twelve neighboring spheres around each particle. In vacuum, the thermal energy through such a colloidal structure can only be transported along the SiO_2 network. Therefore the contact points between adjacent spheres play a paramount role. Concomitantly to the changes of the internal structures, the degree of condensation between two spheres at the contact area is also likely to increase. These subtle changes, however, cannot be characterized or quantified, due to the small amount of atoms involved. From the SEM images (Figure S8.1) we can merely deduce that the contact points between the spheres increase slightly from (46 ± 13) nm at 500 °C to (64 ± 12) nm at 950 °C. In order to separate these two contributions to thermal transport (internal structural changes and contact area changes), we conducted two separate sets of experiments. In the first one, we assembled a colloidal crystal from core/shell particles. After calcination at 500 °C we obtained the hollow sphere colloidal crystal. This monolith was repeatedly characterized after calcination at different temperatures of 650 °C, 800 °C and 950 °C for 12 hours (solid symbols in Figure 8.6b). This experiment is sensitive to both types of internal and interfacial changes at the same time. In the second experiment, we self-assembled hollow silica spheres from an aqueous dispersion, which have beforehand been subjected to calcination at 950 °C. These hollow spheres featured a surface area of roughly 20 m^2g^{-1}, similar to the 950 °C calcined particles of the first experiment, indicating a comparable internal structure. Analogously to the samples of the first experiments (compare Figure 8.1e) a colloidal crystal with large monocrystalline areas was obtained (see Figure S8.8). The degree of crystallinity decreases from top to bottom with some amorphous areas at the lower end. The samples of this set of experiment are only sensitive to changes in the interfacial contact areas since the internal structure already resembles a highly condensed network with small surface area and closed micropores. Annealing of this colloidal crystal at elevated temperatures will consequently only strengthen the interfacial contact points but will leave the internal structure unaffected. By these two sets of experiments (calcined and annealed colloidal crystals), we can differentiate between contributions made from the internal structure and interfacial changes.

We performed xenon flash analysis (XFA) on both types of hollow sphere colloidal crystals. The principle of measurement is depicted in Figure S8.6. A typical measurement along with its fit is provided in Figure 8.5a (further XFA measurement are shown in Figure S8.7 in Chapter 8.7 along with a description of the radiation fit model). At first, we investigated the temperature-dependent thermal diffusivity of a hollow sphere colloidal crystal from room temperature up to 200 °C (note that this sample has been calcined at 500 °C, and was stored at ambient laboratory conditions). The heating and cooling cycles are identical after the initial pre-conditioning as outlined in the experimental section (Figure S8.7b). The pre-conditioning removes adsorbed water in the silica shell (compare ^1H NMR of HSNP calcined at 500 °C in Figure S8.3b). We conducted our experiments on at least three distinct samples of the hollow sphere colloidal crystals, each varying slightly with respect to the overall sample thickness. Figure 8.5b shows only a small increase in thermal diffusivity α in the temperature range from 25 °C to 200 °C. Using the equation

$$\kappa = \alpha \cdot \rho \cdot c_p \tag{8.2}$$

the thermal conductivity κ can be calculated. As demonstrated above, the density ρ of the silica shell and therefore of the hollow sphere colloidal crystal does not change within this temperature range and stays almost constant up to calcination temperatures of 950 °C. The uncertainty of the density determination is about 9 %.

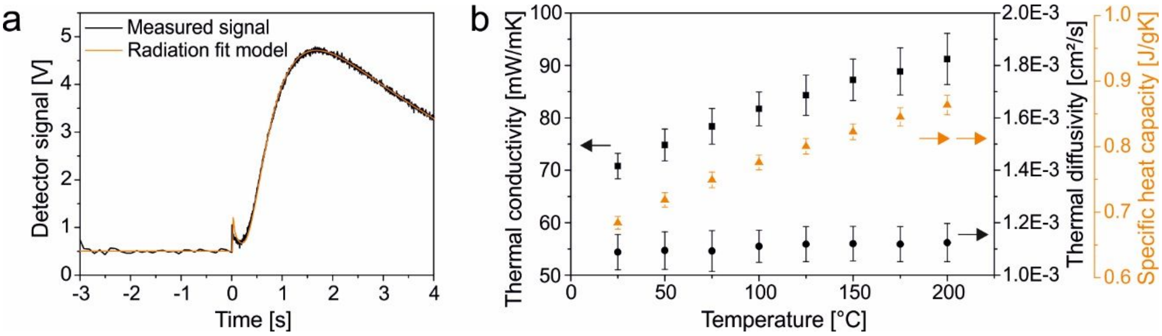

Figure 8.5. LFA measurements of HSNP calcined at 500 °C. (a) Measured signal (black line) with radiation fit model (orange line). (b) Summary of the necessary input parameters (thermal diffusivity – black circles and mean specific heat capacity – orange triangles) to determine the thermal conductivity (black squares).

Since we conduct our measurements in vacuum, we use the c_p obtained from DSC measurements of the silica shell (from compacted hollow spheres). The specific heat capacity shows a monotonic increase in the temperature range of interest but is hardly influenced by the calcination temperature (see Figure S8.5b). We, therefore, used the same average temperature dependent c_p for all samples under consideration here, which is close to the literature value of quartz glass ($c_p = 0.73\ \mathrm{Jg^{-1}K^{-1}}$).[33] The standard deviation of the c_p amounts to about 2 %. The slightly reduced c_p of our silica shell could be attributed to a small amount of porosity and differences in the network condensation, compared to fused quartz glass reported in the literature. Combining the individual uncertainties of the thermal diffusivity, density, and specific heat, we find that the determination of κ is accurate to within ± 5 - 13 % for an individual measurement. Variations from sample to sample during the different calcination steps can be therefore regarded as the main source of error (details are reported in the Supporting Information (Chapter 8.7): uncertainty analysis of the thermal conductivity determination). We, therefore, show the average values and standard deviation of at least three independent samples in Figure 8.6.

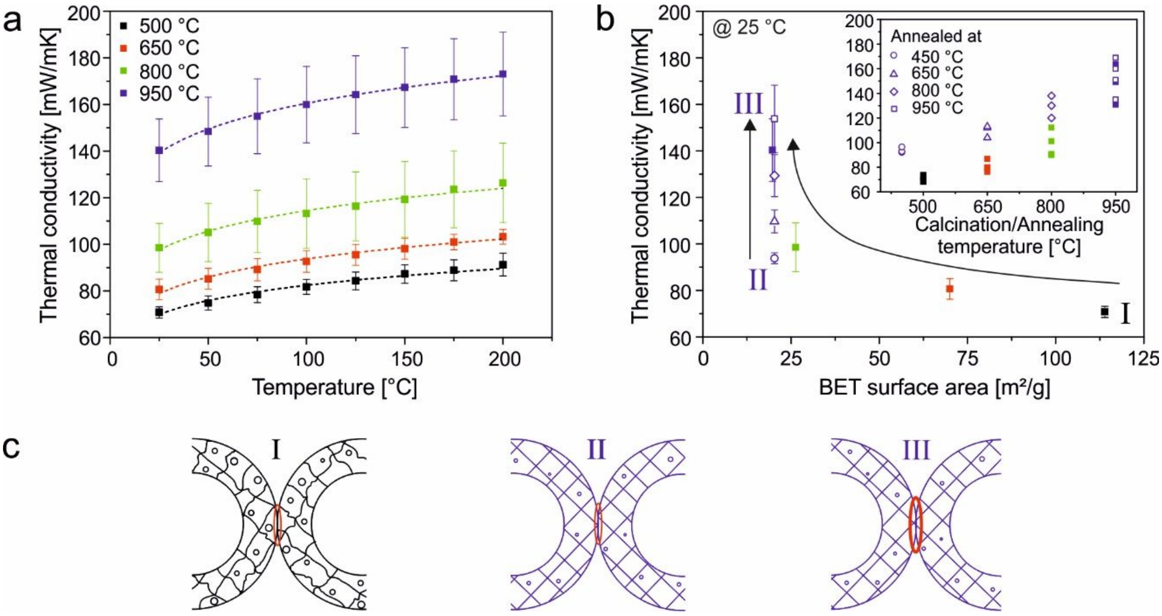

Figure 8.6. Thermal conductivity of calcined (closed symbols) and annealed HSNP colloidal crystals (open symbols). (a) Thermal conductivity of HSNP monoliths calcined at different temperature (500 – 950 °C) as a function of the measurement temperature. The dashed lines represent $\kappa \sim T^x$. (b) BET surface area and calcination temperature (inset) as a function of the thermal conductivity at 25 °C measurement temperature. (c) Schematic representation of the internal structural changes and the increase in interfacial adhesion within a colloidal crystal ensemble.

Figure 8.6a shows all temperature-dependent data for one sample, which was calcined at 500 °C. The thermal conductivity of a hollow sphere colloidal crystal consisting of 316 nm diameter and 44 nm shell capsules is very low with $\kappa = 71\ \mathrm{mW m^{-1} K^{-1}}$. The thermal conductivity increases monotonically to a value of $\kappa = 91\ \mathrm{mW m^{-1} K^{-1}}$ at 200 °C, which is known for glassy materials at high temperatures.[34-35] It is higher compared to most bulk silica aerogels and previously reported hollow spheres, however, the effective density of colloidal crystal under investigation here is relatively high with $\rho = 1.044\ \mathrm{gcm^{-3}}$. Calcination at elevated temperatures leads to a systematic increase in thermal conductivity, the absolute magnitude doubles at room temperature from $\kappa = 71\ \mathrm{mWm^{-1}K^{-1}}$ (calcination at 500 °C) to $\kappa = 140\ \mathrm{mWm^{-1}K^{-1}}$ (calcination at 950 °C). In comparison to calcination dependent investigations that have been carried out on silica aerogel samples we attribute this increase not to a loss in methyl groups or increase in density, but solely to microstructural changes, since the density of our silica shell is constant from calcination between 500 and 950 °C.[36] This is corroborated by a thermogravimetric analysis of the 500 °C calcined hollow spheres (Figure S8.5a).

In the further discussion, we only want to focus on the thermal conductivity at 25 °C. Concomitant with the increase in thermal conductivity at higher calcination temperatures, the standard deviation also increases. This can be understood by small, but random changes from sample to sample during the calcination process. Those changes can be the evolution of cracks or line defects or a change in the adhesion between the neighboring spheres. As outlined above, the individual spheres remain almost constant in size even at high calcination temperatures. However, within an ensemble of particles, those minute changes can accumulate to distinct defects. Such changes are small and we could not observe any structural changes by optical microscopy or SEM (see Figure S8.1). Since also the samples of annealed colloidal crystals demonstrate the same amount of increase in data scattering, the evolution of the mutual contact points seems to be the major source for this scattering. Additionally, an increase in thermal conductivity can lead to higher losses into the sample holder during the LFA measurement. This, in turn, can reduce the accuracy of the radiation fit model.

Despite some scatter in the data, the unambiguous trend of an increase in thermal conductivity can be inferred from the inset of Figure 8.6b (closed symbols). Due to the well-defined structure, we can now relate this apparent increase to microstructural changes in the SiO_2 network. We, therefore, plot the same data against the BET surface area, which changes sensitively with the calcination temperature as shown above. The reduction in surface area by a factor of almost six leads to a doubling of the thermal conductivity (Figure 8.6b, solid symbols). However, this change is accompanied by closure of micropores, a small increase in Q^4 Si atoms (Figure S8.7c), a large increase in spin-lattice relaxation time, and most importantly an increase of the interfacial adhesion between the spheres. These changes are schematically shown in Figure 8.6c. The relative area (based on the total particle surface) involved in interfacial contact points, increases with higher calcination temperatures from ~6 % at 500 °C to ~13 % at 950 °C (see Figure S8.1). This can additionally contribute to an improved thermal transport between the individual particles due to less constriction resistance. We therefore also investigated the thermal transport properties of annealed colloidal crystals as outlined above. Figure S8.7d shows all temperature-dependent measurements of the annealed samples, similar to Figure 8.6a. The data from the 450 °C up to 950 °C annealed colloidal crystals are shown with open symbols in Figure 8.6b and correspond to a transition from Figure 8.6c II to III. The BET surface area of the hollow spheres and therefore of the colloidal crystal has already been reduced to only 20.3 m^2g^{-1} prior to the colloidal crystal formation. This surface area does not change with increasing annealing temperatures any more, as the SiO_2 network has already been brought into its highly condensed form. Consequently, the data lie on a straight vertical line in Figure 8.6b (open symbols). One recognizes that the loss of micropores and increase in rigidity of the silica network (i.e. the T_1 relaxation) leads to a distinct increase in thermal conductivity from $\kappa = 71\ mWm^{-1}K^{-1}$ to $\kappa = 92\ mWm^{-1}K^{-1}$ – while the interfacial contact between the spheres can be regarded similar to the 500 °C calcined crystal (closed black square). On the contrary, it demonstrates also the large influence of interfacial adhesion as the thermal conductivity is drastically reduced compared to the fully annealed case (open blue circles, $\kappa = 154\ mWm^{-1}K^{-1}$). Annealing at 650 °C, 800 °C, and ultimately 950 °C strengthens the covalent linkage at the contact points of adjacent spheres, but will not change the internal structure any further (transition from Figure 8.6c II to III). This increase in adhesion reflects in a marked increase in thermal conductivity of the annealed hollow sphere monoliths (open symbols) from $\kappa = 94\ \mathrm{mWm^{-1}K^{-1}}$ (500 °C) to $\kappa = 110\ \mathrm{mWm^{-1}K^{-1}}$ (650 °C), $\kappa = 129\ \mathrm{mWm^{-1}K^{-1}}$ (800 °C), and $\kappa = 154\ \mathrm{mWm^{-1}K^{-1}}$ (950 °C). The final value of $154\ \mathrm{mWm^{-1}K^{-1}}$ is a little higher, compared to the calcined colloidal crystal ($\kappa = 140\ \mathrm{mWm^{-1}K^{-1}}$). This could be due to the absence of shrinkage in case of annealing in contrast to calcination where the spheres shrink slightly from 316 to 310 nm (compare Table S8.1). This could reflect in fewer defects and broken contact points.

What do we learn about the transport of thermal energy through such an amorphous, nanostructured silica material? The transport of thermal energy in this amorphous material is influenced by two distinct contributions: the microstructure of the "bulk" silica network (the thickness is only 44 nm) and the interfacial contact between the adjacent spheres. The influence of the bulk silica network can be seen by the difference between the colloidal particles calcined after (Figure 8.6b solid symbols) and before (Figure 8.6b open symbols) the assembly process. Assuming a comparable adhesion between the silica spheres at the respective calcination and annealing temperatures, the annealed colloidal crystals always demonstrate a higher thermal conductivity. Apparently, the minimum amount of micropores in combination with a higher degree of Q^4 atoms and smaller BET surface area leads to less scattering of delocalized modes at point defects or interfaces. Furthermore, the increase in spin-lattice relaxation time can be interpreted as a measure to increase the coherence length of the vibrational modes in the amorphous network, which will result in an increased thermal transport. A similar effect has been reported for amorphous polymers, where weak van-der-Waals bonds have been replaced by stronger hydrogen-bonds.[37] Accordingly, we also observe a decrease in the temperature dependence from $\kappa \sim T^{0.5}$ for 500 °C calcination to $\kappa \sim T^{0.4}$ for 950 °C calcination (determined by a linear fit to a double-log plot of the κ vs. T graph). The annealed samples show a $\kappa \sim T^{0.4}$ dependency, which slightly decreases with higher annealing temperatures (see Figure S8.7d). As a reference, fused quartz glass demonstrates a proportionality of $\kappa \sim T^{0.3}$ in the respective temperature range between 0 °C and 200 °C. The temperature dependence of the thermal conductivity can give insights on how thermal energy is transported. For crystalline materials the temperature-dependent thermal conductivity is known to scale with T^{-1} (at high temperatures) due to phonon-phonon Umklapp scattering.[34, 38] For disordered materials the scaling behavior exhibits typically a positive slope due to an increase in heat capacity and the diffusive thermal conduction of propagons and diffusons. In our amorphous material, we find the expected increase in thermal conductivity with increasing temperatures. This dependency, however, decreases slightly from $T^{0.5}$ to $T^{0.4}$ with increasing calcination temperature. We attribute this decrease to an increased anharmonic coupling between localized modes or between localized and delocalized modes, caused by the microstructural changes during the calcination.[39]

Even more important, particularly when considering the small amount of atoms involved, are the interfacial contact points between the adjacent spheres. Due to the *fcc* structure, each particle contacts twelve neighboring particles. For the case of annealed colloidal crystals, the adhesion and the degree of crosslinking between the spheres, respectively, govern predominantly the thermal transport, since the internal structure is already fully condensed. Whereas we cannot quantify the bonding strength between the hollow silica particles, one can deduce from Figure 8.6b (open symbols) that the thermal conductivity can be increased by more than 160 %, when strengthening the contact points. Analogously to the calcined samples, a slight increase in the mutual particle contact area may also contribute to the enhanced thermal transport.

The absolute thermal insulation properties of the hollow silica colloidal crystals presented here are less compared to their aerogel analogues; however, they still demonstrate a very low thermal conductivity in particular in the light of the relatively high density ($\rho \approx 1.04$ gcm^{-3}).

8.3 Conclusion

Colloidal crystals consisting of hollow silica nanoparticles represent a porous material class, with very well defined nano- and mesostructure. The monodispersity of the constituting building blocks, which comprise two distinct length scales (44 nm shell thickness and 316 nm diameter), translates into highly ordered colloidal crystals. Yet, for thermal transport applications, this material can be considered entirely amorphous, due to the glassy microstructure of the condensed silica network. We employed a range of characterization techniques to determine the structural entities from the nano- to the macroscale. SAXS, electron and optical microscopy showed the structural integrity even after calcination up to 950 °C, whereas NMR, N_2 sorption, and XRD demonstrated significant changes on the nanoscale. These changes result in an increase in thermal conductivity through this porous material. We identified two distinct contributions to this increase in thermal conduction. The first being internal structural changes of the condensed silica network, which are: loss of micropores, loss of BET surface area, increase in Q^4 Si atoms and increase in spin-lattice relaxation time. The second being an increase in interfacial bonding between the individual spheres. Both result in a higher thermal conductivity of our porous silica material. Even though only a fraction of the total amount of Si and O atoms contribute to interfacial adhesion, the thermal conductivity predominantly depends on it. Combining low adhesion forces and microstructure leads consequently to the lowest thermal conductivity of $\kappa = 71\,\mathrm{mW\,m^{-1}\,K^{-1}}$ for the system under investigation here. Colloidal crystals of hollow silica nanoparticles not only represent a highly insulating material. The well-defined structure further allows to thoroughly investigate thermal transport processes in amorphous silica materials. Further research will build upon these concepts and may lead to extremely efficient insulation layers.

8.4 Experimental Section

Materials

Styrene (≥99 %, Aldrich), 2,2′-azobis(2-methylpropionamidine) dihydrochloride (AIBA; 97 %, Aldrich), [2-(methacryloyloxy)ethyl]trimethylammonium chloride (MTC; 70 % solution in water, Polyscience), polyvinylpyrrolidone K30 (PVP; $M_w \sim 55$ kg/mol, Aldrich), tetraethyl orthosilicate (TEOS; ≥ 99 %, Aldrich) and ammonium hydroxide solution (30 – 33 % in water, Aldrich) were used as received. Ethanol (EtOH) was used in technical grade and water was taken from a Millipore Direct Q3UV unit for the entire synthesis and purification steps.

Synthesis of monodisperse hollow silica nanoparticles

The synthesis of monodisperse hollow silica nanoparticles comprises three steps. First monodisperse polystyrene (PS) latex particles were synthesized by emulsifier-free emulsion polymerization. The reaction was carried out in a 500 mL three-neck flask, equipped with a gas inlet and a reflux condenser. Solid chemicals were dissolved in water prior to addition. Firstly 200 mL water, 26 mL styrene, 1.8 g PVP and 100 µL MTC were heated to the reaction temperature of 70 °C at a stirring speed of 850 rpm using a large egg-shaped magnetic stirring bar. After equilibrating for 20 min, 600 mg AIBA initiator, dissolved in 40 mL water, were quickly added to initiate the polymerization. After nucleation, the stirring speed was reduced to 450 rpm and the polymerization was allowed to continue overnight at 70 °C under a slight inert gas flow. In the second step, the PS template particles were coated with a silica shell to obtain core/shell particles. The silica coating was achieved by a Stöber condensation process.[40] Therefore 17.5 mL neat PS dispersion (9.14 wt.%) were diluted with 122.5 mL ethanol and 9.1 mL ammonium hydroxide solution and stirred at 500 rpm. After stepwise addition of 13 mL TEOS the reaction was stirred overnight at room temperature. The core/shell particles were purified by repeated centrifugation and redispersion in water. In order to prepare hollow spheres, the sample was dried and kept in a furnace (Nabertherm L5/11/P33) at 500, 650, 800 or 950 °C in air for 12 h. The hollow spheres could be redispersed in water using mild sonication in a sonication bath.

Colloidal crystal via evaporation induced self-assembly of hollow silica nanoparticles

To obtain colloidal crystals a concentrated aqueous solution of core shell particles (~ 7 wt.%) or hollow silica spheres (~ 5 wt.%) was slowly evaporated in a Teflon beaker with a diameter of 2 cm for several days.

Characterization

Transmission electron microscopy (TEM) images were performed on a Zeiss CEM 902 instrument in bright field imaging mode at an acceleration voltage of 80 kV.

Elemental analysis (EA) was performed on a Vario Elementar EL III apparatus.

Nitrogen sorption measurements were carried out on a Quantachrome Autosorb AS-1 pore analyzer at 77 K. Prior to the measurements, all samples were preconditioned in vacuum at 350 °C for 12 hours. For the analysis, the Quantachrome ASiQ v3.0 software was used. The specific surface areas were calculated using the BET method. Pore volumes and pore size distributions were obtained by applying the nonlocal density functional theory (NLDFT) adsorption branch model for silica materials with cylindrical pore geometry.

Solid-state ^{29}Si NMR and hyperpolarized ^{129}Xe NMR measurements were carried out on a Bruker Avance II spectrometer in combination with a 7.05 T magnet (Oxford) corresponding to a larmor frequency ω_0 = 59.6 MHz for ^{29}Si and 83.0 MHz for ^{129}Xe equipped with a BVT 3000 VT-Unit (Bruker).[41] Si spectra were recorded with single pulse excitation using a 7 mm triple resonance probe at a spinning frequency of 5 kHz. The chemical shifts were referenced to tris(trimethylsilyl)amine (2.4 ppm) relative to tetramethylsilane (TMS). A 90° pulse at a nutation frequency of 38 kHz was used. The repetition times were set to 60 s. The number of scans was adapted such that a sufficient S/N ratio was obtained.

Spin-lattice relaxation was measured by using a saturation recovery experiment with a pulse train of five 90° pulses to ensure complete saturation of the system. The spectra were deconvoluted using a pseudo-Voigt profile by fitting to the least squares. The formula of the applied profile is expressed by

$$I(\delta) = A \cdot \left\{ \eta \cdot \frac{\sqrt{4\log 2}}{\sqrt{\pi} \cdot w} \cdot \exp\left[-\frac{4\log 2}{w^2}(\delta - \delta_0)^2 \right] + (1-\eta) \cdot \frac{2}{\pi} \frac{w}{[4 \cdot (\delta - \delta_0)]^2 + w^2} \right\} \tag{8.3}$$

where A is the amplitude of the peak, δ_0 is its center, η is the weight factor (1: Gaussian function, 0: Lorentzian function) and w is the full width at half maximum (FWHM).

For variable-temperature (VT) hyperpolarized ^{129}Xe NMR measurements a 5 mm wideline double resonance probe (Bruker) was used. The NMR chemical shifts were referenced to the signal of gaseous Xenon at 0 ppm. The probe was modified with a 3 mm inner diameter PEEK sample holder to incorporate hyperpolarized ^{129}Xe in continuous flow mode to the sample. The spectra were acquired with single pulse excitation using 52.62 kHz nutation frequency and 32 to 128 transients. The recycle time was set to 1 s and is not dependent on the spin-lattice relaxation but limited by the flow rate and the exchange between hyperpolarized and depolarized ^{129}Xe in the pore.[40] The hyperpolarized ^{129}Xe was generated using a self-built polarizer. A gas mixture of Xe:N$_2$:He = 1:2:97 (vol.%) at an overall pressure of 5 bar was irradiated with an 80 W diode laser (Coherent Inc.) at a central frequency of the Rb D$_1$-line (l = 794.8 nm). The polarized gas was exchanged over the sample with a flow rate of about 200 cm^{3}min^{-1}. A polarization of ~ 5 % was reached.

Solid-state ^{1}H NMR measurements were carried out on a Bruker Avance III HD spectrometer using a 14.1 T magnet (Bruker Ascent) corresponding to a larmor frequency of ω_0 = 600.1 MHz and a 1.3 mm double resonance probe at a spinning frequency of 62.5 kHz. Spectra were acquired with 8 transients at nutation frequency of 161 kHz and a repeating time of 5 s.

Small-angle X-ray scattering (SAXS) data reported here were measured using the small-angle-x-ray system Double Ganesha AIR (SAXSLAB, Denmark). The X-ray source of this laboratory-based system is a rotating anode (copper, MicoMax 007HF, Rigaku Corporation, Japan) providing a micro-focused beam at $\lambda = 0.154$ nm. The data were recorded by a position sensitive detector (PILATUS 300K, Dectris). To cover the range of scattering vectors between 0.026 – 2.6 nm^{-1} different detector positions were used. The measurement was recorded using a powder of hollow silica nanoparticles between two Kapton foils at room temperature. The scattering curve was evaluated with a vesicle fit in the program SCATTER.[42]

Powder X-ray diffraction (XRD) measurements were performed using a STOE STADI P ($\text{CuK}_{\alpha 1}$ radiation, transmission geometry) diffractometer equipped with a fast, high-resolution silicon strip detector DECTRIS Mythen1K. The samples were mounted on a flat disk using Scotch® tape. A stepsize of 0.2° and integration time of 20 s was used.

Differential scanning calorimetry (DSC) measurements were recorded using a Q1000 DSC (TA Instruments). Compressed powders of the hollow spheres (12 – 15 mg) were scanned in covered aluminum pans under dry nitrogen purge (50 mLmin^{-1}) at different heating rates over a temperature range from -50 °C to 200 °C with a heating rate of 10 $°\text{Cmin}^{-1}$. The heat flow and heat capacity were calibrated using a standard sapphire sample. The received data was evaluated with Universal Analysis 2000 2.5A software.

Thermogravimetric analysis (TGA) was done with a Mettler Toledo TGA/STDA 851e Star System at a heating rate of 10 Kmin^{-1} under air flow. The initial sample weight was 16.8018 mg.

Thermal diffusivity of the colloidal crystals was measured by xenon flash analysis (XFA) on an XFA 500 XenonFlash apparatus (Linseis) with an InSb infrared detector. The measurements were taken over a temperature range from 25 to 200 °C in vacuum. Prior to the measurements, the samples were coated with approximately 15 µm of graphite on each side. In order to eliminate any potential contribution from intercalated water inside the SiO_2 network, we pre-heated the samples up to 200 °C for 15 min in vacuum. The received data was evaluated by the software AproSoft Laser Flash Evaluation v1.06. The thicknesses of the colloidal crystals were determined with a Litematic VL-50 (Mitutoyo).

Correlative light-electron microscopy (CLEM) images were recorded on an Axio Imager.A2m (Carl Zeiss Microscopy) equipped with a motorized stage and a digital camera AxioCam ICc 1. Using the shuttle & find module the samples were transferred into a scanning electron microscope (SEM) Zeiss Ultraplus mounted on the sample holder KorrMik MAT universal B. SEM images were recorded on pre-defined spots based on the optical light microscope image using acceleration voltages between 2 and 3 kV and InLens SE detection as well as Everhart-Thornley detection (80/20 or 70/30 ratio).

8.5 Acknowledgements

The authors thank Lena Geiling and Nadine Popp for BET, Anna-Maria Dietel for EA, Markus Drechsler for TEM, Martin Dulle for SAXS, Ute Kuhn for DSC, and Beate Förster for CLEM measurements. This project was funded by the Volkswagen foundation. SFB 840 is acknowledged for financial support. P.R. acknowledges support by the Elite Network Bavaria (ENB). M.R. thanks the VCI for financial support.

8.6 References

1. Jelle, B. P.; Gustavsen, A.; Baetens, R., The path to the high performance thermal building insulation materials and solutions of tomorrow. *Journal of Building Physics* **2010,** *34* (2), 99-123.

2. Dorcheh, A. S.; Abbasi, M. H., Silica aerogel; synthesis, properties and characterization. *Journal of Materials Processing Technology* **2008,** *199* (1-3), 10-26.

3. Hüsing, N.; Schubert, U., Aerogels—Airy Materials: Chemistry, Structure, and Properties. *Angewandte Chemie* **1998,** *37*, 22-45.

4. Kistler, S. S., Coherent Expanded-Aerogels. *J Phys Chem* **1931,** *36* (1), 52-64.

5. Koebel, M.; Rigacci, A.; Achard, P., Aerogel-based thermal superinsulation: an overview. *J Sol-Gel Sci Technol* **2012,** *63* (3), 315-339.

6. Heinemann, U., Influence of Water on the Total Heat Transfer in 'Evacuated' Insulations. *Int J Thermophys* **2008,** *29* (2), 735-749.

7. Smith, D. M.; Maskara, A.; Boes, U., Aerogel-based thermal insulation. *Journal of Non-Crystalline Solids* **1998,** *225* (0), 254-259.

8. Heinemann, U.; Caps, R.; Fricke, J., Radiation-conduction interaction: an investigation on silica aerogels. *International Journal of Heat and Mass Transfer* **1996,** *39* (10), 2115-2130.

9. Hrubesh, L. W.; Pekala, R. W., Thermal properties of organic and inorganic aerogels. *Journal of Materials Research* **1994,** *9*, 731-738.

10. Knudsen, M., Die molekulare Wärmeleitung der Gase und der Akkommodationskoeffizient. *Ann. Phys.* **1911,** *339* (4), 593-656.

11. Schiffres, S. N.; Kim, K. H.; Hu, L.; McGaughey, A. J. H.; Islam, M. F.; Malen, J. A., Gas Diffusion, Energy Transport, and Thermal Accommodation in Single-Walled Carbon Nanotube Aerogels. *Adv. Funct. Mater.* **2012,** *22* (24), 5251-5258.

12. Lu, X.; Arduini-Schuster, M. C.; Kuhn, J.; Nilsson, O.; Fricke, J.; Pekala, R. W., Thermal Conductivity of Monolithic Organic Aerogels. *Science (New York, N.Y.)* **1992,** *255*, 971-972.

13. Allen, P.; Feldman, J., Thermal conductivity of disordered harmonic solids. *Phys Rev B* **1993,** *48* (17), 12581-12588.

14. Allen, P. B.; Feldman, J. L.; Fabian, J.; Wooten, F., Diffusons, locons and propagons: Character of atomic vibrations in amorphous Si. *Philos Mag B* **2009,** *79* (11-12), 1715-1731.

15. Larkin, J. M.; McGaughey, A. J. H., Thermal conductivity accumulation in amorphous silica and amorphous silicon. *Phys. Rev. B* **2014,** *89* (14), 144303.

16. Regner, K. T.; Sellan, D. P.; Su, Z.; Amon, C. H.; McGaughey, A. J. H.; Malen, J. A., Broadband phonon mean free path contributions to thermal conductivity measured using frequency domain thermoreflectance. *Nat Comm* **2013,** *4*, 1640-7.

17. Coquil, T.; Fang, J.; Pilon, L., Molecular dynamics study of the thermal conductivity of amorphous nanoporous silica. *International Journal of Heat and Mass Transfer* **2011,** *54* (21–22), 4540-4548.

18. Coquil, T.; Richman, E. K.; Hutchinson, N. J.; Tolbert, S. H.; Pilon, L., Thermal conductivity of cubic and hexagonal mesoporous silica thin films. *J Appl Phys* **2009,** *106*, 034910.

19. Desai, T. G., Thermal transport in nanoclusters. *Appl Phys Lett* **2011,** *98* (19), 193107.

20. Fricke, J.; Tillotson, T., Aerogels: production, characterization, and applications. *Thin Solid Films* **1997,** *297* (1–2), 212-223.

21. Chen, M.; Ye, C.; Zhou, S.; Wu, L., Recent Advances in Applications and Performance of Inorganic Hollow Spheres in Devices. *Adv Mater* **2013,** *25* (37), 5343-5351.

22. Zhang, L.; D'Acunzi, M.; Kappl, M.; Auernhammer, G. K.; Vollmer, D.; van Kats, C. M.; van Blaaderen, A., Hollow silica spheres: synthesis and mechanical properties. *Langmuir* **2009,** *25* (5), 2711-2717.

23. Retsch, M.; Schmelzeisen, M.; Butt, H.-J.; Thomas, E. L., Visible Mie Scattering in Nonabsorbing Hollow Sphere Powders. *Nano Lett* **2011,** *11* (3), 1389-1394.

24. Zhang, L.; D'Acunzi, M.; Kappl, M.; Imhof, A.; van Blaaderen, A.; Butt, H.-J.; Graf, R.; Vollmer, D., Tuning the mechanical properties of silica microcapsules. *PCCP* **2010,** *12*, 15392.

25. Yin, J.; Retsch, M.; Thomas, E. L.; Boyce, M. C., Collective Mechanical Behavior of Multilayer Colloidal Arrays of Hollow Nanoparticles. *Langmuir* **2012,** *28* (13), 5580-5588.

26. Yin, J.; Retsch, M.; Lee, J.-H.; Thomas, E. L.; Boyce, M. C., Mechanics of Nanoindentation on a Monolayer of Colloidal Hollow Nanoparticles. *Langmuir* **2011,** *27* (17), 10492-10500.

27. Sandberg, L. I. C.; Gao, T.; Jelle, B. P.; Gustavsen, A., Synthesis of Hollow Silica Nanospheres by Sacrificial Polystyrene Templates for Thermal Insulation Applications. *Adv Mater Sci & Engin* **2013,** *2013*, 1-6.

28. Gao, T.; Jelle, B. P.; Sandberg, L. I.; Gustavsen, A., Monodisperse hollow silica nanospheres for nano insulation materials: synthesis, characterization, and life cycle assessment. *ACS Appl Mater Interfaces* **2013,** *5* (3), 761-7.

29. Yue, Q.; Li, Y.; Kong, M.; Huang, J.; Zhao, X.; Liu, J.; Williford, R. E., Ultralow density, hollow silica foams produced through interfacial reaction and their exceptional properties for environmental and energy applications. *J. Mater. Chem.* **2011,** *21* (32), 12041.

30. Liao, Y.; Wu, X.; Liu, H.; Chen, Y., Thermal conductivity of powder silica hollow spheres. *Thermochim Acta* **2011,** *526* (1-2), 178-184.

31. Demarquay, J.; Fraissard, J., 129Xe NMR of xenon adsorbed on zeolites. *Chemical Physics Letters* **1987,** *136* (3), 314-318.

32. Moudrakovski, I. L.; Terskikh, V. V.; Ratcliffe, C. I.; Ripmeester, J. A.; Wang, L.-Q.; Shin, Y.; Exarhos, G. J., A 129Xe NMR Study of Functionalized Ordered Mesoporous Silica. *The Journal of Physical Chemistry B* **2002,** *106* (23), 5938-5946.

33. Touloukian, Y. S., *Thermophysical properties of matter: Specific heat / Nonmetallic Solids*. IFI Plenum: New York, 1970; Vol. 5, p 1649.

34. Cahill, D. G.; Pohl, R. O., Lattice-Vibrations and Heat-Transport in Crystals and Glasses. *Annual Review of Physical Chemistry* **1988,** *39*, 93-121.

35. Cahill, D.; Pohl, R., Thermal conductivity of amorphous solids above the plateau. *Phys Rev B* **1987,** *35* (8), 4067-4073.

36. Hopkins, P. E.; Kaehr, B.; Piekos, E. S.; Dunphy, D.; Jeffrey Brinker, C., Minimum thermal conductivity considerations in aerogel thin films. *J Appl Phys* **2012,** *111* (11), 113532.

37. Kim, G. H.; Lee, D.; Shanker, A.; Shao, L.; Kwon, M. S.; Gidley, D.; Kim, J.; Pipe, K. P., High thermal conductivity in amorphous polymer blends by engineered interchain interactions. *Nat Mater* **2015,** *14* (3), 295-300.

38. Kittel, C., *Einführung in die Festkörperphysik*. 14 ed.; Oldenbourg: Wien, 2005.

39. Shenogin, S.; Bodapati, A.; Keblinski, P.; McGaughey, A. J. H., Predicting the thermal conductivity of inorganic and polymeric glasses: The role of anharmonicity. *J Appl Phys* **2009,** *105* (3), 034906.

40. Stoeber, W.; Fink, A.; Bohn, E., Controlled growth of monodisperse silica spheres in the micron size range. *J. Colloid Interf. Sci.* **1968,** *26* (1), 62-69.

41. Goodson, B. M., Nuclear Magnetic Resonance of Laser-Polarized Noble Gases in Molecules, Materials, and Organisms. *Journal of Magnetic Resonance* **2002,** *155* (2), 157-216.

42. Förster, S.; Apostol, L.; Bras, W., Scatter: software for the analysis of nano- and mesoscale small-angle scattering. *J. Appl. Crystallogr.* **2010,** *43* (3), 639-646.

8.7 Supporting Information

Table S8.1. Elemental analysis – N, C, O content in HSNPs calcined at different temperatures.

	N content [%]	*C content [%]*	*O content [%]*
HSNP-500	0.054	0.254	0.317
HSNP-650	0.021	0.067	0.106
HSNP-800	0.026	0.035	0.010
HSNP-950	0.025	0.069	0.002

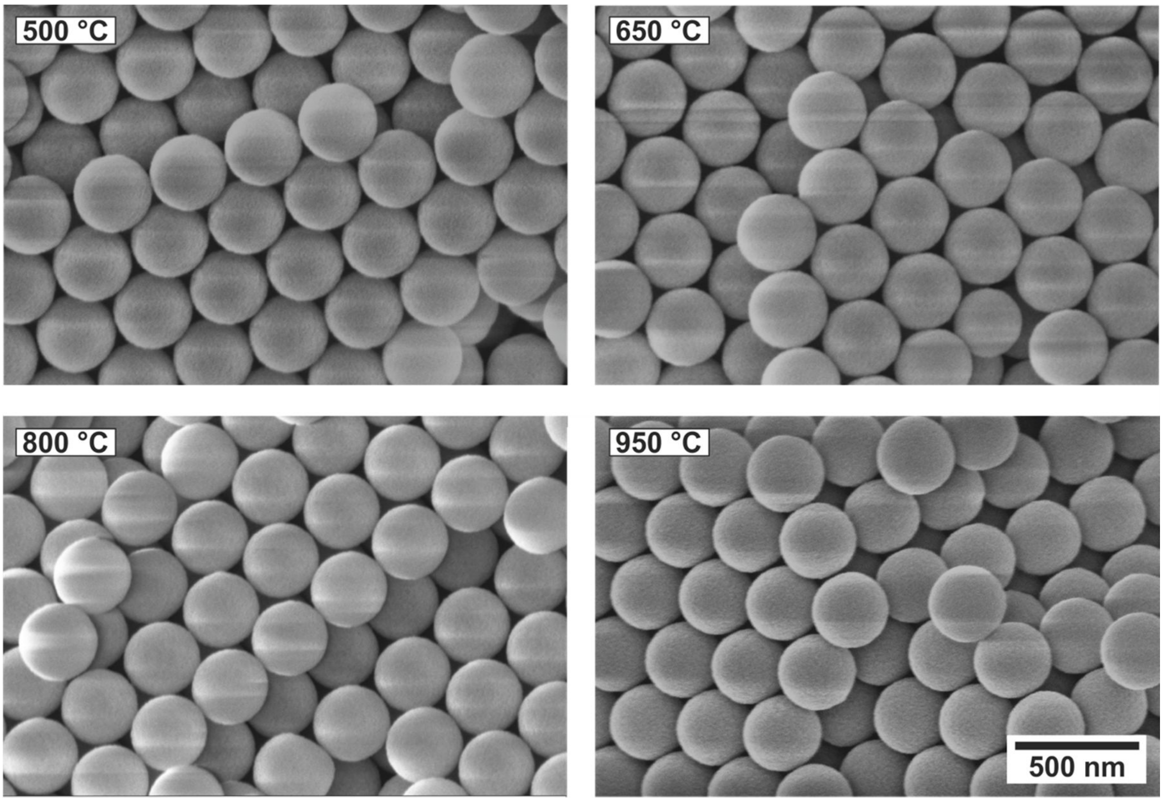

Figure S8.1. High magnification SEM images of HSNPs calcined at different temperatures (500 – 950 °C). No sinter necks between adjacent spheres can be observed, the particles retain their spherical shape and hexagonal assembly symmetry.

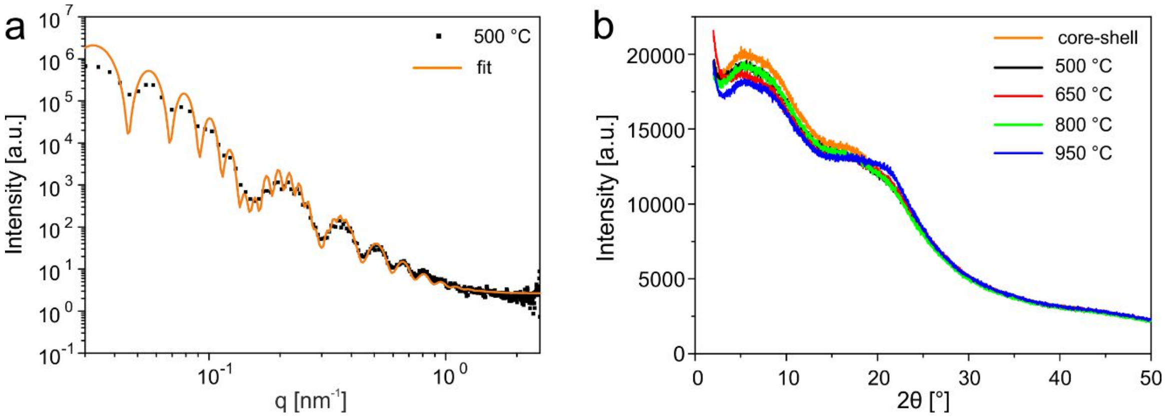

Figure S8.2. Internal structural characterization of HSNPs. (a) SAXS pattern for hollow silica nanoparticles calcined at 500 °C: experimental scattering profile (black line) and the fitting curve (orange line). The fit parameters are 315 nm diameter and 42.5 nm shell thickness, (b) XRD measurements of HSNPs calcined at different temperatures (500 – 950 °C).

Table S8.2. Summary of data received from NMR measurements.

	^{29}Si NMR [a]		**^{129}Xe NMR [c]**	
	$Q^4/(Q^3+Q^4)$	**T_1 relaxation time [s]**	**Delta [ppm]**	**Cylindrical pore [nm]**
HSNP-500	0.88	33 ± 7 (20 ± 2) [b]	57, 105	1.11, 0.71
HSNP-650	0.92	96 ± 20	42, 105	1.42, 0.71
HSNP-800	0.94	272 ± 60	-	-
HSNP-950	0.94	6400 ± 1000	-	-

[a] *Relative amount of* Q^4 *units and spin-lattice relaxation times obtained from solid state* ^{29}*Si NMR,* [b] *Spin-lattice relaxation time of HSNP-500 after drying to remove water residues,* [c] *Limiting shift of* ^{129}*Xe and corresponding pore sizes according to the Fraissard model for cylindrical pore geometries.*

$$D(\partial) = \frac{243 \cdot 2.054}{\delta} - 2.054 + D_{Xe}$$

δ = Limiting shift, D_{Xe} = VdW-Diameter of Xe

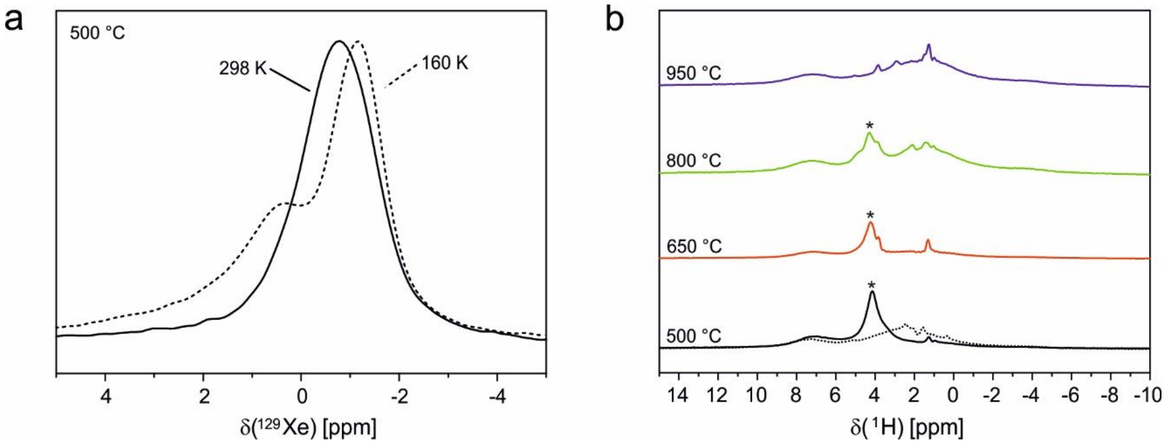

Figure S8.3. NMR characterization of HSNPs. (a) ^{129}Xe NMR: Single xenon gas peak at 0 ppm of silica hollow spheres at a measurement temperature of 298 K and 160 K, (b) ^{1}H NMR spectra of silica hollow spheres calcined at different temperatures (500 – 950 °C). The dotted line shows a pre-dried sample. The stars mark the peak caused by adsorbed water.

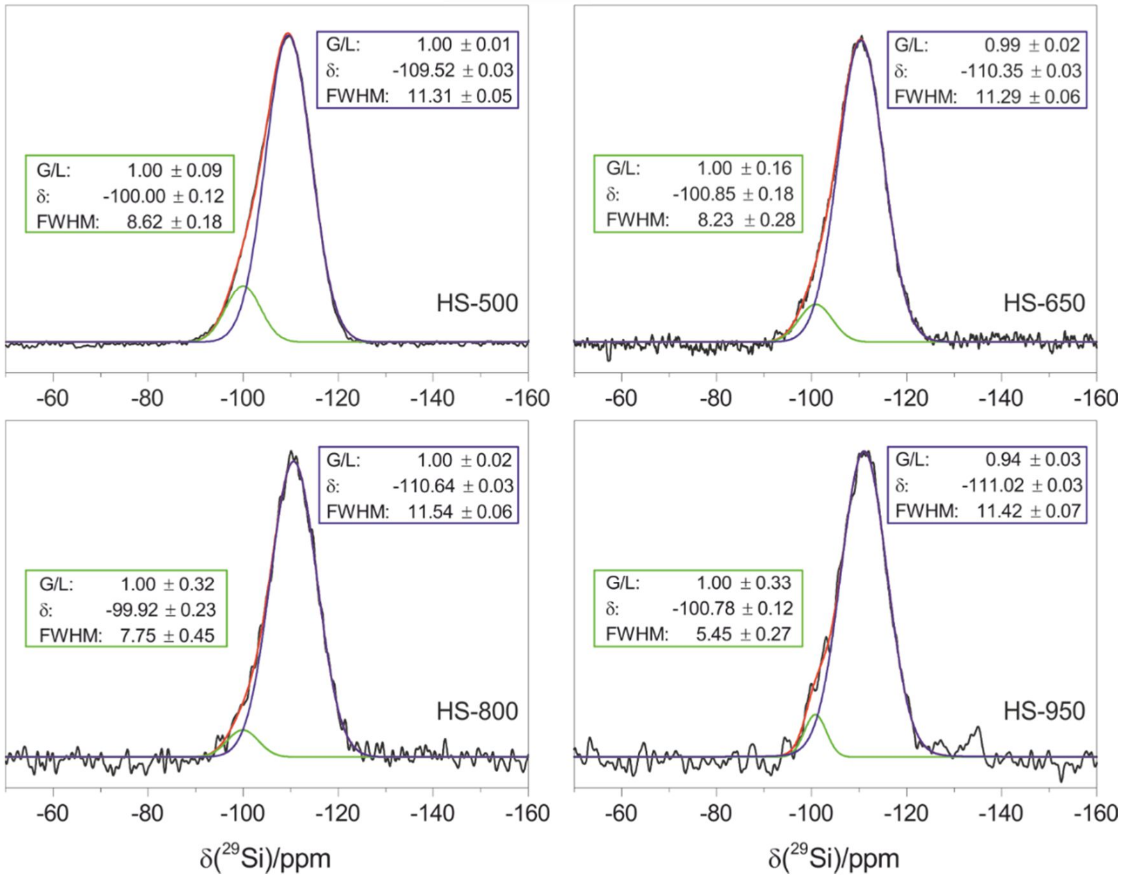

Figure S8.4. Deconvoluted projection of the ^{29}Si spectra of HSNPs calcined at 500 – 950 °C; measured signal (black), cumulative fit (red), simulated signals (green, blue).

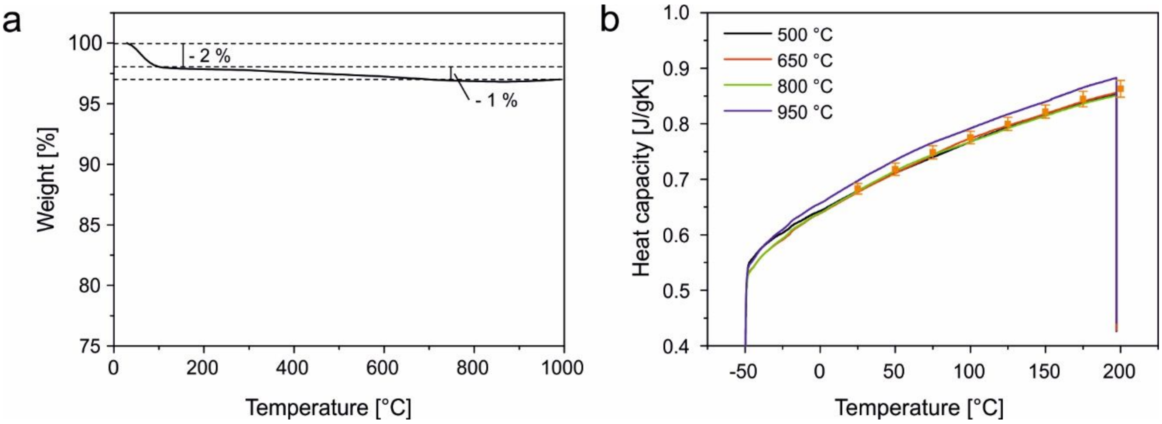

Figure S8.5. (a) Thermogravimetric analysis (TGA) results of silica hollow spheres calcined at 500 °C. The weight loss step (~ 2 %) at temperature up to 100 °C relates to the loss of adsorbed water. Another 1 % of mass is lost up to 950 °C, which can be attributed to the removal of trace amounts of silica condensation products. (b) Differential scanning calorimetry (DSC) measurements of the compacted silica hollow spheres calcined at 500 – 950 °C and the corresponding mean values (orange dots).

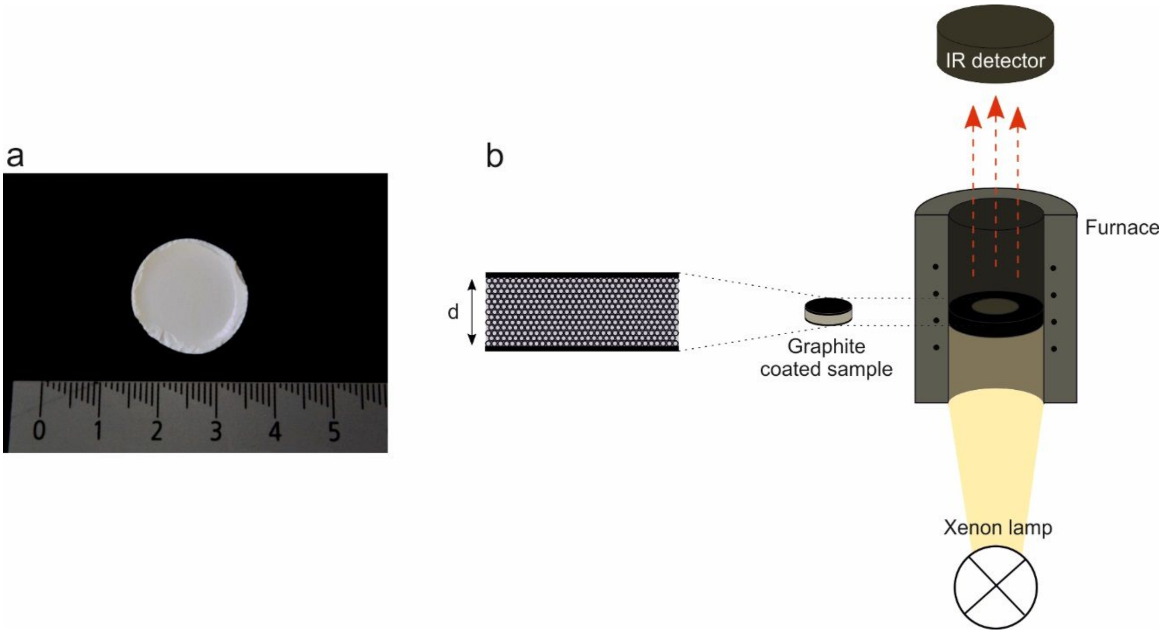

Figure S8.6. (a) Photograph of a silica hollow sphere colloidal crystal with a diameter of 2 cm, (b) XFA measurement principle and sample setup.

In brief, the colloidal crystals were coated on the top and bottom side with a thin graphitic layer (< 20 µm). Using a short light flash from a Xe white light source (2 ms) the bottom side of the sample is subjected to a temperature increase. The absorbed heat diffuses through the sample and consequently heats the top surface. An IR detector measures this time-dependent temperature increase. Using a radiation fit model the thermal diffusivity of the hollow sphere colloidal crystal sample can be extracted.

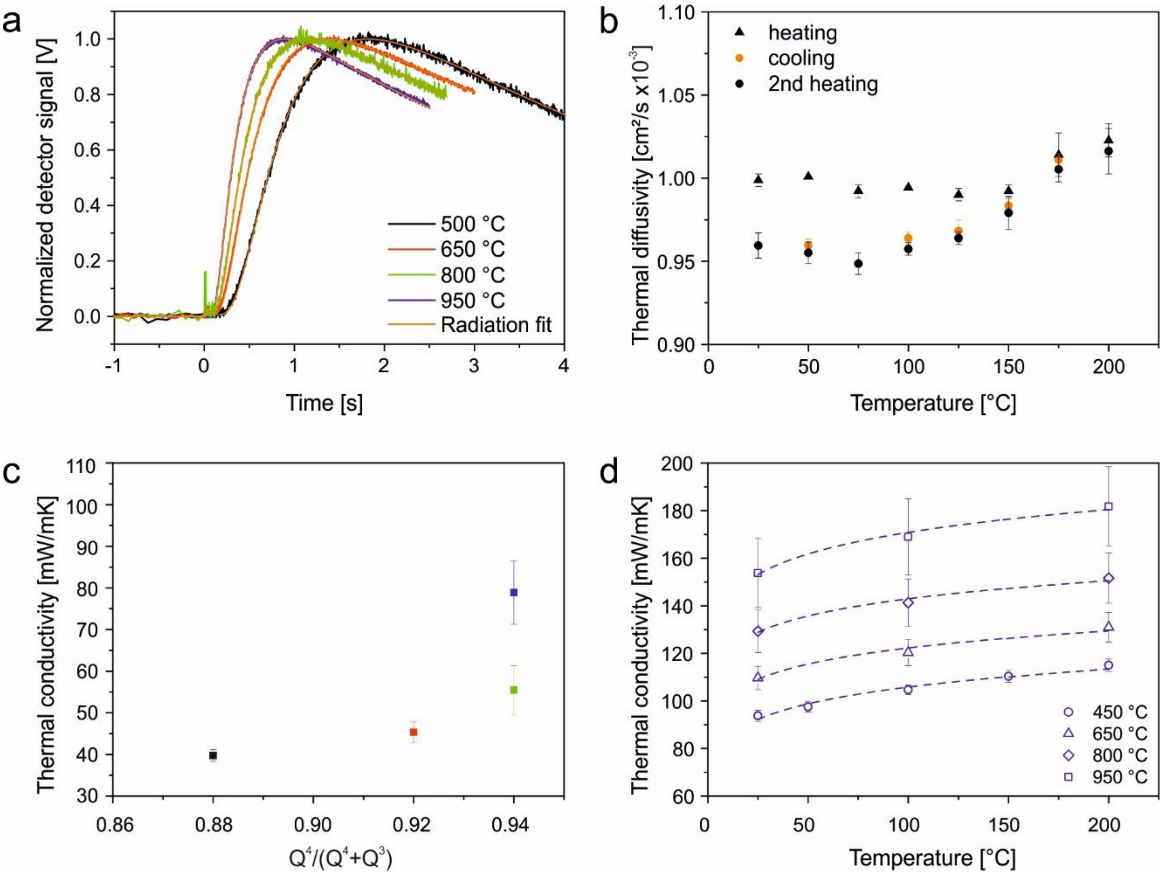

Figure S8.7. Xenon flash analysis (XFA) of silica hollow sphere colloidal crystals (a) Examples of LFA measurement signals of HSNP monoliths after calcination at elevated temperatures and the corresponding radiations fits (orange lines). The raw data were normalized to (0,1). Sample thicknesses were: 500 °C: 812 µm, 650 °C: 686 µm, 800 °C: 654 µm, 950 °C: 665 µm. (b) Thermal diffusivity as a function of the temperature of a HSNP colloidal crystal calcined at 500 °C with heating (black) and cooling cycles (orange). (c) Thermal conductivity of HSNP crystals calcined at different temperatures in dependence of the degree of condensation, (d)Thermal conductivity of annealed colloidal crystals (450 – 950 °C), calcined at 950 °C prior to the assembly of the monoliths. The dashed lines represent $\kappa \sim T^x$.

The radiation fit model represents an expansion to the finite-pulse and heat-loss corrections implemented in the Combined fit model from Dusza (L. Dusza, High Temperatures - High Pressures, 1995, 27, 467-473). It accounts for a portion of the Xe flash to be directly transmitted to the top surface, leading to an instantaneous temperature jump analogous to Blumm *et al.*.(J. Blumm, J. Henderson, O. Nilsson and J. Fricke, High Temperatures-High Pressures, 1997, 29, 555-560).

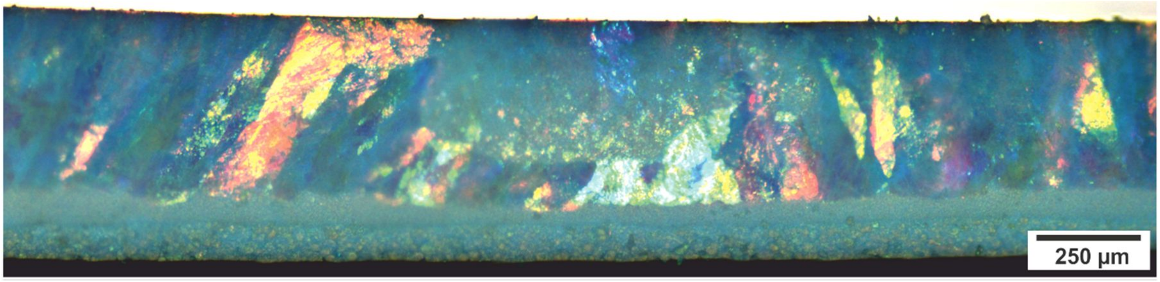

Figure S8.8. Bright field microscopy image of a colloidal crystal consisting of HSNPs calcined prior to the assembly process (annealed colloidal crystal).

Uncertainty analysis of the thermal conductivity determination

In the following, the uncertainty analysis of an individual sample based on independent measurements for the 500 °C calcined HSNP colloidal crystal is shown exemplarily. The different contributions will be introduced separately:

Thermal conductivity κ:

$$\kappa = \alpha \cdot c_p \cdot \rho = (\frac{0.138 \cdot d^2}{t_{\frac{1}{2}}}) \cdot c_p \cdot (\frac{(r^3 - (r-t)^3) \cdot \rho_{SiO_2}}{r^3})$$

Thermal diffusivity determination: $\alpha = \frac{0.138 \cdot d^2}{t_{\frac{1}{2}}}$

$$\sigma_\alpha = \sqrt{\left(\frac{\sigma\alpha}{\sigma t_{\frac{1}{2}}}\right)^2 \cdot \sigma_{t_{\frac{1}{2}}}^2 + \left(\frac{\sigma\alpha}{\sigma d}\right)^2 \cdot \sigma_d^2 = (-\frac{0.138 \cdot d^2}{\left(t_{\frac{1}{2}}\right)^2})^2 \cdot \sigma_{t_{\frac{1}{2}}}^2 + (\frac{2 \cdot 0.138 \cdot d}{t_{\frac{1}{2}}})^2 \cdot \sigma_d^2}$$

Measured parameters and their standard deviation:

Half-rise time $t_{1/2}$: (0.926 ± 0.009) s

Layer thickness d: (812 ± 8) µm

Average thermal diffusivity and standard deviation:

$\alpha = (9.83 \pm 0.22)\cdot 10^{-8}$ m²/s

i) Heat capacity c_p determination: $\sigma_{c_p} = \sqrt{\frac{\sum(x-\bar{x})^2}{n-1}}$

Average c_p and standard deviation:

c_p: (0.683 ± 0.010) J/gK

ii) Particle density ρ determination: $\rho = \left(\frac{(r^3-(r-t)^3)\cdot\rho_{SiO_2}}{r^3}\right)$

$$\sigma_\rho = \sqrt{\begin{gathered}\left(\frac{\sigma\rho}{\sigma r}\right)^2\cdot\sigma_r^2+\left(\frac{\sigma\rho}{\sigma t}\right)^2\cdot\sigma_t^2+\left(\frac{\sigma\rho}{\sigma\rho_{SiO2}}\right)^2\cdot\sigma_{\rho_{SiO2}}^2= \\ (-3\cdot \mathrm{t}(\mathrm{t}-\mathrm{r})^2\cdot\frac{\rho}{r^4})^2\cdot\sigma_r^2+(3\cdot(\mathrm{r}-\mathrm{t})^2\cdot\frac{\rho}{r^3})^2\cdot\sigma_t^2+\left(\frac{(r^3-(r-t)^3)}{r^3}\right)^2\cdot\sigma_{\rho_{SiO2}}^2\end{gathered}}$$

Measured parameters and their standard deviation:

Shell thickness t: (43.7 ± 1.6) nm

Particle radius r: (157.9 ± 1.9) nm

Density of the shell by He pycnometry ρ_{SiO2}: (2.27 ± 0.13) g/cm³

Average density and standard deviation:

ρ= (1.044 ± 0.089) g/cm³

Calculation of the thermal conductivity κ:

$$\kappa = \alpha \cdot c_p \cdot \rho$$

Standard deviation of κ:

$$\sigma_\kappa = \sqrt{\left(\frac{\sigma\kappa}{\sigma\alpha}\right)^2 \cdot \sigma_\alpha^2 + \left(\frac{\sigma\kappa}{\sigma c_p}\right)^2 \cdot \sigma_{c_p}^2 + (\frac{\sigma\kappa}{\sigma\rho})^2 \cdot \sigma_\rho^2}$$

Average thermal conductivity and standard deviation:

κ= (70.1 ± 6.3) mW/mK

We determined the standard deviation for each calcination dependent thermal conductivity measurement of our samples and confirmed that the relative error is < 10 % for most of the cases. The highest uncertainty was found to be 13 %.

We, therefore, conclude that the major source of uncertainty is given by variations from sample to sample. This is the data and uncertainty that we present in our manuscript, which is based on at least three independent samples at each calcination temperature.

9 Thermal Transport in Binary Colloidal Glasses: Composition Dependence and Percolation Assessment

Pia Ruckdeschel, Alexandra Philipp, Bernd A. F. Kopera, Flora Bitterlich, Martin Dulle, Nelson W. Pech-May, and Markus Retsch

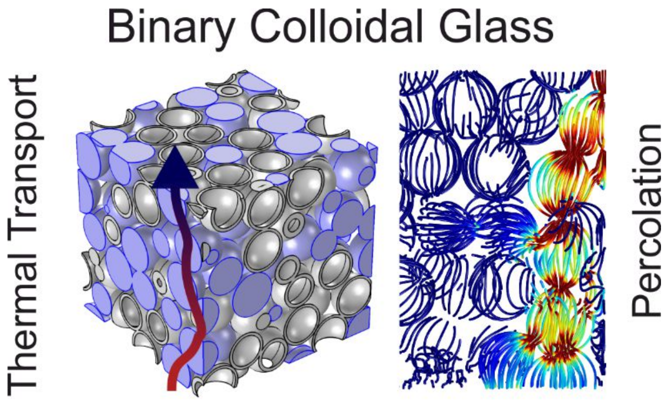

Submitted version - reprinted with permission from Ruckdeschel *et al.*, Phys. Rev. E, **2018**, 97 (2), 022612.

Abstract

The combination of various types of materials is often used to create superior composites, which outperform the pure phase components. For any rational design, the composite performance needs to be accurately described in dependence of the volume fractions of the component mixture. When approaching the nanoscale, the homogeneous mixture of various components poses an additional challenge. Here, we investigate binary nanocomposite materials based on polymer latex beads and hollow silica nanoparticles. These form randomly mixed colloidal glasses on a sub µm scale. We focus on the heat transport properties through such binary assembly structures. The thermal conductivity can be well described by the effective medium theory. However, film formation of the soft polymer component leads to phase segregation and a mismatch to existing mixing models. We confirm our experimental data by finite element modeling. This additionally allowed us, to assess the onset of thermal transport percolation in such random particulate structures. Our study contributes to a better understanding of thermal transport through heterostructured particulate assemblies.

9.1 Introduction

Nanostructured materials have been the driving force for the tremendous development of many modern technologies such as computational power and storage, sensors, or communication. Especially, (opto)electronic devices benefited from the ongoing miniaturization, which allowed to increase the device density according to Moore's law. However, this miniaturization is also accompanied by an increased energy density and, consequently, by much higher, much more localized temperatures. Thus, it becomes increasingly important to control the way heat flows through these structures; one particular challenge is the dissipation of heat in electronic elements.[1] Therefore, electrically insulating heat spreading materials are used to prevent the formation of hot spots, which reduce the lifetime and reliability of electronic materials.[2-3] Common heat sinks are polymers filled with a highly thermally conductive micro- or nanomaterial.[4-5] The thermal properties of these polymer composites depend mainly on the geometry of the filler (i.e., shape and size)[6], the volume fraction and distribution of the filler material in the matrix (lattice type)[7], the contact between the filler particles[8], and the thermal properties of the components[8]. Advantages of polymer filled materials are good mechanical properties and easy processing.

For the application as heat spreading material, a composite material needs to enhance the effective thermal conductivity greatly compared to that of its neat matrix. The filler material is typically much more expensive and/or less available than the matrix component. Consequently, low loading fractions of the filler material are highly desirable. An important quantity to characterize the minimum amount of necessary filler is given by its percolation threshold. Percolation describes the formation of long-range connectivity in randomly ordered systems. Expectedly, the threshold shifts to lower filler volume fractions in composites by using small particles with a large aspect ratio[9], a lattice type with a large number of neighbors (such as a face-centered cubic structure)[7], and a low contact resistance between the filler particles[10].

The percolation theory can analytically describe the composition dependence of binary mixture of isotropic objects.[7] It describes the relationship between the effective thermal conductivity of the composite, κ_{eff}, and the volume fraction of the filler, V_{filler},

$$\kappa_{eff} \propto \kappa_{filler}\left(V_{filler} - V_c\right)^n \tag{9.1}$$

where κ_{filler} is the thermal conductivity of the filler, V_c the percolation threshold and n the percolation exponent (typically 2 in a 3D experiment). Based on this equation, Mamunya et al.[11] developed an analytic expression for the electrical conductivity in composites, which can be also assigned to the effective thermal conductivity (κ_{eff}):[8]

$$\kappa_{eff} = \left(\frac{\Phi_1 - \Phi_c}{F - \Phi_c}\right)^t \cdot (\kappa_1 - \kappa_2) + \kappa_2 \tag{9.2}$$

where κ_1, κ_2 are the thermal conductivities of the two components 1 and 2 ($\kappa_1 >> \kappa_2$), F is the maximum filling packing factor (here: $F = 1$), Φ_c is the percolation threshold ($\Phi_c = \chi_c{\cdot}F$), which depends on the lattice structure (χ_c is the critical percolation probability, $\chi_c = 0.27$ for random close-packed structures)[12], Φ_1 is the volume concentration of component 1, and t is a critical exponent, which depends on the dimension of the structure (3D structures: $t = 2$)[7]. However, the percolation theory cannot be applied to mixing ratios lower than the percolation threshold.

Therefore, the thermal conductivity of a composite material is often predicted by binary mixing models. These can be applied to the entire mixing phase diagram. The most common ones are the series and parallel model, the Maxwell-Eucken 1 and 2 model and the effective medium theory (EMT).[13-14] These are summarized with their corresponding formulas in Figure S9.1 in the Supporting Information (Chapter 9.7). The upper and lower bounds are given by the parallel and series model, respectively, in which the layers are parallel or perpendicularly aligned to the heat flow direction. The Maxwell-Eucken model 1 and 2 assume separated inclusions in a dispersed phase.[15] Thus, materials with percolating pathways cannot be described by the Maxwell-Eucken models. A better description is given by the effective medium theory (EMT) model. It considers a structure in which two components are randomly distributed with neither phase being dispersed or continuous. Thus, both materials can form heat conduction pathways depending on the respective volume fraction.

Our contribution addresses two important aspects of composite materials. Firstly, choosing a colloidal approach, we are able to fabricate nanostructured colloidal materials with any mixing ratio, which otherwise often suffer from demixing or clustering. This allows us to investigate the applicability of the existing mixing models. Secondly, we shed light onto thermal transport percolation in an isotropic particle ensemble. We compare our experimental results with FEM simulation, which provides a deeper understanding of the percolation evolution. We base our study on two types of electrically insulating building blocks: polymer latex beads and hollow silica nanoparticles. These are self-assembled into randomly close-packed colloidal ensembles.

9.2 Results and Discussion

Binary Colloidal Assemblies

The binary colloidal assemblies are built from two types of particles with comparable outer diameters and surface charges: copolymer particles poly(methyl methacrylate-*co*-*n*-butyl acrylate) (P(MMA-*co*-nBA)) with a diameter of 441 ± 9 nm (zeta potential of -43 mV) and hollow silica nanoparticles (HSNPs) with a diameter of 423 ± 8 nm, a shell thickness of 25.3 ± 1.2 nm (zeta potential of -27 mV). The electron microscopy images of these particles are shown in Figure S9.2. Both images highlight the monodispersity of the particles. The polymeric particles feature a shrunk and rough surface due to the sensitivity of the PMMA to the electron beam.

We used vacuum filtration (see Figure S9.3 and Experimental Section for more details) for the self-assembly process since this method enables a fast and facile assembly of the particles into a colloidal glass with a random distribution of the two particle types. Particularly, minor density differences do not influence the particle distribution in the colloidal glass using the filtration process. The number of polymer particles was varied from 100 % to 0 % particles (see Table S9.1). The comparable particle size and surface potential lead to a good particle distribution on the sub-µm scale in the composite. This is validated by side-view scanning electron microscopy (SEM) images. Figure 9.1a shows the 50/50-mixture with red-colored hollow spheres for easier identification. The other particle composites are shown in Figure S9.4.

Thermal Transport Properties of Binary Colloidal Glasses – Percolation Effect

The thermal transport properties of the colloidal glasses were determined by xenon flash analysis. The method allows the direct determination of the thermal diffusivity. The thermal conductivity κ can be calculated using the following equation:

$$\kappa = \alpha \cdot c_p \cdot \rho \tag{9.3}$$

The specific heat capacity c_p and density ρ data are shown in Figure S9.6.

Figure 9.1a shows the thermal conductivity data of the binary colloidal glasses for different polymer particle volume fractions. For a colloidal glass, consisting of hollow silica spheres (0P), the thermal conductivity is extremely low with a thermal conductivity of only 13 $\mathrm{mWm^{-1}K^{-1}}$. The heat transport is limited in these colloidal glasses due to several structural properties on the nano- and mesoscale.[16-17] These are (i) the hollow structure, which reduces the density to only 0.30 $\mathrm{gcm^{-3}}$, (ii) the large amount of interfaces due to the particulate structure, which increases the thermal resistance by means of interparticle constriction, and (iii) the low packing parameter of the particles to reduce the density and interparticle contact points even further. Thus, silica hollow sphere colloidal glasses represent a highly insulating material class. The thermal conductivity of the investigated P(MMA-*co*-nBA) particle colloidal glass is about 57 $\mathrm{mWm^{-1}K^{-1}}$ at a density of 0.77 $\mathrm{gcm^{-3}}$, which compares well to the value reported for 366 nm polystyrene colloidal crystals.[18] By mixing the two types of particles, the thermal conductivity can be tuned within these bounds. We find that the thermal conductivity increases monotonically with increasing polymer particle ratio within the colloidal assemblies. Thus, we do not find any sign of reduced thermal conductivity caused by mixing unlike particles, e.g., by additional interfacial resistances. We also cannot infer a distinct percolation threshold, which would be indicative for a preferred energy transport along a specific particle pathway.

We compare now our binary colloidal alloys to the existing set of mixing models.[13] The EMT model describes our system across the whole volume fraction range reasonably well. However, at low and high volume fractions, the Maxwell-Eucken (ME) models are also in reasonable agreement. For these regions, the separated inclusion assumption of the ME model is valid since the minority particle phase is dispersed in the majority phase. Furthermore, the parallel and the series model are not adequate for our colloidal alloys. Thus, besides the extreme mixing models, EMT and ME (in the respective volume fraction range) provide a reasonably good estimate of nanoscopically mixed materials.

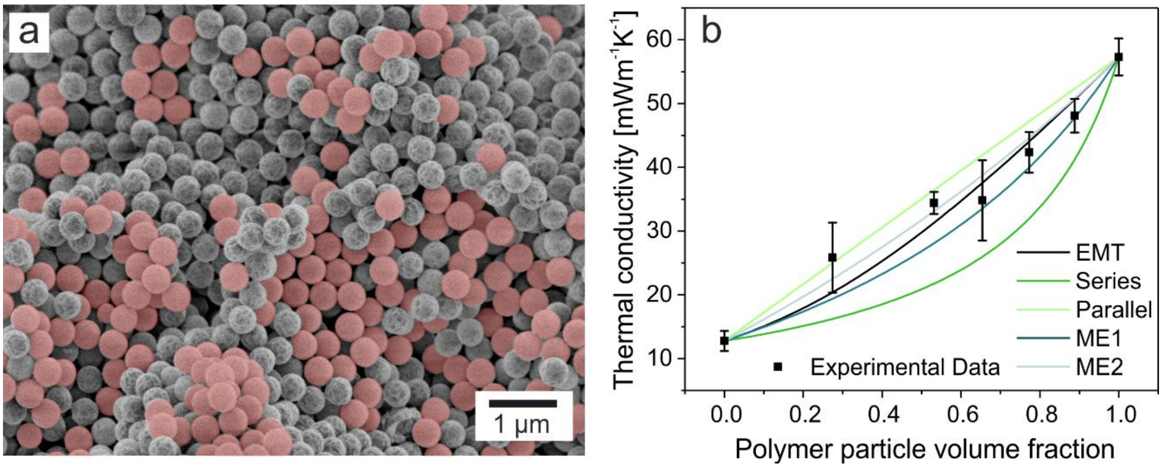

Figure 9.1. (a) Side-view scanning electron microscopy (SEM) image of the colloidal assembly with a polymer particle volume fraction of 53 % (53P). The hollow spheres are red-colored. (b) Thermal conductivity data of the binary colloidal glasses measured in vacuum at 25 °C (black squares) in comparison to different mixing models: effective medium theory (EMT), series model, parallel model, Maxwell-Eucken (ME) model 1 and 2.

Finite element modeling (FEM) is a useful tool to validate and understand the experimental data. Figure 9.2a compares the experimental values to the simulation results based on a random close-packed particle structure with random binary particle selection. FEM allows the screening of various composition ratios easily. The resulting thermal conductivity data (solid circles and squares) are plotted along with the EMT mixing model (solid line). The data obtained from finite element modeling fits very well to the experimental data and are well described by the EMT model. Thus, FEM and the EMT model are both suitable methods to predict the thermal conductivity of binary colloidal glasses. Furthermore, the assumptions implemented in the FEM simulation such as diffusive thermal transport and no interfacial thermal contact resistance between adjacent spheres describe the experimental situation adequately well.

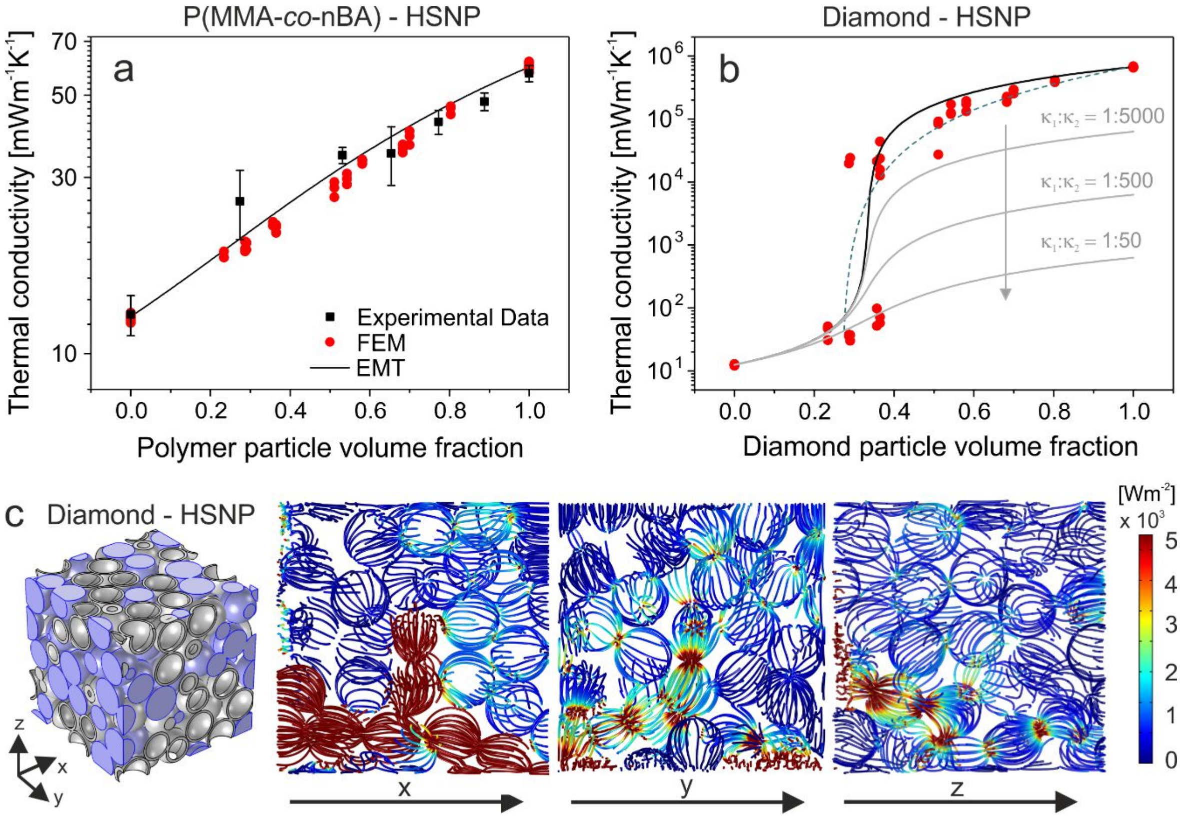

Figure 9.2. Finite element modeling (FEM) of binary colloidal assemblies with hollow silica spheres. (a) Thermal conductivity data of the binary particle mixtures and the EMT model in comparison to simulated data obtained from FEM. (b) Thermal conductivity data from FEM of binary colloidal glasses consisting of hollow spheres and diamond particles and the corresponding EMT model (black line). The gray lines show the EMT model for binary particle mixtures with a decreasing thermal conductivity difference (κ_1:κ_2) between the two types of particles. The blue dashed line represents the fit by a percolation model (Equation (9.2)). (c) The geometry of the binary colloidal glass with a diamond particle volume fraction of 36.5 % (blue particles) used for the FEM simulations and the corresponding heat flux streamlines for the different directions (x, y, and z).

We can now use FEM simulations to investigate the onset of percolation in binary colloidal crystals in greater detail. Therefore, we selected two types of dielectric particles, which possess a large thermal conductivity contrast, which is experimentally hardly accessible: hollow silica nanospheres and diamond particles. The large thermal conductivity contrast should allow for a clear assessment of the percolation through the colloidal assembly. The FEM results in comparison to the EMT model are shown in Figure 9.2b. The formation of percolation pathways is found at a particle ratio of about 30 % diamond particles. This mixing ratio range coincides with the onset of a high degree of variability between the individual simulation results. As outlined in the experimental part, each simulation was conducted along the x, y, and z axis of the simulation cube. In Figure 9.2c heat flow streamlines are shown for the different directions with a diamond particle volume ratio of 0.365. While in y- and z-direction the heat flow is relatively low (thermal conductivity of ~60 – 70 $\mathrm{mW\,m^{-1}\,K^{-1}}$), the heat flow in x-direction shows a percolation pathway, which increases the thermal conductivity to ~23590 $\mathrm{mW\,m^{-1}\,K^{-1}}$. This large variability is indicative of a critical mixing ratio close to the percolation threshold. Owing to the hardware limitation of the size of our simulation cube, fully percolated pathways only span across distinct orientations at this regime. Increasing the number of diamond particles (> 50 %) leads to a colloidal glass with robust percolating pathways in all directions. The effective medium theory describes this mechanism also quite well but overestimates the thermal conductivity at high diamond particle ratios. The percolation threshold is visible at a diamond particle volume ratio of about 30 %. The explicit percolation model (Equation (9.2)) provides a better way to describe the simulated data. In this equation, κ_1 and κ_2 are the effective thermal conductivities of the pure hollow sphere or polymer particle colloidal assembly. Therefore, the maximum filling packing factor F equals 1. The percolation model is plotted in Figure 9.2b as a blue dashed line and shows a clear consistency with the simulated data above the percolation threshold at a mixing ratio of 27 %.

To sum up, the EMT model describes the mixing of nanoparticles reasonably well, even for a significant difference between the distinct thermal conductivities. The percolation theory best describes the onset of percolation. Our results of the simulation thereby confirm the analytical solution. The ratio between the respective components should at least amount to 1:500 to observe a step-like increase in thermal conductivity (gray, solid lines in Figure 9.3b).

Thermal Transport Properties of Binary Colloidal Glasses – Temperature-Dependency

Exploiting the known temperature dependence of polymer colloidal crystals[18], we followed an alternative route to investigate percolation in our binary colloidal mixture experimentally. Briefly, upon crossing the glass transition temperature

(T_g) of the constituting polymer, the effective thermal conductivity of a polymer colloidal crystal increases by 200 – 300 %. We, therefore, measured the temperature-dependent thermal conductivity data at 1000 mbar in helium. The thermal conductivity for the different particle ratios is shown in Figure 9.3a.

The thermal conductivity of the pure hollow silica nanoparticle colloidal glasses shows a monotonic increase driven by the specific heat capacity, and no hysteresis. At the other extreme, the pure polymer particle glass exhibits the expected sharp increase of the thermal conductivity after exceeding the T_g due to the loss of the particulate structure (see SEM images in Figure 9.3d). The other particle mixtures feature a transient behavior between these two cases, however, with marked differences between the heating and cooling cycle. Figure 9.3b summarizes the differences before and after heating. In this case, any contribution from gaseous transport can be excluded since these data were measured in vacuum. While the thermal conductivity increases only minor up to 50 % polymer content, the rise is distinct for higher ratios, where the polymer constitutes the majority phase. This can be attributed to the formation of a continuous polymer network due to the loss of interfaces. Thus, heat can be conducted faster through the polymer phase, leading to a type of percolation after heating above the T_g (compare SEM image in Figure 9.3d). This is accompanied by an increase of the density shown in Figure 9.3c. Comparing this sort of percolation effect to the one discussed above, we find a discrepancy in the percolation onset. A percolating polymer network should form at about 27 % polymer beads; yet, the temperature induced percolation only sets in at polymer particle ratios > 50 %. Considering the concomitant increase in density, we conclude that the temperature-induced percolation is rather a measure of the structural integrity of overall particle ensemble. This starts to break down as soon as polymer particles constitute the majority phase.

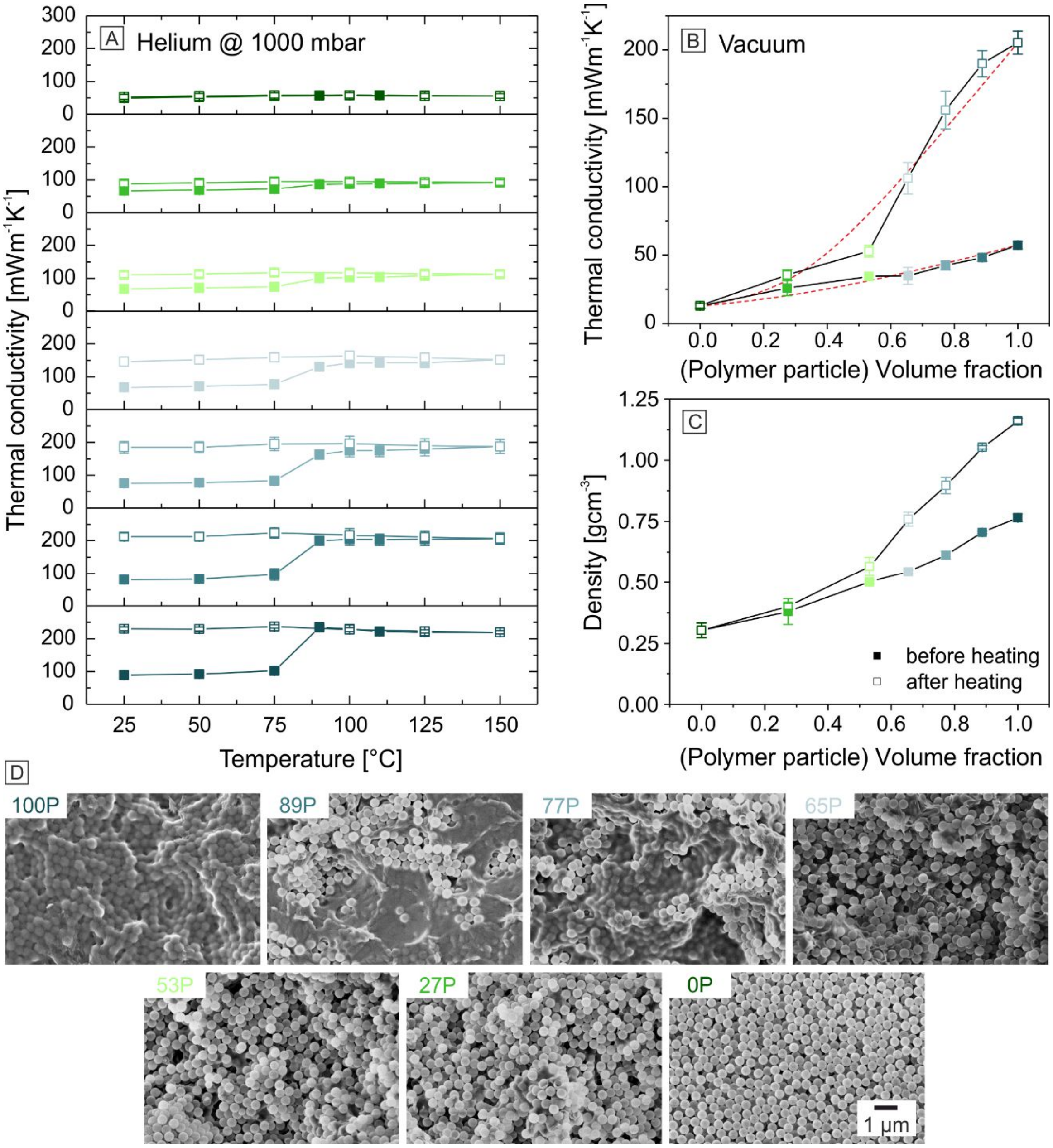

Figure 9.3. (a) Temperature-dependent thermal conductivity of colloidal glasses in helium at 1000 mbar. (b) Thermal conductivity of the particle assemblies before and after heating to 150 °C in vacuum. The red dashed line represents the EMT model (Figure S9.1). (c) Density of the colloidal assemblies before and after heating to 150 °C. (d) Scanning electron microscopy (SEM) images of the colloidal assemblies after heating to 150 °C.

The comparison of the molten film to the effective medium model reveals a second severe change to the homogeneity of the nanocomposite. The agreement between the EMT model and the measurement is much worse compared to the initial particle mixture. It now underestimates the thermal conductivity of high polymer mixing ratios and overestimates it at lower ratios. This hints towards a concomitant phase separation upon polymer annealing. The SEM images after the heating cycle qualitatively support this interpretation. Particularly for the case of low hollow sphere contents (89P and 77P) areas with large hollow sphere aggregates – even with a high degree of local order – can be inferred. These could originate from a relocation of the silica hollow spheres upon polymer film formation and confirm the challenge to fabricate homogeneous composite materials on the nanometer scale.

9.3 Conclusion

We investigated the thermal transport properties of binary colloidal glasses consisting of hollow silica nanoparticles and P(MMA-*co*-nBA) polymer particles. Mixing these two types of particles enables the fabrication of a nanocomposite material with a homogeneous distribution of the two components. The thermal conductivity increases from 13 $\mathrm{mW m^{-1} K^{-1}}$ to 57 $\mathrm{mW m^{-1} K^{-1}}$ in vacuum, depending on the particle mixture. Established mixing models are suitable to describe the effective thermal conductivity adequately. However, no percolation threshold can be observed in these particle mixtures. This is also validated by finite element modeling and the effective medium theory. Using finite element modeling, we validated our experimental results and provided a thorough understanding of the percolation threshold. We find that the thermal conductivity ratio (κ_1:κ_2) between two types of particles must be at least 1:500 to observe a distinct step in the mixing ratio dependency.

Heating the binary colloidal glasses above the glass transition temperature leads to a melting of the polymer and a loss of the interparticle interfaces. Thus, a continuous polymer network forms with solid particle inclusions for polymer contents > 50 %. This can be understood as a threshold of structural integrity. Concomitantly, the film formation induces a demixing of the hollow silica beads resulting in a heterogeneous structure. This is less well described by the EMT mixing model. Our study contributes to a thorough understanding of percolation, structural integrity, and effective thermal transport properties in particulate nanocomposite materials.

9.4 Experimental Section

Materials

Styrene (≥ 99 %, Aldrich), 2,2′-azobis(2-methylpropionamidine) dihydrochloride (AIBA; 97 %, Aldrich), [2-(methacryloxy)ethyl]trimethyl-ammonium chloride (MTC; 70 % solution in water, Polyscience), polyvinyl-pyrrolidone K30 (PVP, M_w ~ 55 kgmol^{-1}, Aldrich), tetraethylorthosilicate (TEOS, ≥ 99 %, Aldrich) and ammonium hydroxide solution (30 – 33 % in water, Aldrich) were used as received. Methyl methacrylate (MMA, 99 %, Aldrich) and *n*-butyl acrylate (nBA, ≥ 99 %, Aldrich) were purified by filtration over an alumina column (activated, basic, Brockmann I, Sigma-Aldrich). Ethanol was used in technical grade, and water was taken from a Millipore Direct Q3UV unit for the entire synthesis and purification steps.

Synthesis of Hollow Silica Nanoparticles

The synthesis of hollow silica spheres comprises three steps. (I) First, monodisperse polystyrene (PS) particles were prepared by emulsifier-free emulsion polymerization.[19] For the synthesis, 1.8 g PVP were dissolved in 10 mL water and added to a 500 mL three-necked flask, equipped with a reflux condenser and a gas inlet. 225 mL water, 26 mL styrene, and 75 µL MTC were added. The emulsion was degassed and heated to the reaction temperature of 70 °C at a stirring speed of 850 rpm for 30 min. For the initiation of the polymerization, 0.6 g AIBA, dissolved in 5 mL water, were added. After the nucleation, the stirring speed was reduced to 450 rpm, and the reaction was carried out overnight under an argon atmosphere. (II) In the second step, the polystyrene particles were coated with a thin silica shell by a modified Stoeber condensation process to obtain core/shell particles.[20] For the synthesis, 1.9 vol.% TEOS were added to an 81.4 vol.% ethanol, 10.7 vol.% water, 6.0 vol.% ammonium hydroxide solution containing 9.73 mgmL^{-1} PS latex particles. (III) Subsequently, the polystyrene core was removed by calcining the particles at 500 °C for 12 h in air.

Synthesis of P(MMA-*co*-nBA) particles

The polymer particles were prepared by emulsifier-free emulsion polymerization. For the synthesis, 450 mL water and a mixture of 40 ml and 10 mL MMA and nBA were added to a 1000 mL three-necked flask, equipped with a reflux condenser and a gas inlet. The emulsion was degassed and heated to the reaction temperature of 75 °C at a stirring speed of 650 rpm. After 15 minutes, 2 mL of acrylic acid were added to the mixture followed by a further equilibration step for 5 min. The polymerization was initiated by a rapid injection of 150 mg KPS dissolved in 5 mL water. After the nucleation, the stirring speed was reduced to 400 rpm to avoid the formation of aggregates. The reaction was carried out overnight under an argon atmosphere. Residual reagents were removed by dialysis against water for five days, changing water twice a day.

Assembly into Colloidal Glasses

Colloidal assemblies were prepared by a vacuum filtration system from Merck Millipore (see Figure S9.3). As a filter paper, an MF-Millipore membrane filter with a pore size of 0.2 µm was used. The sample size was reduced by a Teflon inset with a diameter of 2 cm. After the assembly, the samples were dried in vacuum overnight.

Characterization Methods

Scanning electron microscopy (SEM) was performed using a Leo 1530 instrument (Zeiss) using acceleration voltages of 2 or 3 kV. The images were taken with an InLens and Everhart-Thornley secondary electron detector.

Differential scanning calorimetry (DSC) measurements were performed on a Discovery Q2500 DSC (TA Instruments). For the determination of the specific heat capacity the ASTM E1269 standard test method was used. Powders of the particles (~10 mg) were scanned in closed aluminum pans under a dry nitrogen flow of

50 mLmin^{-1} over a temperature range from -40 to 210 °C with a heating rate of 20 °Cmin^{-1}. Two heating cycles were conducted, whereas only the second cycle was used for evaluation.

Thermal diffusivity measurements of the colloidal assemblies were performed on a xenon Flash apparatus (Linseis, XFA500) equipped with an InSb infrared detector. Before the measurements, the samples were coated with a thin graphitic layer (~15 µm) on each side to ensure a good absorbance at the bottom and a high emissivity at the top side of the sample. The thickness of the graphite layer is negligible compared to the thickness of the colloidal glasses (700 – 1500 µm). The measurements were performed on at least three samples in vacuum (~0.05 mbar) at room temperature, and in helium (1000 mbar) in the temperature range from 25 to 150 °C. The received data were evaluated by the software AproSoft Laser Flash Evaluation v1.06 using the radiation fit model. The schematic setup and the corresponding measurement signal, fitted by the radiation model, are shown in Figure S9.5.

The thicknesses of the colloidal glasses were measured using a Litematic VL50 (Mitutoyo) measuring unit.

The densities of the hollow sphere assemblies and the unmolten colloidal glasses (0P – 100P) were determined from the mass and volume of the monoliths. The volume was measured using a 3D digital surface profiler (Keyence V3100), and the mass was determined by weighing the colloidal glasses. The densities of the molten colloidal assemblies (27P – 100P) were measured using Archimedes' principle (buoyancy method). The colloidal glasses were hydrophobized by chemical vapor deposition using hexamethyldisilazane (HMDS) to avoid the adsorption of water by the hygroscopic silica network.

Finite Element Modeling

An amorphous structure of equally sized particles was compiled using a molecular dynamics simulation. Precisely, we used the gran/hooke pairpotential[21-23] in LAMMPS on a set of 20000 particles that were pulled by a gravitational force to the bottom of a simulation box with periodic boundaries in x and y direction. The *g(r)* of the resulting structure (Figure S9.7) shows the distinct features of a random sphere packing as described in literature.[24-28]

This amorphous particle structure was used for the finite element modeling (FEM) of the effective thermal transport properties using COMSOL Multiphysics®. A random selection process assigned the two types of particles (hollow silica nanoparticles and P(MMA-*co*-nBA) particles) to the simulated colloidal glass, yielding a binary colloidal assembly with different polymer particle volume fractions. The particle size has been adjusted such that the mutual contact points between the spheres resemble the experiment. There, we find a relative contact area of about 0.6 – 1 % of the total particle surface area per contact point. The absolute value of this contact area is of minor relevance for the discussion as it will only offset the overall thermal conductivity. For the hollow silica spheres, the experimental shell thickness-to-radius ratio was used. Three cubes per mixture, each with around 100 particles, were cut out of the amorphous structure. The allowed number of particles in the cube is limited by the physical memory of the simulation computer (128 GB). An exemplary structure used for FEM is shown in Figure 9.2c. A temperature difference was applied to opposite faces of the cube, while all remaining surfaces were thermally insulating. Therefore, purely one-dimensional thermal transport can occur. Furthermore, no thermal resistance between the particles was considered. The computed heat flux normal to the isothermal faces was used to calculate the effective thermal conductivity using Fourier's law (see Equation (S9.1)). The simulation was conducted along all three directions (x, y, and z) of the cube. The same simulations were undertaken using diamond instead of P(MMA-*co*-nBA) to obtain data for a binary colloidal assembly having a higher thermal conductivity contrast. The specific heat capacity, density, and thermal conductivity of all materials used in FEM simulations are listed in Table S9.2.

9.5 Acknowledgements

We acknowledge the help of Dr. Martin Dulle for MD simulation of the amorphous colloidal glass structure and the help of Bernd Kopera for the automated random selection procedure. Further support was provided by the SFB 840.

9.6 References

1. Tan, F. L.; Tso, C. P., Cooling of mobile electronic devices using phase change materials. *Appl. Therm. Eng.* **2004,** *24* (2), 159-169.

2. Moore, A. L.; Shi, L., Emerging challenges and materials for thermal management of electronics. *Materials Today* **2014,** *17* (4), 163-174.

3. Xia, Y.; Gates, B.; Yin, Y.; Lu, Y., Monodispersed Colloidal Spheres: Old Materials with New Applications. *Adv. Mater.* **2000,** *12* (10), 693-713.

4. Lee, G.-W.; Park, M.; Kim, J.; Lee, J. I.; Yoon, H. G., Enhanced thermal conductivity of polymer composites filled with hybrid filler. *Composites Part A: Applied Science and Manufacturing* **2006,** *37* (5), 727-734.

5. Han, Z.; Fina, A., Thermal conductivity of carbon nanotubes and their polymer nanocomposites: A review. *Progress in Polymer Science* **2011,** *36* (7), 914-944.

6. Hasselman, D. P. H.; Johnson, L. F., Effective Thermal Conductivity of Composites with Interfacial Thermal Barrier Resistance. *J. Compos. Mater.* **1987,** *21* (6), 508-515.

7. Stauffer, D.; Aharony, A., *Introduction To Percolation Theory*. Taylor & Francis: 1994.

8. Tian, W.; Yang, R., Phonon transport and thermal conductivity percolation in random nanoparticle composites. *Computer modeling in engineering and sciences* **2008,** *24* (2/3), 123.

9. Xue, Q., The influence of particle shape and size on electric conductivity of metal–polymer composites. *European Polymer Journal* **2004,** *40* (2), 323-327.

10. Kumar, S.; Alam, M. A.; Murthy, J. Y., Effect of percolation on thermal transport in nanotube composites. *Appl. Phys. Lett.* **2007,** *90* (10), 104105.

11. Mamunya, Y. P.; Davydenko, V. V.; Pissis, P.; Lebedev, E. V., Electrical and thermal conductivity of polymers filled with metal powders. *European Polymer Journal* **2002,** *38* (9), 1887-1897.

12. Lux, F., Models proposed to explain the electrical conductivity of mixtures made of conductive and insulating materials. *Journal of Materials Science* **1993,** *28* (2), 285-301.

13. Carson, J. K.; Lovatt, S. J.; Tanner, D. J.; Cleland, A. C., Thermal conductivity bounds for isotropic, porous materials. *International Journal of Heat and Mass Transfer* **2005,** *48* (11), 2150-2158.

14. Wang, J.; Carson, J. K.; North, M. F.; Cleland, D. J., A new approach to modelling the effective thermal conductivity of heterogeneous materials. *International Journal of Heat and Mass Transfer* **2006,** *49* (17–18), 3075-3083.

15. Hashin, Z.; Shtrikman, S., A Variational Approach to the Theory of the Effective Magnetic Permeability of Multiphase Materials. *J. Appl. Phys.* **1962,** *33* (10), 3125-3131.

16. Ruckdeschel, P.; Kemnitzer, T. W.; Nutz, F. A.; Senker, J.; Retsch, M., Hollow silica sphere colloidal crystals: insights into calcination dependent thermal transport. *Nanoscale* **2015,** *7* (22), 10059-10070.

17. Ruckdeschel, P.; Philipp, A.; Retsch, M., Understanding Thermal Insulation in Porous, Particulate Materials. *Adv. Funct. Mater.* **2017**.

18. Nutz, F. A.; Ruckdeschel, P.; Retsch, M., Polystyrene colloidal crystals: Interface controlled thermal conductivity in an open-porous mesoparticle superstructure. *J. Colloid Interf. Sci.* **2015,** *457*, 96-101.

19. Goodwin, J. W.; Hearn, J.; Ho, C. C.; Ottewill, R. H., Studies on the preparation and characterisation of monodisperse polystyrene laticee. *Colloid Polym. Sci.* **1974,** *252* (6), 464-471.

20. Graf, C.; Vossen, D. L. J.; Imhof, A.; van Blaaderen, A., A General Method To Coat Colloidal Particles with Silica. *Langmuir* **2003,** *19* (17), 6693-6700.

21. Brilliantov, N. V.; Spahn, F.; Hertzsch, J.-M.; Pöschel, T., Model for collisions in granular gases. *Physical Review E* **1996,** *53* (5), 5382-5392.

22. Silbert, L. E.; Ertaş, D.; Grest, G. S.; Halsey, T. C.; Levine, D.; Plimpton, S. J., Granular flow down an inclined plane: Bagnold scaling and rheology. *Physical Review E* **2001,** *64* (5), 051302.

23. Zhang, H. P.; Makse, H. A., Jamming transition in emulsions and granular materials. *Physical Review E* **2005,** *72* (1), 011301.

24. Mason, G., Radial Distribution Functions from Small Packings of Spheres. *Nature* **1968,** *217* (5130), 733-735.

25. Seidler, G. T.; Martinez, G.; Seeley, L. H.; Kim, K. H.; Behne, E. A.; Zaranek, S.; Chapman, B. D.; Heald, S. M.; Brewe, D. L., Granule-by-granule reconstruction of a sandpile from x-ray microtomography data. *Physical Review E* **2000,** *62* (6), 8175-8181.

26. Clarke, A. S.; Jónsson, H., Structural changes accompanying densification of random hard-sphere packings. *Physical Review E* **1993,** *47* (6), 3975-3984.

27. Yang, R. Y.; Zou, R. P.; Yu, A. B., Computer simulation of the packing of fine particles. *Physical Review E* **2000,** *62* (3), 3900-3908.

28. Kansal, A. R.; Torquato, S.; Stillinger, F. H., Diversity of order and densities in jammed hard-particle packings. *Physical Review E* **2002,** *66* (4), 041109.

9.7 Supporting Information

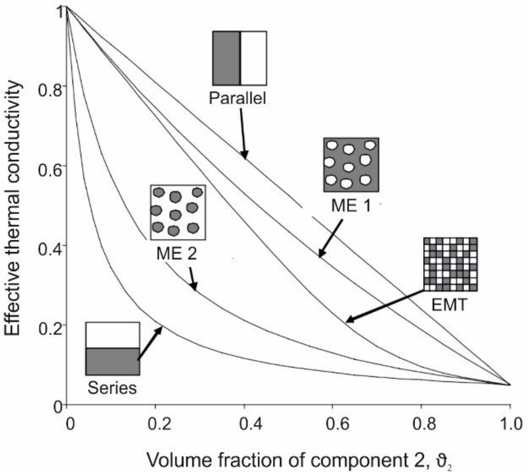

Series model	$\kappa_e = \frac{1}{\frac{1-\vartheta_2}{\kappa_1} + \frac{\vartheta_2}{\kappa_2}}$
Parallel model	$\kappa_e = (1-\vartheta_2)\kappa_1 + \vartheta_2\kappa_2$
Maxwell-Eucken 1	$\kappa_e = \kappa_1 \frac{2\kappa_1 + \kappa_2 - 2(\kappa_1 - \kappa_2)\vartheta_2}{2\kappa_1 + \kappa_2 + (\kappa_1 - \kappa_2)\vartheta_2}$
Maxwell-Eucken 2	$\kappa_e = \kappa_2 \frac{2\kappa_2 + \kappa_1 - 2(\kappa_2 - \kappa_1)(1-\vartheta_2)}{2\kappa_2 + \kappa_1 + (\kappa_2 - \kappa_1)(1-\vartheta_2)}$
Effective medium theory (EMT)	$\kappa_e = 1/4((3\vartheta_2 - 1)\kappa_2 + [3(1-\vartheta_2) - 1]\kappa_1$ $+\sqrt{[(3\vartheta_2 - 1)\kappa_1 + (3\{1-\vartheta_2\} - 1)\kappa_1]^2 + 8\kappa_1\kappa_2}$

Figure S9.1. Relative effective thermal conductivities κ_e for the series, the parallel, the Maxwell-Eucken (ME) and the effective medium theory (EMT) model and the corresponding equations. In the ME1 model, 1 is the continuous phase, whereas, in the ME2 model, 1 is the dispersed phase. Adapted with permission from Carson et al. (Carson, J. K.; Lovatt, S. J.; Tanner, D. J.; Cleland, A. C., Thermal conductivity bounds for isotropic, porous materials. Int. J. Heat Mass Tran. 2005, 48 (11), 2150-2158).

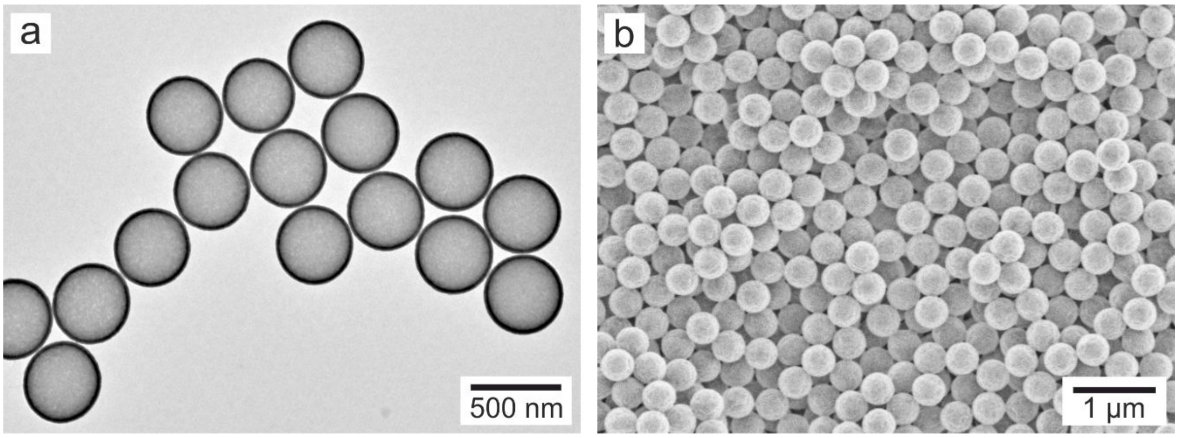

Figure S9.2. (a) Transmission electron microscopy (TEM) images of the hollow silica nanoparticles, (b) Scanning electron microscopy (SEM) images of the P(MMA-*co*-nBA) particles.

Table S9.1. Designation of the binary colloidal assemblies and the corresponding polymer particle volume fraction.

	100P	87.5P	75P	62.5P	50P	25P	0P
Number of Polymer Particles [%]	100	87.5	75	62.5	50	25	0
Polymer Particle Volume Fraction	1	0.89	0.77	0.65	0.53	0.27	0

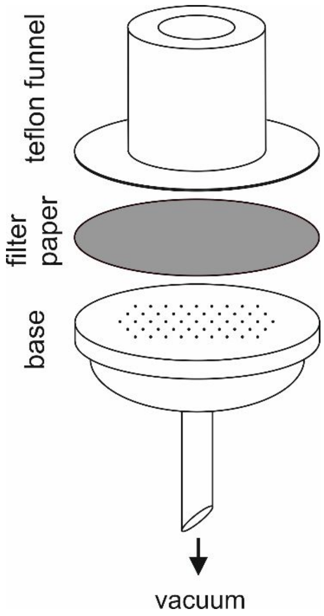

Figure S9.3. Schematic setup of the vacuum filtration system. The parts were held together by a spring clamp and put on a filter flask.

SEM images, before heating:

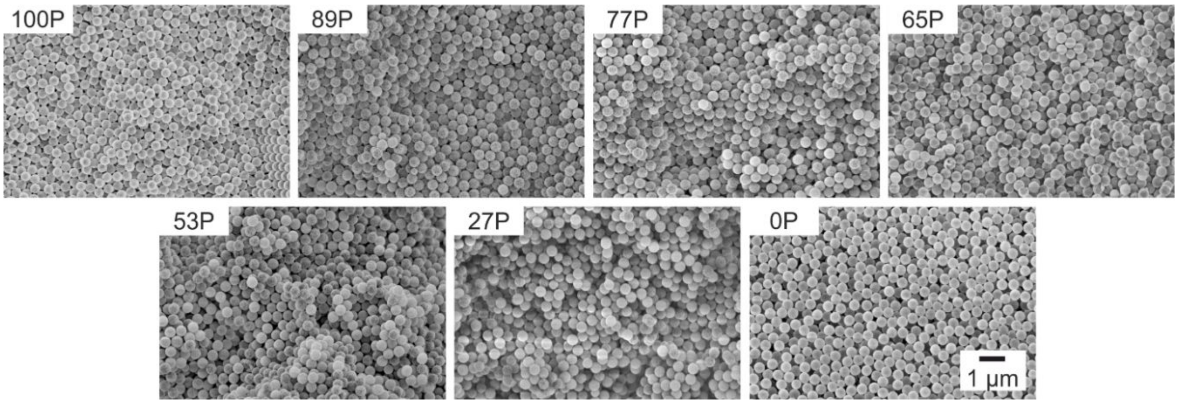

Figure S9.4. Scanning electron microscopy images of the binary colloidal glasses comprising 100% - 0 % polymer particles.

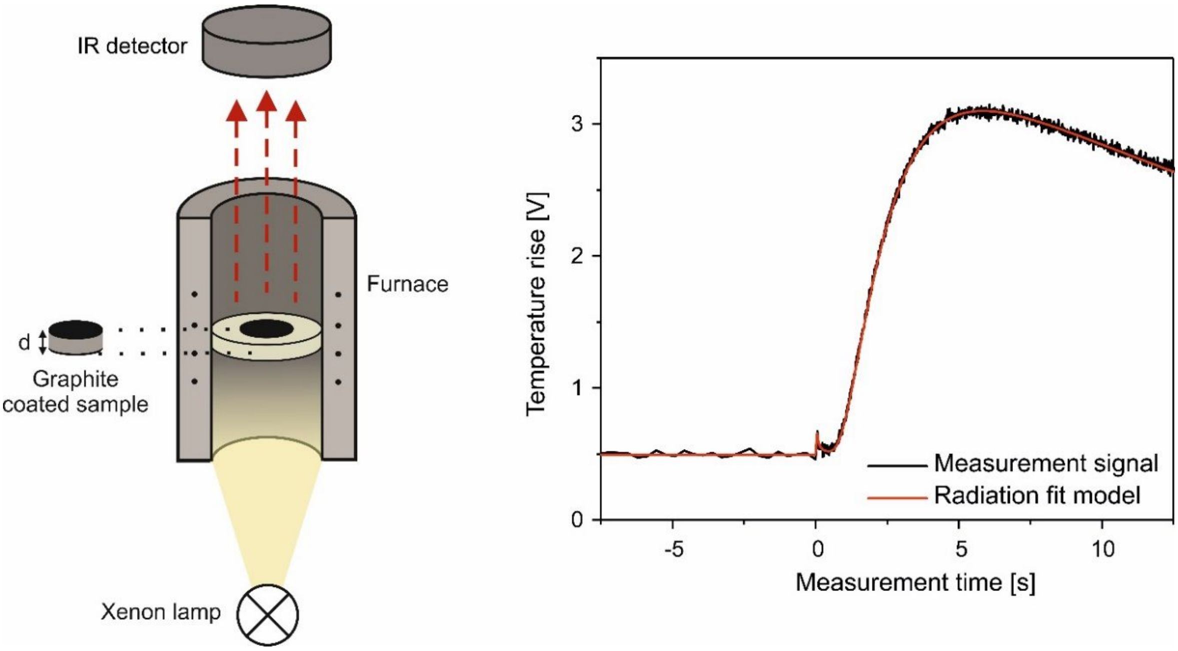

Figure S9.5. Schematic setup of the xenon flash analysis and the corresponding measurement signal with radiation fit. This fit model represents an extension to the finite-pulse and heat loss corrections given by the Combined fit model from Dusza (L. Dusza, High Temperatures – High Pressures, **1995**, 27, 467-473). By contrast, it allows the xenon flash to be partly transmitted to the rear sample surface, leading to an instantaneous temperature jump analogous to Blumm et al. (J. Blumm, J. Henderson, O. Nilsson and J. Fricke, High Temperatures-High Pressures, **1997**, 29, 555-560).

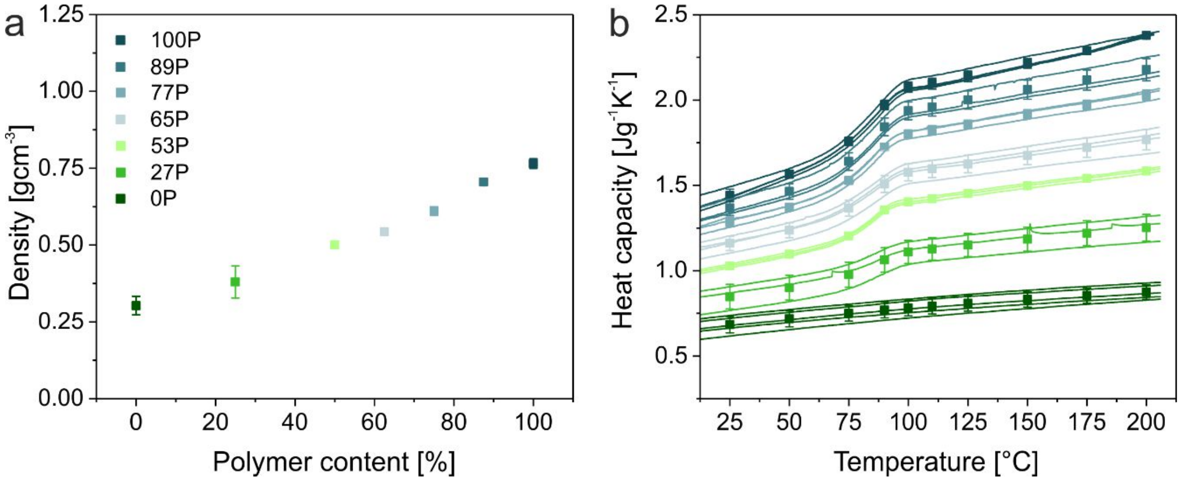

Figure S9.6. (a) The density of the different binary colloidal glasses. (b) Differential scanning calorimetry (DSC) measurements of the particle mixtures.

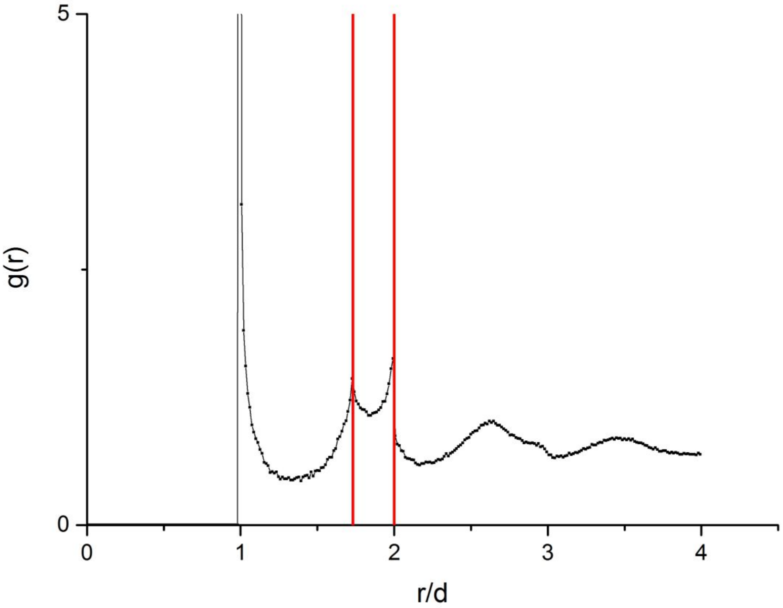

Figure S9.7. The radial distribution function of a random close-packed particle assembly from molecular dynamics simulation (program LAMMPS). The two red lines are at √3/d and 2/d.

Fourier's law of heat conduction:

For the FEM simulation, a temperature difference was applied to opposite faces of the cube. This defines the temperature gradient across the colloidal structure and serves at the same time as a heat source and a heat sink, respectively. Thermal insulation boundary conditions are imposed on all other faces of the cube. The computed heat flux normal to the isothermal faces was used to calculate the effective thermal conductivity using Fourier's law:

$$\kappa_{eff} = \frac{Q/A}{\Delta T/h} \tag{S9.1}$$

where Q is the heat flow rate normal to the isothermal faces, A the cross-sectional area of the cube, ΔT the temperature difference ($T_{hot} - T_{cold}$), and h the cube edge length.

Table S9.2. Specific heat capacity, density, and thermal conductivity of silica, P(MMA-*co*-nBA), and diamond used in FEM simulations.

	Specific heat capacity [Jg^{-1}K^{-1}]	**Density [gcm^{-3}]**	**Thermal conductivity [mWm^{-1}K^{-1}]**
Silica	0.684	2.20	173[a)]
P(MMA-*co*-nBA)	1.441	1.16	205
Diamond[b)]	0.507	3.51	2,300,000

[a)] *The thermal conductivity of silica is chosen such that the same effective thermal conductivity is obtained as experimentally in vacuum.*

[b)] *The literature values were obtained from Salazar (Salazar, A., On thermal diffusivity. Eur. J. Phys. 2003, 24 (4), 351.) and Slack (Slack, G. A., Thermal Conductivity of Pure and Impure Silicon, Silicon Carbide, and Diamond. J. Appl. Phys. 1964, 35 (12), 3460-3466.).*

10 Interface and Morphology Control of the Thermal Conductivity in Core-Shell Particle Colloidal Crystals

Pia Ruckdeschel, and Markus Retsch

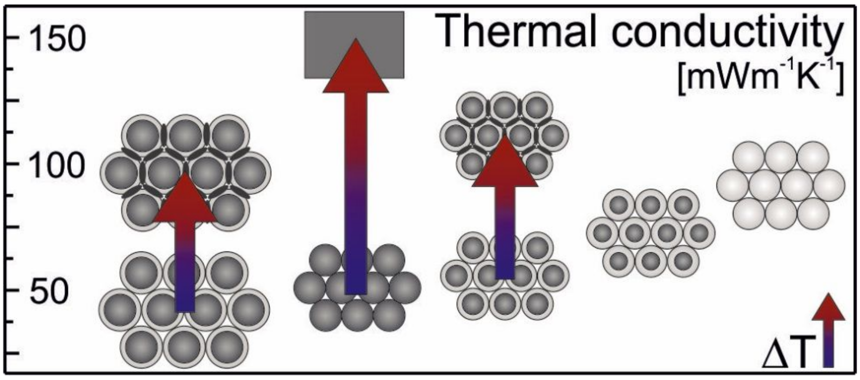

Submitted version - reprinted with permission from Ruckdeschel *et al.*, *Adv. Mater. Interf.*, **2017**, 4 (24)**,** 1700963. Copyright© 2017 Wiley VCH.

Abstract

We investigate the thermal transport properties of nanostructured composite colloidal assemblies. These are of importance for future phase change material applications, which increasingly address the µm and sub µm range. We use polystyrene silica core shell colloidal particles sizes of 270 – 460 nm and shell thicknesses of 15 – 42 nm as a structurally well-defined model system. We can deduce precise structure property relationships with the lowest thermal conductivity being observed for particles with a large diameter, a thin shell thickness, and the highest polymer content. Importantly, we find clear evidence for polymer leakage through 15 nm silica shells when exceeding the glass transition temperature of the core polymer. This leads to a strong increase in thermal conductivity but also presents a lower limit for the silica shell thickness to contain a second phase. The leakage temperature is influenced by the overall particle size and can be completely suppressed by the use of thicker shell geometries. The leakage starts at temperatures way above the glass transition temperature of the polymer and is governed by the porosity of the silica shell.

For a complete understanding, we discuss our findings in the light of colloidal crystals consisting of pure silica and polystyrene particles. Solid silica sphere colloidal crystals possess the highest thermal conductivity, pure polymer beads the lowest. This demonstrates to which extent the thermal transport properties can be solely adjusted by the particle composition and morphology.

10.1 Introduction

Nanomaterials and materials with nanostructured interfaces have attracted a lot of attention in the last decades. Besides the trend of achieving smaller and smaller structures, for example for microelectronics, the reduction of the structural size towards the nanometer scale established materials with novel properties compared to the corresponding bulk phase.[1] This originates from the large surface-to-volume ratio of nanomaterials, and the accompanying large number of interfaces.[2] These unique properties have opened the opportunity for application such as catalysis[3], energy conversion and storage[4], photocatalysis[5], sensing[6], and photonics[7]. Quite recently, heat management has also increasingly attracted attention.[8-9] Emerging applications based on nanostructured materials are thermal energy storage[10-11], thermal barrier coatings[12], thermal insulation[13-14], and thermoelectricity[15], to name a few.

It is essential to have access to structurally and chemically well-defined materials to develop a good understanding of the heat transport in such nanomaterials. Colloidal assemblies provide a versatile platform to fulfill this challenging demand. Colloidal assemblies are highly ordered superstructures, consisting of monodisperse nanoparticles with a defined chemical composition.[16] Key properties of colloidal superstructure comprise: (i) wide variability of material composition (i.e., polymer, metal oxides, and composites), (ii) scalability due to the ease of fabrication, (iii) adjustment of the symmetry (crystalline or amorphous packing), and (iv) large number of interfaces. Furthermore, with colloidal particles being available in sizes from a few nanometers up to micrometers[17-20] a vast range of length scales with relevance to many diverse heat management applications can be addressed.

Important concepts of thermal transport through colloidal assembly structures have been reported in the recent literature on nanocrystal arrays[21-23], nanolaminates[24], and colloidal crystals[25-26]. Briefly, a lot of interfaces in these (heterostructured) materials represent a strong interface resistance for the transport of thermal energy in the form of vibrational modes. Thus, colloidal assemblies have typically low thermal conductivities, and their thermal transport properties can be adjusted by modifying the composition, the interfacial binding strength, the packing symmetry, and order. In the quite common case of spherical colloidal building blocks, the effective thermal conductivity critically depends on the contact area and the interfacial adhesion between the individual spheres.[25-26]

The latent heat storage provides an emerging heat management application in phase change materials. The major goal is to convert excess heat into chemical energy using a first order transition (typically melting of low melting compounds such as wax). In principle two categories of phase change materials are being discussed: (i) the phase change material is the continuous majority phase with dispersed nanoparticle inclusion,[27] (ii) the phase change materials is encapsulated and is used either in a dispersed state or as a dried particulate film (e.g., as a wall paint).[28] In either case, the heat transfer through such highly heterostructured materials is of great importance for the melting and solidification process. This question becomes, even more, pressing with the continuing trend toward micro- and nano-encapsulation of phase change materials.[10, 27-30] Therefore, one needs to control and understand the various contributions of thermal transport in colloidally derived materials as outlined above.

This paper presents a thorough investigation of structure-property relationship of the thermal transport properties of polystyrene-silica core-shell particles. Silica is a promising shell material for future phase change applications due to its structural rigidity.[28] We choose polystyrene as the core material due to its unbeaten monodispersity in the form of sub-µm latex beads, giving us a maximum of structural control. Clearly, it is not suitable as core material for phase change applications, so we will not assess any latent heat storage capacity of this system. Instead, using particles in the size range from 269 to 469 nm and shell thicknesses from 15 to 42 nm, we focus on the influence of the composition and the mutual interfaces on the temperature-dependent thermal diffusivity and conductivity. We contrast our findings to the respective pure particulate phases (pure PS and pure SiO_2 beads) to provide a comprehensive picture on the thermal transport through such materials.

10.2 Results and Discussion

Polystyrene Silica Core Shell Particle Colloidal Crystals

We determine the influence of the particle size and morphology on the thermal transport properties via five different core-shell particles (size and shell thickness series). The monodisperse template particles are shown in Figure S10.1 in the Supporting Information (Chapter 10.7).

We keep the shell thickness constant at ~15 nm, to single out the influence of the overall particle size. The resulting core-shell particle sizes range from 269 to 479 nm. To elaborate the influence of the shell thickness, the overall particle size was kept constant at ~270 nm, and the shell thickness was adjusted between 14.5 and 42 nm. The particle morphology was determined by evaluating scanning electron microscopy (SEM) images, and the shell thicknesses were identified using small-angle X-ray scattering (SAXS). The results and the corresponding core/shell ratios are summarized in Figure S10.2 and Table 10.1. For the nomenclature, the size or the shell thickness is used (CS-xxx). Both measurement techniques highlight the low polydispersity of the structural entities.[31]

Table 10.1. The diameter (d), the shell thickness (t), and the PS/SiO_2 ratio received from SEM and SAXS measurements, as well as the density of the corresponding colloidal crystals (CCs).

	SEM	*SAXS*		*Density*[a]
	d **[nm]**	**t** **[nm]**	**PS/SiO_2** **[%]**	**ρ (CC)** **[g/cm³]**
CS-479	479 ± 13	18	79	0.80 ± 0.01
CS-392	392 ± 6	15	79	0.82 ± 0.01
CS-269/15	269 ± 5	14.5	71	0.89 ± 0.02
CS-29	266 ± 5	29	48	1.01 ± 0.01
CS-42	268 ± 5	42	32	1.08 ± 0.02

[a] *The densities were determined by measuring the volume and weight of the samples (see Experimental Part).*

The monodispersity of the core-shell particles enables an assembly into highly ordered 3D colloidal crystals with well-defined contact points and well-defined densities. Side-view images of the particle assemblies are shown on the left side in

Figure 10.1. The high ordering induces brilliant colors resulting from Bragg reflections. Another evidence for the dense packing is given by side-view SEM images (Figure 10.1, right side). This allows us to assume the volume fraction of the particles in the colloidal crystal to be close to its ideal value of 74 %. This is an upper limit since small amorphous regimes will lower this volume fraction. The resulting density ranges from 0.80 gcm^{-3} (CS-479) to 1.08 gcm^{-3} (CS-42).

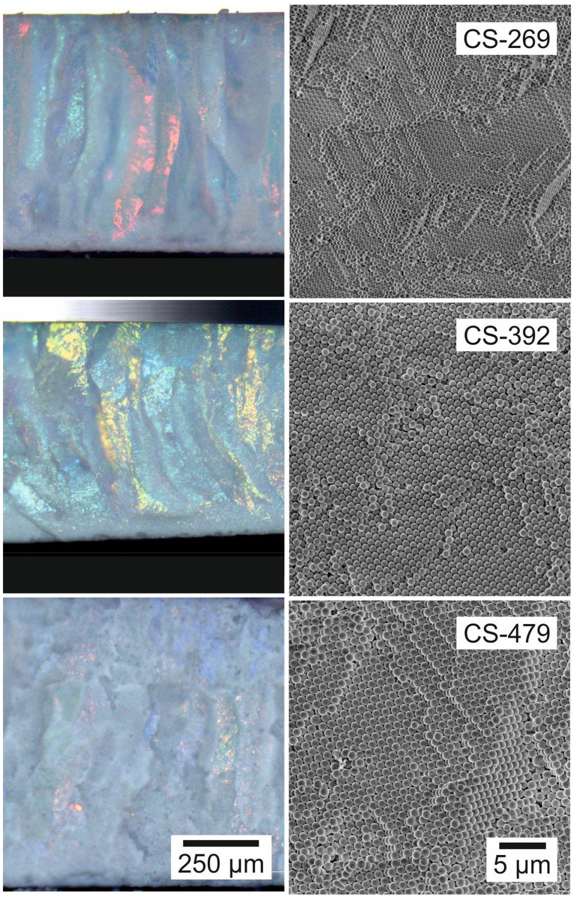

Figure 10.1. Bright field light microscopy and scanning electron microscopy (SEM) images of the core-shell particle colloidal crystals with three different sizes (479 nm, 392 nm, and 269 nm). The opalescence (left panel) indicates a high degree of crystallinity throughout the entire colloidal monolith. The hexagonally close-packed structure is confirmed by SEM (right side).

Thermal Transport Properties

The thermal diffusivities of the colloidal crystals were determined by xenon flash analysis (XFA). It gives a measure of how fast temperature diffuses through a material. Hence, it is a measure of how fast a phase change material may exceed its melting point T_m. Details about the measurement method are provided in Figure S10.3 and the Experimental Part. The measurements were conducted in vacuum and helium in a temperature range from 25 °C to 200 °C. Using the thermal diffusivity α, the heat capacity c_p, and the density ρ, the thermal conductivity can be calculated:

$$\kappa = \alpha \cdot c_p \cdot \rho \tag{10.1}$$

With the thermal conductivity, we gain knowledge about how much energy is conducted through a material. This is of relevance for the duration of the melting/solidification process.

Size Influence

First, the temperature-dependent thermal diffusivity for the three different sizes of core-shell particles are presented in Figure 10.2a. We find an increase of the thermal diffusivity with decreasing particle diameter by about 25 %. This can be traced back to a density increase from 0.80 gcm^{-3} to 0.89 gcm^{-3} and a slight increase in the contact area between adjacent particles (see Table S10.1). However, heating the colloidal crystal above the glass transition temperature (T_g) changes the thermal diffusivity tremendously. The thermal diffusivity increases strongly during the first heating cycle between 100 and 175 °C. For all sizes, a large hysteresis between the heating and cooling cycle is observed. During the second heating cycle, the thermal diffusivity remains at the higher level. This is exemplarily shown for CS-269 in Figure S10.4. This step-like increase is quite unexpected due to the silica shell surrounding the polystyrene particles, which is supposed to hinder the polystyrene to leak out. Furthermore, this step is broadened compared to polystyrene colloidal crystals, which possess a sharp phase transition at the glass transition temperature.[26]

By using SEM, we could validate that indeed polymer leakage through the silica shell is the reason for this substantial increase in thermal diffusivity (Figure 10.2d).

This is indicated by necks emerging after the first heating cycle. The polystyrene leakage increases the thermal diffusivity at room temperature by about 80 – 115 %. This increase is strongest for the largest particles (CS-479) and less pronounced for the smallest particles (CS-269). It correlates well with the change to the neck size between adjacent spheres and thereby with the contact area (see Table S10.1). Before heating, the total contact area is measured to be between 11 % for the larger spheres and 13 % for the smallest ones. This reverses after the heating process with a total contact area of about 34 % for the largest spheres and only 29 % for the smallest particles. The stronger increase of the contact area of the sample CS-479 explains well that the increase of the thermal diffusivity is more pronounced for these colloidal crystals.

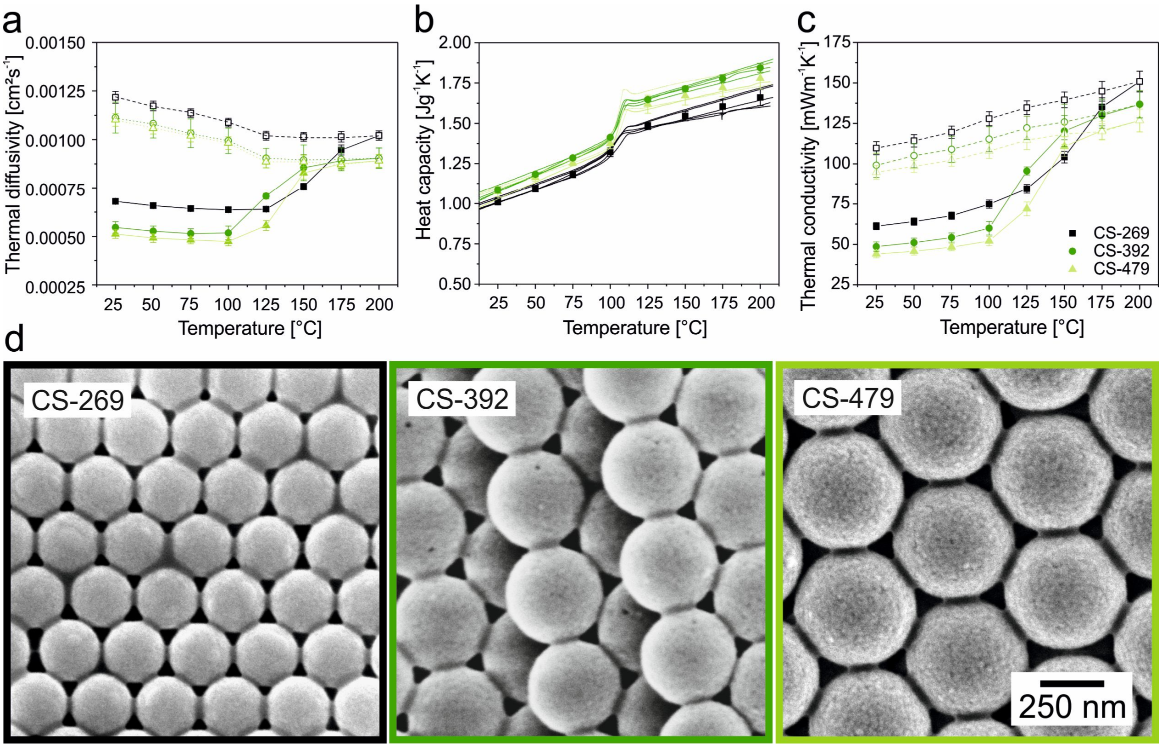

Figure 10.2. Thermal properties of the core-shell particle colloidal crystals CS-269, CS-392, and CS-479. The samples are measured in dependence of the temperature in vacuum. The open symbols and the dashed lines represent the cooling cycles. (a) Thermal diffusivity data, (b) specific heat capacity, and (c) thermal conductivity data. (d) SEM images of the core-shell particles of the size series after heating up to 200 °C.

Using the temperature-dependent heat capacity (Figure 10.2b) and density (Table 10.1) of the individual particle we calculated the thermal conductivity (Figure 10.2c).

At room temperature, the thermal conductivity of the colloidal crystals increases with decreasing particle diameter from 44 $\mathrm{mW\,m^{-1}K^{-1}}$ to 61 $\mathrm{mW\,m^{-1}K^{-1}}$. With increasing temperature, the thermal conductivity at first increases slightly as expected for amorphous materials. After exceeding the glass transition temperature, the thermal conductivity exhibits a strong and broad increase due to the leakage of the polystyrene through the silica shell. This transition is located between 125 °C and 175 °C for the smallest core-shell particles (CS-269) and between 100 °C and 150 °C for the larger core-shell particles (CS-392 and CS-479). In accordance to literature[32], we want to stress that the differences in leakage temperature are not caused by changes in the glass transition temperature. This remains constant at about 105 °C for all samples (Figure 10.2b). Alternative explanations for the different leakage temperatures could be given by differences (i) in the Laplace pressure acting on the polystyrene melt surrounded by the silica shell,[33] (ii) of the pressure on the polystyrene core caused by differences in the thermal expansion coefficient,[32] or (iii) in the porosity of the silica shell.

In general, the pressure has a strong effect on the viscosity of polymer melts. By increasing the pressure, the free volume between the polymer chains decreases, which is particularly important for amorphous polymers with large side groups such as polystyrene. Thus, Brownian motion of the chains is inhibited, and the viscosity increases.[34-35]

The Laplace pressure is relatively low (less than 1 MPa) for all particle sizes, assuming a surface tension of 5 – 35 $\mathrm{Nm^{-1}}$ for the polystyrene melt.[36] The different thermal expansion coefficients of the core ($\sim 2\cdot 10^{-4}\ \mathrm{K^{-1}} < T_g < 6\cdot 10^{-4}\ \mathrm{K^{-1}}$)[37] and the shell ($5.5\cdot 10^{-7}\ \mathrm{K^{-1}}$)[38] material generate an appreciable pressure at the glass transition temperature of about 60 MPa, and even higher beyond T_g[32] However, this pressure increase is independent of the particle size. Therefore, we attribute the different leakage temperature to the meso- and macroporosity of the silica shell. While the microporosity is similar for all particles (see Figure S10.5 and Table S10.2), the meso- and macroporosity differ between the particles although the shell thickness has been kept constant. To emphasize the porosity difference, the core-shell particles are calcined in air to remove the polymer core (Figure S10.6). It is apparent from the bright speckles on the silica shell that the macroporosity is higher for the larger particles CS-479 and CS-392 and lower for the smaller particles CS-269. Thus, the resistance to leak through the silica shell is higher for the smaller particles leading to a retarded release. This is further verified by an even smaller core-shell particle with a diameter of (216 ± 6) nm but a similar shell thickness of 16 nm (Figure S10.7a,b). Here, the leakage starts at an even higher temperature at around 150 °C (Figure S10.7c,d)

Overall we can conclude from the size dependence that nanostructuring and reducing the overall capsule size indeed helps to increase the thermal diffusivity and thermal conductivity. This may also be beneficial in the light of a rapidly responding phase change material. However, when using silica as the shell material, one has to consider leakage issues through the silica shell. Again, a reduced particle size is beneficial as the degree of meso- and macroporosity decreases with particle size.

Shell Thickness Series

To fully exclude any leakage issues, increasing the shell thickness is the obvious choice. We, therefore, synthesized particles with the same outer diameter of about 270 nm but with shell thicknesses varying between 14.5 nm and 42 nm. Thus the polystyrene/silica ratio changes from 71 to 32 %. The change of the particle composition can also be followed by the heat capacity measurements for the three different particles (Figure 10.3). The heat capacity decreases with increasing amounts of silica. The measured heat capacities correspond well to the volume average of a mixture of pure PS and pure SiO_2. Additionally, the step at the glass transition temperature of polystyrene becomes less pronounced for thicker shells.

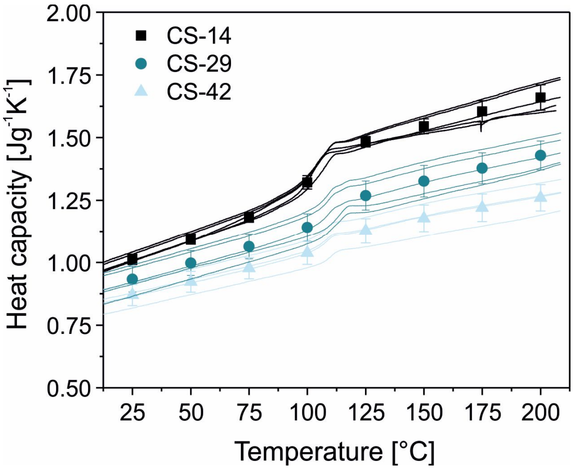

Figure 10.3. The heat capacity of core-shell particles with 270 nm diameter but different shell thicknesses. The increasing ratio of SiO_2 in the composite particle is reflected in a systematic decrease in the heat capacity.

Whereas, the heat capacity decreases with increasing shell thickness, the density, and thermal diffusivity of the colloidal crystals behaves reversely (light microscopy and SEM side-view images are shown in Figure S10.8). The thermal diffusivity data, shown in Figure S10.9, exhibits an increase of the thermal diffusivity of about 36 % from the thinnest to the thickest shell. This can be traced back to the higher temperature diffusion through the silica component compared to the polymer network. Figure 10.4a-c shows the corresponding thermal conductivity data. The thermal conductivity increases by 43 % from 61 $\mathrm{mW\,m^{-1}K^{-1}}$ to 87 $\mathrm{mW\,m^{-1}K^{-1}}$ at 25 °C with increasing shell thickness. Doubling the shell thickness from 15 nm up to 29 nm, was indeed sufficient to suppress the polymer leakage completely. Consequently, for the thicker silica shells CS-29 and CS42 (see SEM images, Figure 10.4d), the contact area between the particles did not change after the first heating cycle, and the thermal conductivity remained constant during the heating and cooling cycles. The small decrease of the thermal conductivity for the cooling cycle (Figure 10.4c) can be explained by the loss of absorbed water in the hygroscopic silica network.

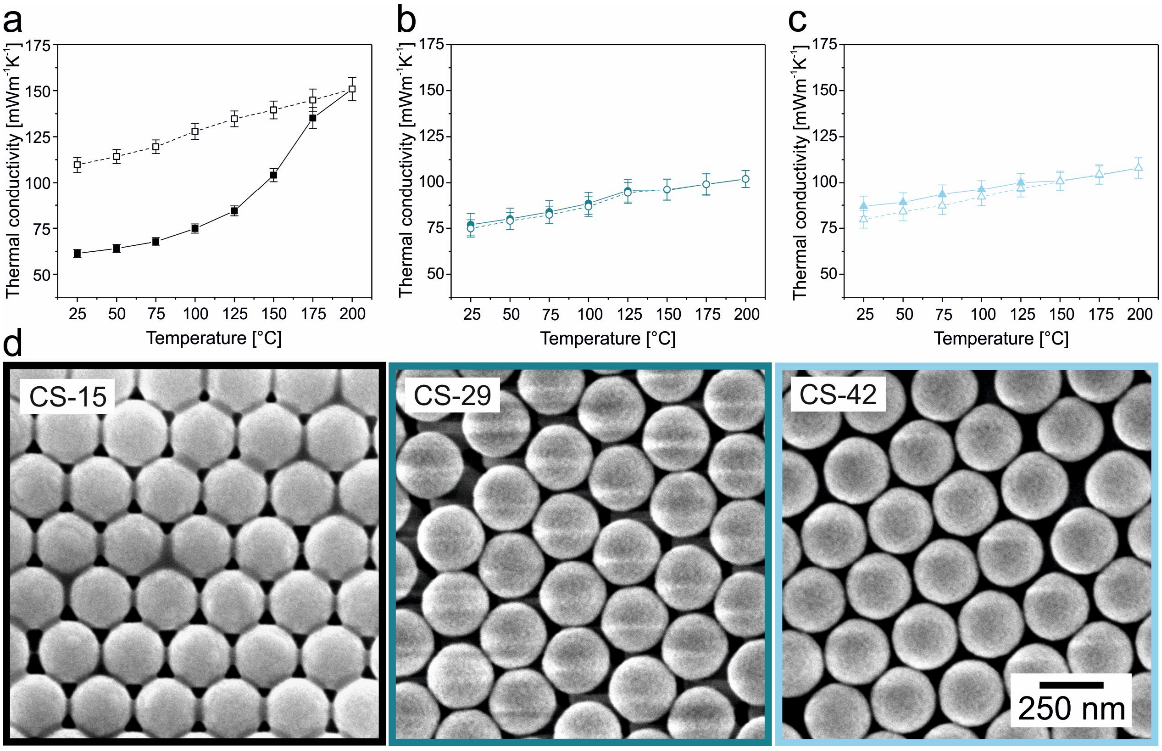

Figure 10.4. (a-c) Temperature-dependent thermal conductivity of the core-shell particles with different shell thicknesses (a) CS-15, (b) CS-29 and (c) CS-42. The open symbols and the dashed lines represent the cooling cycles. (d) SEM images of the core-shell particles after heating up to 200 °C.

Thus a sufficient encapsulation efficiency for potential phase change materials can be expected with a silica shell thickness between 15 – 29 nm. This, however, needs to be balanced to the overall volume fraction and therefore heat exchange capacity of the phase change material, as already pointed out by Salunkhe and Shembekar.[28]

Influence of the Morphology

Whereas the effect of the different capsule morphologies is important for a detailed understanding of thermal transport through such phase change architectures, we now want to complement our investigation by including the respective pure particle compositions. Therefore we synthesized solid silica and polystyrene spheres of comparable size to the core-shell particles CS-15, CS-29, and

CS-42. The size of the polystyrene particles is 261 ± 6 nm and of the silica particles 265 ± 10 nm. Thus no size influence should be expected in these ensembles.

For the thermal transport measurements the particles were assembled into colloidal crystals (Figure S10.10). Whereas in the polystyrene colloidal crystal (Figure S10.10b) Bragg colors are visible throughout the complete colloidal assembly, the silica colloidal crystal (Figure S10.10a) exhibits a minor crystallinity in two-thirds of the sample. This can be traced back to the higher density of the silica particles, which impede a high packing during the evaporation-induced self-assembly process. This will slightly reduce the thermal diffusivity and conductivity.

First, we want to compare the temperature-dependent thermal transport through the pure silica pure polystyrene and CS-269/15 colloidal crystal (Figure 10.5a). We find a strong increase of the thermal diffusivity with increasing silica content. Thus, the highest thermal diffusivity at 25 °C is obtained for the pure silica colloidal crystal and amounts to 0.00104 cm^2s^{-1}.This is about 62 % higher than the pure polystyrene ensemble, and the core-shell sample falls in between. The first heating cycle reveals three distinct differences on the thermal transport: 1) the thermal diffusivity of the silica colloidal assembly remains almost constant over the whole temperature range, 2) the core-shell particle exhibit at first a slight decrease, followed by a broad increase after T_g, and 3) the pure polystyrene colloidal crystal shows a small decrease, followed by a large and sharp increase at T_g. The sharp increase of the polystyrene sample is due to the loss of the particulate structure and the formation of a relatively dense polymer film (Figure S10.11). The delayed transition of the core-shell particle assembly is now clearly visible. After cooling down to 25 °C, the temperature diffusion of the polystyrene and the core-shell particle assembly exceeds the thermal diffusivity of the silica colloidal crystal. This can be traced back to the increase in the contact area or the formation of a film for the polystyrene sample. The thermal conductivity data demonstrate a similar behavior (Figure 10.5b). It was calculated using the DSC data (Figure S10.12) and the density data (Table S10.3). It shows quite clearly the transition from the pure polymer to the pure silica phase, with the polymer being the lowest conducting colloid structure. Upon film formation, this trend inverts and again reflects the respective contents of silica and polymer. While the pure SiO_2 colloidal crystal remains unaffected, an increasing step in thermal conductivity can be inferred for lower shell thicknesses. The highest thermal conductivity is obtained for pure PS, which additionally increases its density upon film formation. Also, the transition itself is affected by the colloid architecture. It ranges from none (SiO_2), to broad and delayed (thin core-shell), to sharp (pure PS).

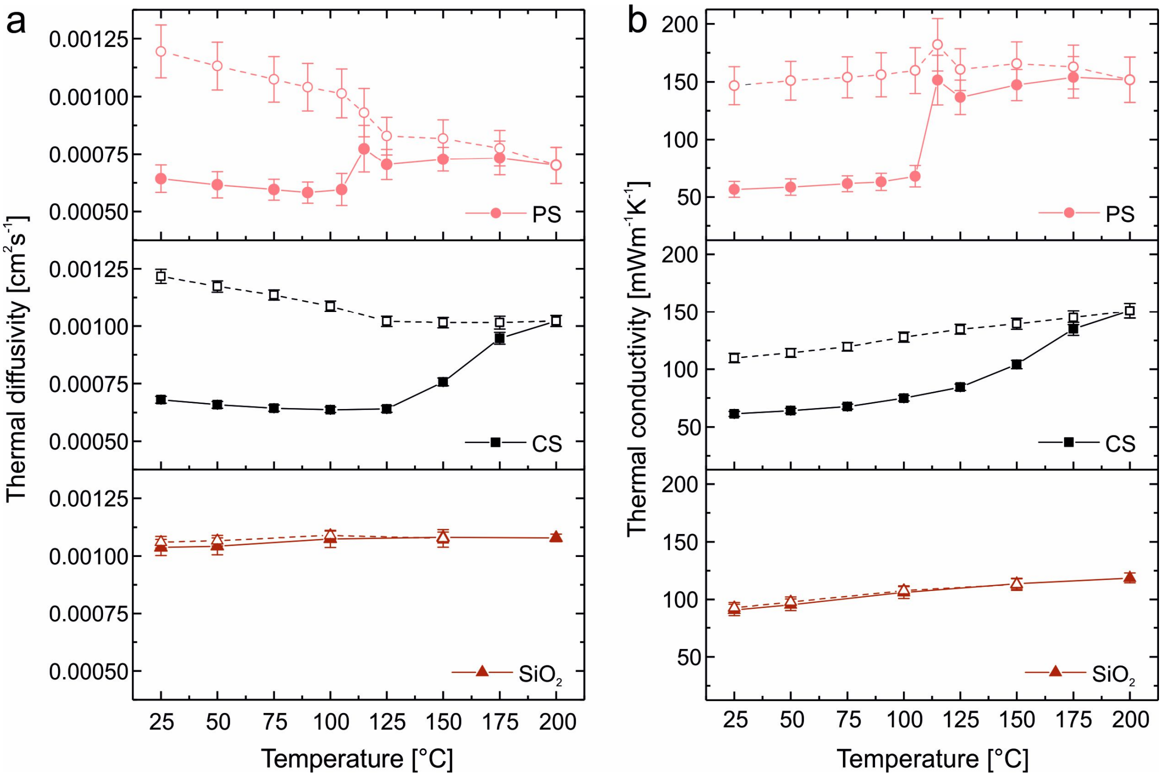

Figure 10.5. Thermal transport properties of polystyrene and silica particles in comparison to core-shell particles CS-269/15. (a) Thermal diffusivity data, and (b) thermal conductivity data. The open symbols and the dashed lines represent the cooling cycles.

Figure 10.6a summarizes the influence of the morphology on the thermal conductivity at room temperature before and after heating (thermal diffusivity data are shown in Figure S10.13a). The initial thermal conductivity systematically increases with increasing density and increasing silica content. Hence, by tuning the morphology, the thermal conductivity was varied between 44 $mWm^{-1}K^{-1}$ and 91 $mWm^{-1}K^{-1}$. Heating of these colloidal assemblies up to 200 °C further widens the range up to 147 mWm-1K-1 for the case of polystyrene. A sufficient encapsulation is reached latest by a 29 nm silica shell, preventing polymer leakage.

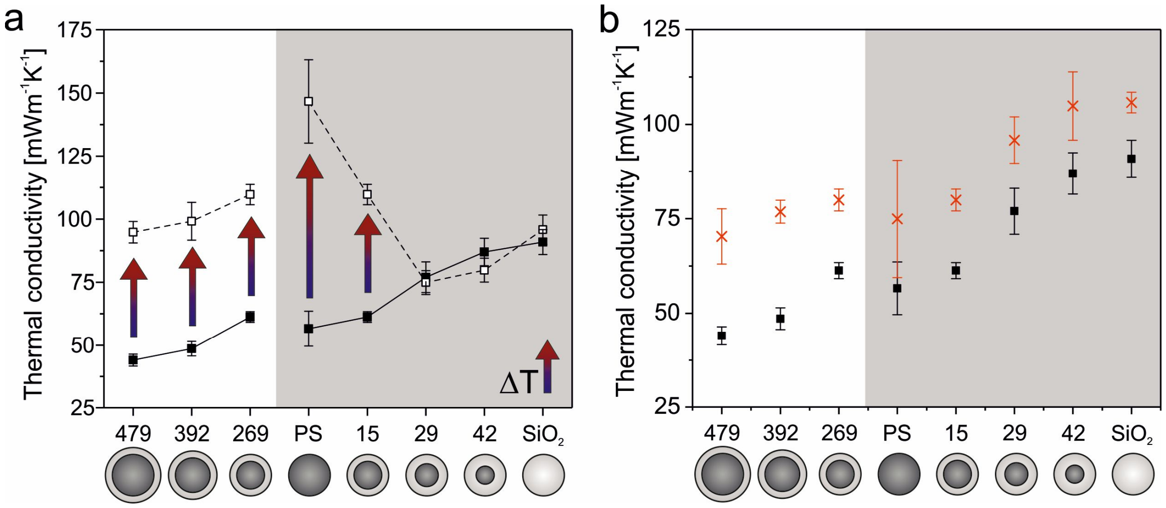

Figure 10.6. Influence of the morphology on the thermal conductivity of the different core-shell, polystyrene, and silica particle assemblies at 25 °C. (a) Influence of the morphology before and after heating to 200 °C on the thermal conductivity. The closed symbols show the vacuum data before heating, and the open symbols show the vacuum data after heating to 200 °C. (b) Influence of the additional gaseous transport through the colloidal assemblies on the thermal conductivity. The black data symbols show the vacuum measurements and the red crosses show the helium measurements at 1000 mbar.

Influence of the Gaseous Thermal Transport

Considering the open porous structure of such colloidal ensembles one can easily conceive the introduction of a second, continuous phase to increase the overall thermal transport through and within this structure. We focus on the influence of the gaseous thermal transport provided by the good thermal conductor helium. Figure 10.6b compares the thermal conductivity measured on the pristine colloidal ensembles at room temperature – under vacuum and helium conditions (Figure S10.13 shows the corresponding thermal diffusivity data). Expectably, the thermal conductivity in helium is higher for all colloidal assemblies due to the additional thermal transport through the gaseous phase. However, the increase compared to vacuum conditions differs. For the same outer diameter, the thermal conductivity increase is comparably independent of the material composition. This can be traced back to the comparable void sizes in the colloidal assembly, which depends on the outer diameter of the particle.[39] Thus, for an equal outer diameter of ~270 nm (gray-shaded area), the thermal conductivity increases by about the same amount (18 – 19 $\mathrm{mW\,m^{-1}\,K^{-1}}$). The influence of the helium becomes stronger when increasing the interstitial void size by using larger particles CS-392 and CS-479. There, a difference of up to 26 $\mathrm{mW\,m^{-1}\,K^{-1}}$ can be found between the vacuum and helium measurement. An even higher increase may be anticipated for other materials filling the interstitial space. Liquids or polymers, for instance, would not be influenced by the Knudsen effect, and thereby their thermal conductivity would not be constricted by the geometry of the small voids.

10.3 Conclusion

In summary, we have investigated the thermal transport properties of polystyrene-silica core-shell particle colloidal crystals as a structurally well-defined model system for future nanostructured phase change materials. We also compared these to their respective pure particle counterparts to provide for a comprehensive understanding of the morphologically controlled thermal transport through such heterostructures. The focus was laid on the influence of the morphology of the particles (size and shell thickness), and the interfaces between adjacent spheres in the assembly. We determined the thermal diffusivity, the specific heat capacity and the thermal conductivity in vacuum in dependence of the temperature (room temperature up to 200 °C), and the surrounding atmosphere (vacuum vs. helium).

We found an increase in thermal diffusivity and thermal conductivity with decreasing particle size and increasing silica content. Consequently, the pure silica colloidal assembly features the highest thermal diffusivity and conductivity. Owing to the amorphous structure of silica shell, the thermal conductivity ranges consistently below 100 $\mathrm{mW\,m^{-1}\,K^{-1}}$, which could impede a fast response for a potential phase change application. An additional route to increase the temperature and heat distribution in such capsule ensembles is given by thermal transport through the open porous space between adjacent spheres. For helium as a gaseous conductor, we found an increase of up to 26 $\mathrm{mW\,m^{-1}\,K^{-1}}$. This, however, depends on the size of the open porous voids. Using liquids or polymers instead as a second percolating network may further increase to overall thermal transport.

For any phase change application, one has to carefully balance the ratio between the shell thickness and the core volume. Apparently, this ratio determines the capacity of latent heat storage, quite importantly there is also a lower limit to the shell thickness at which leakage of the core material occurs. For polystyrene, even a 15 nm silica shell thickness is not sufficient to fully seal the inner core. Consequently, leakage occurs at temperatures much higher than the T_g. While the concomitant increase in thermal conductivity of up to 115 % is certainly helpful for a better temperature and heat distribution in such materials, the loss of core material will deteriorate the storage capacity on the long run.

Our findings are of great importance for heterostructured materials, in particular for systems with (nano)inclusions for future phase change applications. We demonstrated the relevance of the interparticle contact area, which governs the overall thermal transport, and the ability to use the particle morphology to tailor various temperature-dependent thermal properties. The particle size in return influences the physicochemical properties of its interior material such as the polymer mobility. We hope that this thoughtful insight into the morphology driven thermal transport behavior of particulate superstructures helps to conceive novel particle composition and particle ensemble designs, which may lead to high capacity and high response rate latent heat storage devices in the future.

10.4 Experimental Section

Materials

Styrene (≥ 99 %, Aldrich), 2,2′-azobis(2-methylpropionamidine) dihydrochloride (AIBA; 97 %, Aldrich), [2-(methacryloxy)ethyl]trimethyl-ammonium chloride (MTC; 70 % solution in water, Polyscience), polyvinyl-pyrrolidone K30 (PVP; M_w ~ 55 $\mathrm{kgmol^{-1}}$, Aldrich), tetraethylorthosilicate (TEOS; ≥ 99 %, Aldrich) and ammonium hydroxide solution (30 – 33 % in water, Aldrich) were used as received. Water was taken from a Millipore Direct Q3UV unit, and ethanol (EtOH) was used in technical grade for the entire synthesis and purification steps.

Synthesis of Polystyrene and Polystyrene-Silica Core-Shell Particles

Monodisperse polystyrene-silica core-shell particles were prepared in two steps. In the following, the synthesis procedure for the smallest particles with the thinnest shell (CS-269/15) is shown. First, monodisperse polystyrene (PS) particles were prepared by emulsifier-free emulsion polymerization.[17] In a three-necked flask, equipped with a reflux condenser and a gas inlet, 100 mL water, 13 mL styrene, 100 µL MTC and 0.9 g PVP K-30 were introduced. The mixture was degassed and heated to the reaction temperature of 70 °C at a stirring speed of 850 rpm. After an equilibration time of 30 min, 0.3 g AIBA, dissolved in 20 mL water, were added to initiate the polymerization. After nucleation, the stirring speed was reduced to 450 rpm. The reaction was carried out overnight under argon atmosphere.

In the second step, the polystyrene particles were coated with a thin silica shell by a modified Stoeber condensation process to obtain core-shell particles.[40] Therefore, 2.2 vol.% TEOS were added to an 81.3 vol.% EtOH, 10.5 vol.% water, 6.0 vol.% ammonium hydroxide solution containing 102.5 mg/mL PS latex particles.

For the synthesis of larger PS particles less comonomer MTC, more initiator AIBA, and more solvent were used. The shell thickness was increased by using higher amounts of TEOS relative to the PS particles.

Synthesis of Silica Particles

Monodisperse silica particles were synthesized using a semi-batch seeded growth synthesis. Firstly, small seed particles were synthesized by the Stoeber process, using 5 mL TEOS and 10 mL ammonia (30 – 33 %) in 145 mL ethanol at 40 °C. These particles had a hydrodynamic diameter of 86 nm. In the next step, 50 mL of the raw dispersion were filled into a flask and stirred with a magnetic stirrer at room temperature. TEOS (1:3 diluted with EtOH) and ammonium hydroxide solution (13.125 mL ammonia (30 – 33 %) and 1 mL Milli-Q water) were added to the solution in 21 steps over the course of two weeks. With each step, 1 – 2 mL of diluted TEOS and 400 µL ammonium hydroxide solution were added. The final particle diameter was (265 ± 10) nm.

Assembly into Colloidal Crystals and Glasses

Colloidal assemblies were prepared by slow evaporation of a concentrated solution of the particles (~7 wt.%) in a Teflon beaker with a diameter of 2 cm for several days.

Characterization Methods

Scanning electron microscopy (SEM) images were taken on a Leo 1530 instrument (Zeiss) using acceleration voltages between 2 and 3 kV and InLens SE detection as well as Everhart-Thornley detection.

Small-angle X-ray scattering (SAXS) data were measured using the small-angle X-ray system Double Ganesha AIR (SAXSLAB). The X-ray source of this laboratory-based system is a rotating copper anode (MicroMax 007HF, Rigaku Corporation), which provides a micro-focused beam at $\lambda = 0.154$ nm. The data were recorded by a position sensitive detector (PILATUS 300 K, Dectris). To cover the range of scattering vectors between 0.003 and 0.266 nm^{-1} different detector positions were used. The measurement was performed at room temperature, using a powder of core-shell particles packed in a capillary tube. The scattering data were evaluated using a vesicle fit in the program SCATTER.[41]

Thermal diffusivity measurements of the colloidal crystals were performed on an XFA 500 xenon flash apparatus (Linseis) equipped with an InSb infrared detector. Before the measurements, the samples were coated with a thin graphite layer (approx. 15 µm) on each side to ensure a good absorbance at the bottom and a high emissivity at the rear surface of the sample. The thickness of the graphite layer is negligible compared to the thickness of the colloidal crystals

(600 – 1000 µm). The measurements were performed on at least three samples at 25 °C in vacuum (~0.05 mbar), helium (1000 mbar) and air (~1000 mbar). The received data were evaluated by the software AproSoft Laser Flash Evaluation v1.06 using the radiation fit model.

Differential scanning calorimetry (DSC) measurements were carried out using a Q1000 DSC (TA Instruments). Powders of the core-shell particles (11 – 20 mg) were scanned in covered aluminum pans under a dry nitrogen purge of 50 mLmin^{-1} over a temperature range from -50 to 210 °C with a heating rate of 10 °Cmin^{-1}. The heat flow and heat capacity were calibrated using a standard sapphire sample. The received data were evaluated with Universal Analysis 2000 2.5A software.

The thicknesses of the colloidal crystals were determined with a Litematic VL-50 (Mitutoyo).

The densities of the unmolten core-shell and silica particle colloidal crystals were determined from the mass and volume of the monoliths. The volume was measured using a 3D digital surface profiler (Keyence V-3100), and the mass was determined by weighing the colloidal crystals. The densities of the polystyrene particle colloidal crystals and the molten core-shell particle colloidal crystals are performed using Archimedes' principle (buoyancy method) using a Mettler balance. The colloidal crystals are hydrophobized by chemical vapor deposition using hexamethyldisilazane (HMDS), to avoid the adsorption of water by the hygroscopic silica network,

Nitrogen sorption measurements were taken on a Quantachrome Autosorb AS-1 pore analyzer at 77 K. All samples were preconditioned in vacuum at 90 °C for 12 hours before the measurements. The data evaluation was done using the Quantachrome ASiQ v3.0 software. The specific surface areas were calculated using the Brunauer-Emmett-Teller (BET) method. Pore volumes and pore size distributions were obtained by applying the nonlocal density functional theory (NLDFT) adsorption branch model for silica materials with cylindrical pore geometry.

10.5 Acknowledgments

PR acknowledges support by the Elite Network Bavaria (ENB). Fabian Nutz is acknowledged for DSC measurements. Additional support was provided by the SFB840.

10.6 References

1. Roduner, E., Size matters: why nanomaterials are different. *Chem. Soc. Rev.* **2006,** *35* (7), 583-592.

2. Allara, D. L., A perspective on surfaces and interfaces. *Nature* **2005,** *437* (7059), 638-639.

3. Zhou, Z.-Y.; Tian, N.; Li, J.-T.; Broadwell, I.; Sun, S.-G., Nanomaterials of high surface energy with exceptional properties in catalysis and energy storage. *Chem. Soc. Rev.* **2011,** *40* (7), 4167-4185.

4. Arico, A. S.; Bruce, P.; Scrosati, B.; Tarascon, J.-M.; van Schalkwijk, W., Nanostructured materials for advanced energy conversion and storage devices. *Nat. Mater.* **2005,** *4* (5), 366-377.

5. Tong, H.; Ouyang, S.; Bi, Y.; Umezawa, N.; Oshikiri, M.; Ye, J., Nano-photocatalytic Materials: Possibilities and Challenges. *Adv. Mater.* **2012,** *24* (2), 229-251.

6. Yang, W.; Ratinac, K. R.; Ringer, S. P.; Thordarson, P.; Gooding, J. J.; Braet, F., Carbon Nanomaterials in Biosensors: Should You Use Nanotubes or Graphene? *Angew. Chem. Int. Ed.* **2010,** *49* (12), 2114-2138.

7. Ozbay, E., Plasmonics: Merging Photonics and Electronics at Nanoscale Dimensions. *Science* **2006,** *311* (5758), 189-193.

8. Cahill, D. G.; Ford, W. K.; Goodson, K. E.; Mahan, G. D.; Majumdar, A.; Maris, H. J.; Merlin, R.; Phillpot, Sr., Nanoscale thermal transport. *J. Appl. Phys.* **2003,** *93* (2), 793-818.

9. Cahill, D. G.; Braun, P. V.; Chen, G.; Clarke, D. R.; Fan, S. H.; Goodson, K. E.; Keblinski, P.; King, W. P.; Mahan, G. D.; Majumdar, A.; Maris, H. J.; Phillpot, S. R.; Pop, E.; Shi, L., Nanoscale thermal transport. II. 2003-2012. *Appl. Phys. Rev.* **2014,** *1* (1).

10. Dai, L.; Chang, D. W.; Baek, J.-B.; Lu, W., Carbon Nanomaterials for Advanced Energy Conversion and Storage. *Small* **2012,** *8* (8), 1130-1166.

11. Zhu, J.; Yang, D.; Yin, Z.; Yan, Q.; Zhang, H., Graphene and Graphene-Based Materials for Energy Storage Applications. *Small* **2014,** *10* (17), 3480-3498.

12. Zhao, G.; Hu, P.; Zhou, S.; Chen, G.; An, Y.; Cheng, Y.; An, J.; Zhang, X.; Han, W., Ordered Silica Nanoparticles Grown on a Three-Dimensional Carbon Fiber Architecture Substrate with Siliconborocarbonitride Ceramic as a Thermal Barrier Coating. *ACS Appl. Mater. Inter.* **2016,** *8* (6), 4216-4225.

13. Zhang, Q.; Hao, M.; Xu, X.; Xiong, G.; Li, H.; Fisher, T. S., Flyweight 3D Graphene Scaffolds with Microinterface Barrier-Derived Tunable Thermal Insulation and Flame Retardancy. *ACS Appl. Mater. Inter.* **2017,** *9* (16), 14232-14241.

14. Hayase, G.; Kanamori, K.; Abe, K.; Yano, H.; Maeno, A.; Kaji, H.; Nakanishi, K., Polymethylsilsesquioxane–Cellulose Nanofiber Biocomposite Aerogels with High Thermal Insulation, Bendability, and Superhydrophobicity. *ACS Appl. Mater. Inter.* **2014,** *6* (12), 9466-9471.

15. Vineis, C. J.; Shakouri, A.; Majumdar, A.; Kanatzidis, M. G., Nanostructured Thermoelectrics: Big Efficiency Gains from Small Features. *Adv. Mater.* **2010,** *22* (36), 3970-3980.

16. Vogel, N.; Retsch, M.; Fustin, C.-A.; del Campo, A.; Jonas, U., Advances in Colloidal Assembly: The Design of Structure and Hierarchy in Two and Three Dimensions. *Chem. Rev.* **2015,** *115* (13), 6265-6311.

17. Goodwin, J. W.; Hearn, J.; Ho, C. C.; Ottewill, R. H., Studies on the preparation and characterisation of monodisperse polystyrene laticee. *Colloid Polym. Sci.* **1974,** *252* (6), 464-471.

18. Tseng, C. M.; Lu, Y. Y.; El-Aasser, M. S.; Vanderhoff, J. W., Uniform polymer particles by dispersion polymerization in alcohol. *J. Polym. Sci. Part A* **1986,** *24* (11), 2995-3007.

19. Stoeber, W.; Fink, A.; Bohn, E., Controlled growth of monodisperse silica spheres in the micron size range. *J. Colloid Interf. Sci.* **1968,** *26* (1), 62-69.

20. Claridge, S. A.; Castleman, A. W.; Khanna, S. N.; Murray, C. B.; Sen, A.; Weiss, P. S., Cluster-Assembled Materials. *ACS Nano* **2009,** *3* (2), 244-255.

21. Ong, W.-L.; Rupich, S. M.; Talapin, D. V.; McGaughey, A. J. H.; Malen, J. A., Surface chemistry mediates thermal transport in three-dimensional nanocrystal arrays. *Nat. Mater.* **2013,** *12* (5), 410-415.

22. Ong, W.-L.; Majumdar, S.; Malen, J. A.; McGaughey, A. J. H., Coupling of Organic and Inorganic Vibrational States and Their Thermal Transport in Nanocrystal Arrays. *J. Phys. Chem. C* **2014,** *118* (14), 7288-7295.

23. Liu, M.; Ma, Y.; Wang, R. Y., Modifying Thermal Transport in Colloidal Nanocrystal Solids with Surface Chemistry. *ACS Nano* **2015,** *9* (12), 12079-12087.

24. Losego, M. D.; Blitz, I. P.; Vaia, R. A.; Cahill, D. G.; Braun, P. V., Ultralow Thermal Conductivity in Organoclay Nanolaminates Synthesized via Simple Self-Assembly. *Nano Lett.* **2013,** *13* (5), 2215-2219.

25. Ruckdeschel, P.; Kemnitzer, T. W.; Nutz, F. A.; Senker, J.; Retsch, M., Hollow silica sphere colloidal crystals: insights into calcination dependent thermal transport. *Nanoscale* **2015,** *7* (22), 10059-10070.

26. Nutz, F. A.; Ruckdeschel, P.; Retsch, M., Polystyrene colloidal crystals: Interface controlled thermal conductivity in an open-porous mesoparticle superstructure. *J. Colloid Interf. Sci.* **2015,** *457*, 96-101.

27. Ma, Z.; Lin, W.; Sohel, M. I., Nano-enhanced phase change materials for improved building performance. *Renew. Sust. Energ. Rev.* **2016,** *58* (C), 1256-1268.

28. Salunkhe, P. B.; Shembekar, P. S., A review on effect of phase change material encapsulation on the thermal performance of a system. *Renew. Sust. Energ. Rev.* **2012,** *16* (8), 5603-5616.

29. Phadungphatthanakoon, S.; Poompradub, S.; Wanichwecharungruang, S. P., Increasing the Thermal Storage Capacity of a Phase Change Material by Encapsulation: Preparation and Application in Natural Rubber. *ACS Appl. Mater. Inter.* **2011,** *3* (9), 3691-3696.

30. Lencer, D.; Salinga, M.; Wuttig, M., Design Rules for Phase-Change Materials in Data Storage Applications. *Adv. Mater.* **2011,** *23* (18), 2030-2058.

31. Ruckdeschel, P.; Dulle, M.; Honold, T.; Förster, S.; Karg, M.; Retsch, M., Monodisperse hollow silica spheres: An in-depth scattering analysis. *Nano Res.* **2016,** *9* (5), 1366-1376.

32. Zhang, C.; Guo, Y.; Priestley, R. D., Glass Transition Temperature of Polymer Nanoparticles under Soft and Hard Confinement. *Macromolecules* **2011,** *44* (10), 4001-4006.

33. Butt, H.-J.; Graf, K.; Kappl, M., Liquid Surfaces. In *Physics and Chemistry of Interfaces*, Wiley-VCH Verlag GmbH & Co. KGaA: 2004; pp 4-25.

34. Cogswell, F. N., The Influence of Pressure in the Viscosity of Polymer Melts. *Plast. Polym.* **1973,** *41*, 39-43.

35. Sedlacek, T.; Zatloukal, M.; Filip, P.; Boldizar, A.; Saha, P., On the effect of pressure on the shear and elongational viscosities of polymer melts. *Polymer Engineering & Science* **2004,** *44* (7), 1328-1337.

36. Wu, S., Surface and interfacial tensions of polymer melts. II. Poly(methyl methacrylate), poly(n-butyl methacrylate), and polystyrene. *J. Phys. Chem.* **1970,** *74* (3), 632-638.

37. Mark, J. E., *Polymer Data Handbook*. Oxford University Press: 2009.

38. Kreith, F., *The CRC Handbook of Mechanical Engineering, Second Edition*. Taylor & Francis: 1998.

39. Wang, J.; Ahl, S.; Li, Q.; Kreiter, M.; Neumann, T.; Burkert, K.; Knoll, W.; Jonas, U., Structural and optical characterization of 3D binary colloidal crystal and inverse opal films prepared by direct co-deposition. *J. Mater. Chem.* **2008,** *18* (9), 981-988.

40. Graf, C.; Vossen, D. L. J.; Imhof, A.; van Blaaderen, A., A General Method To Coat Colloidal Particles with Silica. *Langmuir* **2003,** *19* (17), 6693-6700.

41. Förster, S.; Apostol, L.; Bras, W., Scatter: software for the analysis of nano- and mesoscale small-angle scattering. *J. Appl. Crystallogr.* **2010,** *43* (3), 639-646.

10.7 Supporting Information

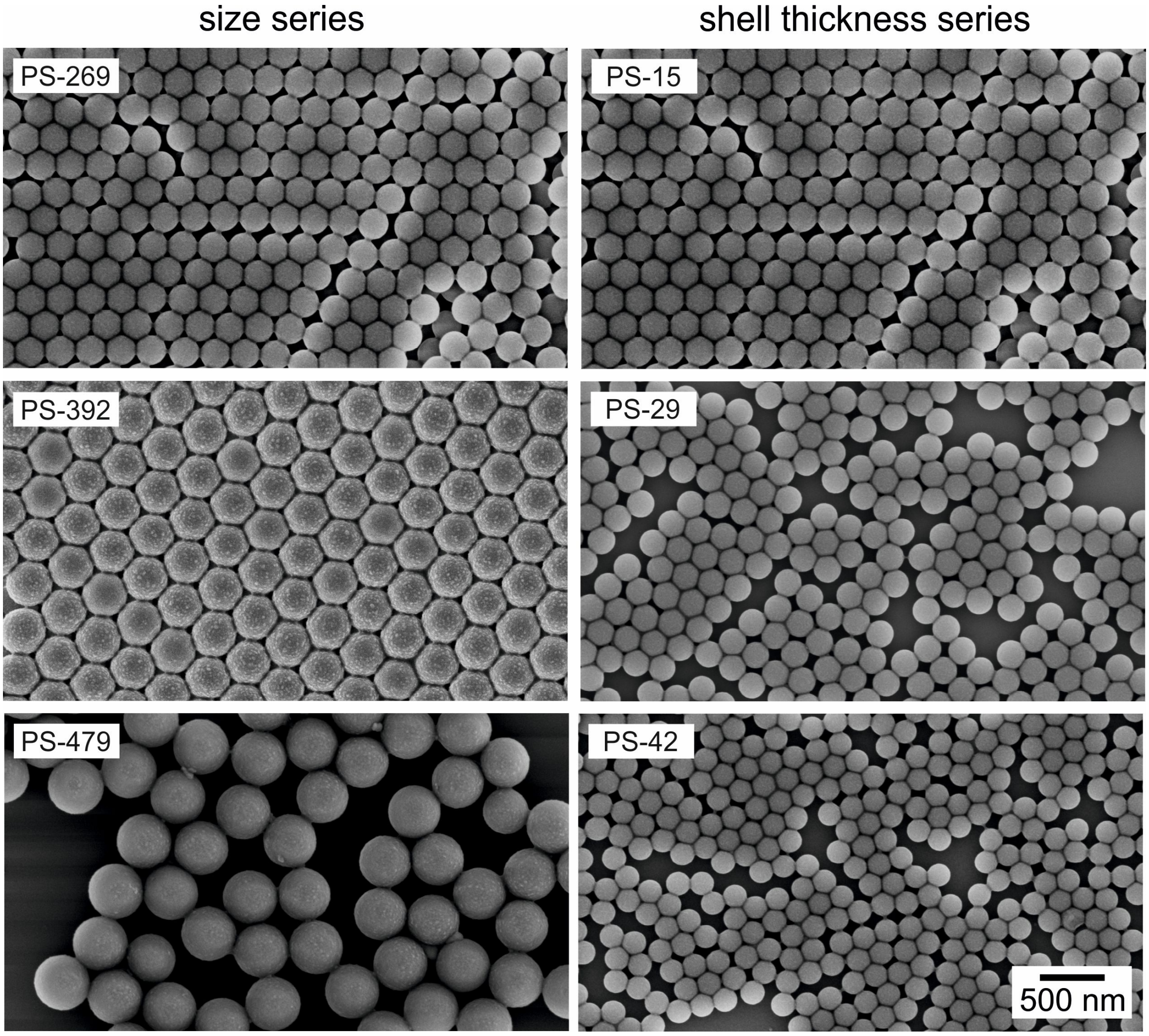

Figure S10.1. SEM images of the polystyrene template particles.

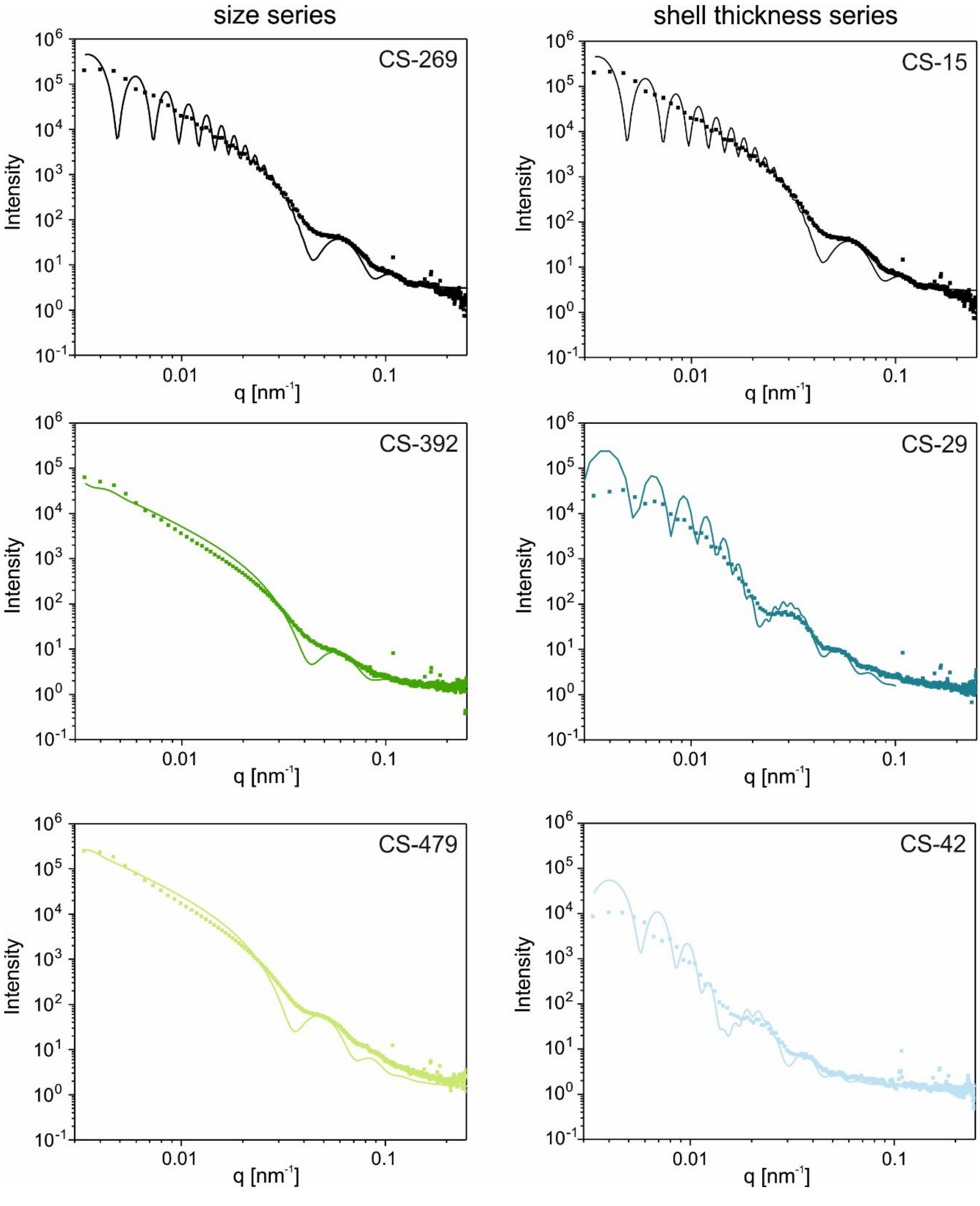

Figure S10.2. Small-angle X-ray scattering of the core-shell particles.

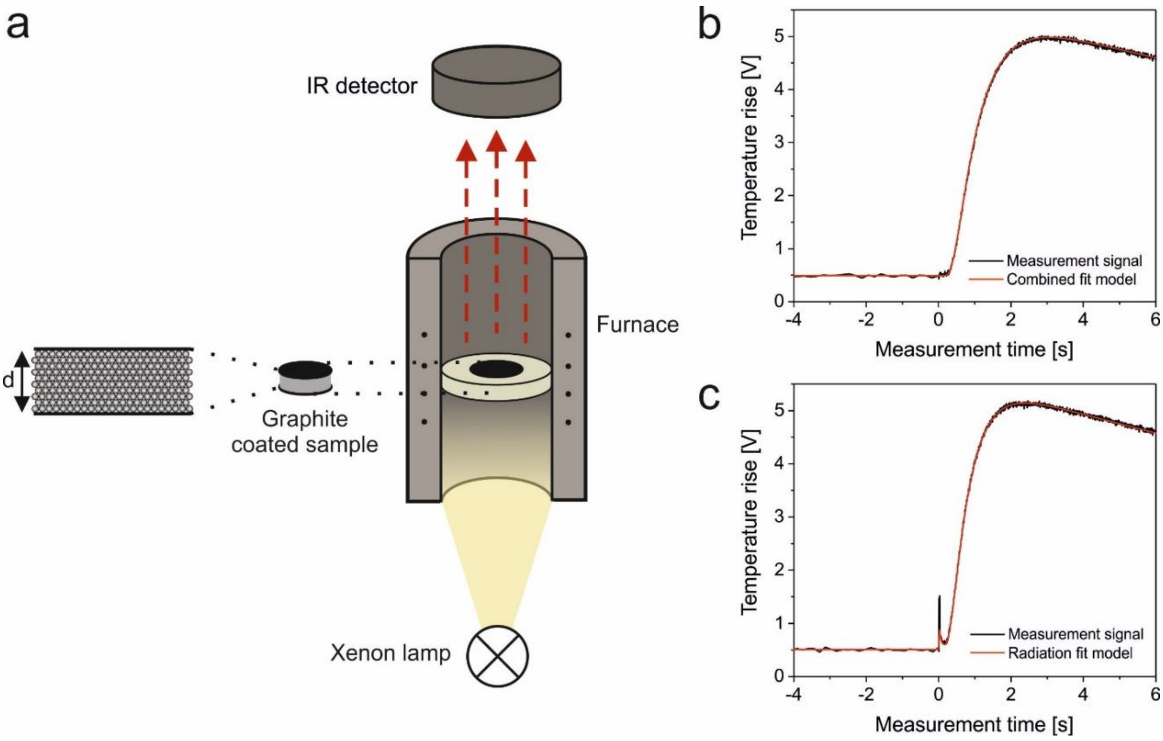

Figure S10.3. Xenon flash analysis. (a) Schematic setup, modified from Ruckdeschel et al. (Ruckdeschel, P. et al. Hollow silica sphere colloidal crystals: insights into calcination dependent thermal transport. Nanoscale **2015**, 7, 10059) and (b, c) two typical measurement signals of a core-shell colloidal crystal modeled with the combined fit model (b) and the radiation fit model (c). The radiation fit model extends the finite-pulse and heat loss corrections given by the combined fit model from Dusza (Dusza, L. Combined Solution of the Simultaneous Heat Loss and Finite Pulse Corrections with the Laser Flash Method. HTHP **1995**, 27-28, 467-473). It considers radiation effects, leading to an instantaneous temperature jump analogous to Blumm et al. (Blumm, J.; Henderson, J.; Nilsson, O.; Fricke, J. Laser flash measurement of the phononic thermal diffusivity of glasses in the presence of ballistic radiative transfer. HTHP **1997**, 29, 555-560).

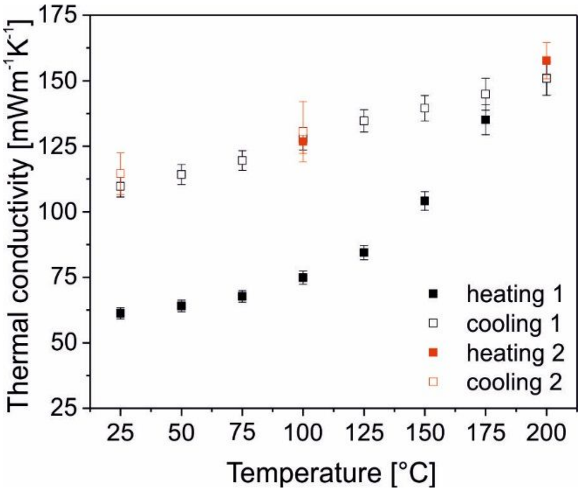

Figure S10.4. Thermal conductivity data of the second heating and second cooling cycle (red squares) of the sample CS-269. The open symbols represent the cooling cycles.

Table S10.1. Neck sizes and contact areas between adjacent particles of the size series in the colloidal crystals, determined by measuring the necks in the SEM images. A_c is the sum of the contact areas of a particle with its 12 neighbors in an fcc symmetry, and A_p is the surface area of a particle. The ratio A_c/A_p give the total contact area in relation to the particle surface area.

	Before the heating		*After the heating*	
	Neck size [nm]	**A_c/A_p [%]**	**Neck size [nm]**	**A_c/A_p [%]**
CS-479	87.8 ± 13.1	10.8	154.8 ± 11.8	33.7
CS-392	77.5 ± 12.6	12.0	123.51 ± 17.2	30.6
CS-269	55.1 ± 10.0	12.6	83.5 ± 15.8	28.9

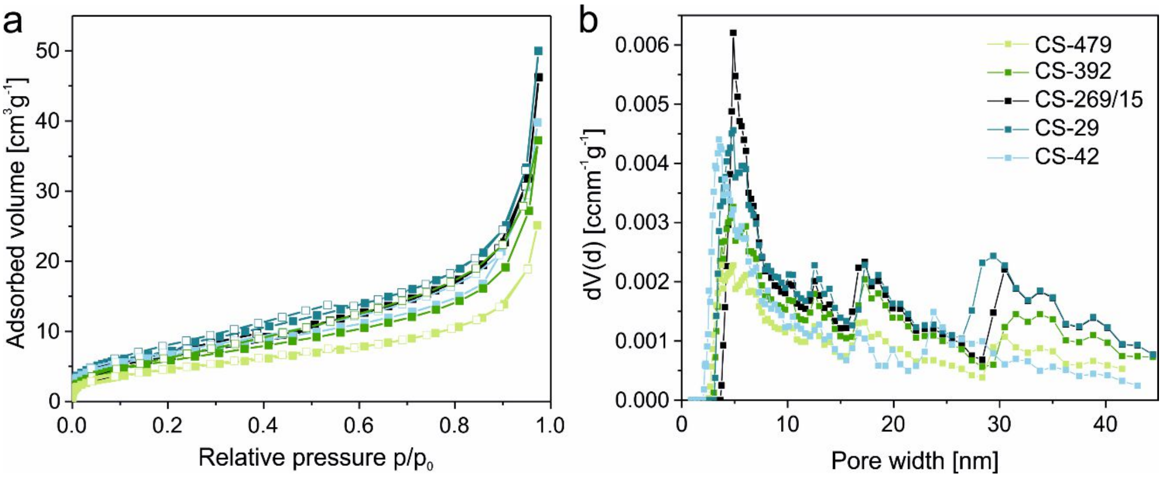

Figure S10.5. Nitrogen sorption measurements. (a) Isotherms, (b) Pore size distribution determined by DFT analysis.

Table S10.2. Summary of data received from N_2 sorption measurements.

	N_2 sorption measurements			
	BET SA [m²/g]	**DFT SA [m²/g]**	**Pore vol. [cc/g]**	**Pore size [nm]**
CS-479	17.183	13.472	0.037	3.775
CS-392	22.185	17.869	0.055	4.887
CS-269/15	24.128	20.874	0.068	4.887
CS-29	26.495	23.621	0.073	4.887
CS-42	24.281	20.114	0.043	3.537

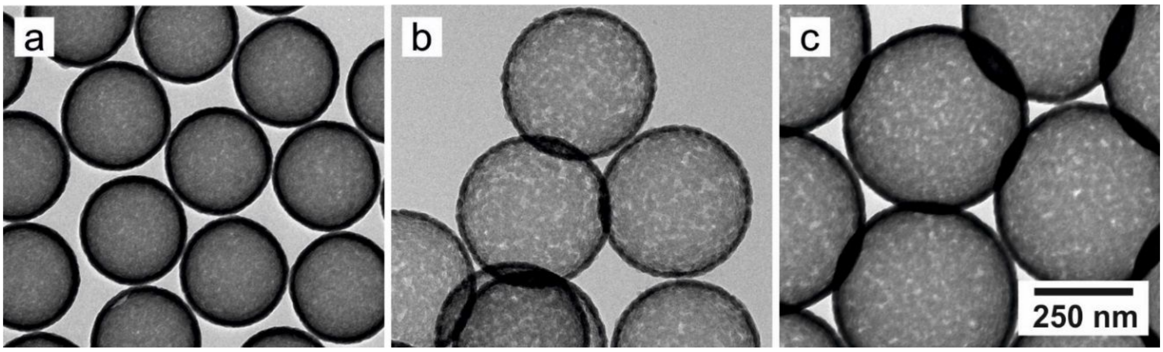

Figure S10.6. Transmission electron microscopy images of the core-shell particles (a) CS-269, (b) CS-392, (c) CS-479) after calcining at 500 °C to remove the polystyrene core.

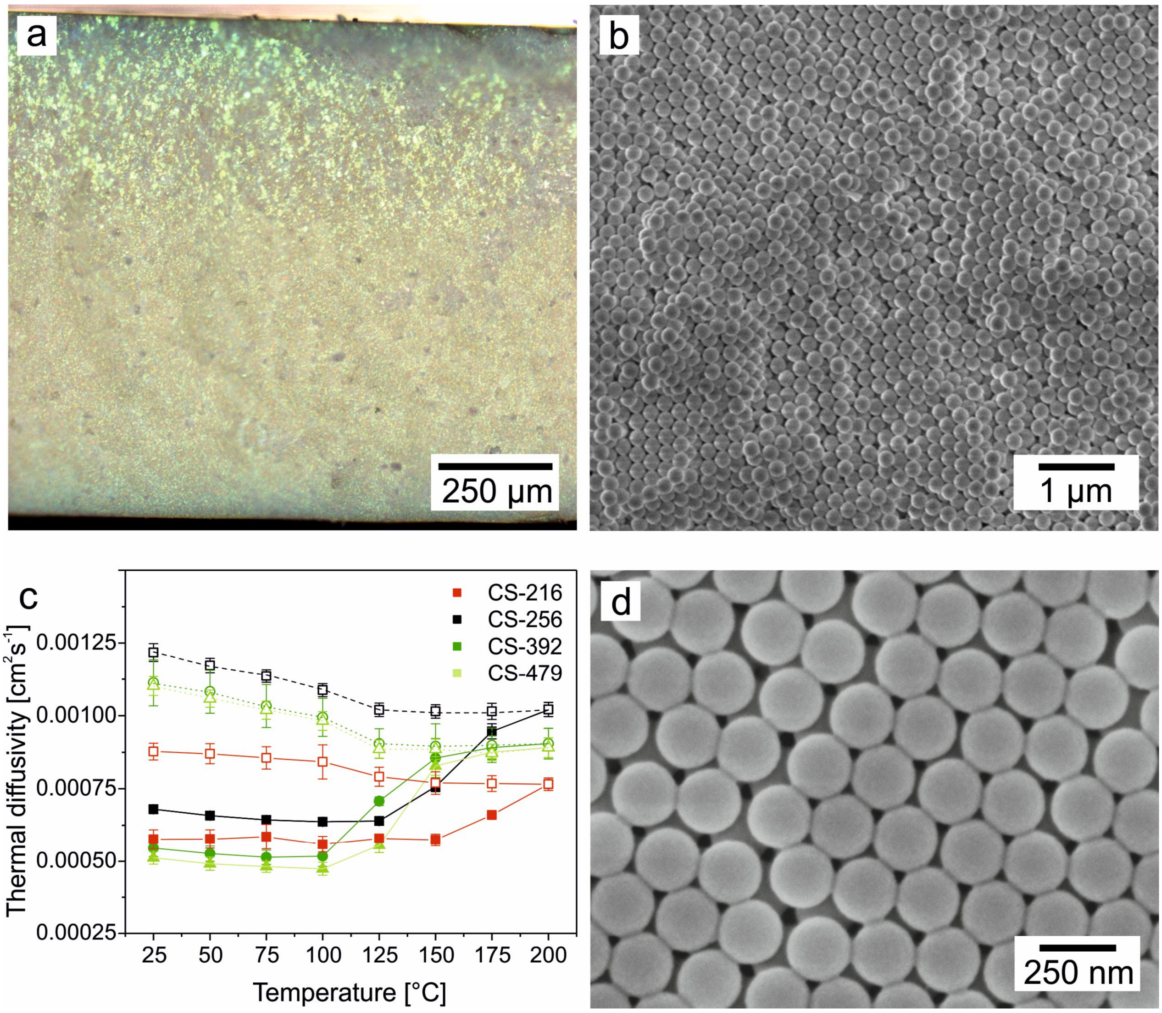

Figure S10.7. (a,b) Light microscopy side-view image (a) and SEM side-view image (b) of the colloidal crystal CS-216. (c) Temperature-dependent thermal diffusivity data of the colloidal crystal CS-216 in comparison to the size series. The open symbols and the dashed lines represent the cooling cycles. (d) SEM image of the particles CS-216 after heating to 200 °C.

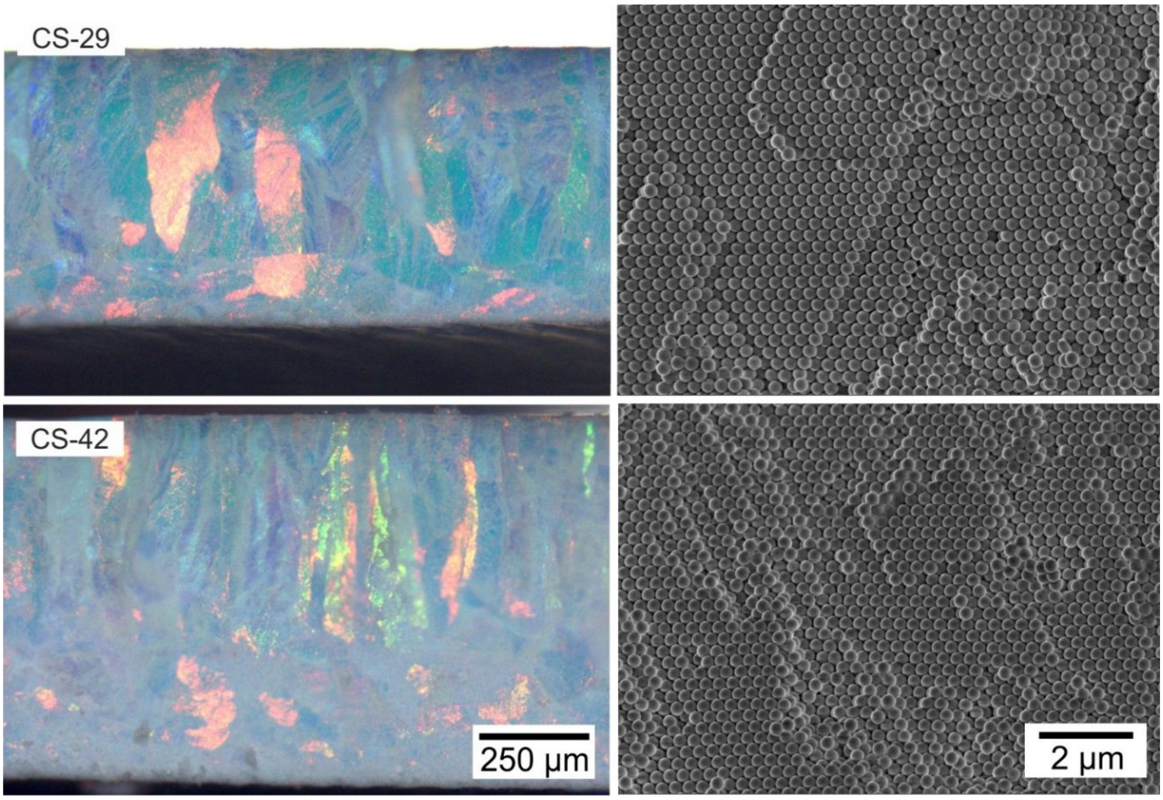

Figure S10.8. SEM images and bright field light microscopy images of the core-shell particle colloidal crystals with the similar diameter but different shell thicknesses (29, 42 nm).

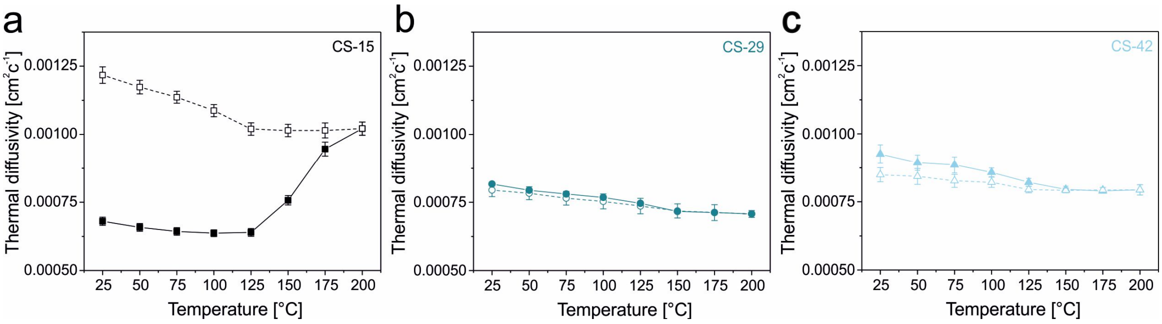

Figure S10.9. Temperature-dependent thermal diffusivity of the core-shell particles possessing different shell thicknesses (15, 29, 42 nm). The open symbols and the dashed lines represent the cooling cycles.

Table S10.3. Summary of data received from SEM and SAXS measurements as well as the density of the resulting colloidal crystals.

	SEM	*SAXS*	*PS/Silica*	*Density*
	d_a [nm]	**t [nm]**	**[%]**	**ρ (CC) [b] [g/cm³]**
PS	261 ± 6	-	100	0.76 ± 0.02
SiO_2	265 ± 10	-	0	1.28 ± 0.03

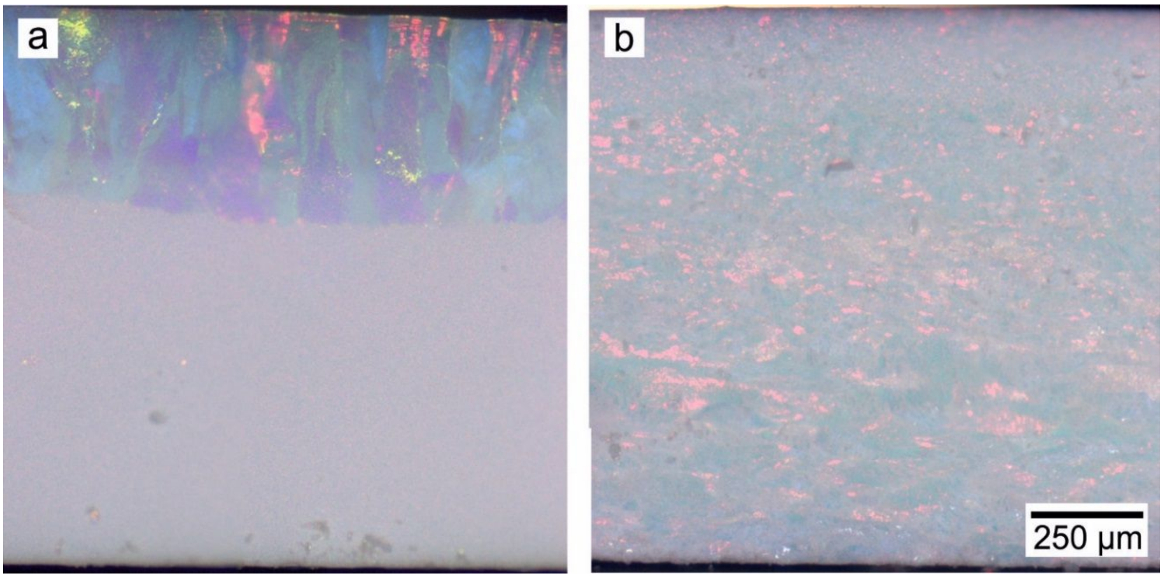

Figure S10.10. Optical microscopy image of the (a) silica and (b) polystyrene colloidal crystal.

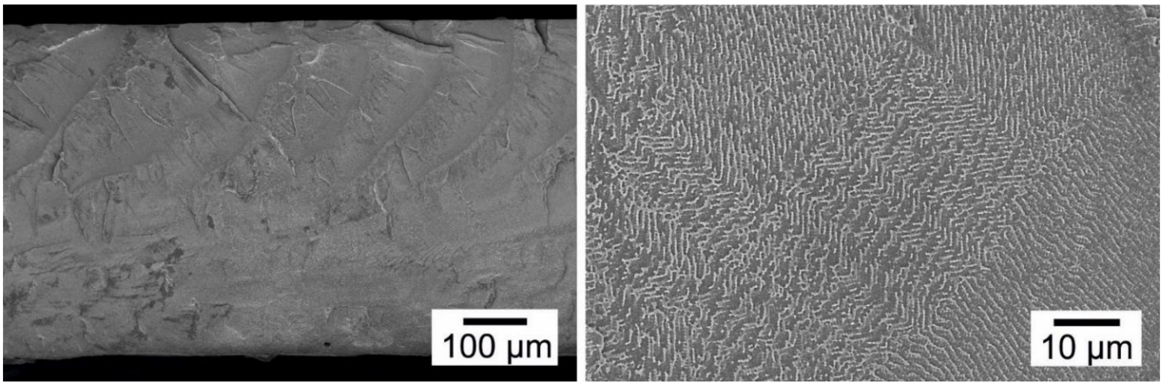

Figure S10.11. SEM side-view images of the polystyrene films after heating up to 200 °C.

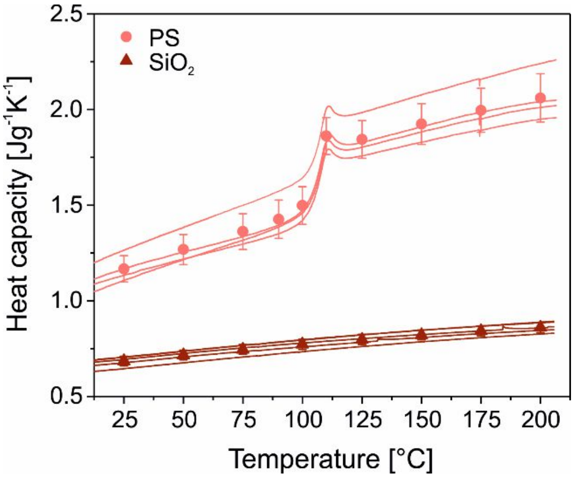

Figure S10.12. Specific heat capacity of the polystyrene and silica particles.

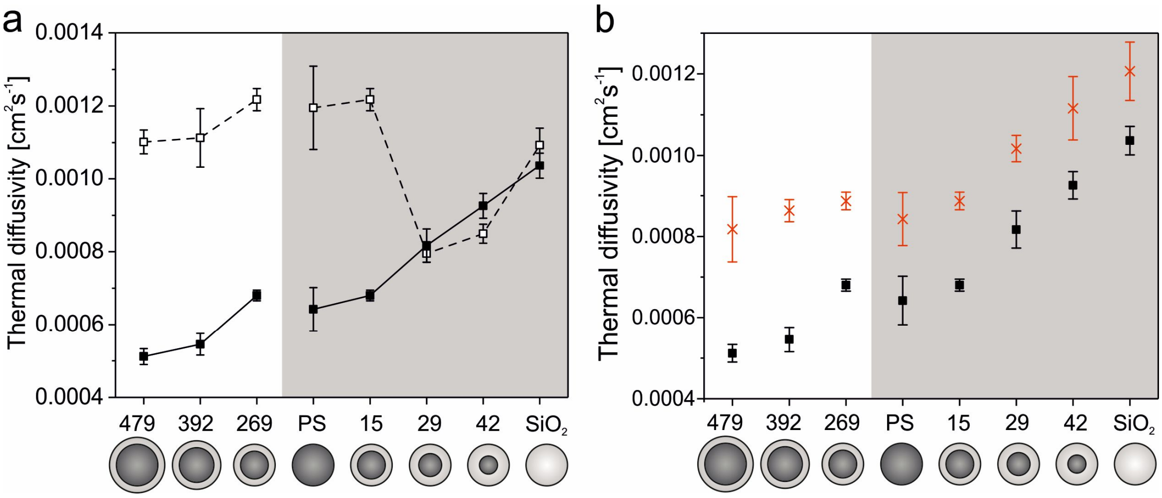

Figure S10.13. Influence of the morphology on the thermal diffusivity of the different core-shell, polystyrene, and silica particle assemblies at 25 °C. (a) Influence of the morphology before and after the heating up to 200 °C on the thermal diffusivity. The closed symbols show the vacuum data before the heating, and the open symbols show the vacuum data after the heating to 200 °C. (b) Influence of the additional gaseous transport through the colloidal assemblies on the thermal diffusivity. The black data symbols show the vacuum measurements and the red crosses show the helium measurements at 1000 mbar.

11 Homogeneous Nucleation of Ice Confined in Hollow Silica Spheres

Yang Yao, Pia Ruckdeschel, Robert Graf, Hans-Jürgen Butt, Markus Retsch, and George Floudas

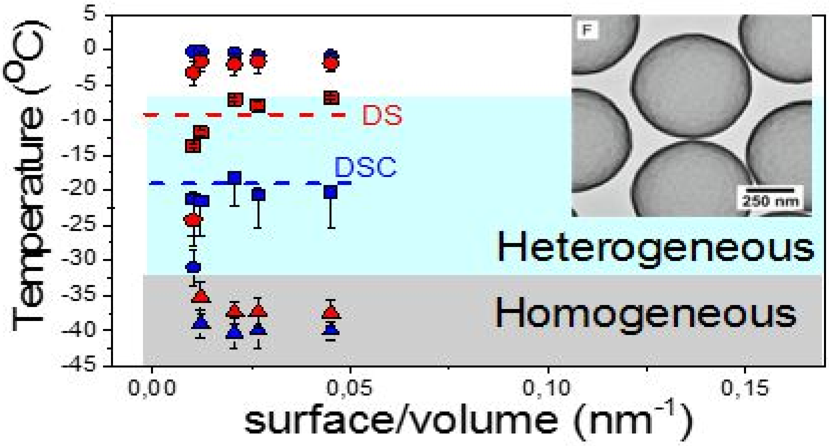

Reprinted with permission from Yao *et al.*, *The Journal of Physical Chemistry B* **2017**, **121 (1)**, 306. Copyright ©2017 American Chemical Society.

Abstract

Ice nucleation is studied in hollow silica (HS) spheres. These hierarchical materials comprise ~3 nm pores within the silica network, which are confined to a ~20 nm shell of a hollow sphere (with diameters in the range ~190-640 nm). The multiple length scales involved in hollow silica spheres affect the ice nucleation mechanism. We find homogeneous nucleation inside the water-filled capsules, whereas heterogeneous nucleation prevails in the surrounding dispersion medium. We validate our findings for a series of hollow sphere sizes and demonstrate the absence of homogeneous nucleation in case of polystyrene-silica core-shell particles. The present findings shed new light on the interplay between homogeneous and heterogeneous nucleation of ice with possible implications in undercooled reactions and the storage of reactive or biologically active substances.

11.1 Introduction

Water, the most important liquid, behaves differently under confinement.[1-5] Bulk water freezes due to impurities via *heterogeneous* nucleation. In contrast, confined water can be supercooled to -38 °C or even below, with an intrinsic process known as *homogeneous* nucleation. Understanding and eventually controlling supercooling via exerting control over the nucleation mechanism of ice is important in several fields: from atmospheric chemistry (by controlling cloud formation and precipitation) to anti-icing surfaces, to construction materials (avoiding ice formation is essential for the durability of building materials like cement) and to molecular biology (storage of biologically relevant substances). A common route towards supercooling is by confining water in micrometer to nanometer scales that limits the growth of crystals formed by heterogeneous nucleation and thus reduces the effect of heterogeneous nucleation. Of importance here have been measurements of ice nucleation in supercooled water microdroplets;[6-9] these experiments reported a freezing rate proportional to the droplet volume with a proportionality constant (*i.e.*, the nucleation rate) maximized at -38 °C.[6-8] However, despite fundamental importance in science and technology control of heterogeneous, and more importantly, of homogeneous nucleation of ice at atmospheric conditions remains a challenge. Recent efforts focused on confining water within the nanometer size cavities of porous silica materials, including sol-gel disordered silica, MCM-41, and SBA-15.[10-19] They have shown suppressed crystallization of water below the bulk freezing temperature -depending on the pore size- according to the Gibbs-Thomson equation. Furthermore, a fraction of molecules at the pore surface remained liquid-like through hydrogen bonding between water molecules and the silica surface. Other studies demonstrated the sensitivity of this interfacial water to details of surface chemistry by, e.g., inducing orientation order of water molecules in contact with the surface.[19,20]

In this work, we employ a new confining medium composed of hollow silica spheres as the means to control the nucleation mechanism of ice. It is composed of monodisperse hollow silica (HS) spheres, which are dispersed in an aqueous phase. These hollow spheres can be regarded as capsules and represent a well-defined porous material with a number of interesting thermal, optical and mechanical properties.[21-23] These hierarchical materials exhibit structure over several length scales; they comprise micropores within the silica network (with a size of ~3 nm), which are then confined to a thin shell (~20 nm) of a hollow sphere (~190 – 640 nm). We hypothesize that these multiple length scales may play a role in the nucleation mechanism of water and study ice nucleation within a series of HS having comparable microporous cavities and shell thickness but variable sphere radii resulting in different inner pore volumes. We provide clear evidences for well-separated nucleation mechanisms of ice at higher and lower supercooling originating, respectively, from water molecules located inside and outside the spheres. Lastly, the results on the nucleation mechanism are compared to the mechanism of ice formation within another well-defined porous material, namely self-ordered anodic aluminum oxide (AAO), having a single pertinent length scale, the pore diameter. [24-26]

11.2 Results and Discussion

The synthesis of hollow silica spheres comprises three steps: synthesis of polystyrene particles, coating of polystyrene template particles with a silica shell *via* a modified Stoeber process and calcination of the core-shell particles to remove the polystyrene core.[21, 27] With respect to polystyrene particles two different techniques were used. Smaller particles (140 – 275 nm) were obtained by emulsifier-free emulsion polymerization and larger particles (495 – 580 nm) by dispersion polymerization. Silica coating of the polystyrene particles was achieved by a Stoeber condensation process followed by calcination. The characteristics of the hollow spheres (HS) are shown in Table 11.1 and Table 11.2 and details are given in the Supporting Information (Chapter 11.7).

Table 11.1. Summary of the results obtained from TEM analysis and corresponding data based on individual hollow silica nanoparticle as well as data based on dispersion.

	TEM data[a]		**Data based on individual HS particle**[b]		**Data based on dispersion**[c]	
	d **[nm]**	***t*** **[nm]**	V_{pore} **[nm³]**	$S_{\text{pore}}/V_{\text{pore}}$ **[nm⁻¹]**	$V_{\text{in}}/V_{\text{ex}}$	**wt.% [%]**
HS-185	185.1 ± 3.7	20.6 ± 1.3	$1.6\cdot10^{6}$	0.042	0.048	10.7
HS-257	256.2 ± 4.7	15.6 ± 1.0	$6.0\cdot10^{6}$	0.027	0.082	7.9
HS-341	340.7 ± 7.5	20.1 ± 1.2	$1.4\cdot10^{7}$	0.020	0.062	5.8
HS-533	533.4 ± 12.5	23.5 ± 1.6	$6.0\cdot10^{7}$	0.012	0.071	4.8
HS-533-s	533.4 ± 12.5	23.5 ± 1.6	$6.0\cdot10^{7}$	0.012	0.037	2.5
HS-533-l	533.4 ± 12.5	23.5 ± 1.6	$6.0\cdot10^{7}$	0.012	0.116	7.5
HS-637	636.6 ± 13.4	21.9 ± 1.8	$1.1\cdot10^{8}$	0.010	0.087	4.3
CS-261	260.8 ± 4.6	~16	0	0	0	10.8

[a] *d: Diameter, t: Shell thickness,* [b] V_{pore}*: Inner pore volume of a single hollow silica nanoparticle,* S_{in}*: Inner surface area per particle,* [c] V_{in}*: Inner pore volume in 1 cm³,* V_{ex}*: Outer volume in 1 cm³, wt.%: Weight percentage.*

As can be seen from transmission electron microscopy (TEM) measurements, the diameter, *d*, ranges from 185 to 637 nm whereas the shell thickness, *t*, is around 20 nm. TEM images of polystyrene-silica core-shell particles (CS) and hollow silica spheres (HS) are shown in Figure 11.1. They demonstrate nearly perfect uniformity.

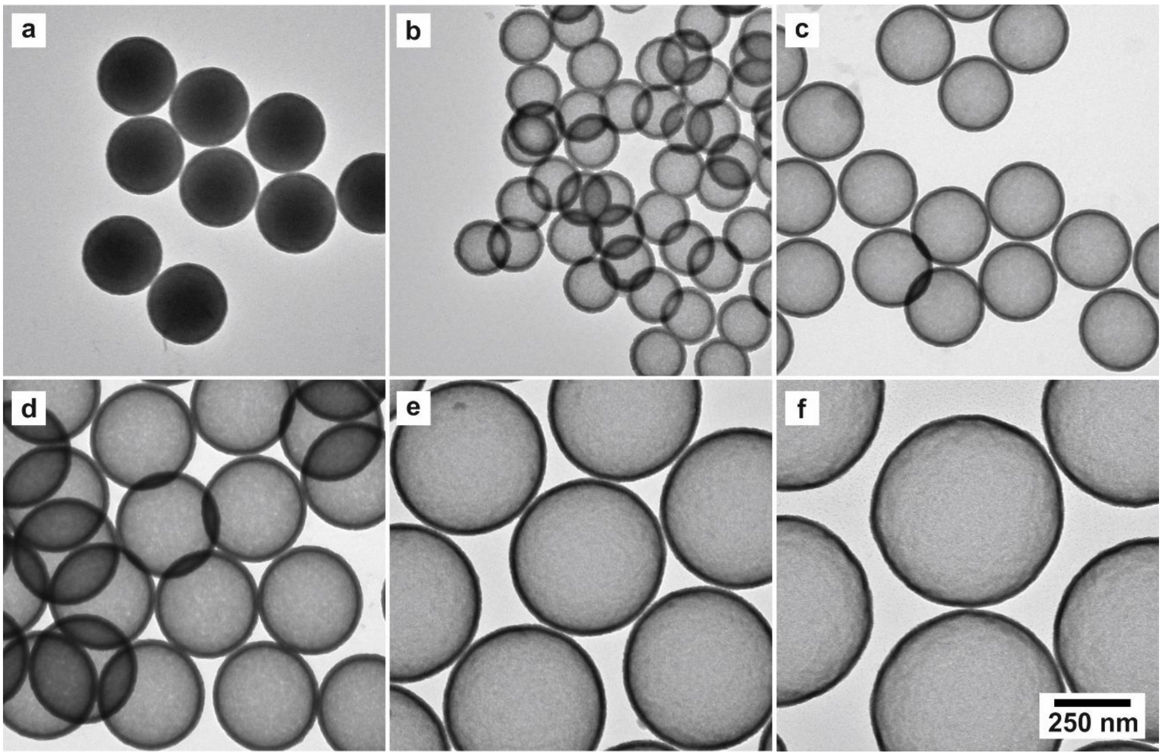

Figure 11.1. TEM images of polystyrene-silica core-shell particles (a) CS-261 and silica hollow spheres (b) HS-185, (c) HS-256, (d) HS-341, (e) HS-533 and (f) HS-637.

Characterization of the porous wall of HS spheres (pore volume and surface area) was made by nitrogen adsorption/desorption isotherms at 77 K. Pore volumes and pore size distributions were obtained by applying the nonlocal density functional theory (NLDFT) adsorption model for silica materials with cylindrical or spherical pore geometry (Figure S11.1 in the Supporting Information, Chapter 11.7). The isotherms do not exhibit a pronounced hysteresis. Furthermore, microporous cavities with a diameter of about 2 – 3 nm were derived using the Fraissard model for cylindrical pore geometry.

Thermal analysis of the aqueous dispersion was carried out using a Mettler Toledo differential scanning calorimeter (DSC-822). DSC traces of water/HS spheres were recorded using empty reference pans. All samples were first cooled at a rate of 10 °C/min from ambient temperature to -100 °C and then heated to 30 °C at the same rate under a nitrogen atmosphere (Supporting Information, Chapter 11.7). Dielectric measurements were performed as a function of temperature in the range from -90 °C to 30 °C, at atmospheric pressure, under isochronal conditions ($f = 1$ MHz) using a Novocontrol Alpha frequency analyzer (frequency range from 10^{-2} to 10^{6} Hz). For bulk water, the DS measurements were carried out with a Novocontrol cylindrical cell with electrodes of 10 mm in diameter and a sample thickness of 1 cm. For water/HS dispersions, a 20 mm electrode and silica spacers of 50 µm thickness were used (Supporting Information, Chapter 11.7).

Table 11.2. Summary of the results from nitrogen sorption analysis.

	N_2 sorption analysis		
	BET SA[a] **[m²/g]**	**DFT SA**[b] **[m²/g]**	**V_{pore}**[c] **[cm³/g]**
HS-185	170.3	151.1	0.137
HS-257	167.3	160.7	0.182
HS-341	170.6	161.1	0.166
HS-533	289.5	263.9	0.256
HS-533-s	89.5	63.9	0.256
HS-533-l	289.5	263.9	0.256
HS-637	189.3	179.6	0.213
CS-261	24.6	20.5	0.037

[a] BET SA: Surface area calculated by using BET method, [b] DFT SA: Surface area obtained from DFT analysis using NLDFT model on silica at 77 K, [c] V_{pore}: Pore volume obtained from DFT analysis using NLDFT model on silica at 77 K.

DSC of ice formation in water/hollow spheres shows two exothermic peaks (Figure 11.2): a major one in the temperature range from -19 to -22 °C and a smaller one in the range from -39 to -40 °C. For HS-637, the low-temperature exothermic process appears at -24 °C. With the exception of HS-637, we assign the crystallization peaks at higher and lower temperatures to water crystallized outside/inside the HS spheres, respectively (see below). Water outside the HS spheres is the majority component and crystallization proceeds via heterogeneous nucleation at low supercooling. Naturally, the heat associated with heterogeneous nucleation is high (ΔH_E~271 J/g and 250 J/g, respectively, for HS-637 and HS-185). The respective heats for the homogeneous nucleation process are ΔH_O~4 J/g and 5 J/g. On the other hand, the melting process shows a broad featureless peak with heats of 319 and 274 J/g, respectively, for HS-637 and HS-185. These heats should be compared with the enthalpy of melting of bulk ice of 328 J/g.[28]

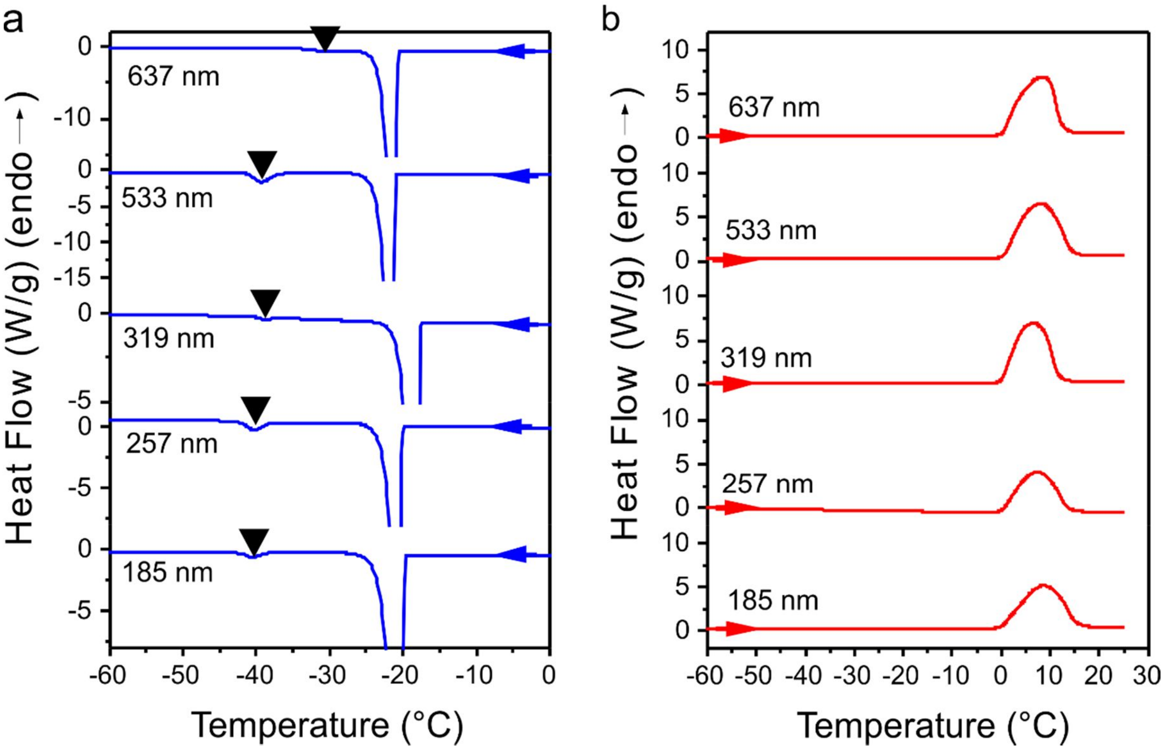

Figure 11.2. Differential scanning calorimetry traces of water/hollow silica spheres with different diameters obtained on (a) cooling and (b) heating with a rate of 10 °C/min. The vertical dashed line in (a) is a guide to the eye corresponding to the homogeneous nucleation temperature of confined water.

The higher crystallization temperature of HS-637 could be traced to less dense walls of this specific silica capsule. Furthermore, cracked spheres during dispersion via sonication and during repeated freeze-thawing have been more prominent in this case (the pressure-induced collapse of a thin spherical cell scales as Et^2/d, where E is the Young modulus).[23] This demonstrates that an intact and densely condensed silica shell is of paramount importance to support homogeneous nucleation in its interior. Such robust silica shells also withstand multiple freeze-thawing cycles without rupture or degradation.

Next, the high dielectric permittivity of water and its temperature-dependence was employed as a fingerprint of the mechanism of ice nucleation. At a cooling rate of 5 °C/min, bulk water freezes at -7.9 °C. The bulk dielectric permittivity first increases on cooling and below freezing assumes a low value corresponding to the limiting high-frequency permittivity of hexagonal ice (ε'_∞~3.2) (Figure 11.3). The dielectric permittivity of water/HS shows similar features: an increase in cooling and a discontinuous decrease within the temperature range from -7 to -11 °C to a permittivity value of ~4.5. Interestingly, on further cooling, there exists another small step towards a permittivity value of ~3.7. The values of the dielectric permittivity at high and low temperatures are in agreement with the prediction of an effective medium theory for heterogeneous dielectrics (Supporting Information, Chapter 11.7).[29] As with the DSC results, we assign these processes to ice formation via heterogeneous and homogeneous nucleation at low and high supercooling, respectively. The temperature location of the two nucleation mechanisms can better be seen in the derivative representation, $d\varepsilon'/dT$, in Figure 11.3c. On subsequent heating, there is a single melting process at 0 °C. Informative is the effect of increasing the HS content (from 2.5 wt.% to 7.5 wt.%) on the nucleation mechanisms (Figure 11.3d-f). The figure depicts dielectric permittivity measurements on cooling and subsequent heating of water/HS samples with increasing weight fraction of hollow silica spheres (HS-533) with a diameter of 533 nm. There is a clear increase in the step of dielectric permittivity ($\Delta\varepsilon_O$) for the low temperature mechanism in comparison to the step at higher temperatures ($\Delta\varepsilon_E$). Moreover, the ratio $\Delta\varepsilon_O/\Delta\varepsilon_E$ increases from 0.006 to 0.024 with increasing HS content as expected from the ratio of inner to outer volumes (Table 11.2). These results on the effect of HS content are supported by DSC measurements made on the same dispersions (Figure S11.2). The DSC results show an increasing heat of crystallization via the homogeneous nucleation mechanism ($\Delta H_E/\Delta H_O$~29, 13, and 7 for 2.5 wt.%, 4.8 wt.% and 7.5 wt.% of HS-533) with increasing HS content.

To verify further that homogeneous nucleation prevails in the HS we studied the crystallization of water in dispersions with polystyrene-silica core-shell particles (CS-261). This test is expected to differentiate between the two mechanisms as CS particles do not contain water and water exists only in one environment, *i.e.*, bulk-like water. Results on the dielectric permittivity and heat flow are depicted in Figure S11.3 and Figure S11.4, respectively. They both reveal crystallization via a *single* mechanism at low supercooling (ΔT~-2 °C). These findings suggest two well–resolved nucleation mechanisms correspond to two different water environments;

a bulk-like water crystallizing via heterogeneous nucleation at low supercooling and a confined water within the HS spheres crystallizing via homogeneous nucleation at higher supercooling. The likelihood of finding a heterogeneous nucleus inside a HS is low. The walls do not seem to be efficient nuclei. Of importance here is the role of the microporous cavities on the HS spheres (see below).

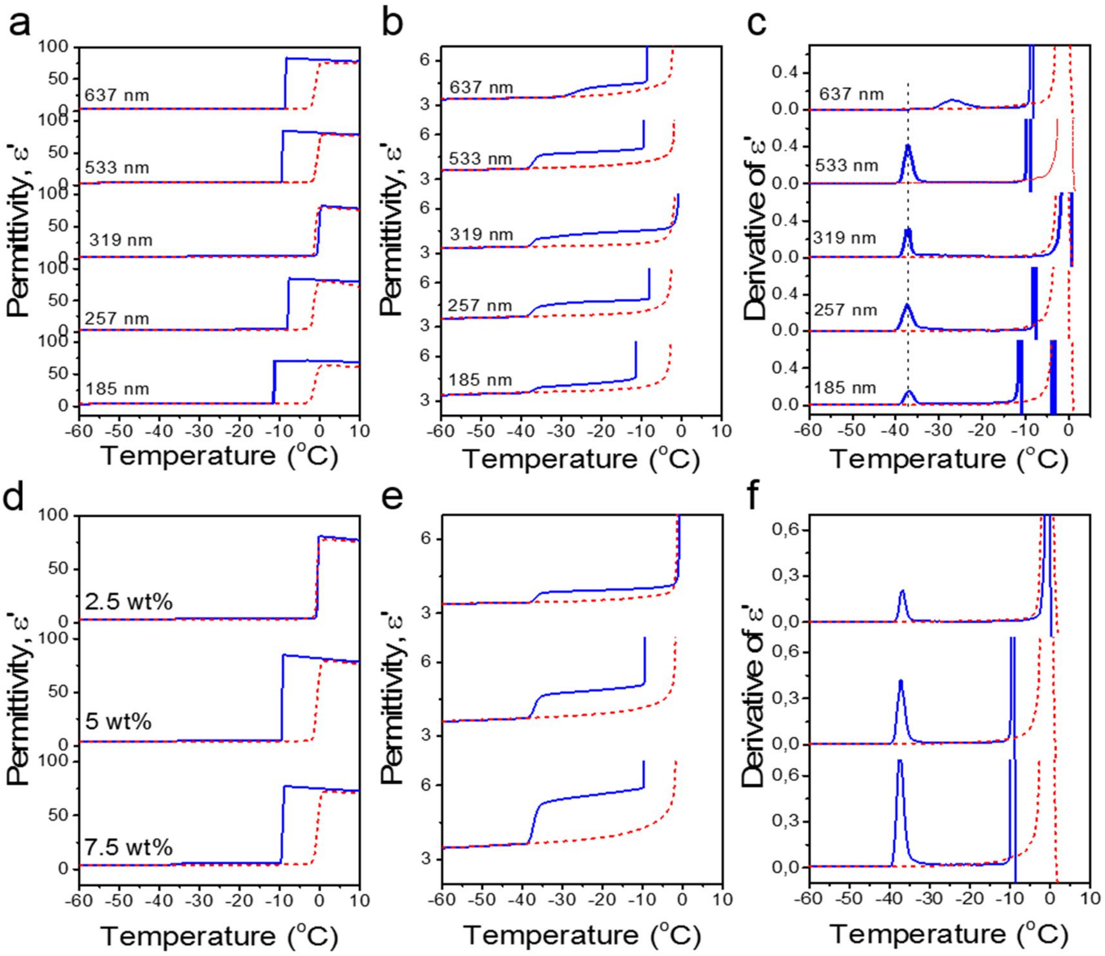

Figure 11.3. (a) Temperature dependence of the dielectric permittivity of water/hollow silica spheres with different diameters obtained on cooling (blue curves) and subsequent heating (red curves) with a rate of 5 °C /min. (b) Magnification of (a) in the region of low permittivity. (c) Derivative of dielectric permittivity, dε'/dT, as a function of temperature for the data shown in (a). (d) Temperature dependence of the dielectric permittivity of water/hollow silica spheres with a diameter of 533 nm for different weight fractions of hollow silica spheres as indicated. (e) Magnification of (d) in the region of low permittivity. (f) Derivative of dielectric permittivity as a function of temperature for the data shown in (d). In all cases, the frequency is 1 MHz.

The results of water crystallization in hollow silica spheres can be summarized in a pertinent "phase diagram". In Figure 11.4, the crystallization/melting temperatures are depicted as a function of the surface-to-volume ratio of spheres. This plot facilitates the comparison with water crystallization inside self-ordered AAO investigated earlier by some of us.[24-26] The temperatures of homogeneous nucleation, in the two -distinctly different- systems are in remarkable coincidence. In contrast, the temperatures of heterogeneous nucleation in HS spheres are independent of the surface-to-volume ratio whereas a strong dependence was found for water crystallized inside AAO. In addition, the temperature of crystallization via heterogeneous nucleation is identical to the crystallization temperature in dispersions of polystyrene-silica core-shell particles. In the latter system, bulk-like heterogeneous nucleation is the only possible crystallization mechanism, hence the high-temperature crystallization process in HS spheres has the same origin, *i.e.*, crystallization initiated via heterogeneous nuclei. Note that differences in crystallization temperatures by DSC and DS reflect the different cooling rates (see also Figure S11.5). The mechanism at lower temperatures deserves some attention. It is assigned to homogeneous nucleation since water molecules are infiltrated through the microporous cavities in the silica shell. Effectively, this filters away all heterogeneities above a size of ~3 nm, leaving homogeneous nucleation as the sole nucleation mechanism for water located inside HS spheres. The assignment of the low-temperature process in the smaller HS spheres to homogeneous nucleation (and of the low-temperature feature of HS-637 to heterogeneous nucleation) becomes more evident by comparison with the onset of homogeneous ice nucleation in supercooled water microdroplets as a function of the droplet volume (Figure 11.4).[7] Overall, our results support the notion that nucleation of ice is volume-dominated. On the other hand, the possibility that the low-temperature process originates from nucleation within the micropores of the silica network (and not in the HS interior) can be excluded as the corresponding nucleation temperatures (Figure 11.4) for such volumes is well below -40 °C.

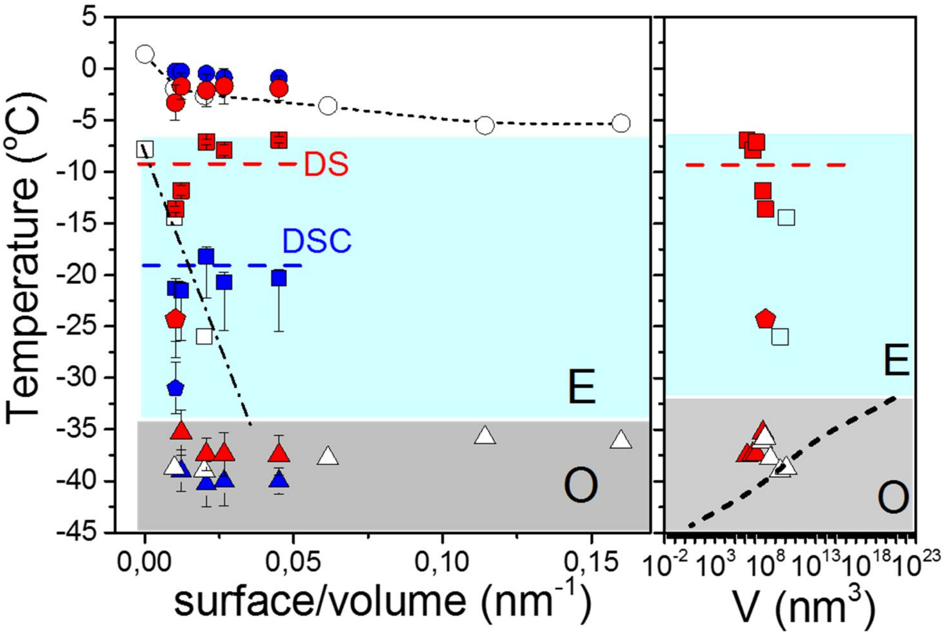

Figure 11.4. (Left) Phase diagram of water in hollow silica spheres (filled symbols) compared to water located inside self-ordered AAO (open symbols)[24] as a function of the surface-to-volume ratio. Red and blue symbols represent results from DS and DSC, respectively. The circles indicate the melting temperatures. The squares indicate the process of heterogeneous nucleation. The triangles indicate crystallization via homogeneous nucleation. Grey and blue areas correspond to ice formation via homogeneous (O) and heterogeneous (E) nucleation, respectively. The dash-dotted line gives the heterogeneous nucleation of ice in self-ordered AAOs.[24] The horizontal dashed line gives the temperature of heterogeneous nucleation in polystyrene-silica core-shell particles (CS-261) from DS (red) and DSC (blue). (Right) Dependence of the homogeneous nucleation temperature on volume. The black dashed line gives the reported lowest temperatures for homogeneous nucleation of water droplets as a function of their volume (cooling rate of ~1 °C/min). [7]The symbols and shaded areas have the same meaning.

Valuable information on the state of supercooled water/ice in the confined environment of HS spheres can be obtained from ^{1}H MAS NMR measurements. Figure 11.5 gives the MAS spectra of water/HS spheres with a diameter of 533 nm at -20 °C. The spectrum is composed of a narrow and a broad component associated, respectively, with a small fraction of undercooled water and a larger fraction of ice. In general, the linewidth of liquid water is determined by the chemical shift distribution of all populated states of water molecules in the liquid state, as well as from the exchange rate of the molecules between those different states. Moreover, differences in the dipolar dephasing efficiency of water, typically expressed as T_2 relaxation time, will contribute to the linewidth of liquid water.

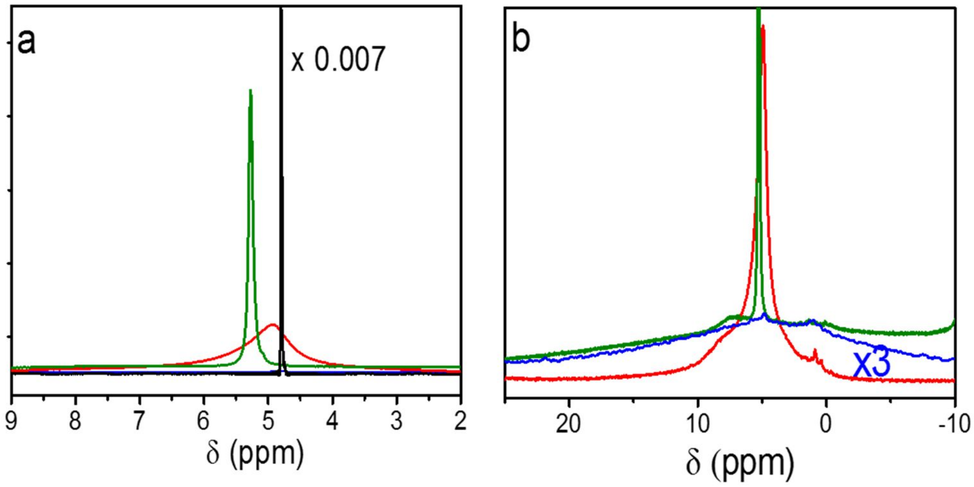

Figure 11.5. MAS spectra at a Larmor frequency of 20 KHz for (i) water/HS spheres with diameter of 533 nm at -20 °C (green line), (ii) water located inside AAO with pore diameter of 400 nm at -20 °C (red line), (iii) bulk water at 1 °C (black line), and (iv) bulk hexagonal ice at -20 °C (blue line), and in the regions of (a) liquid and (b) solid components. Bulk water and bulk ice spectra in (a) and (b), respectively, have been scaled (respective factor x0.007 and x3).

By comparing the linewidth of the broader component with that of bulk hexagonal ice recorded at the same temperature (Figure 11.5b) we conclude that ice in water/HS spheres at -20 °C has the same characteristics (broadening, chemical shift) as bulk hexagonal ice.[26] This is understandable as at this temperature ice formation takes place via heterogeneous nucleation at the bulk of the dispersion, *i.e.*, outside the HS spheres. The narrower component associates with a small fraction of undercooled water, that based on DS and DSC, will freeze only at a lower temperature (-37 °C) via homogeneous nucleation. A quantitative analysis comparing the signal intensity of the ice and water signals -by peak deconvolution- is not feasible (the background suppression sequence will suppress some very broad contributions to the ice spectrum and therefore lead to a systematic overestimation of supercooled water). Interestingly, this fraction of supercooled water is much more mobile than water located inside AAO pores with a diameter of 400 nm and measured at the same temperature (Figure 11.5b)[26] but slower than bulk water measured at 1 °C (Figure 11.5a).

11.3 Conclusions

In conclusion, increasing the hollow silica sphere content engenders ice nucleation via homogeneous nucleation as opposed to the expected heterogeneous nucleation found in water located outside polystyrene-silica core-shell particles. These results support the observation already made with water in nanoporous alumina; heterogeneous nucleation is suppressed in small volumes irrespective of the geometry of confinement. The present findings shed new light on the interplay between homogeneous and heterogeneous nucleation of ice with possible implications in the storage of reactive or biologically active substances. As an example, we refer to supercooled micro flow in microchannels of an aqueous/organic two-phase reaction with a chiral phase-transfer catalyst. There enantiomeric selectivity was found to increase with decreasing temperature of supercooled water.[30]

11.4 Experimental Details

Materials

Styrene (≥ 99 %, Aldrich), 2,2′-Azobis(2-methylpropionamidine) dihydrochloride (AIBA; 97 %, Aldrich), 2-Methacryloxy-ethyltrimethylammonium chloride (MTC; 70 % solution in water, Polyscience), Polyvinylpyrrolidone K30 (PVP; Mw ~ 55 kg/mol, Aldrich), Tetraethyl orthosilicate (TEOS; ≥99 %, Aldrich) and Ammonium hydroxide solution (30 - 33 % in water, Aldrich) were used as received. 2,2′-Azobis(2-methylpropionitrile) (AIBN; ≥98.0%, Aldrich) was recrystallized from methanol. Ethanol (EtOH) was used in technical grade and water was taken from a Millipore Direct Q3UV unit for the entire synthesis and purification steps.

Synthesis of hollow silica spheres

The synthesis of hollow silica spheres comprises three steps: (1) Synthesis of polystyrene particles, (2) Coating of polystyrene template particles with a silica shell *via* a modified Stoeber process and (3) Calcination of the core-shell particles to remove the polystyrene core.

(1) Synthesis of polystyrene particles

Two different techniques were used to obtain monodisperse polystyrene particles. Smaller particles (140 - 275 nm) were obtained by emulsifier-free emulsion polymerization[31] and larger particles (495 - 580 nm) by dispersion polymerization. In the following, the synthesis of the smallest and largest particles is described.

Emulsifier-free emulsion polymerization: The synthesis was carried out in a three-necked flask, equipped with a reflux condenser and a gas inlet, which allows a slight argon flow during the synthesis. First, 100 mL water, 13 mL styrene, 300 µL MTC and 0.9 g PVP were heated to 70 °C at a stirring rate of 850 rpm with a magnetic stirrer egg. After an equilibration time of 30 min, 0.3 g AIBA, dissolved in 20 mL water, were added to initiate the polymerization. After nucleation, the stirring speed was reduced to 450 rpm and the reaction was carried out overnight.

Dispersion polymerization: The dispersion polymerization was carried out in a single-neck flask connected to a KPG stirrer rotating at a rate of 60 rpm. First, 130 mL ethanol (EtOH), 14 mL water, 10 mL styrene and 5 g PVP were purged with argon, while heating the reaction mixture to 75 °C. After an equilibration time of 30 min, the gas inlet was removed, 0.136 g AIBN, dissolved in 6 mL ethanol, were added to initiate the polymerization and the stirrer was set to 60 rpm. After 1.5 h, 400 µL MTC were added. The reaction was carried out overnight.

For both polystyrene synthesis methods, different sizes can be obtained by adjusting the amount of comonomer, initiator and the ethanol/water ratio in the dispersion polymerization.

(2) Silica coating of the polystyrene particles

The silica coating was achieved by a Stoeber condensation process.[32] In the following, the coating process is exemplarily described for the smallest particles:

84.8 vol.% EtOH, 6.7 vol.% aqueous polystyrene dispersion (8.4 wt.%) and 6.3 vol.% NH_4OH solution were stirred at 400 rpm in a single-neck flask. After stepwise addition of 2.2 vol.% TEOS the reaction was stirred overnight at room temperature. The core/shell particles were purified by repeated centrifugation and redispersed in water.

(3) Calcination of polystyrene-silica core-shell particles

In order to obtain hollow spheres, the samples were dried and calcined in a furnace (Nabertherm L5/11/P33) at 500 °C in air for 12 h. The hollow spheres were redispersed in water using mild sonication in a sonication bath.

Overall five different hollow silica nanoparticles and one core-shell particle as reference sample were synthesized. The concentration of the dispersions were adjusted between 2.5 and 10.7 wt.%. For sample HS-533, dispersions with a small (2.5 wt.%, HS-533-s) and a large (7.5 wt.%, HS-533-l) concentration were additionally prepared. The data for the synthesized particles and the concentrations are shown in Table 11.1.

Characterization

Transmission electron microscopy (TEM) images were taken on a Zeiss CEM 902 instrument in bright field imaging mode at an acceleration voltage of 80 kV.

Nitrogen sorption measurements were carried out on a Quantachrome Autosorb AS-1 pore analyzer at 77 K. Prior to the measurements, all sample were preconditioned to remove water residues. The hollow silica nanoparticle samples were preconditioned in a vacuum at 350 °C for 12 hours and the core-shell particle sample was preconditioned in a vacuum at 90 °C for 20 hours. For the analysis, the Quantachrome ASiQ v3.0 software was used. The specific surface areas were calculated using the BET method and the DFT method. Pore volumes and pore size distributions were obtained by applying the nonlocal density functional theory (NLDFT) adsorption model for silica materials with cylindrical or spherical pore geometry.

Differential scanning calorimetry (DSC) - Thermal analysis was carried out using a Mettler Toledo differential scanning calorimeter (DSC-822). DSC traces of bulk water were acquired using an empty pan as a reference. Samples were weighed with a Mettler Toledo AX205 balance. Subsequently, 10 mg of water/HS solution was sealed in aluminum pans (100 µl). All samples were first cooled at a rate of 50 °C/min from ambient temperature to -100 °C, and then heated to 30 °C at the same rate under a nitrogen atmosphere. In a second experiment, the rate dependence of the melting and crystallization temperatures was investigated for water/HS spheres with a diameter of 533 nm. In this experiment, samples were heated to 100 °C and DSC cooling/heating curves were obtained with rates of 30, 10, 5 and 2 °C /min.

Dielectric measurements were performed at temperatures in the range of -90 °C to 30 °C, at atmospheric pressure, under isochronal conditions ($f = 1$ MHz) using a Novocontrol Alpha frequency analyzer (frequency range from 10^{-2} to 10^{6} Hz) as a function of temperature. For bulk water, the DS measurements were carried out with a Novocontrol cylindrical cell with electrodes of 10 mm in diameter and sample thickness of 1cm. In all cases, the complex dielectric permittivity $\varepsilon^*=\varepsilon'-i\varepsilon''$, where ε' is the real and ε'' is the imaginary part, was obtained at 1 MHz. The dielectric function of heterogeneous dielectric comprising a matrix (m), an interfacial layer (l) and filler (f) contributions are given by an effective medium approach as[33]:

$$\varepsilon_c^* = \frac{\varepsilon_f^*\varphi_f + \varepsilon_l^*\varphi_l R + \varepsilon_m^*\varphi_m S}{\varphi_f + \varphi_l R + \varphi_m S}$$

$$R = \frac{(1-n)\varepsilon_l^* + n\varepsilon_f^*}{\varepsilon_l^*}$$

$$S = \frac{[n\varepsilon_l^* + (1-n)\varepsilon_m^*]\left[n\varepsilon_f^* + (1-n)\varepsilon_l^*\right] + dn(1-n)(\varepsilon_l^* - \varepsilon_m^*)(\varepsilon_f^* - \varepsilon_l^*)}{\varepsilon_l^*\varepsilon_m^*}$$

Here $d=\varphi_f/(\varphi_f+\varphi_l)$, and n is the depolarization factor of the filler particle in the field direction. In the present case, $\varphi_f=\varphi_m=\varphi_{water}$, $n=1/3$ and $\varepsilon_l^*=\varepsilon_l'=3.8$. By further assuming $\varepsilon'_{water}=82$ and $\varepsilon'_{ice}=3.2$ we obtain for the composite $\varepsilon'_c=73$ and 3.7 for water and ice, respectively. These values are very close to the experimentally measured values of permittivity at high and low temperatures.

^{1}H MAS NMR spectroscopy measurements have been performed with a Bruker Avance III console operating at 850 MHz ^{1}H Larmor frequency in the temperature range between 230 and 290K at 20 kHz MAS spinning frequency. The measurements have been performed using a commercial MAS double resonance probe supporting 2.5 mm MAS rotors. The temperature has been calibrated using the temperature dependent ^{79}Pb chemical shift of lead nitrate as described in the literature. A Bruker BCU II cooling unit has been used with a VT gas flow of 1500 l/h. The ^{1}H MAS NMR signals have been recorded using the EASY scheme, in order to suppress the ^{1}H probe back and the ringing artifacts of the rf coil.

11.5 Acknowledgements

P.R. thanks the Elite Network Bavaria. Dr. Markus Drechsler and Dr. Beate Förster are acknowledged for help with the electron microscopy characterization. We thank Marco Schwarzmann for the nitrogen sorption measurements.

11.6 References

1. Mishima, O.; Stanley, H.E. The relationship between liquid, supercooled and glassy water. *Nature* **1998**, 396, 329-335.

2. Debenedetti, P.G. Supercooled and glassy water. *J. Phys.: Condens. Matter.* **2003**, 15, R1669-R1726.

3. Russo, J., Romano, F., Tanaka, H. New metastable form of ice and its role in the homogeneous crystallization of water. *Nature Mater.* **2014**, 13, 733-739.

4. Angell, C.A. Supercooled water. *Ann. Rev. Phys. Chem.* **1983**, 34, 593-630.

5. Alba-Simionesco, C.; Coasne, B.; Dosseh, G.; Dudziak, K.E.; Gubbins, R.; Radhakrishnan, R.; Sliwinska-Bartkowiak, M. Effects of confinement on freezing and melting. *J. Phys. Condens. Matter* **2006**, 18, R15.

6. Huang, J.; Bartell, L.S. Kinetics of homogeneous nucleation in the freezing of large water clusters. *J. Phys. Chem.* **1995**, 99, 3924-3931.

7. Pruppacher, H.R. A new look at homogeneous ice nucleation in supercooled water drops. J. Atmos. Sci. **1995**, 52, 1924-1933

8. Manka, A.; Pathak, H.; Tanimura, S.; Wölk, J.; Strey, R.; Wyslouzil, B.E. Freezing water in no-man's land. *Phys. Chem. Chem. Phys.* **2012**, 14, 4505-4516.

9. Stan, C.A.; Schneider, G.F.; Shevkoplyas, S.S.; Hashimoto, M.; Ibanescu, M.; Wiley, B.J.; Whitesides, G.M. A microfluidic apparatus for the study of ice nucleation in supercooled water droplets. *Lab Chip* **2009**, 9, 2293-2305.

10. Steytler, D.C.; Dore, J.C.; Wright, C.J. Neutron diffraction study of cubic ice nucleation in a porous silica network. *J. Phys. Chem.* **1983**, 87, 2458-2459.

11. Morishige, K.; Kawano, K. Freezing and melting of water in a single cylindrical pore: The pore-size dependence of freezing and melting behavior. *J. Chem. Phys.* **1999**, 110, 4867-4872.

12. Dore, J. Structural studies of water in confined geometry by neutron diffraction. *Chemical Physics* **2000**, 258, 327-347.

13. Rault, J.; Neffati, R.; Judeinstein, P. Melting of ice in porous glass: why water and solvent confined in small pores do not crystallize? *Eur. Phys. J. B*. **2003**, 36, 627-637.

14. Findenegg, G.H., Jähnert, S., Akcakayiran, D., Schreiber, A. Freezing and melting of water confined in silica nanopores. *ChemPhysChem* **2008**, 9, 2651-2659.

15. Johari, G.P. Origin of the enthalpy features of water in 1.8 nm pores of MCM-41 and the large C_p increase at 210 K. *J. Chem. Phys.* **2009**, 130, 124518:1-6.

16. Tombari, E.; Johari, G.P. On the state of water in 2.4 nm cylindrical pores of MCM from dynamic and normal specific heat measurements. *J. Chem. Phys.* **2013**, 139, 064507:1-9.

17. Limmer, D.T.; Chandler, D. Phase diagram of supercooled water confined to hydrophilic nanopores. *J. Chem. Phys.* **2012**, 137, 044509.

18. Seyed-Yazdi, J.; Dore, J.C.; Webber, J.B.W.; Farman, H. Structural characteristics of water and ice in mesoporous SBA-15 silica IV: partially filled case for 86 Å pore diameter. *J. Phys.: Condens. Matter.* **2013**, 25, 465105.

19. Alabarse, F.G.; Haines, J.; Cambon, O.; Levelut, C.; Bourgogne, D.; Haidoux, A.; Granier, D.; Coasne, B. Freezing of water confined at the nanoscale. *Phys. Rev. Lett.* **2012**, 109, 035701.

20. Giovambattista, N.; Rossky, P.J.; de Benedetti, P.G. Effect of temperature on the structure and phase behavior of water confined by hydrophobic, hydrophilic, and heterogeneous surfaces. *J. Phys. Chem.* **2009**, 113, 13723.

21. Ruckdeschel, P.; Kemnitzer, T.W.; Nutz, F.A.; Senker, J.; Retsch, M. Hollow silica sphere colloidal crystals: insights into calcination dependent thermal transport. *Nanoscale* **2015**, 7, 10059.

22. Retsch, M.; Schmelzeisen, M.; Butt, H.-J.; Thomas, E.L. Visible Mie Scattering in Nonabsorbing Hollow Sphere Powders. *Nano Lett.* **2011**, 11, 1389.

23. Yin, J.; Retsch, M; Thomas, E.L.; Boyce, M.C. Collective Mechanical Behavior of Multilayer Colloidal Arrays of Hollow Nanoparticles. *Langmuir* **2012**, 28, 5580.

24. Suzuki, Y.; Duran, H.; Steinhart, M.; Kappl, M.; Butt, H.-J.; Floudas, G. Homogeneous nucleation of predominantly cubic ice confined in nanoporous alumina. *Nano Lett.* **2015**, 15, 1987-1992.

25. Suzuki, Y.; Steinhart, M.; Butt, H.-J.; Floudas, G. Kinetics of ice nucleation confined in nanoporous alumina. *J. Phys. Chem. B.* **2015**, 119, 11960-11966.

26. Suzuki, Y.; Steinhart, M.; Graf, R.; Butt, H.-J.; Floudas, G. Dynamics of ice/water confined in nanoporous alumina. *J. Phys. Chem. B* **2015**, 119, 14814-14820.

27. Zhang, L., M. D'Acunzi, M. Kappl, A. Imhof, A. van Blaaderen, H.-J. Butt, R. Graf, D. Vollmer. Tuning the mechanical properties of silica microcapsules. *Phys. Chem. Chem. Phys.* **2010**, 12, 15392-15398.

28. Sugisaki, M.; Suga, H.; Seki, S. *Bull. Chem. Soc.* Japan **1968**, 41, 2591-2599.

29. Kremer, F.; Schoenhals, A. *Broadband Dielectric Spectroscopy*, Ch. 13: Dielectric properties of inhomogeneous media; Steeman, P.A.M.; van Turnhout, J. Springer: Berlin, 2002.

30. Matsuoka, S.; Hibara, A.; Ueno, M.; Kitamori, T. Supercooled micro flows and application for asymmetric synthesis. *Lab Chip* **2006**, 6, 1236-1238.

31. Chung-li, Y.; Goodwin, J. W.; Ottewill, R. H., Studies on the preparation of monodisperse polystyrene latices. 1976, 60, 163-165.

32. Stöber, W.; Fink, A.; Bohn, E., Controlled Growth of Monodisperse Silica Spheres in Micron Size Range. J Colloid Interface Sci 1968, 26, 62-69.

33. Kremer, F.; Schoenhals, A. Broadband Dielectric Spectroscopy, Ch. 13: Dielectric properties of inhomogeneous media; Steeman, P.A.M.; van Turnhout, J. Springer: Berlin, 2002.

11.7 Supporting Information

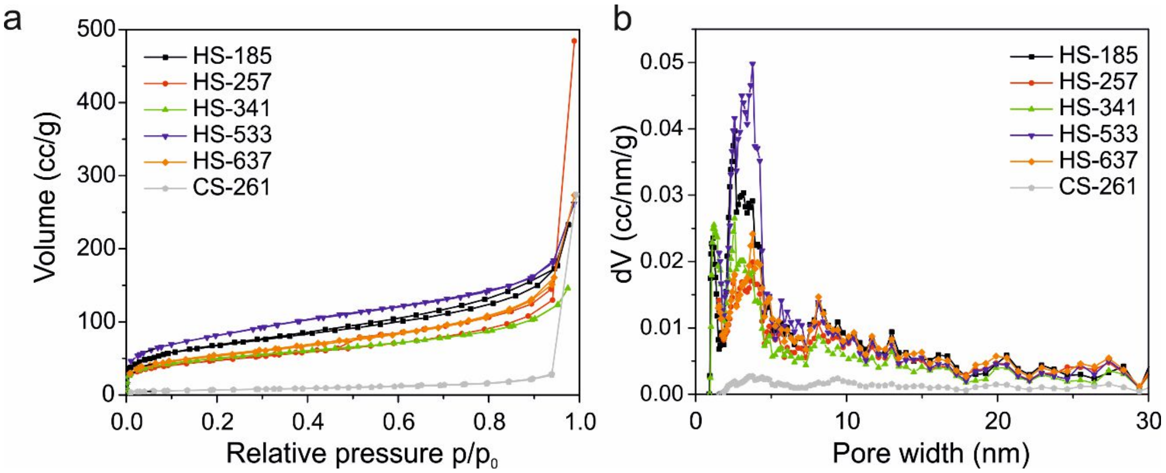

Figure S11.1. Characterization of the internal structure of hollow silica spheres: (a) Nitrogen adsorption/desorption isotherms at 77 K used in determining the pore volume and surface area. (b) Pore radius distribution. Pore volumes and pore size distributions were obtained by applying the nonlocal density functional theory (NLDFT) adsorption model for silica materials with cylindrical or spherical pore geometry.

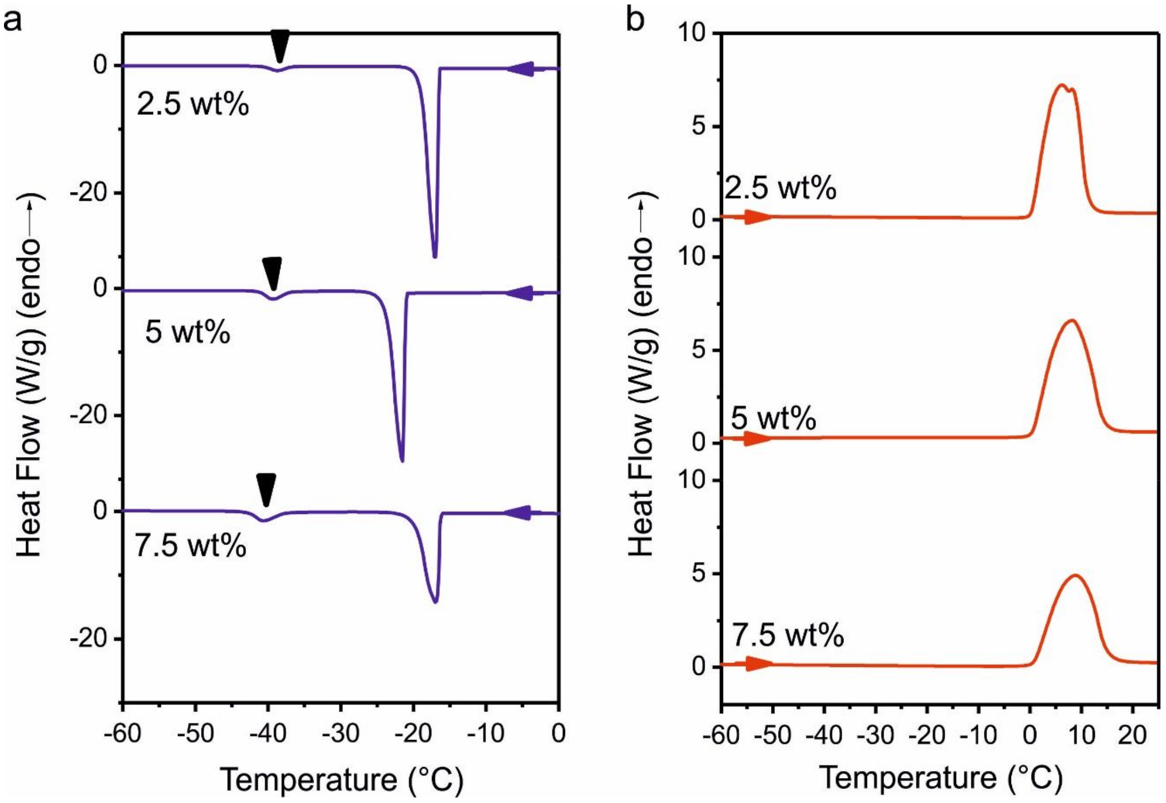

Figure S11.2. Differential scanning calorimetry traces of water/hollow silica spheres with different weight fractions of hollow silica spheres (diameter 533 nm) as indicated obtained on (a) cooling and (b) heating with a rate of 10 °C/min.

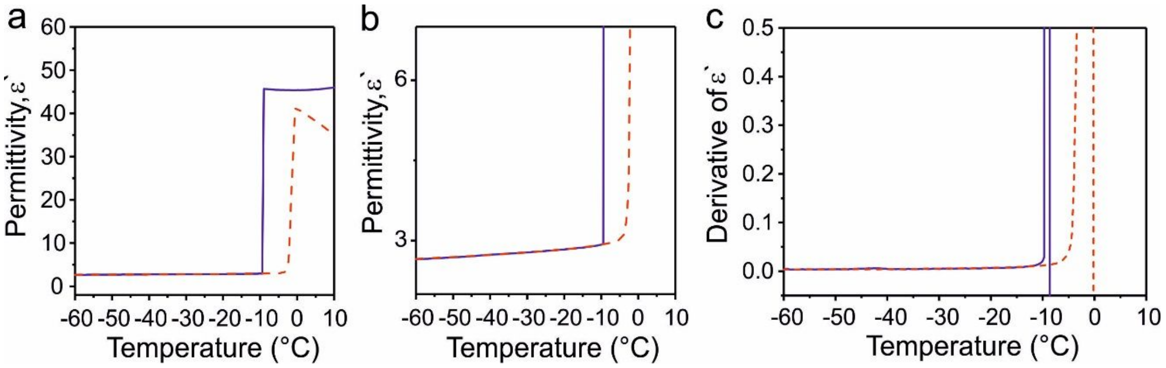

Figure S11.3. (a) Temperature dependence of the dielectric permittivity of water/polystyrene-silica core-shell particles (CS-261) with a diameter of 261 nm obtained on cooling (blue curves) and subsequent heating (red curves) with a rate of 5 °C/min. (b) Magnification of (a) in the region of low permittivity. (c) Derivative of dielectric permittivity, dε'/dT, as a function of temperature for the data shown in (a). In all cases the frequency is 1 MHz.

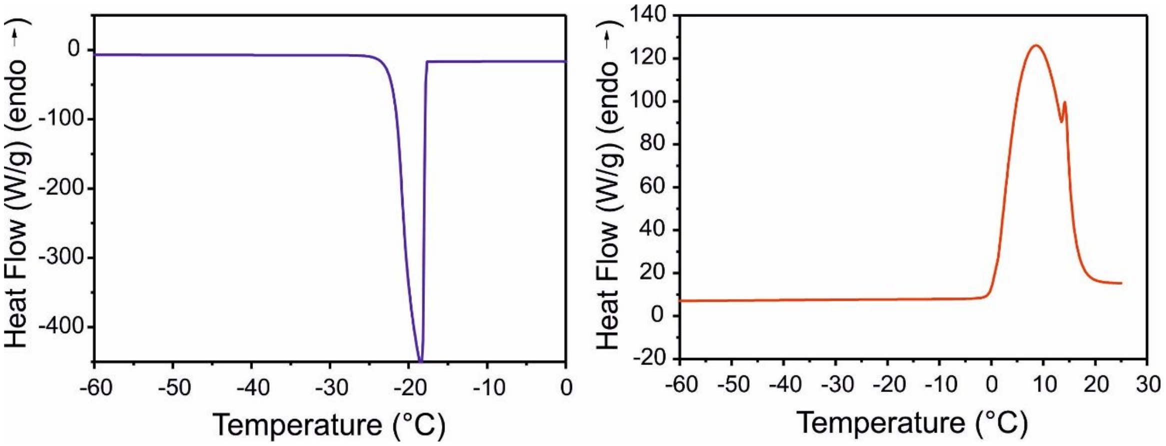

Figure S11.4. Differential scanning calorimetry traces of water/polystyrene-silica core-shell particles (CS-261) with a diameter of 261 nm obtained on cooling (blue curve) and heating (red curve) with a rate of 10 °C/min.

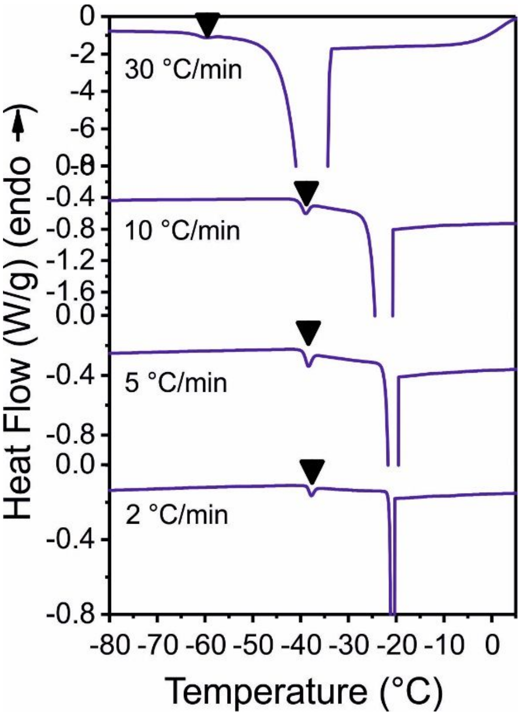

Figure S11.5. Differential scanning calorimetry traces of water/hollow silica spheres (diameter 319 nm) with different cooling rates as indicated.

12 Conclusion and Outlook

In this thesis heat transport in nano- and mesostructured materials is studied in detail. The focus was laid on the structure-property relationship regarding the thermal properties. For this purpose, it was indispensable to have a well-defined material. Colloidal crystals, composed of monodisperse particles, fulfill this demand. As building blocks, silica hollow spheres, polymer latex particles, or core-shell particles were used.

First, silica hollow sphere colloidal crystals were studied. This material class combines several advantageous features, like the breathability due to the open-porous structure, the non-flammability based on the silica network and the dispersion-processability like spraying or painting. A comprehensive study of the heat transport in silica hollow sphere colloidal assemblies revealed the great insulation properties. By adjusting the aspect ratio, the microstructure, the contact points, the symmetry and the pore sizes, a very low thermal conductivity of ~35 $\mathrm{mW\,m^{-1}\,K^{-1}}$ in air and <10 $\mathrm{mW\,m^{-1}\,K^{-1}}$ in vacuum was obtained. The findings of this work are also applicable to other nanoporous, particulate materials and will help to create novel insulation materials. However, a major drawback of these colloidal crystals compared to polymer foams constitute the mechanical properties, which will presumably underperform. Therefore, one can consider adsorbing polymer or sheet materials (e.g., clays, or graphene oxide sheets) to the surface of the silica hollow spheres. These may significantly improve the mechanical stability. Furthermore, silica capsules can be incorporated into a matrix with enhanced mechanical properties, for instance, a polymer matrix.

In the second part of this work, the structure-property control was utilized to investigate hybrid materials, like core-shell particles and binary particle mixtures. These two material classes are model systems for phase change materials and heat spreading materials. In future studies, it would be worthwhile to transfer the knowledge. Especially, for the binary particle mixtures, it would be very interesting to exchange the polymer particles with highly conducting particles like hollow gold spheres. Thus, the simulated results could be validated, and the percolation mechanism could be studied experimentally.

This work reveals the great potential of the underexplored world of thermal transport in colloids. In the future, a wide range of further studies can be conceived to exploit the potential given by such colloidal assemblies fully. One focus may be laid on multifunctional materials, in which the thermal properties are combined with (i) electrical conductivity leading to thermoelectric materials, (ii) optical properties to obtain, for instance, transparent insulation materials, or (iii) improved mechanical properties.

13 Danksagung

Abschließend möchte ich mich gerne bei allen bedanken, die diese Arbeit ermöglicht und zu ihrem Gelingen beigetragen haben.

Mein erster Dank gilt meinem Doktorvater Herrn Prof. Dr. Markus Retsch. Insbesondere für die interessante Themenstellung, die gute Betreuung und die Möglichkeit an zahlreichen Konferenzen teilzunehmen, möchte ich mich herzlich bedanken.

Weiterhin danke ich meinen zahlreichen Kooperationspartnern für die tolle Zusammenarbeit. Vielen Dank insbesondere an Fabian Nutz, Herrn Prof. Senker, Tobias Kemnitzer, Herrn Prof. Floudas, Yang Yao und Alexandra Philipp. In diesem Zuge bedanke ich mich auch bei den Mitarbeitern der Key Labs und anderen Lehrstühlen für die Einweisung in Geräte oder die Messung von Proben: Martina Heider, Dr. Beate Förster, Dr. Markus Drechsler, Ute Kuhn, Lena Geiling und Marco Schwarzmann. Vielen Dank auch an Miriam Mauer und Christian Stelling.

Weiterhin möchte ich allen danken, die den Labor- und Lehrstuhlbetrieb am Laufen gehalten haben: Karlheinz Lauterbach, Julia Moßner, Stephan Hauschild, Elisabeth Düngfelder und Jennifer Hennesy.

Danke auch an alle Praktikanten, Bacheloranden und Masteranden, die ich während meiner Promotion betreuen durfte.

Liebe Retsch-Gruppe, liebe Karg-Gruppe, liebe PC I – vielen Dank für die schöne Zeit und die tolle Atmosphäre am Lehrstuhl! Die Konferenzen, die gemeinsamen Mittagspausen, das Grillen auf der Terrasse und all die anderen Freizeitaktivitäten haben die Zeit am Lehrstuhl wirklich unglaublich bereichert und zu etwas ganz Besonderem gemacht. Ihr seid klasse!

Zum Abschluss möchte ich mich noch bei mir sehr wichtigen Personen außerhalb des Uni-Lebens bedanken. Herzlichen Dank an meine Familie, besonders auch an

Andreas und vielen Dank an meine Mädels Tina, Franzi, Mareike und Mandy. Ich liebe euch! ♥

14 Erklärung des Verfassers

(§ 5 Nr. 4 PromO) Hiermit erkläre ich, dass keine Tatsachen vorliegen, die mich nach den gesetzlichen Bestimmungen über die Führung akademischer Grade zur Führung eines Doktorgrades unwürdig erscheinen lassen.

(§ 8 Nr. 5 PromO) Hiermit erkläre ich mich damit einverstanden, dass die elektronische Fassung meiner Dissertation unter Wahrung meiner Urheberrechte und des Datenschutzes einer gesonderten Überprüfung hinsichtlich der eigenständigen Anfertigung der Dissertation unterzogen werden kann.

(§ 8 Nr. 7 PromO) Hiermit erkläre ich eidesstattlich, dass ich die Dissertation selbständig verfasst und keine anderen als die von mir angegebenen Quellen und Hilfsmittel benutzt habe.

(§ 8 Nr. 8 PromO) Ich habe die Dissertation nicht bereits zur Erlangung eines akademischen Grades anderweitig eingereicht und habe auch nicht bereits diese oder eine gleichartige Doktorprüfung endgültig nicht bestanden.

(§ 8 Nr. 9 PromO) Hiermit erkläre ich, dass ich keine Hilfe von gewerblichen Promotionsberatern bzw. -vermittlern in Anspruch genommen habe und auch künftig nicht nehmen werde.

Bayreuth, 28.08.2017

Pia Ruckdeschel